Friedrich-Alexander-Universität
Faculty of Sciences

Doctoral thesis

2026

Florian Georg Beißer

Spectrometry, Eye Lens Dosimetry Studies, and Electron Beam Monitoring with the Dosepix Detector

Spektrometrie, Studien zu Augenlinsendosimetrie und Elektronenstrahlüberwachung mit dem Dosepix-Detektor

Spectrometry, Eye Lens Dosimetry Studies, and Electron Beam Monitoring with the Dosepix Detector

Spektrometrie, Studien zu Augenlinsendosimetrie und Elektronenstrahlüberwachung mit dem Dosepix-Detektor

der Naturwissenschaftlichen Fakultät

der Friedrich-Alexander-Universität Erlangen-Nürnberg

zur

Erlangung des Doktorgrades Dr. rer. nat.

vorgelegt von

Florian Georg Beißer

Als Dissertation genehmigt
von der Naturwissenschaftlichen Fakultät
der Friedrich-Alexander-Universität Erlangen-Nürnberg

Tag der mündlichen Prüfung: 29.06.2026

Gutachter:
Prof. Dr. Stefan Funk
Prof. Dr. Ivor Fleck

Abstract

In this work, the performance of the hybrid, pixelated, photon-counting, energy-resolving detector Dosepix is tested for various applications. The detector consists of 16 x 16 pixels with a pitch of 220 µm. It is attached to a 300 µm thick silicon sensor, doped to comprise 12 x 16 large quadratic pixels with an edge length of 220 µm and 4 x 16 small quadratic pixels with an edge length of 55 µm. Dosepix measures deposited energies in units of its internal measure *time-over-threshold (ToT)*. Analyzing the ToT-response of Dosepix with 5.6 MeV α-particles reveals a deviation from the previously known linear behaviour for deposited energies $\geq (567 \pm 6)$ keV. The ToT is observed to stay constant until $(1.7 \pm 0.6) \cdot 10^3$ keV before increasing quadratically. On top of those findings, a framework for simulating the ToT-response of the charge-sensitive amplifier of Dosepix with respect to the exposed event rate is presented.

The performance of a Dosepix-based spectrometer for photon and electron fields to characterize spectra in FLASH radiotherapy is investigated with Monte-Carlo simulations. Photon energies from 10 keV to 2500 keV and electron energies from 120 keV to 20×10^3 keV are considered. Spectral reconstruction is performed via pseudo-inversion of the response matrices and least-squares regression methods. However, the Dosepix-based spectrometer fails to match the performance of comparable devices.

Studies of an active eye lens dosemeter prototype based on Dosepix yield promising results. The dosemeter prototype fulfilled the official requirements regarding the temperature dependence of indoor-use devices, since the response deviates less than 18 % and −13 % between ambient temperatures of 15 °C to 30 °C. Tests of the eye lens dosemeter prototype in a clinical environment showed the capability of the device being used for dose monitoring of occupationally exposed medical personnel. In addition, the expressiveness of the $H_\mathrm{p}(3)$-results of the prototype in terms of meaningfully estimating the dose of the eye lens is investigated with and without radiation protection glasses. For that purpose, thermoluminescence dosemeters are placed at the positions of the eyes of an Alderson phantom to estimate the true eye lens dose equivalent. Their results generally match the dose results of the Dosepix-based prototype with < 50 % deviation for mean X-ray energies between 16 keV and 167 keV and irradiation angles from $-75°$ to $75°$. Furthermore, the measured coefficient of variation of $H_\mathrm{p}(3)$ estimations of the active eye lens dosemeter prototype stays far below the officially allowed 5 %.

Finally, Dosepix detectors are used in combination with UV-cameras to monitor FLASH-capable electron beams with an electron energy of 153 MeV and bunch charges ≤ 127 pC at the ARES electron accelerator. While the Dosepix detectors could estimate the position of the beam with an accuracy of ≤ 0.7 mm, the width determination is influenced by large systematic uncertainties up to 60 %. Nevertheless, the introduced reconstruction still requires validation on independent data. A UV-sensitive Basler a2A2840-14gmUV camera is intended to image the emission of nitrogen fluorescence light along the beam as it traverses the air. While the proof of concept for this method is shown for the FXE beamline at the European XFEL, the three orders of magnitude

lower fluorescence intensities at ARES are insufficient to image the beam with the current setup and require a better light collection of the optics and more sensitive cameras.

Kurzzusammenfassung

Diese Arbeit befasst sich mit dem hybriden, pixelierten, photonenzählenden, energieauflösenden Detektor Dosepix in verschiedenen Anwendungsbereichen. Der Detektor besteht aus 16 x 16 Pixeln mit einem Abstand von 220 µm. Der verwendete 300 µm dicke Siliziumsensor ist so dotiert, dass sich daraus 12 x 16 große quadratische Pixel mit einer Kantenlänge von 220 µm und 4 x 16 Pixel mit 55 µm Kantenlänge ergeben. Die Maßeinheit des Dosepix-Detektors für deponierte Energies ist die sogenannte *time-over-threshold (ToT)* (deutsch: Zeit über der Schwelle). Aus Messungen mit 5.6 MeV α-Teilchen ergibt sich, dass die ToT ab einer deponierten Energie von (567 ± 6) keV vom bisher bekannten linearen Verhalten abweicht. Sie bleibt dabei bis zu einer Energie von $(1.7 \pm 0.6) \cdot 10^3$ keV konstant und steigt für noch höhere Energien quadratisch an. Zusätzlich zu diesen Erkenntnissen wird in dieser Arbeit ein Modell zur Simulation der ToT-Antwort des ladungssensitiven Verstärkers des Dosepix-Detektors in Abhängigkeit der Ereignisrate vorgestellt.

Mithilfe von Monte-Carlo-Simulationen wird die Realisierbarkeit eines Dosepix-basierten Spektrometers für Photonen- und Elektronenstrahlung untersucht, welche in der FLASH-Strahlentherapie zum Einsatz kommt. Dabei werden Photonenenergien zwischen 10 keV und 2500 keV sowie Elektronenenergien zwischen 120 keV und 20×10^3 keV berücksichtigt. Die Rekonstruktion der Spektren wird dabei mit den Methoden der Pseudo-Inversion der Ansprechmatrizen und der kleinsten Quadrate durchgeführt, jedoch bleibt das Dosepix-basierte Spektrometer hinter vergleichbaren Spektrometertypen zurück.

Untersuchungen eines aktiven Augenlinsendosimeterprototyps auf Basis des Dosepix-Detektors liefern positive Ergebnisse. Der getestete Prototyp erfüllt die gesetzlichen Vorgaben für die Temperaturabhängigkeit bei Innenraumnutzung, da sein Ansprechvermögen zwischen 15 °C und 30 °C um weniger als 18 % oder −13 % abweicht. Außerdem ist der Prototyp für die Überwachung von beruflich exponiertem medizinischem Personal geeignet, wie in Untersuchungen in klinischer Umgebung gezeigt wird. Darüber hinaus wird untersucht, wie aussagekräftig die ermittelte $H_\mathrm{p}(3)$ des Prototyps bezüglich der realen Dosis der Augenlinse ist, wobei die Fälle mit und ohne zusätzliche Strahlenschutzbrillen berücksichtigt werden. Zu diesem Zweck werden Thermolumineszenzdosimeter (TLDs) auf den Augen eines Aldersonphantoms platziert, um die wahre Äquivalentdosis der Augenlinse zu bestimmen. Im Wesentlichen stimmen die Ergebnisse der TLDs mit denen des Dosepix-basierten Prototyps im untersuchten Bereich mittlerer Röntgenenergien von 16 keV bis 167 keV und Einstrahlwinkeln von $-75°$ bis $75°$ mit Abweichungen < 50 % überein. Außerdem bleibt der gemessene Variationskoeffizient des aktiven Augenlinsendosimeters weit unter den offiziell vorgeschriebenen 5 %.

Im letzten Abschnitt werden Dosepix-Detektoren und UV-Kameras zur Echtzeitüberwachung von FLASH-kompatiblen Elektronenstrahlen mit 153 MeV kinetischer Energie und Ladungsbündeln von bis zu 127 pC am ARES-Beschleuniger verwendet. Zwar kann die Strahlposition mithilfe der Dosepix-Detektoren mit einer Genauigkeit von ≤ 0.7 mm

bestimmt werden, jedoch sorgen große systematische Unsicherheiten bei der Bestimmung der Strahlbreite für systematische Ungenauigkeiten bis zu 60 %. Allerdings muss die Qualität des vorgestellten Modells noch durch unabhängige Daten validiert werden. Die beim Gang des Elektronenstrahls durch die Luft ausgesandten Stickstofffluoreszenzen sollen mit einer UV-sensitiven Kamera vom Typ Basler a2A2840-14gm-UV abgebildet werden. Das Verfahren wird erfolgreich für den FXE-Strahl am European XFEL gezeigt, beim deutlich schwächeren ARES-Strahl mit drei Größenordnungen niedrigerer Fluoreszenzausbeute reicht die Lichtmenge jedoch nicht für die Bildgebung mit dem aktuellen Aufbau aus. Um den Strahl auch an dieser Anlage abbilden zu können, werden eine höhere Lichtsammeleffizienz und eine sensitivere Kamera benötigt.

Contents

1. Introduction

Since its discovery by Wilhelm Conrad Röntgen in 1895, ionizing radiation, like X-rays or charged particles, has found its way into many different aspects of medical practice [1]. On one hand, its capability of breaking molecular junctions can cause severe damage to biological organisms [2, 3]. Most importantly, exposure to ionizing radiation can lead to damaged DNA in the cells of the organism, potentially leading to cancer formation [4]. Therefore, individuals with higher expected radiation exposure than the average person must be guarded from harm by radiation protection measures [5]. Such measures include proper distance and shielding from the ionizing radiation as well as monitoring of the exposed dose via dosemeters at representative and radiation-sensitive positions [5]. For example, the eye lenses are highly susceptible to damage, induced by ionizing radiation, which destroys the proteins in the lenses and leads to cataract formation [6–9]. This danger was acknowledged by the *International Commission of Radiation Protection (ICRP)* by tightening their recommended limit for the eye lens dose of occupationally exposed staff down to 20 mSv per year in a 5-year average and no annual dose exceeding 50 mSv [6]. Regarding this example, the Erlangen Centre of Astroparticle Physics, as part of Friedrich-Alexander-Universität Erlangen-Nürnberg (FAU), has developed a prototype of an active eye lens dosemeter in 2022 to monitor the eye lens dose in real-time [10].

On the other hand, ionizing radiation also benefits medicine. X-rays are widely used to image the body's inner structures because they can penetrate macroscopic thicknesses of organic tissue [1]. Moreover, the damaging potential of ionizing radiation is specifically used in radiation therapy to destroy tumorous tissue and treat cancer [11]. Yet, this requires a very precise knowledge of the applied radiation to optimize the benefits while simultaneously minimizing potential risk [12]. The exact energy deposition of ionizing radiation depends on the species of particles, their energy, and their impact position on the tissue [13]. Although the particles' species are usually known, their energy distributions and track positions must be determined externally.

This work presents investigations concerning the characterization and monitoring of ionizing radiation in the context of radiation protection and radiation therapy with high dose rates. Most experiments were conducted with the hybrid photon-counting energy-resolving semiconductor detector Dosepix [14–16]. It was developed in a collaboration between the Friedrich-Alexander-Universität Erlangen-Nürnberg (FAU) and the European Organization for Nuclear Research (CERN) for the usage in medical applications and has shown a wide range of applicability in dosimetry and X-ray spectrometry [10, 17–21]. After an overview of the theoretical background of this work in chapter 2, novel insights about the signal response of the Dosepix detector are presented in chapter 3. Subsequently, the usability of Dosepix in a spectrometer for photon and electron fields is examined with Monte Carlo simulations in chapter 4. Spectral deconvolution is performed via pseudo-inversion of the response matrices and least-squares regression. Thereafter, the aforementioned eye lens dosemeter prototype

is tested in terms of its temperature dependence, performance under realistic clinical conditions, validity of its results in the presence of radiation protection glasses, and result reproducibility in chapter 5. Chapter 6 concerns the beam position and width determination of 150 MeV electron beams for FLASH radiation therapy by measuring scattered electrons in air with Dosepix detectors and imaging the nitrogen fluorescence light, emitted by the electron beam.

2. Theoretical Background

Contents

2.1. Radioactive Decay

Many atomic nuclei are not stable, but will change their composition over time [22]. By doing so, they are able to reach an energetically more favourable state and emit the energy difference as electromagnetic or particle radiation. For most types of radioactive decay, this will change the atomic number Z or the mass number A of the initial isotope ${}^{A}_{Z}X$. Not all nuclei in a given sample will decay at the same time. Further, it is impossible to predict the decay time for an individual nucleus. Only statistical predictions about the number of remaining particles in a radioactive sample N can be drawn [22]. The change in time of the number of particles due to radioactive decay $-\frac{dN}{dt}$ is directly proportional to the absolute number of particles, i.e.:

$$-\frac{dN}{dt} = \lambda N \tag{2.1}$$

with the proportionality constant λ, incorporating the properties of the respective isotope. This simple differential equation is solved by the function [23]

$$N(t) = N_0 \exp\left(-\frac{\log 2}{T_{1/2}} t\right), \text{ with } \lambda = -\frac{\log 2}{T_{1/2}}. \tag{2.2}$$

There, N_0 encodes the initial number of particles and $T_{1/2}$ the so-called half-life time, i.e., the time it takes for half of the initial particles to have decayed. This parameter depends on the observed isotope and can range from milliseconds to billions of years [22]. A similar equation holds for the activity of the radioactive sample $A = -\frac{dN}{dt}$, which describes the number of decays per unit time:

$$A(t) = A_0 \exp\left(-\frac{\log 2}{T_{1/2}} t\right). \tag{2.3}$$

with the initial activity A_0. Its unit is $1\,\text{Becquerel} = 1\,\text{Bq} = 1\,\frac{1}{\text{s}}$. The three main interaction channels of radioactivity are briefly discussed in the following:

α-Decay: In the first discussed type of radioactivity, the initial radioactive isotope ${}^{A}_{Z}X$ emits a Helium nucleus ${}^{4}_{2}\text{He}$, which is also called α-particle [22]. The general process is given by the relation

$${}^{A}_{Z}X \rightarrow {}^{A-4}_{Z-2}Y + {}^{4}_{2}\text{He} + Q, \tag{2.4}$$

where Q denotes the mass difference of the initial and final particles and is given to the α-particle as kinetic energy. Since only discrete energy states are allowed for atomic nuclei according to quantum mechanics, the magnitude of Q for a given decay type is fixed, and so is the energy of the emitted α-particles.

$\beta-$Decay: During this decay, the mass number of the decaying isotope A does not change, but only its atomic number Z [22]. The two basic types of the decay are the β^-- and the β^+-decay with their processes given by

$$\begin{aligned} \beta^+ &: {}^{A}_{Z}X \rightarrow {}^{A}_{Z-1}Y + \text{e}^+ + \nu_\text{e} + Q, \\ \beta^- &: {}^{A}_{Z}X \rightarrow {}^{A}_{Z+1}Y' + \text{e}^- + \overline{\nu}_\text{e} + Q. \end{aligned} \tag{2.5}$$

Depending on the decay type, the atomic number is decreased or increased by 1. Accordingly, either a positron and an electron neutrino or an electron and an electron antineutrino are emitted. Since there are three final particles, the kinetic energy is arbitrarily divided among them to obey momentum conservation. In all experiments presented in this thesis, the neutrinos are undetectable and, thus, an unknown fraction of Q is unavailable for any direct investigation.

$\gamma-$Decay: In many cases, a previous $\alpha-$ or $\beta-$decay does not end up in the ground state of the daughter nucleus ${}^{A}_{Z}Y$, but in an excited state ${}^{A}_{Z}Y^*$. Then, this excited nucleus is able to relax to the ground state via the emission of one or several photons, carrying the energy difference Q [22]:

$${}^{A}_{Z}Y^* \rightarrow {}^{A}_{Z}Y + Q. \tag{2.6}$$

Similar to α-decay, only distinct photon energies are allowed due to the discreteness of the energy levels and the combinations of allowed quantum numbers of the nuclei and photons. In particular, it is possible to characterize specific isotopes and decay chains from their emitted energies.

The most utilized radioactive isotope in this thesis is ${}^{241}_{95}\text{Am}$. It undergoes $\alpha-$decay

into $^{237}_{93}$Np with a half-life time of $T_{1/2} = 432.6\,\text{a}$ [24]. With the dominant probability of 84.45 %, the *alpha*−decay culminates in the second excited state of $^{237}_{93}$Np, corresponding to a kinetic energy of the α-particles of 5485.56 keV. Subsequently, the excited neptunium nucleus deexcites by emitting one photon with an energy of $E_\gamma = 59.5409\,\text{keV}$ [24].

2.2. Interactions of Particles and Matter

Detecting particles fundamentally depends on the direct or indirect interaction of those particles with sensor materials. The type and probability of such interactions as well as their respective produced signal depend on many different properties of the incoming radiation and on the sensor material. This enables the examination of different particles by analyzing their induced signals and assigning them to their initial properties. A brief overview of the interaction channels of photons and electrons is provided, since most measurements of this thesis rely on those two particles.

2.2.1. Photons

The interaction types of photons with matter can be divided into those with energy transition and those without, like Rayleigh Scattering. As this overview is provided in the context of detecting photons and their energies, only the energy-transferring interactions, which are responsible for their detectability, are discussed in the following. For the photon energy range, relevant for this work ranging from 10 keV to 2.5 MeV, three main types of interactions dominate:

Photoelectric Effect: Photons, interacting with the electron shell of an atom, can transfer their entire energy E_γ to one of the electrons if the energy exceeds the binding energy of the electron W. The energy of the electron E_e is then given by the subtraction

$$E_\text{e} = E_\gamma - W \tag{2.7}$$

and the photon is completely absorbed in the process [13]. Therefore, the initial energy of the photon is obtained by measuring the energy of the released electron, which is very attractive for energy-resolving experiments [13]. The interaction cross section for the photoelectric effect σ_ph depends on the atomic number of the material and E_γ as [22]

$$\sigma_\text{ph} \propto \frac{Z^5}{E_\gamma^{3.5}}. \tag{2.8}$$

Thus, detector materials with higher atomic numbers drastically increase the probability for photoelectric absorption. Also, it is the dominant interaction type for lower photon energies ($\approx 60\,\text{keV}$ in Si [25]) because of its strong energy dependence.

Compton Scattering: For higher photon energies, this type of interaction replaces the photoelectric effect as the dominant interaction. Compton scattering takes place between the photon and a weakly-bound electron that is released in the process. In contrast to the photoelectric effect, the photon only transfers a part of its energy to the electron, changing its wavelength λ and its direction of flight by the angle θ. The

change of the wavelength of the photon $\Delta\lambda$ is described by

$$\Delta\lambda = \lambda_{\mathrm{C}} \left(1 - \cos\theta\right) \tag{2.9}$$

with $\lambda_{\mathrm{C}} \approx 2.43\,\mathrm{pm}$ the so-called Compton wavelength [26]. λ is directly connected to the photon energy via $E_\gamma = \frac{hc}{\lambda}$ with Planck's constant h and the speed of light c. Therefore, the deposited energy $E_{\mathrm{dep}} = E_{\mathrm{e}}$ depends on the scattering angle θ and is given by [22]:

$$E_{\mathrm{dep}} = E_{\mathrm{e}} = E_\gamma \left(\frac{\frac{E_\gamma}{m_{\mathrm{e}}c^2}\left(1 - \cos\theta\right)}{1 + \frac{E_\gamma}{m_{\mathrm{e}}c^2}\left(1 - \cos\theta\right)} \right). \tag{2.10}$$

Thus, Compton scattering produces a continuum of deposited energies from 0 to

$$E_{\mathrm{dep,max}} = E_\gamma \left(\frac{2E_\gamma}{m_{\mathrm{e}}c^2 + 2E_\gamma} \right), \tag{2.11}$$

corresponding to backscattering with $\theta = 180°$. This maximum deposited energy is called the Compton edge. The interaction cross-section

$$\sigma_{\mathrm{C}} \propto \frac{Z \log E_\gamma}{E_\gamma} \tag{2.12}$$

shows significantly weaker dependencies with respect to Z and E_γ compared to the photoelectric effect, making it the dominant type of interaction for energies $60\,\mathrm{keV} < E_\gamma < 15\,\mathrm{MeV}$ in Si [25, 26]. Although Compton scattering does not result in a complete absorption of the initial photon, the final photon might undergo subsequent interactions in the sensor, still potentially leading to an eventual full absorption.

Pair Production: If their energy becomes even higher, photons can convert their energy into the production of an electron-positron pair, vanishing in the process. For that to happen, the initial photon energy E_γ must be larger than the sum of the rest masses of the produced particles, i.e. $E_\gamma > 1.022\,\mathrm{MeV}$ but it requires even higher energies for pair production to become the dominant interaction channel, e.g. 15 MeV in Si [25]. Its interaction cross-section

$$\sigma_{\mathrm{pp}} \propto Z^2 \log E_\gamma \tag{2.13}$$

is the only one of the discussed interactions to increase for higher photon energies [22]. Pair production only results in a full absorption of the initial photon energy if the created positron immediately annihilates with an ambient electron and the resulting photons are again absorbed via the described interaction mechanisms.

Adding up all individual cross-sections yields the total photon interaction cross-section which is proportional to the photon attenuation coefficient μ. This parameter describes the decrease in the intensity $I(x)$ of a photon beam as it has traversed a material by the distance x: The intensity is then determined by

$$I(x) = I_0 \exp\left(-\mu x\right) \tag{2.14}$$

with the initial intensity I_0 [26]. Figure 2.1 shows the components of μ for silicon with

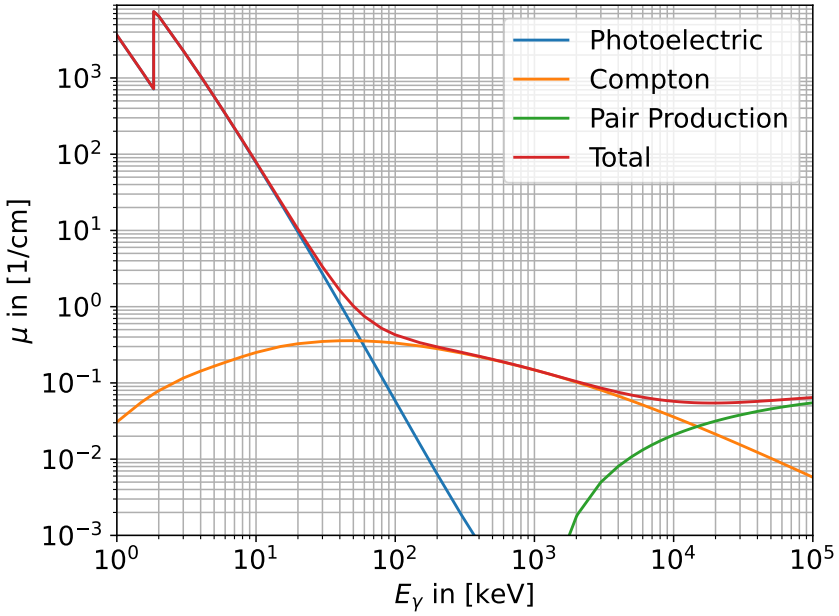

Figure 2.1.: Attenuation coefficient μ and its components for silicon as a function of the photon energy E_γ. The data is taken from [25].

respect to E_γ, showing the discussed trends for all three interaction types. It is obvious that μ decreases with higher energies between 2 keV and 20 MeV. Thus, photons with higher energies are less absorbed by filter materials or radiation protection shielding.

2.2.2. Electrons

Ionization: Charged particles interact differently with matter than photons. For lower energies, depending on the particle type and material, they mainly interact via Coulomb collisions with their surrounding atoms [13]. The energy loss of heavy charged particles is determined by the so-called Bethe-Bloch equation, which takes into account the energy of the particle and the mean excitation potential of the material [13]. A correct description of electrons requires some adjustments to the basic Bethe-Bloch equation to take into account their low mass and their indistinguishability from the electrons of the atomic shells of the medium. The adjusted formula for the loss of the electron energy E_e per length element x due to collision is then approximately given by

$$\left(\frac{dE_\mathrm{e}}{dx}\right)_\mathrm{coll} \approx \frac{e^4 n_\mathrm{e}}{4\pi\epsilon_0^4 m_\mathrm{e} v^2} \log\left(\frac{m_\mathrm{e} v^2}{2\overline{E_\mathrm{b}}}\right) \tag{2.15}$$

with e the elementary charge, n_e the electron density of the material, ϵ_0 the permittivity of free space, m_e the electron rest mass, v the velocity of the electron, and $\overline{E_\mathrm{b}}$ the mean binding energy of the electrons in the material [26]. Those collisions excite and ionize the surrounding atoms of the material, producing pairs of free electrons and holes in the process. On average, the number of produced electron-hole pairs is proportional to the initial kinetic energy of the electrons. For example, one electron and one hole are,

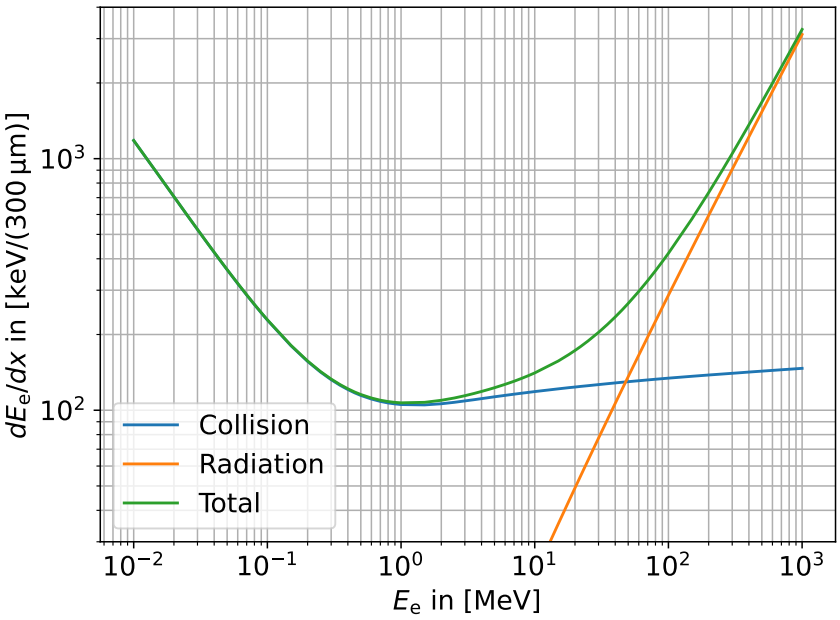

Figure 2.2.: Mean energy loss of electrons in silicon with respect to their kinetic energy E_e, normalized to the sensor thickness of the Dosepix detector. The data was taken from [28].

on average, generated for every 3.62 eV, lost by an electron in silicon [27]. Therefore, the kinetic energy of the initial electrons can be reconstructed from the total produced charge. This is the fundamental detection principle of many energy-resolving detectors, including Dosepix, which is used for most measurements, presented in this thesis.

Bremsstrahlung: Starting from electron energies of about 50 MeV for Si, the energy loss of electrons due to the deceleration in the Coulomb field of the surrounding atoms becomes the dominant source of energy loss [28]. This deceleration of a charged particle leads to the emission of electromagnetic radiation. Calculating electron radiation losses is beyond the scope of this theoretical overview but a more detailed discussion of this topic is provided in [13] and [26]. The total energy loss of electrons per travelled distance is given by the sum of both interaction types

$$\frac{dE_e}{dx} = \left(\frac{dE_e}{dx}\right)_{coll} + \left(\frac{dE_e}{dx}\right)_{rad}. \tag{2.16}$$

Figure 2.2 shows the contributions and the total energy loss of electrons in silicon. As discussed, collision losses dominate for lower energies while bremsstrahlung becomes more important for higher energies. In contrast to photons, electrons lose their energy more gradually through many interactions with the medium. That also impacts the signals that they induce in sensor layers, like the 300 µm thick silicon sensor, which is used most throughout this work. For example, electrons with energies of ≈ 150 MeV were examined in this thesis. As shown in the plot, those are not expected to deposit their entire kinetic energy in the utilized sensor layer. Instead, the energy deposition

spectrum is described by a Landau distribution with the most probable deposited energy

$$E_{\mathrm{e},0} \approx \xi \left(\log \left(\frac{2 m_{\mathrm{e}} c^2 \beta^2 \gamma^2 \xi}{I^2} \right) + 0.198 - \beta^2 - \delta \right) \tag{2.17}$$

with $\beta = \frac{v}{c}$, $\gamma^2 = \frac{1}{1-\beta^2}$, I the mean ionization potential of the material, δ the so-called density effect correction, taking into account polarization shielding of the initial particle by the material, and

$$\xi = (0.1536\,\mathrm{MeV}) \cdot \frac{Z}{A} \frac{\rho x}{\beta^2},$$

where ρ denotes the mass density of the material [29]. This quantity hardly depends on the energy of the electron in the $10\,\mathrm{MeV} - 150\,\mathrm{MeV}$ range, because β will always be very close to 1 and γ only appears in the logarithm. $E_{\mathrm{e},0}$ was measured previously to approximately equal 80 keV for the utilized silicon sensor [30]. Nevertheless, much higher energy depositions are possible, described by the long high-energy tail of a Landau distribution because it is possible for electrons to lose large fractions of their energy in one or few interactions [13].

2.3. X-Ray Fluorescence

Electrons, bound by atoms, can only exist in discrete energy levels which are specific to the respective element. By gaining energy via interactions, shell electrons can be excited to higher energy levels or be completely ionized, i.e., escape the atom. In either case, the previous state of the electron becomes vacant and will be re-filled by the initial atom itself or another electron on a higher atomic shell [23]. The energy difference will then be emitted as electromagnetic radiation, known as fluorescence. Accordingly, the frequency of that light is then also specific to the observed element. This is used to generate radiation with well-known energies or to identify elements from their fluorescence spectrum. The exemplary fluorescence spectrum of nitrogen is shown in Figure 2.3. Most of the nitrogen fluorescence wavelengths λ are below the visible light with $\lambda < 400\,\mathrm{nm}$, requiring special cameras to image. One way to excite the shell electrons and produce fluorescence light is via the Coulomb collision interaction with other charged particles, as long as the kinetic energy of the latter exceeds the excitation energy (see subsection 2.2.2). After a short excitation time in the order of 40 ns depending on the specific nitrogen transition, the electron relaxes and emits the fluorescence photons isotropically [32, 33].

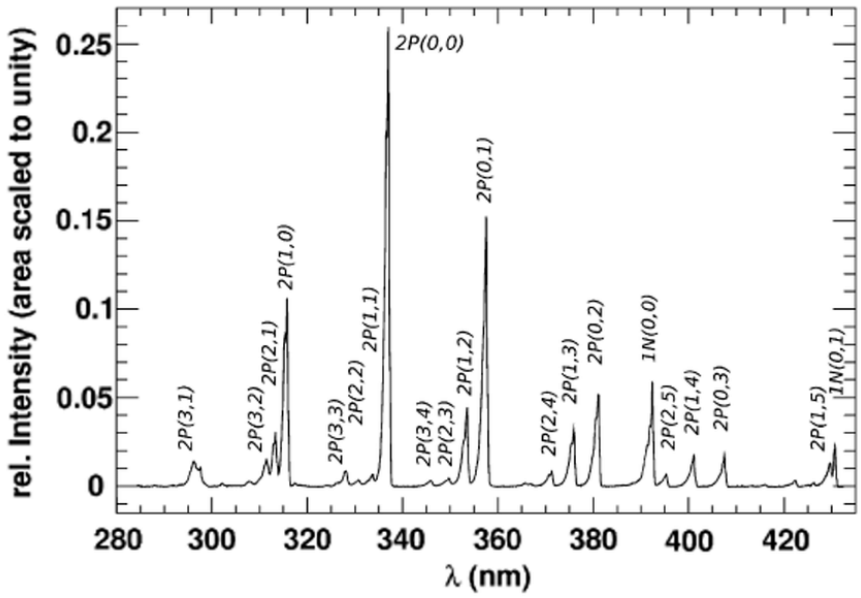

Figure 2.3.: Fluorescence spectrum of nitrogen with respect to the photon wavelength λ, measured by the AIRFLY collaboration. The picture is taken from [31].

2.4. Dosimetric Quantities

The following overview of the most important quantities in dosimetry and radiation protection is based on the official German regulations, provided in Report Dos-23 of the National German Metrology Institute (Physikalisch-Technische Bundesanstalt (PTB)) [34]. The goal of dosimetry is to correctly determine the absorbed ionizing radiation in a given biological tissue and to derive the damage potential caused by that radiation.

Kerma: Neutral particles like photons are only indirectly ionizing, as they first have to produce free charged particles via the interactions, summarized in subsection 2.2.1. The quantity Kerma K_{mat} (**k**inetic **e**nergy **r**eleased per unit **ma**ss)) encodes the transferred kinetic energies to the first-generation secondary particles:

$$K_{\text{mat}} = \frac{dE_{\text{kin}}}{dm_{\text{mat}}}. \tag{2.18}$$

It depends on the flux and energy of the primary particles as well as on the specific material. Therefore, the reference material must always be stated for transparency. The air-kerma K_{air} at normal pressure and room temperature is often used as a reference quantity. The unit of kerma is $1\,\text{Gray} = 1\,\text{Gy} = 1\,\frac{\text{J}}{\text{kg}}$.

Absorbed Dose: Fundamentally, the damaging effects of ionizing radiation are a consequence of the finally deposited energies of the radiation in the tissue because that energy might then be capable of causing molecular damage or heat deposition. That

finally deposited energy in a given material is quantized by the absorbed dose D:

$$D = \frac{dE_{\mathrm{abs}}}{dm_{\mathrm{mat}}}, \tag{2.19}$$

with dE_{abs} the absorbed energy in the mass element dm_{mat}. For low primary photon energies, the absorbed dose is approximately equal to the kerma because the produced secondary electrons deposit their energy along a short path length via ionization [13]. In contrast, photons with higher energies can produce electrons that can deposit their energy over a longer path or emit some energy from the system via bremsstrahlung, leading to a difference of the kerma and the absorbed dose. The unit of the absorbed dose is also 1 Gy. The absorbed dose as a function of the penetration depth is used as the reference quantity for radiation therapy treatment planning (see section 2.5). It is then often referred to as depth dose or depth dose profile.

Equivalent Dose: While the absorbed dose describes the basic physical processes, it does not take into account any biological sensitivities. This is done via the so-called equivalent dose

$$H_{\mathrm{T}} = \sum_{R} w_{\mathrm{R}} D_{\mathrm{T,R}} \tag{2.20}$$

for a certain tissue T and different radiation types R. $D_{\mathrm{T,R}}$ denotes the absorbed doses in the observed tissue, originating from the radiation type R. The dimensionless radiation weighting factors w_{R} take into account the biological effectiveness of the radiation type. It roughly becomes larger for heavier particles, since those are capable of depositing high energies in a small volume, leading to a high cancer production risk. For example, w_{R} is 1 for photons and electrons, and 20 for α-particles. Although the equivalent dose is also measured in Joules per kilogram, its unit is changed to 1 Sievert = 1 Sv = 1 $\frac{\mathrm{J}}{\mathrm{kg}}$ to imply the inclusion of the weighting factors.

Effective Dose: Expanding the definition of the organ equivalent dose to the whole body yields the effective dose

$$E = \sum_{T} w_{\mathrm{T}} H_{\mathrm{T}} = \sum_{T,R} w_{\mathrm{T}}\, w_{\mathrm{R}}\, D_{\mathrm{T,R}}. \tag{2.21}$$

It also introduces dimensionless tissue weighting factors w_{T} accounting for the relative sensitivities of different biological tissues. The effective dose serves as a parameterization of the total radiation exposure of an organism, but it cannot be measured directly.

Operational Dose Quantities: Those quantities are designed for the actual measurements of dosemeters. They do not parametrize the biological exposure. Instead, they are defined as the equivalent dose at a certain point inside a thoroughly defined metrological setup. The only operational dose quantity used in this work is the personal dose equivalent $H_{\mathrm{p}}(3)$, which was designed to approximately estimate the dose of the eye lens. The number in the brackets of operational dose quantities always indicates the tissue depth in units of mm. $H_{\mathrm{p}}(3)$ is defined as the equivalent dose at a depth of 3 mm of ICRU soft tissue [35]. It is usually measured by putting the respective dosemeter in front of a water cylinder phantom with a height and edge length of 20 cm

to approximately resemble the scattering of a human head [36]. Other examples for operational dose quantities are $H_{\mathrm{p}}(10)$ for full-body monitoring or $H_{\mathrm{p}}(0.07)$ to estimate the skin dose.

Response and Normalized Response: The response R is a characterization parameter for dosemeters and is defined as the ratio of the measured dose and the true dose value. It is the main measure of quality for dosemeters. The response is often normalized to equal 1 for a specific radiation quality and is then referred to as the normalized response. Most of the requirements for officially approving dosemeters refer to the normalized response, which must not exceed certain limits for various influence quantities, like particle energy, angle of irradiation, etc. [37].

Coefficient of Variation: This parameter v quantifies the reproducibility of dose measurements. It is determined by

$$v = \frac{\sigma}{\mu}, \tag{2.22}$$

with σ the standard deviation of the dose results after N repetitions and μ the mean measured dose. There are also official limits for the maximum allowed coefficient of variation, which depend on the specific dose quantity and the applied dose [37]. For $H_{\mathrm{p}}(3)$, this limit varies between 15 % for $H_{\mathrm{p}}(3) < 0.3\,\mathrm{mSv}$ and 5 % for $H_{\mathrm{p}}(3) \geq 3.3\,\mathrm{mSv}$. It is discussed in more detail for the presented eye lens dosemeter prototype in section 5.5.

2.5. Radiation Therapy

2.5.1. Overview

The first medical approaches to treating cancer in the 19th century mainly focused on mechanically removing the tumor tissue from the organism [38]. Yet, soon after the harmfulness of ionizing radiation had been discovered, it was used to purposefully irradiate tumor tissue and destroy it that way. This is called radiation therapy. It is now the most common technique of fighting cancer in Germany [11]. The main challenge of radiation therapy is to apply the highest reasonably achievable dose inside the tumor, while also minimizing the radiation exposure of any surrounding healthy tissue. The dose range at which the tumor control is sufficiently high, while healthy tissue is still reasonably spared, is called the therapeutic window. Achieving both requires meticulous treatment planning [12]. For example, a treatment planning CT is usually performed before the actual treatment to precisely determine the position, size, and shape of the tumor, as well as the surrounding tissue. A treatment plan is then derived from that information. It has to take into account the sparing of the healthy tissue, but also the potential movement of the tumor, e.g., due to breathing. The treatment plan is usually tested before the real radiation therapy by applying the same treatment to special phantoms [39]. Ionization chambers or other detector types measure the radiation at the neuralgic points in the phantom during quality assurance. If everything fits, the real radiation therapy with the patient is conducted while permanently monitoring the properties and position of the beam. Typical irradiations with tumor doses from 1 Gy to 2 Gy last several minutes and are repeated several times over the course of a few weeks to minimize healthy tissue complications [40].

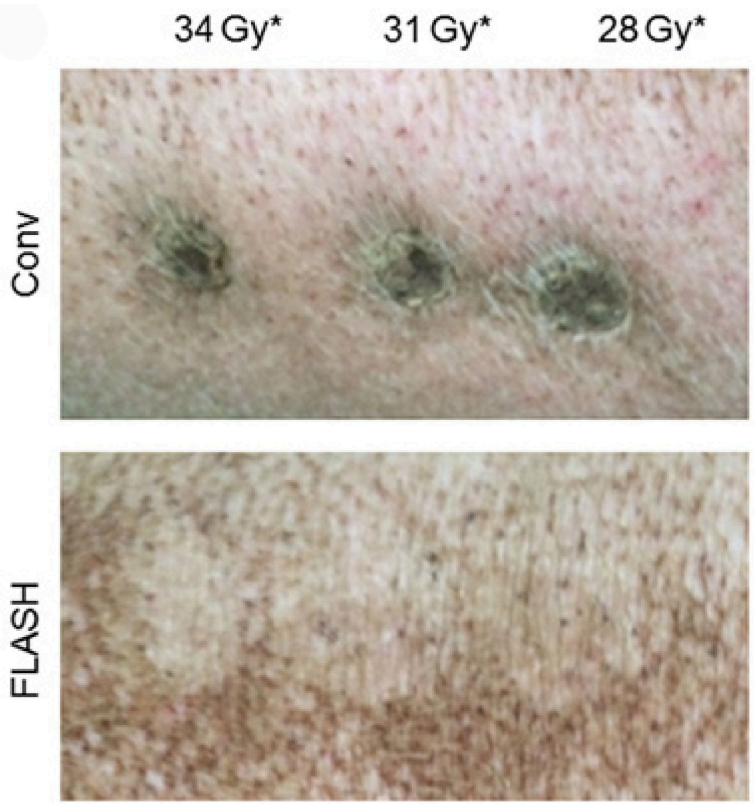

Figure 2.4.: Photograph of the skin of a mini-pig, 36 weeks after being treated conventionally and under FLASH conditions. The figure is taken from [45].

2.5.2. FLASH Radiation Therapy

Although the tumor control capabilities of radiation therapy have increased steadily due to the evolution of the treatment planning, the therapeutic window is still limited by the complications to the healthy tissue, increasing with higher doses [11]. This major caveat is addressed by a new approach to radiation therapy, called FLASH therapy [41, 42]. It utilizes much higher dose rates $> 40\,\frac{\mathrm{Gy}}{\mathrm{s}}$ to reduce the treatment duration of the radiation therapy to milliseconds. Studies showed that those ultra-high dose rates lead to a significant improvement in the sparing of the healthy tissue while not affecting the tumor control [43–45]. One of the most famous examples of the advantage of FLASH therapy is shown in Figure 2.4, where the skin of a mini-pig was irradiated under conventional ($5\,\frac{\mathrm{Gy}}{\mathrm{min}}$) and FLASH conditions ($\approx 300\,\frac{\mathrm{Gy}}{\mathrm{s}}$) [45]. Only the conventional treatment has caused severe skin reactions like fibronecrosis, whereas the reactions to the FLASH treament was mostly limited to depilation, proving the enhanced normal tissue sparing of radiotherapy with ultra-high dose-rates. This would extend the therapeutic window of radiation therapy, improving the field as a whole and potentially enabling the control of previously untreatable tumors [46]. The concept of the increased therapeutic window is also visualized in Figure 2.5 [47]. While the tumor control (TC) is hardly affected by the change from conventional to FLASH therapy, the normal tissue complication (NTC) decreases, extending the available range of doses for the treatment. In 2019, the first patient was treated with FLASH radiation

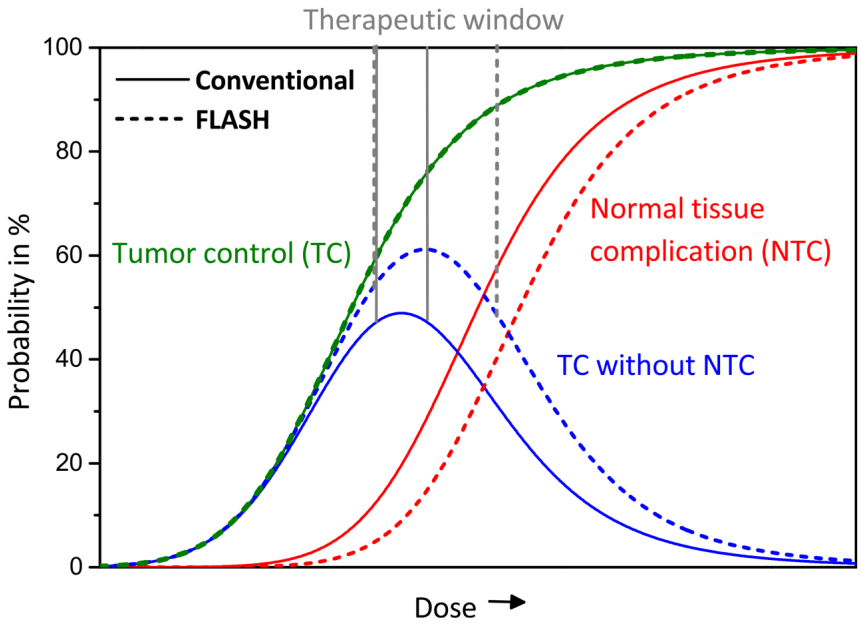

Figure 2.5.: Sketch of the tumor control, normal tissue complication probability, and resulting therapeutic window with respect to the applied dose. The figure is taken from [47].

therapy, backing the theory of better sparing of the healthy tissue [48]. Yet, there remain fundamental and technical challenges to overcome before FLASH therapy may be performed routinely. Some of them are briefly summarized in the following.

First, many of the underlying biological principles that give rise to the FLASH effect remain incompletely understood [42]. Most studies suggest a lower threshold of about 40 $\frac{\mathrm{Gy}}{\mathrm{s}}$ for the FLASH effect to occur, but that has only been an empirical value without theoretical backup [49]. Furthermore, many possible tissue differences or spatial dependencies are unknown so far [49, 50]. There are even some investigations that did not witness the FLASH effect at all, although the majority of studies did [51–53].

Second, producing particle beams with the necessary ultra-high dose rates requires novel particle accelerators in clinical environments. Different research groups currently pursue different realizations with electrons, protons, and photons [54–59]. All of them come with advantages and disadvantages for certain applications. This work focuses on very high energy electrons of 153 MeV, which seem to prove especially useful for deep-seated tumors (see subsection 2.5.3 and section 6.2).

Lastly, quality assurance and online beam monitoring become significantly more challenging for such high dose rates and short treatments [50]. Correction and stopping mechanisms require a much faster response to hold up to the shorter treatment durations [60]. Yet, there are currently no established beam monitors and dosemeters capable of precisely measuring the position, shape, and dose of the radiation at the patient positions [61]. Some detector systems have proven the capability of handling ultra-high dose rates, e.g., diamond detectors, calorimeters, or thin ionization chambers [62–64]. However, most of them are destroying detection systems, meaning they can be used for quality assurance between irradiations, but not during the treatment itself, as the detectors affect the beam. Beam current monitors close to the exit windows might be

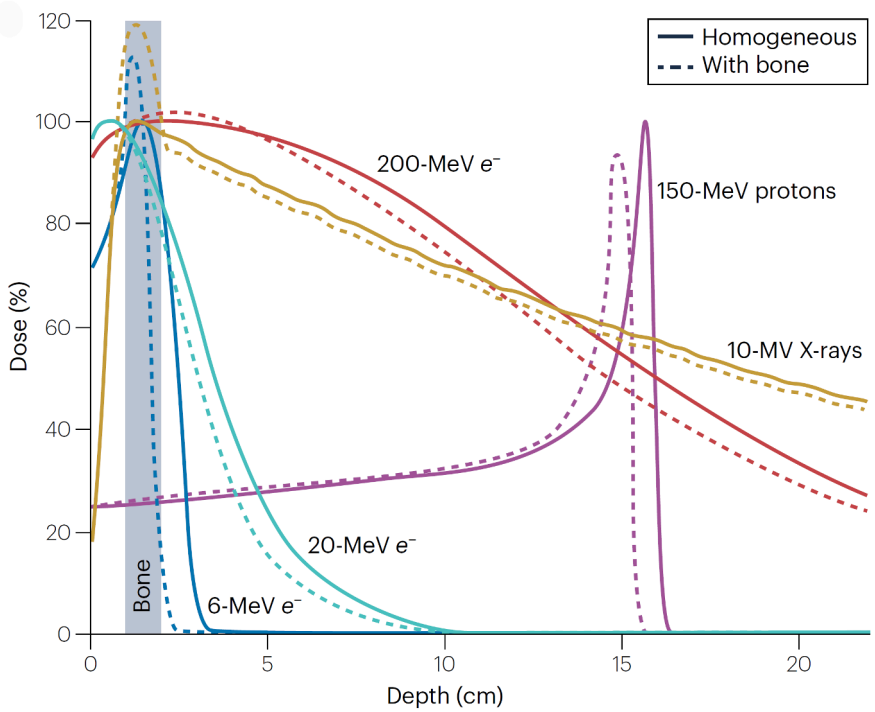

Figure 2.6.: Absorbed dose in water with respect to the depth for different particles. The second centimeter was changed to bone material, resulting in the dashed lines. The figure is taken from [50].

able to fulfill this function, but still require additional research [65–67]. Developing a fully reliable control system for ultra-high dose rates remains a paramount step toward establishing FLASH therapy in clinical practice.

2.5.3. Advantages of VHEE Beams

This work focuses on FLASH therapy with very-high energy electrons, which is usually defined as the range from 100 MeV to 250 MeV although the exact definition varies between different studies [68, 69]. Those electrons come with some advantages compared to proton therapy or lower-energy electrons. Figure 2.6 depicts the depth dose profiles for different particles in water [50]. In addition, dashed lines show how the depth doses change when 1 cm of water is exchanged with bone material. The 200-MeV e^- and the 10-MV X-rays display the flattest dose profiles and show the lowest relative dose changes for the variant bone case. Therefore, those particles are best suited for treating tumors in deeper regions, as they still deposit energy in 20 cm tissue. Their weaker dependence on the exact material composition also increases the robustness of the treatment plan with respect to small deviations. In contrast, protons show a large relative dependence on the bone material because the position of the Bragg-peak changes by about 1 cm. Additionally, protons are much more expensive to produce than electrons, making the latter a prime candidate for FLASH radiotherapy, especially in deeper layers of the organism [70, 71]. Photons may also serve that purpose, but are difficult to provide at ultra-high dose rates [58, 59].

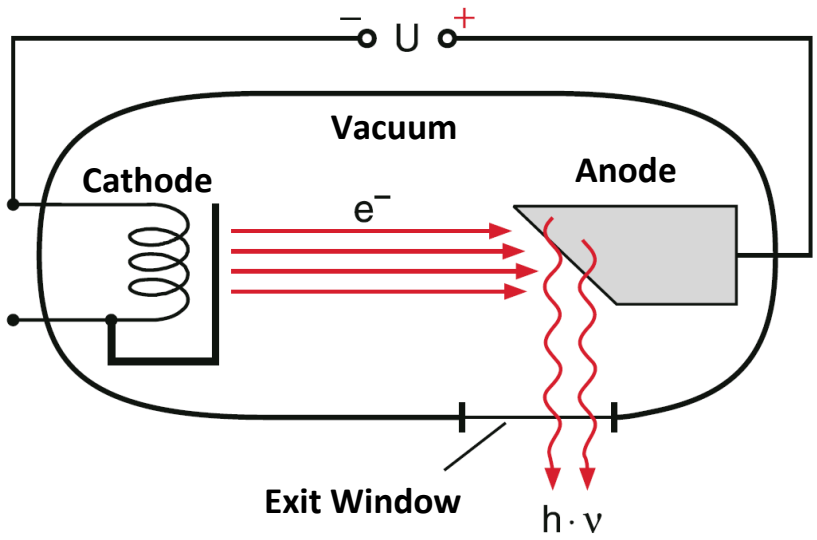

Figure 2.7.: Basic concept of an X-ray tube. Electrons are released at the cathode and accelerated in an electric field until they impinge on the anode and emit photons via bremsstrahlung and fluorescence. The figure is taken from [23] and modified.

2.6. X-Ray Tubes

X-ray tubes are a common method of producing X-rays used for medical applications or non-destructive testing [72, 73]. Figure 2.7 shows their fundamental design [23]. A voltage U creates an electric field between a hot cathode and an anode, often made out of tungsten. The space inside the X-ray tube is evacuated to enable free travel of the electrons, which are produced at the cathode. They are accelerated towards the anode and their final kinetic energy equals $e \cdot U$, with e the elementary charge. When the electrons impinge on the anode, a small fraction of the energy is converted into bremsstrahlung which leaves the X-ray tube and constitutes the main part of the X-rays (see subsection 2.2.2). The bremsstrahlung spectrum contains all energies between 0 and the electron energy $e \cdot U$. Apart from that, characteristic lines from the fluorescence of the anode material appear in the spectrum. They result from the refilling of atomic shell vacancies, produced by energy transfer from the accelerated electrons to the atomic electrons. X-ray spectra are often modified by placing filter layers of certain materials and thicknesses behind the exit window of the tube. The energy dependence of the photon absorption will lead to a dominant absorption of the lower energies (see subsection 2.2.1). This technique will be used to create different X-ray spectra throughout this work. Example of X-ray spectra with the same tube voltage of $U = 80\,\mathrm{kV}$, but different filtrations are shown in Figure 2.8. They are simulated with the Python package *xpecgen* [75, 76]. The spectrum, named "unfiltered", is only affected by a typical internal filtration of X-ray tubes of 1.5 mm Al [77]. Characteristic lines occur at 58 keV and 67 keV, originating from the tungsten fluorescence lines [78]. The other spectra correspond to filter combinations of metrological spectra, as defined in [74], used throughout this work. H-80 is filtered by 7.2 mm of Al, W-80 by 4.0 mm of

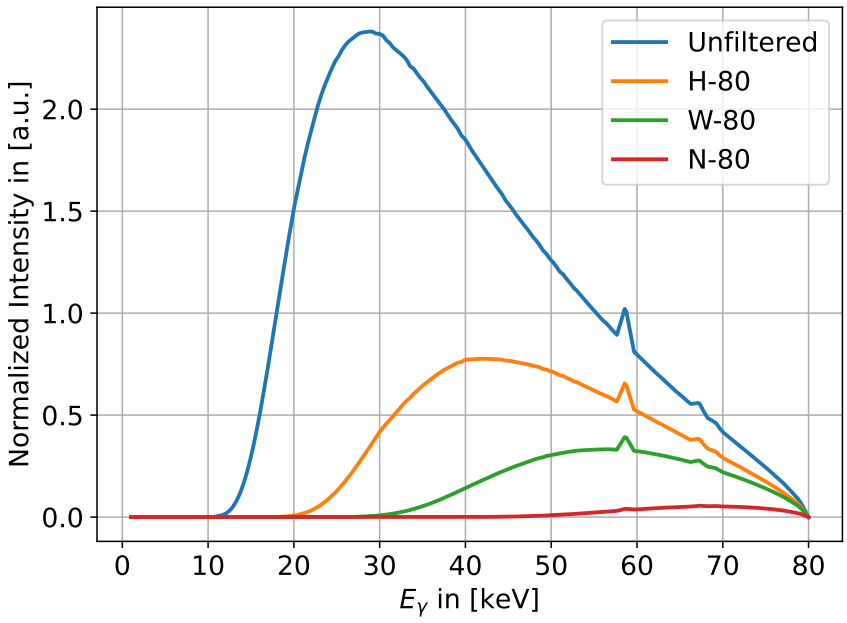

Figure 2.8.: Exemplary X-ray spectra with respect to the photon energy E_γ for different filter combinations from [74]. The ünfilteredspectra still contains 1.5 mm of internal aluminum filtration. All spectra correspond to $U = 80\,\mathrm{kV}$.

Al and 0.5 mm of Cu, and N-80 by 4.0 mm of Al and 2.0 mm of Cu. Stronger filtrations lead to an absolute decrease in the intensity and a decreasing width of the spectrum because of the stronger absorption of the lower energies.

2.7. Electron Accelerators at PITZ and ARES

Electron accelerators are a common method to produce bunches of monoenergetic electrons. The charge per bunch and bunch repetition rate of some facilities even reach the FLASH regime (see subsection 2.5.2). Therefore, electron accelerators are a very relevant topic of current research for radiation therapy. The following paragraphs provide a brief overview of the functionalities of electron accelerators with two specific examples: the Photo Injector Test Facility at DESY, Zeuthen site (PITZ) [57] and the Accelerator Research Experiment at Sinbad (ARES) [79, 80], which are of importance for this work. The electrons are produced in a radiofrequency gun, where a photocathode with an electric field of several $\frac{\mathrm{MV}}{\mathrm{m}}$. In this work, the gun frequency is always set to 10 Hz.

In ARES, laser pulses synchronized with the gun transport the electrons downstream. The electrons are further accelerated and shaped by several magnets before the pulses arrive at the exit window. Final electron energies between 100 MeV and 155 MeV are stated officially in [80] but smaller energies down to 75 pC are also achievable in practice (see section 6.3). ARES is able to generate bunch charges at the exit window from about 0.003 pC to 200 pC with a duration of 30 fs [80]. The charge is measured with a Turbo Integrated Current Transformer before the exit window and an optional Faraday

Cup [79]. This facility mainly specializes in low energy and arrival time uncertainties of 0.06 MeV FWHM and few tens of femtoseconds [79, 80].

On the other hand, the PITZ accelerator utilizes a different laser which is capable of generating up to 1000 pulses within 1 ms, thus resulting in that many bunches per gun cycle. This electron formation is called a bunch train. Each bunch lasts from < 1 ps to 30 ps and contains up to 5 nC of charge, i.e., up to 5 µC of total charge are possible for a complete bunch train at PITZ [81]. The relative charge uncertainty was determined in [81] to be < 1 %. Only the kinetic energy of the electrons of 22 MeV is lower for PITZ than for ARES, but an upgrade for PITZ is planned that will extend the energy range to up to 250 MeV [81]. This upgrade will also include a kicker setup, which will be capable of spatially adjusting the individual positions of every bunch in a train. That way, a complete FLASH radiotherapy session may be conducted within 1 ms [57].

2.8. The Dosepix Detector

2.8.1. General Structure

Most measurements, presented in this work, are conducted with the hybrid, pixelated, photon-counting, energy-resolving semiconductor detector Dosepix [14–16]. Figure 2.9 shows a photograph of the detector. The hybrid design of Dosepix means that the application-specific integrated circuit (ASIC) and the radiation-sensitive layer are produced separately and then assembled via flip-chip bonding. Therefore, different sensor materials and thicknesses may be attached to Dosepix for different applications. All measurements in this work were performed with a 300 µm thick p-in-n-doped silicon sensor layer. The ASIC and the sensor layer are divided into 16x16 quadratic pixels with a pixel pitch of 220 µm. If not stated otherwise, the pixels in the upper two and lower two rows have an active area of 55 µm x 55 µm, while the middle twelve rows are densely packed with an edge length of 220 µm. A bias voltage of 48 V for the eye lens dosemeter prototype (see chapter 5) and 100 V otherwise is applied to the sensor to induce a depletion layer, approximately covering the whole sensor.

A charged particle, impinging on the sensor layer, is decelerated and, in the process, ionizes the surrounding sensor atoms until it is stopped or leaves the sensor layer (see subsection 2.2.2 and [13]). The total amount of produced charge is proportional to the energy deposited by the particle and is called the charge cloud. Similarly, deposited photon energies are also measurable when the photon interacts with a sensor atom via the interactions described in subsection 2.2.1, transferring energy to an electron in the process, which then produces the charge cloud. Due to the PN-junction in the sensor layer and the bias voltage, the ionized electrons and holes do not immediately recombine but drift towards the electrodes of the sensor. Here, the holes drift towards the ASIC and induce a signal in the pixel electronics. The charge cloud may span over multiple pixels or some charge may enter the electric field of another pixel during the drift. In such cases, the energy deposition information is divided and the different charge contributions are processed separately. This effect is called charge sharing.

Incoming signals are processed by the pixel electronics. It consists of an analog and a digital component and is sketched in Figure 2.10. The analog part of the pixel electronics mainly consists of a charge-sensitive amplifier (CSA). It converts the incoming charge signal from the sensor into a proportional voltage. At the same time, the signal is

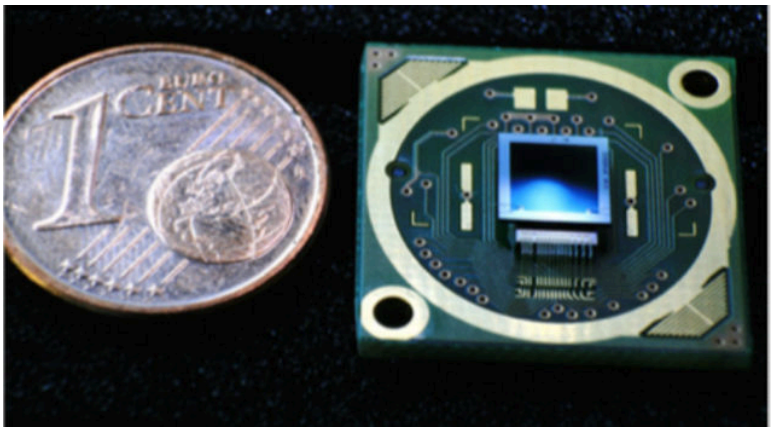

Figure 2.9.: Photograph of the hybrid pixelated Dosepix detector with a Si sensor layer and attached to an adapter PCB. The picture is taken from [82].

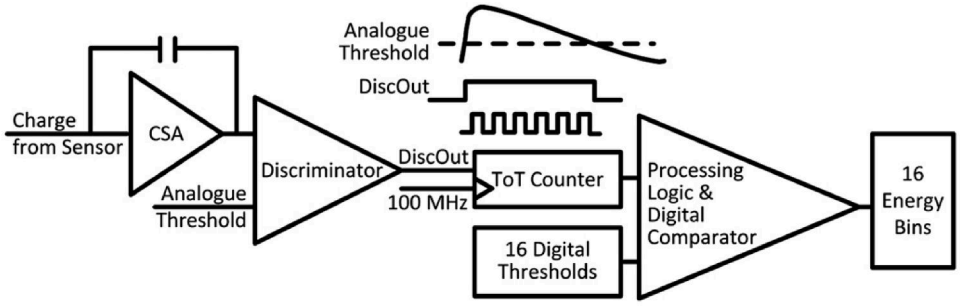

Figure 2.10.: Schematics of the Dosepix pixel electronics. The charge sensitive amplifier (CSA) produces a voltage signal, proportional to the deposited charge in the sensor pixel, which is discharged by a constant current, resulting in the time-dependent voltage, drawn at the top of the sketch. This signal is compared to the analog threshold by the disciminator and the resulting ToT is further analyzed by the processing logic. The figure is taken from [14].

discharged at a constant rate via a feedback circuit and a constant current, called I_{Krum}. This current is also responsible for leakage current compensation [83]. However, the theoretical leakage current compensation capabilities of $\frac{I_{\mathrm{Krum}}}{2}$ per pixel are not reached in reality, leading to systematic uncertainties in the measured energies [84–86]. The output signal of the CSA with respect to time looks like the curve, drawn at the top of Figure 2.10. This voltage curve enters a discriminator, which compares the signal to an adjustable analog threshold, corresponding to a deposited energy of 8 keV to 12 keV, depending on the application [16]. The discriminator measures the duration for which the voltage signal exceeds the analog threshold. Since the discharge rate of the CSA signal is constant and the initial signal height is proportional to the original charge, this duration also depends on the collected charge and, thus, approximately on the deposited energy. Therefore, this time duration, called *time-over-threshold (ToT)* serves as Dosepix's measure of the deposited energy. It is a digital value, given as a number of clock cycles of a 100 MHz reference clock, i.e., as a multiple of 10 ns. The further processing of the ToT in the digital pixel electronics depends on the chosen operation mode. It may occur that the next event in a pixel enters the processing chain while the previous one is still being discharged. In that case, the CSA outputs of both signals overlap and the discriminator treats them as a single event with an overestimated energy. This effect is called analog pile-up and leads to a distortion of the detector output towards higher energies and lower event numbers, depending on the irradiated intensity.

2.8.2. Modes of Operation

Dosepix provides 4 effective modes of operation. Only one of them is available at a time, because Dosepix only comprises one data output channel [14]. All four modes and their main use case are briefly presented in the following paragraphs. A more detailed description of them is provided in [16].

ToT-Mode: The last measured ToT of each pixel is stored in a ToT-register with a depth of 12 bit. Reading those registers for all pixels provides direct access to the measured deposited energies. The ToT-values can be calibrated via the procedure described in [21] to translate them into physical energies. Histogramming the resulting energies yields the shape of the observed energy deposition spectrum. However, the total fluence is not available in ToT-mode because writing the ToT-register of a pixel overwrites its previous entry. Therefore, only the information about the last event before the readout is accessible in this mode. It is thus used for applications where only the information about the shape of the spectra, like peak positions or widths, is important, e.g., energy calibration.

Photon-Counting Mode: In this mode, no information about the absolute value of the ToT is stored. Instead, just the number of threshold passages is counted for each pixel during a set measurement time. This mode is used when only the event rate or the binary information about the presence or absence of events is important. An example of such an experiment is the measurement of the pixel noise level, where the energy threshold is changed until signals are detected, although no radiation source is present. Unfortunately, the photon-counting register depth is only 8 bit deep, leading to a high

risk of overflowing counters, called digital pile-up. If that happens, the counter just restarts from 0 while the previous 256 events are lost.

Energy-Binning Mode: Serving as the central working mode of Dosepix, this mode was designed to optimally fulfill the requirements of radiation protection [16]. Every pixel of the Dosepix detector contains 16 programmable energy thresholds. Incoming ToTs are sorted by the pixel electronics, according to those bin edges. This results in an event histogram with 16 bins, where the last serves as an overflow bin without an upper bound. After the set measurement duration, this histogram is read out for all pixels via a rolling shutter, which means that the pixel columns are read one after another, while the remaining pixel matrix stays active. That way, Dosepix does not have a global dead time [16]. Each bin register has a depth of 12 bit. The same energy bin edges for all pixels are usually chosen for dose estimation (see subsection 2.8.3) but other applications have also experimented with different bin edges for all pixels [21]. The output data in the energy-binning mode yield information about the number of registered events since the last readout and the shape of the energy deposition spectrum, although with a worse energy resolution than in ToT-mode.

Integration Mode: The last operation mode of Dosepix adds up the individual ToTs, measured by each pixel. After the measurement time, this summed value, called *integrated time-over-threshold (iToT)*, is read out for all pixels. The largest obvious disadvantage of this mode is that all information about individual events is lost and Dosepix is effectively reduced to a charge-integrating detector. Nevertheless, this mode is especially useful in environments with high dose rates, where individual ToT determinations were pile-up-dominated, because the integration mode is not affected by analog pile-up. On top of that, this mode comprises the largest data register with a depth of 24 bit per pixel, greatly reducing the risk of count overflowing compared to the other modes [16].

2.8.3. Dose Estimation

The classical approach to determining the value of a dose quantity with Dosepix is based on measurements acquired in the energy-binning mode, with a fixed set of bin edges applied to all pixels. Afterwards, the sum of the histogram entries of all equally-sized pixels is calculated. The entries of this summed histogram are called N_i, with $i \in [1, 16] \cap \mathbb{N}$. An arbitrary dose quantity H is then determined by the weighted sum

$$H = \sum_{i=1}^{16} k_i N_i, \tag{2.23}$$

where k_i denote the so-called dose conversion factors. They are designed to contain all physical information, affecting the dependence of the dose with respect to the measured number of events. The dose conversion factors have usually been determined by a combination of Monte-Carlo simulations and measurements with known particle energies and doses [85, 87]. A detailed description as well as specific conversion factors for the common operational dose quantities are provided in [87]. The only specific dose quantity, calculated in this work, is the operational personal dose in a depth of 3 mm

$H_{\mathrm{p}}(3)$ to estimate the eye lens dose equivalent. The corresponding bin edges and dose conversion factors were determined in [85] and are listed in Appendix A.

If a dose measurement is repeated several times, the statistical fluctuation of the measured dose σ_H is calculated from the standard deviation of the individual dose results. If there is only one dose measurement, the statistical fluctuation is approximated from the expected Poissonian distribution. Thus, the standard deviation of each N_i is given by $\sigma_{N_i} = \sqrt{N_i}$ and Gaussian error propagation of those inidividual uncertainties yields

$$\sigma_H = \sqrt{\sum_{i=1}^{16} \left(\frac{dQ}{dN_i} \sigma_{N_i} \right)^2} = \sqrt{\sum_{i=1}^{16} k_i^2 N_i} \tag{2.24}$$

for the standard deviation of H. Equation 2.24 may only serve as an approximation because it assumes linearly-independent events [13] and no other contributions to the statistical fluctuation except Poissonian fluctuation (see section 5.5).

3. Investigations on the Analog Pixel Electronics

Contents

This chapter focuses on the characterization of the analog pixel electronics of the Dosepix detector, which is used throughout this thesis. Specifically, section 3.1 extends the energy calibration of Dosepix signals towards higher energies up to (5.6 MeV). This is accomplished by combining measurements of α-particles with Geant4 simulations. Section 3.2 explores the possibility of taking into account analog pile-up in simulations by presenting a framework to modify simulated spectra to reflect specific dose rates.

3.1. Extension of the Energy Calibration

Dosepix is a photon-counting and energy-resolving detector. As mentioned in subsection 2.8.2, it measures energies by detecting the reduction time of the charge, which the respective event has produced. This unit is called *time-over-threshold (ToT)*. As this is not a fundamental physical unit, the ToT must be calibrated to receive meaningful energy deposition information. This is performed using a method first described for the TimePix detector [88, 89], which employs analog pixel electronics similar to those of Dosepix [90]. The method was shown in 2014 to similarly hold for Dosepix [91]. In 2021, the calibration procedure was further developed by introducing a convolutional neural network, only requiring one ToT-measurement of $^{241}_{95}$Am and a Mo XRF-target to do the calibration [21]. This functionality is used in this thesis for the standard energy calibration of all Dosepix detectors. There, the relation between ToT and the deposited energy E_{dep} is described by

$$ToT(E_{\mathrm{dep}}) = a \cdot E_{\mathrm{dep}} + b + \frac{c}{E_{\mathrm{dep}} - t}. \tag{3.1}$$

The parameters a, b, c, and t must be determined for each pixel of each Dosepix and also depend on the detector settings, primarily the charge reduction current I_{Krum}. Most measurements, presented in this thesis, are performed with $I_{\mathrm{Krum}} = 6.6\,\mathrm{nA}$ if not stated otherwise. Typically, the hyperbolic part of Equation 3.1 becomes negligible for $E_{\mathrm{dep}} > 20\,\mathrm{keV}$, converting it into a simple affine-linear relation [16]. This behaviour of the analog pixel electronics has been shown for energies up until 500 keV. Yet, a study by Sommer et al regarding TimePix showed severe deviations from that behaviour for

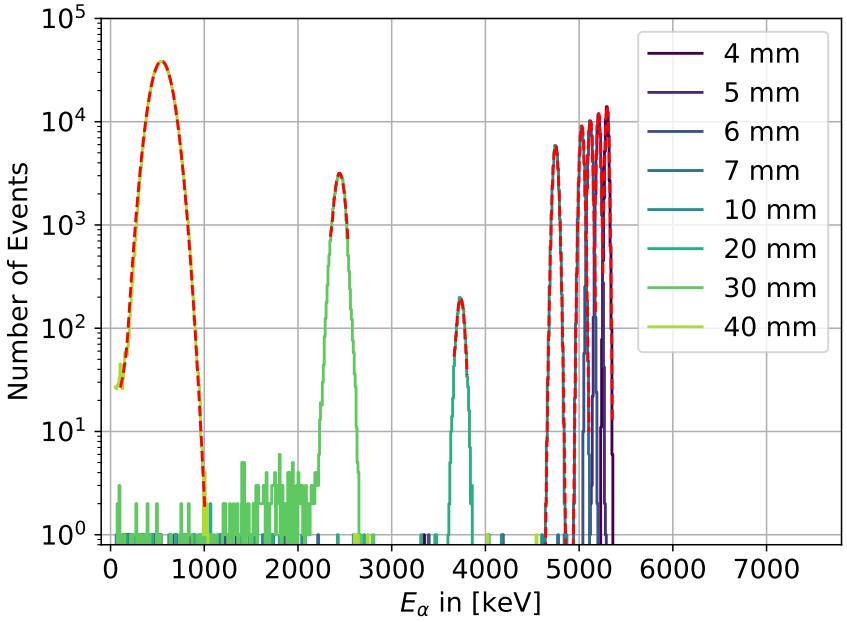

Figure 3.1.: Simulated α-spectra with respect to the kinetic energy E_α at different distances to the production of the particles. The initial energy of the α-particles is $E_\alpha = 5.64\,\mathrm{MeV}$. The red curves represent least-squares adjustments to the data according to Equation 3.2

energies $\geq 850\,\mathrm{keV}$ [92]. Therefore, a similar approach was examined for the Dosepix detector to investigate the relation between ToT and E_{dep} for higher energies.

This experiment is performed by irradiating Dosepix with α-particles from a mixed radioactive source, consisting of 48 % $^{241}_{95}$Am, 40 % $^{239}_{94}$Pu and 12 % $^{244}_{96}$Cm. The mean energy of the α-particles is $E_\alpha = 5.64\,\mathrm{MeV}$. As the stopping power of α-particles is larger than that of electrons or photons, the former deposit their kinetic energy in a smaller volume before being stopped. In silicon, the average path length of α-particles of the stated energy is about 31 µm [93]. Therefore, most particles will deposit their entire kinetic energy in the 220 µm x 220 µm x 300 µm pixel volumes of Dosepix. Yet, the α-particles, reaching the detectors, will have lost some kinetic energy in the air between the radioactive source and the detector. Therefore, the response of the analog pixel electronics to different energies can be investigated by changing the distance between the source and the detector.

However, this requires an independent determination of the expected energies to serve as the reference values. This is accomplished by simulating the α-particles in air via the Monte Carlo particle simulation tool Geant4, v10.07.03 [94]. A parallel source of α-particles with $E_\alpha = 5.64\,\mathrm{MeV}$ is sent through air, and the kinetic energies of the particles are tracked at different positions. The simulated spectra are shown in Figure 3.1. The number of particles depends on the distance, resulting from absorption and scattering in air, as well as the production of secondary particles, which are also tracked by the simulation. Mostly lighter secondary particles, like photons or leptons, are expected to reach the detector, but those will rarely produce full-energy events and, thus, do not affect this investigation [95]. The different peaks are parametrized

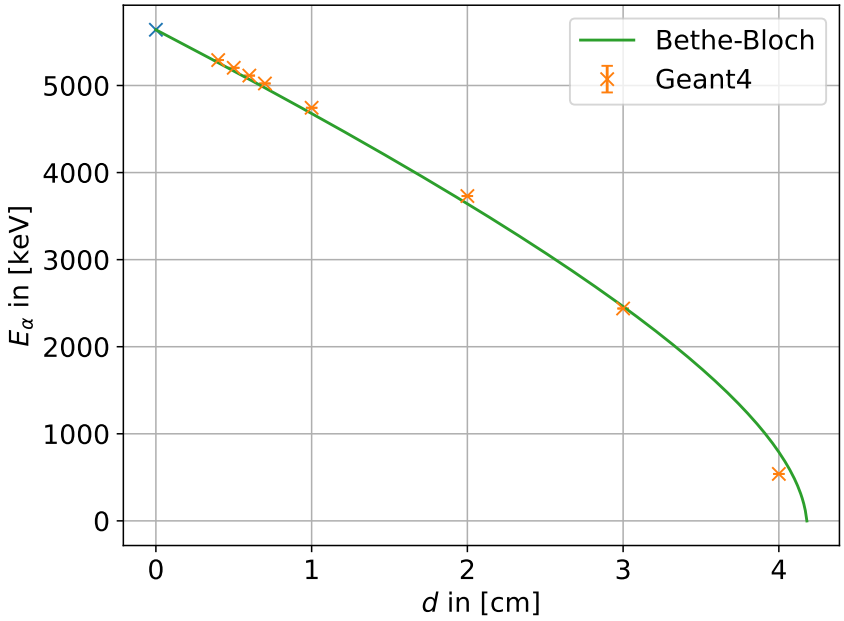

Figure 3.2.: Simulated kinetic energy of α-particles E_α with respect to their flight distance in air d. The uncertainties are derived from the fit uncertainties of μ. The blue cross represents the initial energy of 5.64 MeV. Additionally, the green curve shows a calculation of the same setup via the Bethe-Bloch equation.

empirically by adjusting the function

$$f\left(E_\alpha\right) = \begin{cases} p \cdot \mathrm{e}^{-\frac{(E_\alpha-\mu)^2}{2\sigma^2}} & \frac{E_\alpha-\mu}{\sigma} > -a \\ p \cdot A \cdot \left(\frac{B-(E_\alpha-\mu)}{\sigma}\right)^{-n} & \frac{E_\alpha-\mu}{\sigma} \leq -a \end{cases} \tag{3.2}$$

with $A = \left(\frac{n}{|a|}\right)^n \cdot \exp\left(-\frac{|a|^2}{2}\right)$, $B = \frac{n}{|a|} - |a|$ via a least-squares adjustment with a trust region reflective algorithm [96]. The fit parameters are p, a, μ, and σ. The peak energy is given by μ and the width of the peak by σ. Red dashed lines in Figure 3.1 represent the final adjusted functions. Figure 3.2 shows the resulting peak energies with respect to the distance d. As a sanity check, the energy loss was also estimated via the Bethe-Bloch equation [13]. The simulations and the calculation match except for the largest simulated distance of 4 cm, validating the results of the simulation. Furthermore, the largest possible distance for α-particles reaching the detector is determined as 4.18 cm.

The measurements with Dosepix are performed very similarly to the simulated setup. One unfiltered Dosepix detector is positioned at different distances from the described radioactive source. For that, distances d from 5 mm to 40 mm with a step size of 5 mm are chosen. Each measurement lasts 6 h to receive proper statistics. Unfortunately, the measurement at $d = 30$ mm only contains 1 h of data because of a technical issue with the detector. The data is recorded with the ToT-mode, as only the peak position of events from the α-particles is of interest for this experiment, not the number of detected events. Figure 3.3 shows four exemplary energy deposition spectra as a function of the

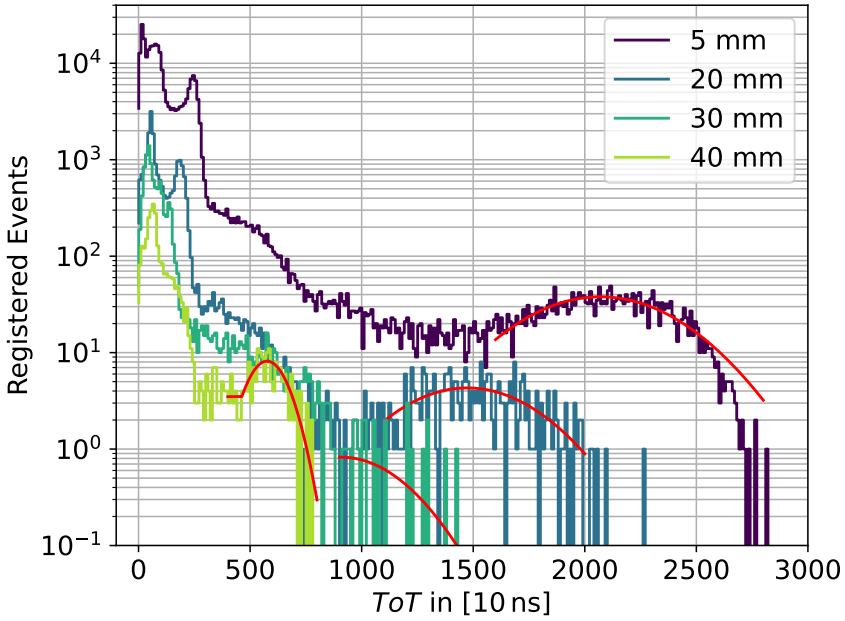

Figure 3.3.: Exemplary measured energy deposition spectra of α-particles with an initial energy of 5.64 MeV for different distances between the radioactive source and the detector. The red lines indicate least squares adjustments to the full-energy peaks.

uncalibrated ToT. Although full energy peaks are present in the measured spectra, they are very small compared to the lower-energy features and only appear in a logarithmic scaling. Because of the limited statistics, the following analysis is performed with respect to the sum of all pixels rather than individual pixels. The shorter measurement at 30 mm even contains hardly enough statistics to be analyzed at all. Energy deposition spectra at shorter distances include broader full-energy peaks, which is, at first glance, contradictory to the results of the simulations, shown in Figure 3.1. However, this is most likely caused by the differences in the energy calibrations of the individual pixels. Therefore, a more detailed investigation with enough statistics to carry out the analysis for every pixel by itself should be performed in the future. The full-energy peaks are again parametrized via Equation 3.2 and the results are drawn as red lines in Figure 3.3. There are some deviations between the adjusted functions and the data, especially in the energies above the average peak energy, but the results are still capable of sufficiently determining the peak position. The resulting ToT peak positions were matched with the simulations via the distance between the source and the detector. Figure 3.4 shows the relation between the measured peak positions and the simulated energies of the α-particles. Additionally, the low-energy calibration of Dosepix is drawn as a dashed blue line.

Obviously, the results of the measurements would not be represented by a linear extrapolation of the blue curve. Instead, the observed trends share some similarities with the results for TimePix [92]. Between about 500 keV and 1500 keV, there is no measurable dependence between the ToT and E_α. As there are only two data points in this region, it is impossible to determine a more precise calibration in that region. For

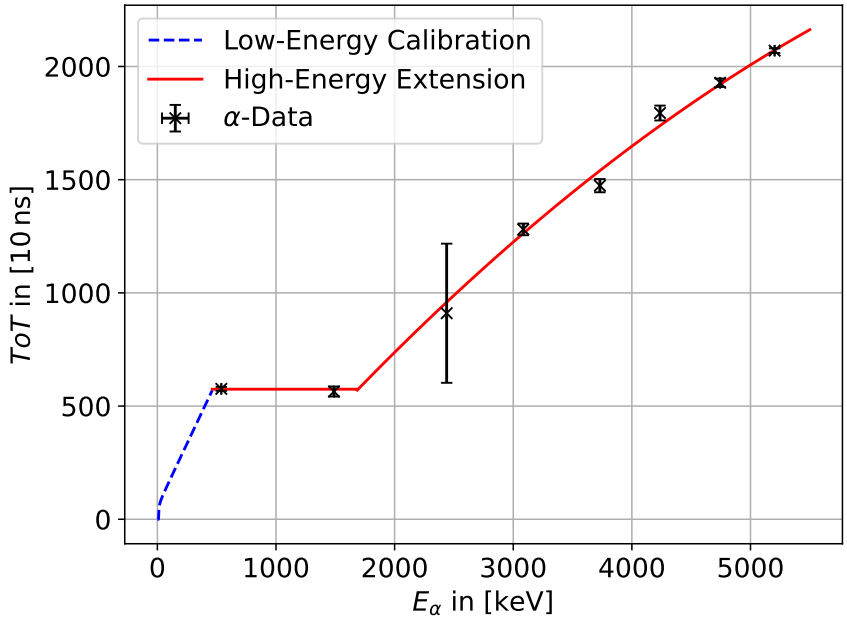

Figure 3.4.: Peak position from the measurements of the α-particles with respect to their simulated energy E_α. uncertainties are determined from the fit uncertainties. The blue dashed line represents the old energy calibration of Dosepix, and the red curve shows the resulting extension of the calibration curve of Dosepix for high energies.

this analysis, the weighted mean $\hat{\mu}$ and its variance $\sigma^2(\hat{\mu})$ of the two data points [13]

$$\hat{\mu} = \frac{\sum x_i/\sigma_i^2}{\sum 1/\sigma_i^2}, \; \sigma^2(\hat{\mu}) = \frac{1}{\sum 1/\sigma_i^2} \tag{3.3}$$

with the mean values x_i and their standard deviations σ_i, are used to parametrize this region. The results are $\hat{\mu} = (574 \pm 7)\,\mathrm{ToT}$ with a reduced χ^2 of 0.25. This small result of χ^2 might result from the very small number of data points or from a potential overestimation of the individual uncertainties. The energy $E_{\mathrm{crit},1} = (567 \pm 6)\,\mathrm{keV}$, at which the description of the energy calibration changes, is determined by the crossing point of $\hat{\mu}$ and the low-energy calibration curve. $E_{\mathrm{crit},1}$ is significantly lower than the corresponding value for TimePix (850 keV), but might also depend on the detector settings, which requires further investigation.

For even higher deposited energies, the relation between ToT and E_α starts increasing monotonically again, but with a decreasing gradient. This is in basic accordance with the findings for TimePix, where a parabolic calibration curve was observed for energies $> 1150\,\mathrm{keV}$ [92]. Therefore, a parabolic function

$$ToT(E_\alpha) = a' E_\alpha^2 + b' E_\alpha + c' \tag{3.4}$$

with fit parameters a', b', and c' is adjusted to the data points. The results are $a' = (-3.2 \pm 2.1) \cdot 10^{-5}\,\frac{\mathrm{ToT}}{\mathrm{keV}^2}$, $b' = (0.65 \pm 0.18)\,\frac{\mathrm{ToT}}{\mathrm{keV}}$, $c' = (-1004 \pm 20)\,\mathrm{ToT}$ and a reduced χ^2 of 2.9. Unfortunately, the data point at about 2400 keV, corresponding

to the shorter measurement at $d = 30\,\text{mm}$, comes with a large uncertainty due to the low statistics of that measurement. This data point increases the ambiguity of the results. Again, the critical energy $E_{\text{crit},2} = (1.7 \pm 0.6) \cdot 10^3\,\text{keV}$ is determined by the crossing point of the parabola and $\hat{\mu}$. No additional fundamental change of the calibration behaviour is found within the observed energies. Especially, no monotonically decreasing region is found, as it appears for TimePix for energies $> 2000\,\text{keV}$ due to saturation effects of the pixel electronics, manifesting in the so-called volcano effect [97]. Not finding this effect for Dosepix is interesting because of the similar analog pixel electronics. One explanation might be the significantly larger pixel size of Dosepix, increasing its robustness against such effects [16].

In summary, the energy calibration of Dosepix significantly deviates from the previously known relation for deposited energies $> (567 \pm 6)\,\text{keV}$. The ToT first stays constant with respect to the energy up to $(1.7 \pm 0.6) \cdot 10^3\,\text{keV}$ before transitioning into a parabolic relation. Therefore, the detector should only be used with much care, when energy depositions in those regions are expected, as a constant relation disables the definitive assignment of ToT to deposited energies. Though the presented investigations are conducted with too few data points to draw final conclusions. Therefore, the measurements should be repeated with higher statistics in the full-energy peaks and at more distances. Also, the settings of Dosepix like I_{Krum} might influence the results, requiring further investigation.

3.2. Analog Pile-Up in Simulations

Simulations are an important part of understanding the behaviour of a detector in many applications [21, 87, 98]. As mentioned earlier, those simulations are often performed in this work with the Monte Carlo simulation framework Geant4 [94]. On top of that, the Geant4 add-on Allpix^2 is used to include the sensor physics from energy deposition to the charge drift towards the electrodes, linking the sensor with the Dosepix ASIC [99]. However, a thorough understanding of the detector must also include the signal processing of the pixel electronics. Especially the analog part of the electronics majorly affects the output, for example, by introducing pile-up [16]. A better understanding of the analog output of Dosepix and an inclusion of the discussed effects in simulations would extend their usability to high-dose-rate experiments, such as [20] and [30]. Although there are some tools to simulate the analog signal voltage at the pixel electronics comparator, by the time of this thesis, most of them either produced nonsensical results for Dosepix or still could not handle event interactions like pile-up [99, 100]. Other electronic simulation tools like VIRTUOSO [101] have been used to simulate the analog output of Dosepix before in other studies [19], but are very cumbersome to operate, as they require a thorough description of the entire pixel electronics, and are often not free to use. Therefore, the following section presents new insights about the signal voltage of the analog Dosepix electronics and describes a preliminary, easy-to-use Python-based simulation framework to convert deposited energies into ToT for the Dosepix pixel electronics, taking into account the dose rate.

As described in subsection 2.8.1, the so-called *time-over-threshold* is Dosepix's internal measurement quantity of deposited energies. It is derived from the number of clock cycles that the voltage signals U_0, produced by deposited charges in the sensor layer, take to fall below the analog threshold U_{THL}. This procedure is encoded in the time-dependent

voltage at the charge-sensitive amplifier $U(U_0, t)$ with the time t. Then, the ToT is given by the difference of the zero-crossings of $U(U_0, t) - U_{\mathrm{THL}}$. Yet, the following calculations are not performed for those voltages directly, but for the proportional energies $E_U(E_0, t) \propto U(U_0, t)$ and $E_{\mathrm{THL}} \propto U_{\mathrm{THL}}$.

The most fundamental aspect of understanding and predicting the signal output is the shape of $E_U(E_0, t)$ with respect to time. Although this has been investigated qualitatively before, an analytical description has not been provided [16, 19, 91]. Kroupa et. al. were able to measure E_U for the TimePix detector with analog test pulses, but that method requires a combination of *time-over-threshold* and *time-of-arrival* [102]. The latter information is unavailable for Dosepix. Nevertheless, their result is expected to qualitatively reflect the results for Dosepix due to the design similarities of both detectors [90]. Taking these findings into account, an indirect approach of determining $E_U(E_0, t)$ is chosen for this evaluation. As discussed in the previous section, the calibration $ToT(E_{\mathrm{dep}})$ for low energies is given by Equation 3.1 with the parameters a, b, c, and t depending on the individual pixel and the settings of the detector. This information is used to recreate an expression for $E_U(E_0, t)$, which delivers the correct ToT for different $E_0 = E_{\mathrm{dep}}$. A measured average energy calibration with $I_{\mathrm{Krum}} = 2.2\,\mathrm{nA}$ and a threshold of $E_{\mathrm{THL}} = 12.3\,\mathrm{keV}$ are used as the reference data. The lower I_{Krum} compared to the other parts of this thesis is chosen because more pile-up events occur for lower I_{Krum} (because the signal processing per event takes longer) and the possibilities of creating significant pile-up with the available infrastructure are limited. After testing different models, the best results are obtained by

$$E_U(E_0, t) = \begin{cases} E_0 \exp\left(-\frac{1}{2}\left(\frac{\log\left(\frac{t}{\tau_0}\right)}{\sigma_0}\right)^2\right), & t \leq t_{\mathrm{trans}} \\ E_0 \exp\left(-\frac{1}{2}\left(\frac{\log\left(\frac{t_{\mathrm{trans}}}{\tau_0}\right)}{\sigma_0}\right)^2\right) + m\,(t - t_{\mathrm{trans}}), & t > t_{\mathrm{trans}} \end{cases} \tag{3.5}$$

with parameters $\tau_0 = 800\,\mathrm{ns}$, $\sigma_0 = 0.678$, and $m = -0.03\,\frac{\mathrm{keV}}{\mathrm{ns}}$. t_{trans} describes the transition time from an exponential to a linear behaviour and is given by the time when the first derivative of E_U matches m, i.e., $\frac{dE_U}{dt}(E_0, t_{\mathrm{trans}}) = m$. For low energies $E_0 < 48\,\mathrm{keV}$, this condition is never met and t_{trans} is set to 1300 ns. All the parameters are determined by a mixture of least-squares regression and brute-force best-fit adjustment, which means testing all possible parameters of the available phase space and quantitatively choosing the combination of best fit. The relative uncertainty of all parameters approximately equals 5 %, estimated from the step sizes of the adjustment procedures. Figure 3.5 shows the shape of Equation 3.5 for different E_0 as well as the corresponding $ToT(E_0)$ calibration curve. The time-dependent voltages approximately represent the shapes, measured for TimePix, although no such strict linear decrease was determined there [102]. Yet, this shape guarantees the reflection of the linear part of the ToT-calibration curve (Equation 3.1) while also keeping the expected proportionality of the height of the voltage pulse with respect to the initial deposited energy [21]. Another approximation in the description of the voltage curves is made by the hard transition between the exponential and the linear behaviour for low E_0. This is most visible in the exemplary voltage curve of 20 keV. For low energies, the exponential function alone

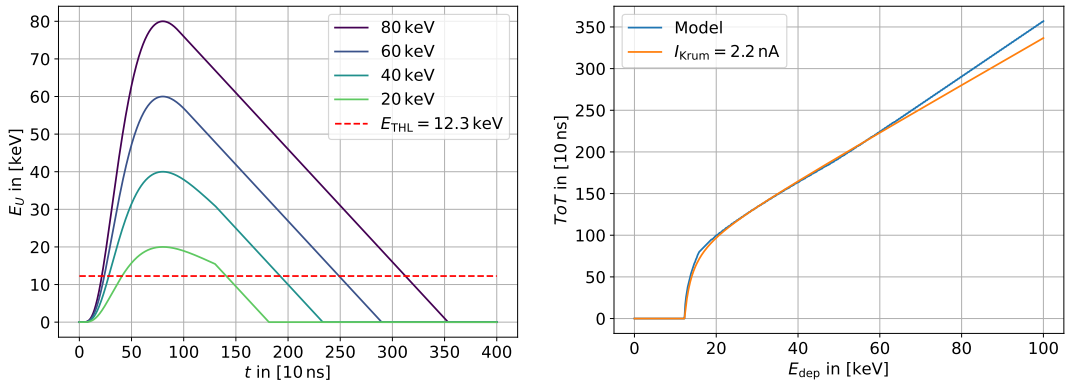

(a) Voltage curves according to Equation 3.5

(b) Dosepix energy calibration curves according to Equation 3.1.

Figure 3.5.: a) Model for the voltage at the charge sensitive amplifier of the Dosepix for different energies with respect to time. b) Comparison of an average measured ToT-energy calibration curve with $I_{\mathrm{Krum}} = 2.2\,\mathrm{nA}$ and the expression of that curve, produced by the voltage model.

would produce too flat results, which would lead to an overestimation of the ToT. The hard transition into a linear behaviour, although the time derivatives do not match at this point in time, corrects this misbehaviour, but does certainly not reflect the real voltages in the pixel electronics. The hard transition is also responsible for the kink in the modeled calibration curve in Figure 3.5b at 15.8 keV. It is located at the maximum energy, where $E_U(t_{\mathrm{trans}}) \leq E_{\mathrm{THL}}$ still applies. Lastly, the linear decrease of Equation 3.5 might not reflect the actual voltages below the threshold. No information about them is available via the chosen method, since the ToT is solely determined by the parts of E_U above the threshold. The findings of [19] hint at a more asymptotic re-approach of the voltage towards the baseline. Despite all the mentioned flaws of the current model, it is capable of recreating the actual calibration curve with a maximum residual of 12 % in the observed energy range and is, therefore, used for the further analysis, but establishing a more accurate description of $E_U(E_0, t)$ is the key to improve this framework.

The main goal is to recreate the ToT-spectra of Dosepix and predict pile-up. To test this, reference measurements with a Megalix Cat 125/35/80-121GW X-ray tube and Dosepix detector are performed [77]. The detector is irradiated by X-rays with a tube voltage of 40 kV, different tube currents from 1 mA to 20 mA and no additional filter, except the internal filter of the X-ray tube, which is equivalent to 1.5 mm of Al [77]. All measurements include 5 min of irradiation and are recorded in Dosepix's ToT-mode. The irradiation with the lowest tube current of 1 mA serves as the base of the analysis without pile-up. Its ToT data are converted into deposited energies in keV by the measured calibration curve. Afterwards, the deposited energy values are converted back into ToT via the framework. For that, time intervals between individual events must be assumed. The differences between two subsequent events are approximated by an exponential distribution, as that describes the independent time distances between Poisson-distributed events [103]. The mean of the exponential distribution is chosen

such that the total time matches the real irradiation time. Simulating the higher tube currents is done by also analyzing the 1 mA measurement, but adjusting the time differences reciprocally to the tube current. That mimics a measurement with a higher event rate, but shorter total irradiation time.

Kolmogorov-Smirnov tests are used to quantify the agreement of the results [104]. In principle, this test provides a measure of the possibility of two samples being drawn from the same probability distribution. In this case, the fitted and true energy spectra are tested for equality. The KS statistics D is calculated by the supremum of the differences between the true sample sets, i.e.:

$$D = \sup \|N_{\mathrm{Sim}} - N_{\mathrm{Meas}}\|, \tag{3.6}$$

with the simulated and measured spectra N^{Sim} and N^{Meas}. The result may be compared to a significance threshold value, which depends on the significance level α and the number of bins, 59. For $\alpha = 5\,\%$, this threshold is equal to 0.15639 [105]. If the results for D are above this threshold, the null hypothesis, i.e., the true and the fitted distributions being identical, is rejected with a certainty of $1 - \alpha = 95\,\%$. The cumulative sums of the presented spectra are used for the test instead of the spectra themselves because the Kolmogorov-Smirnov test is defined for cumulative probability distributions [104].

The results are shown in Figure 3.6. There is an excellent agreement between the measured and the simulated ToT-spectra for low tube currents ≤ 5 mA. The fluctuations of the simulated spectra, which are most present around the peaks of about 140 ToT do not originate from statistical fluctuations, but are a systematic effect. As mentioned earlier, average calibration parameters are used instead of the individual parameters of each pixel, causing slightly incorrect assignments of some ToT values and resulting in the displayed artifacts. Higher X-ray tube currents result in larger deviations from the simulations due to two reasons. First, the measured energy deposition spectrum shifts to lower ToTs, as the tube current increases, whereas the simulations stay stable. This effect has been examined before and is likely a result of an effective decrease of Dosepix's voltage baseline for high event rates [21]. As E_U progresses to 0 at the end of an event procession, some temporal undershoot of the voltage was observed, before relaxing back towards the original baseline. Those undershoots can affect the following events if the time intervals between events become small, leading to the observed effective baseline shift. This effect is currently not taken into account in the simulations but should be included for a better representation. The second effect revolves around the pile-up events, which start to appear for tube currents ≥ 10 mA between 200 ToT and 300 ToT. There are also some pile-up events in the simulated spectra, but significantly fewer than in the measured spectra. Although the Kolmogorov-Smirnov statistics of the entire spectra are still under the discarsion threshold, the pile-up parts of the spectra significantly differ, resulting in an insufficient expression of the high-dose-rate spectra. As an additional comparison, Figure 3.6e shows a simulated spectrum with an even shorter exposure time of 3 s. That spectrum shows the shape of the pile-up events of the 20 mA measurement. Therefore, the simulation is able to reflect pile-up events, but underestimates their amount for a given event rate.

As mentioned earlier, the behaviour of E_U below the threshold possibly differs from the linear model of Equation 3.5, which could result in a longer influence on subsequent signals. Furthermore, no events with energy depositions below the energy threshold are

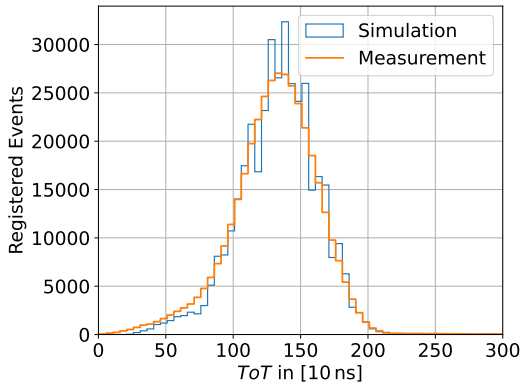

(a) $I = 1\,\mathrm{mA}$, $D = 0.085$

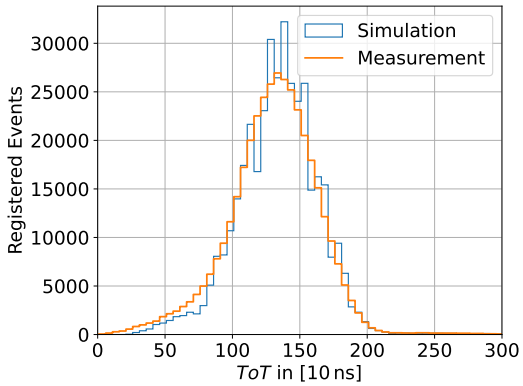

(b) $I = 2\,\mathrm{mA}$, $D = 0.085$

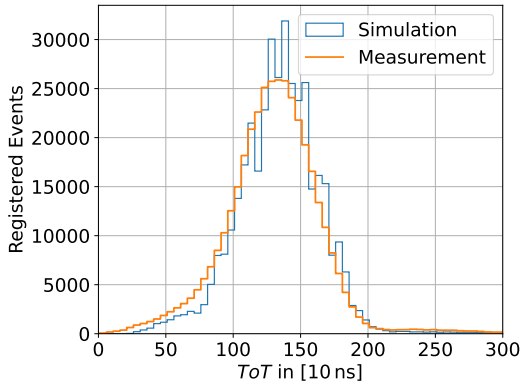

(c) $I = 5\,\mathrm{mA}$, $D = 0.119$

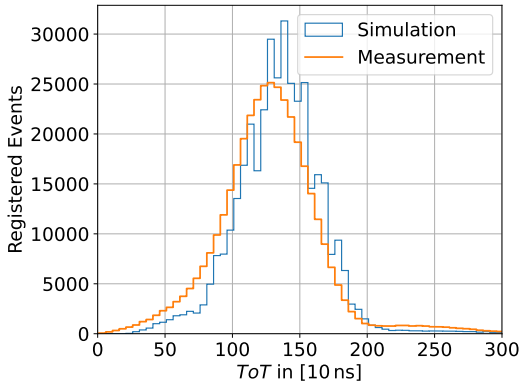

(d) $I = 10\,\mathrm{mA}$, $D = 0.136$

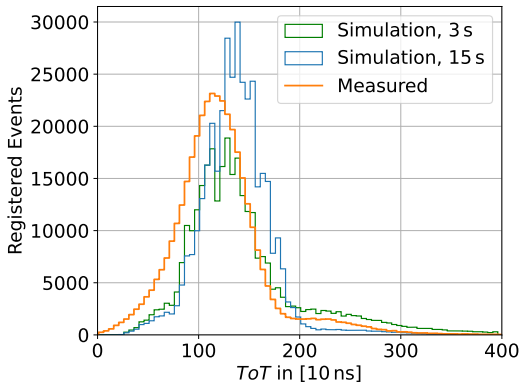

(e) $I = 20\,\mathrm{mA}$, $D = 0.136$

Figure 3.6.: Measured and modeled ToT-spectra of weakly filtered X-ray spectra with a tube voltage of 40 keV an different currents I, indicated by the caption together with the Kolmogorow-Smirnov statistics D. The plot for 20 mA additionally shows a modeled spectrum, corresponding to 3 s (i.e. 100 mA) of irradiation.

taken into account by the simulation, because they are not part of the measurement data, but may indirectly affect the results by also effectively changing the voltage baseline. Taking those low-energy events into account would require additional simulations of the sensor, as they do not directly appear in the measurement output.

In summary, correctly simulating analog pile-up for Dosepix measurements still requires some refinement. The most important aspect is the precise description of the time-dependence of the voltage at the charge-sensitive amplifier. Although the current model is capable of recreating low-flux measurements, its limits show in high fluxes, when the low-energy tail of the voltage curve affects the shape of the next signal, but is ignored in the simulation.

3.3. Conclusion

Despite the previous studies of the analog pixel electronics of the Dosepix detector [14, 16, 21, 91], there are still some unpredicted or not thoroughly characterized aspects in the detector behaviour. The measurements and simulations with α-particles showed that the energy calibration becomes non-linear for energies $\geq (567 \pm 6)\,\mathrm{keV}$. This could, for example, explain the observed discrepancies between the measurements and the expectations in [30]. The high-energy calibration should be further investigated to decrease the current uncertainties of the parameters and to investigate their dependencies with respect to the settings of the detector. Also, it might evolve the understanding of Dosepix and TimePix to examine whether Dosepix also starts experiencing the strong saturation effects, connected to the volcano effect, at some energies [92].

Introducing pile-up events for Dosepix measurements showed promising first results, but require a comprehensive understanding of the analog electronics of Dosepix to correctly reflect all its effects on the signal. An exhaustive method would be to analytically solve the differential equations associated with the analog circuit, as started in [21]. Also, measurements, being more affected by pile-up, should be performed with higher-power X-ray tubes to extend the parameter space of the validation data.

4. Spectrometry with Dosepix in Photon and Electron Radiation Fields

Contents

4.1. Spectrometers

When an energy-resolving semiconductor detector like Dosepix is exposed to ionizing radiation like electrons or X-rays, it is able to return a spectrum of the deposited energies in the sensor material. This energy-deposition spectrum significantly differs from the original particle emission spectrum. Most importantly, particles may not deposit their entire kinetic energy in the sensor material, e.g., photons might interact via single Compton-scattering (see subsection 2.2.1), or electrons are only partly stopped in the sensor (see subsection 2.2.2). Electromagnetic radiation might not even interact at all via an energy-transferring channel but, e.g., only change their direction of propagation by Rayleigh scattering. Thus, the number of registered particles will be lower than the number of particles reaching the detector. Additional exacerbating effects manifest in the case of high event rates, when analog pile-up occurs, and individual events are no longer properly distinguished [26]. Moreover, different types of particles may also produce similar signals and cannot be identified from the sole energy deposition spectrum.

On the other hand, a thorough understanding of the emission spectra is paramount in many applications and fields of research, where high particle fluxes are present. One example is given by the research on laser-induced plasma shocks. There, lasers with high energy densities are focused onto foam targets, producing plasma shocks and emissions of various particle types on very short time scales [106]. High particle fluxes also occur in FLASH radiation therapy to generate the necessary high dose rates for the intended short treatment durations [50]. Controlling such extreme environments depends upon a decent understanding of the emission spectra. Although the initial beam may consist of a singular particle type, e.g., electrons, other particles like photons are produced on

their way from the exit window to the patient by bremsstrahlung and other particle interactions (see section 2.2).

Therefore, more complex devices capable of reconstructing mixed particle spectra need to be developed. While direct measurements are rarely possible in the regimes examined in this thesis, such devices rely on either classical spectral deconvolution techniques or machine-learning-based algorithms. The hybrid pixel detector Dosepix has already been used to develop a low-flux photon spectrometer for X-rays from 10 keV to 120 keV in [21]. This approach relied on a convolutional neural network, trained on simulated spectra from X-ray tubes with various filter combinations. Three Dosepix detectors with filter caps, made of PMMA, aluminum, and tin, were used to gain proper initial information for the neural network to determine the emission spectrum. The use of Dosepix detectors enabled fast, direct readout and the device's compactness.

Another spectrometer using 90 thermoluminescence dosemeters (TLDs) was assembled in 2003 [107, 108]. This device was intended for high-intensity plasma physics. It utilizes the energy-dependent absorption of photons and electrons in different filter materials to reconstruct the particle energies. Triplets of TLDs were assembled in 30 layers, with specific filters of different materials and thicknesses in between each layer. From that, the final doses of all TLDs were used to determine the initial particle types, energies, and fluxes via a Bayesian data evaluation. The three TLDs per layer provide some robustness of the results regarding technical failures or scattered radiation. As the spectral deconvolution was, in principle, performed from just 30 data points, the device was called *few-channel spectrometer*. It has been used in pulsed photon fields [109] and for laser-induced plasma shocks [110]. Despite a general ability to reconstruct the radiation fields, the resulting spectra for the plasma experiments showed some flaws, such as inaccuracies for low particle energies < 200 keV and electron spectra not eventually converging to 0 for very high electron energies. Also, analyzing the data from the few-channel spectrometer is cumbersome and time-consuming, since every TLD has to be removed from the device and read out individually after each irradiation.

The following simulations explore the possibility of developing a Dosepix-based spectrometer, combining the advantages of the Dosepix detector with the absorption filters of the few-channel spectrometer. First, the proposed setup, including ten Dosepix detectors with different filter materials inserted in between, is presented. This is followed by a comparison of a purely mathematical approach, based on pseudo matrix inversion, and a least-squares regression method for simulated photon and electron fields. The chapter concludes by discussing the limits of the proposed setup, leaving it with no improvement over existing devices.

4.2. Simulated Setup

This section presents the concept of an active spectrometer for electron and photon fields, based on hybrid, photon-counting, energy-resolving Dosepix detectors. The core design of the novel Dosepix spectrometer is established from the working principle of the TLD-based few-channel spectrometer [107]. The device consists of layers of Dosepix detectors and filters. A sketch of the setup is shown in Figure 4.1. The individual layers are separated by 2 cm to provide adequate space for the Dosepix detectors and their connectors to the read-out hardware. A list of the filter layers is provided in Table 4.1. The initial thin Al-layer prevents ambient light or low-energy heavy ions from entering

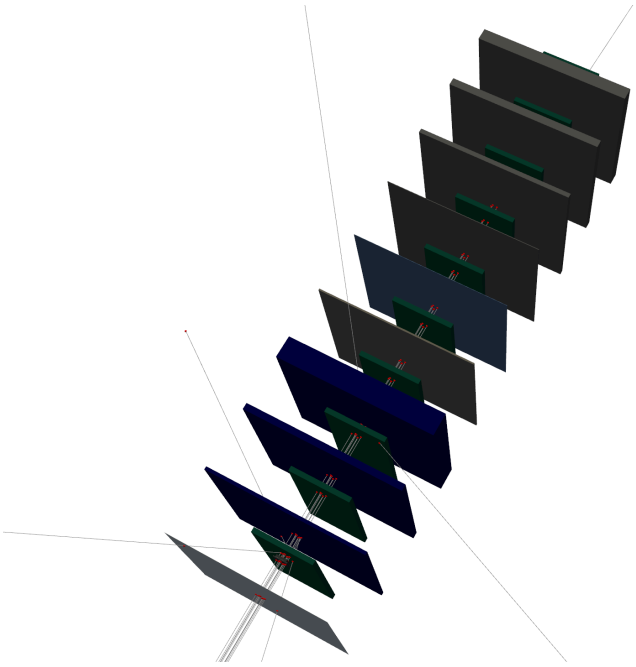

Figure 4.1.: Sketch of the simulated setup of the novel Dosepix spectrometer. Only one Dosepix detector at the front is depicted, although the true setup contains a detector between all layers. Exemplary photon tracks are drawn as gray lines, with red dots marking points of interaction.

Layer	Material	Thickness in [mm]
1	Al	0.025
2	PMMA	1.0
3	PMMA	2.0
4	PMMA	7.0
5	Sn	0.51
6	Mo	0.1
7	Pb	0.2
8	Pb	1.45
9	Pb	2.5
10	Pb	4.0

Table 4.1.: Filter materials and thicknesses of the novel simulated spectrometer setup

the detector and interfering with the signal. Three layers of PMMA with low absorption coefficients provide a high transmission. Behind them, materials with higher atomic numbers are used to eventually stop higher-energy electrons and photons. The actual filter materials and thicknesses are approximately based on the filters of the few-channel spectrometer. A meaningful spectral reconstruction may only function if all events, measured by one of the detectors, originate from particles that have traveled through all the previous filters. For example, scattered particles, hitting a detector from the side, would disrupt the reconstruction and should be shielded. Therefore, a large front surface of 50 mm x 50 mm was chosen for the filter layers, as they may absorb a larger fraction of diagonally impinging radiation that might otherwise enter a detector. Additionally, lead walls with a thickness of 2 mm surround the sides of the spectrometer, but are not drawn in Figure 4.1 in favour of the readability of the sketch. The energy regions of interest were set from 10 keV to 2.6 MeV for photons and from 120 keV to 20 MeV for electrons. Apart from ensuring some comparability with the few-channel spectrometer, these energy ranges were chosen to cover typical parameter spaces for dosimetry and electron radiation therapy [68]. Although the energies of primary electrons mostly fall in the MeV range, lower energies are produced by scattering and attenuation, making lower energies important for spectral reconstruction (see subsection 2.2.2).

All presented simulations are carried out with the Monte Carlo particle simulation tool Geant4, v10.07.03 [94], supported by the semiconductor pixel sensor simulation kit Allpix^2, v1.15 [99]. Silicon sensors with a thickness of 300 µm and dense square-shaped pixels with a pitch and edge length of 220 µm are simulated. This represents the large pixels of the real available Dosepix detectors at the time of this thesis, which would be the primary candidates for a real prototype. However, other sensor materials may better fulfill the requirements of the spectrometer, as will be discussed in detail in section 4.5. Allpix^2 computes the energy depositions and charge propagation in the sensor material for individual events, but does not account for the analog or digital pixel electronics of Dosepix. Also, no pile-up or any effects depending on the dose rate are natively included. Therefore, the outline of the development of the spectral reconstruction algorithm starts with low dose rates and separated emission of either photons or electrons of very limited spectral shapes. Subsequently, this narrow parameter space may be opened to increasingly more general cases. The simulated deposited energies of each Dosepix detector are treated as if they were measured in the energy-binning mode, i.e., each incoming event is sorted in a 16-bin energy histogram. The bin edges for low dose rates were chosen as (12, 15, 20, 25, 30, 35, 40, 50, 60, 70, 80, 90, 100, 110, 130, 150) keV. These values have shown excellent results for eye lens dosimetry in X-ray fields [10].

4.3. Deconvolution of Low-Flux Photon Fields

4.3.1. Response to Monoenergetic Spectra

The fundamental step to determine emission spectra from the composition of the energy deposition spectra is to gain quantitative knowledge about the energy-dependent response of each Dosepix on its specific position within the spectrometer. This key concept is first encoded in a basic mathematical formalism. For that purpose, a true emission spectrum shall be given by the vector components I_i. The energy index i represents the energy intervals used to describe the spectrum, which are different

from the previously mentioned 16 energy bins of Dosepix. For this analysis, 47 energy intervals between 0 keV and 2500 keV are chosen. An additional 48th interval represents all photon energies > 2500 keV. All interval edges are listed in Table A.2 and Table A.3 in Appendix A. These energy intervals are chosen heuristically. The widths of the intervals increase with higher energies, because the variations of the detector response are expected to decrease for higher energies in thin silicon sensors [25]. The vector components of Ψ_j represent the measured energy deposition spectra of all detectors. Here, the index j runs from 1 to 160, encoding the registered events in each energy bin of each detector, summing over the pixels of each detector. Thus, j is sorted as following: Dosepix1-Bin1, Dosepix1-Bin2,...,Dosepix1-Bin16, Dosepix2-Bin1,...,Dosepix10-Bin16. The original emission spectrum I_i and Ψ_j are connected by the response matrix of the spectrometer M_{ji} via

$$\Psi_j = \sum_i M_{ji} I_i. \tag{4.1}$$

The fundamental goal of this investigation and of the operation of the spectrometer is to invert Equation 4.1 and to find an expression for $I_i(\Psi_j)$.

The columns of the response matrix M_i are determined by the response of the spectrometer to monoenergetic photon spectra. This is investigated by simulating such monoenergetic spectra and their resulting response with Allpix^2. 47 spectra with photon energies in the centers of all energy intervals, accompanied by one spectrum with an energy of 2600 keV are investigated. The particles are emitted as a parallel beam from a 3.52 mm x 3.52 mm square, targeting the Dosepix detectors directly. 10^5 photons per energy are initialized to receive proper statistics. The resulting spectra do not yet take into account the limited energy resolution of Dosepix. For that purpose, each simulated deposited energy is replaced by an arbitrary energy, where the probability distribution is given by a Gaussian distribution with its mean equal to the original deposited energy, and a width of 1.2 keV, corresponding to the empirically determined value of Dosepix's energy resolution [21].

Figure 4.2 shows the detector response for six exemplary photon energies, divided by the number of initial photons. For lower energies < 100 keV, the response decreases for deeper layers in the spectrometer due to the increasing absorption of the filters. The spectra of each detector consist of a prominent full-energy peak at the primary photon energy and lower-energy contributions from Compton scattering and charge sharing. The shape of the energy deposition spectra of low energies hardly changes in deeper layers. This is because photons do not lose their kinetic energy continuously like charged particles. Instead, they only interact once or a few times, depositing their entire energy or getting deflected away from the line of Dosepix detectors. For higher energies, the back detectors also start measuring signals, and the energy deposition spectra do not show clear structures. The full-energy peaks disappear due to the decreasing interaction cross section for the photoelectric effect, and because the peak would, nevertheless, be located at higher energies than the highest energy bin (see subsection 2.2.1). On top of that, the mean path length of the electrons, produced in the sensor material from the photon interactions, increases with higher energies, leading to more charge sharing and smearing of the deposition spectra (see subsection 2.2.2). Furthermore, there is no strictly monotonously decreasing behaviour of the signal strength with respect to deeper layers anymore. That results from the dose build-up effect [111]. When the path length of the produced electrons is not negligible anymore, those electrons may travel

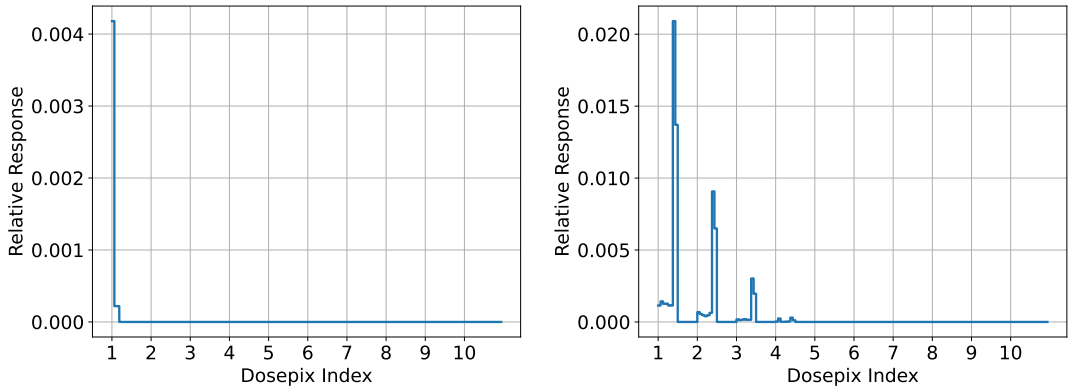

(a) 10 keV

(b) 50 keV

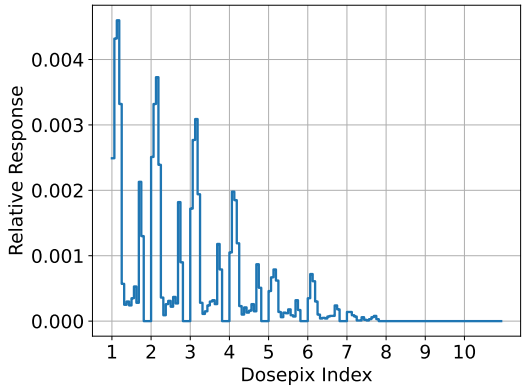

(c) 100 keV

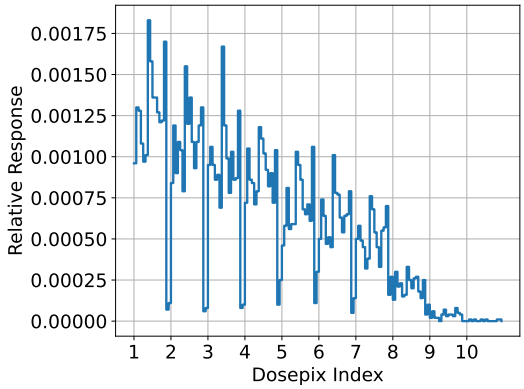

(d) 250 keV

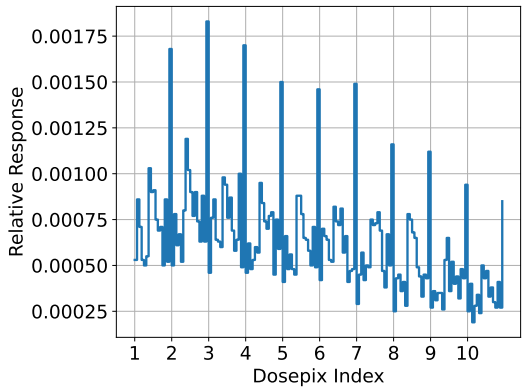

(e) 1000 keV

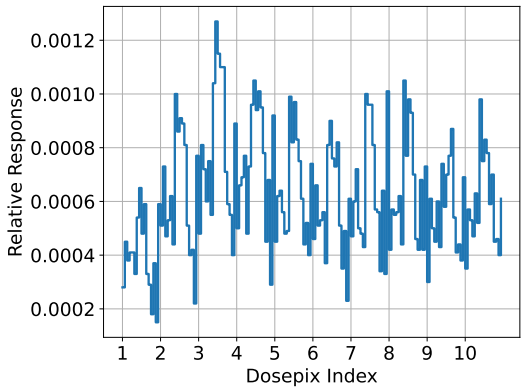

(f) 2600 keV

Figure 4.2.: Detector response of all Dosepix detectors within the spectrometer, divided by the number of initial photons. Each figure shows the response to a different primary monoenergetic spectrum, as indicated by the captions. The ticks on the x-axis state the respective Dosepix detector. In between, the 16-channel histogram, simulated for this detector, is shown.

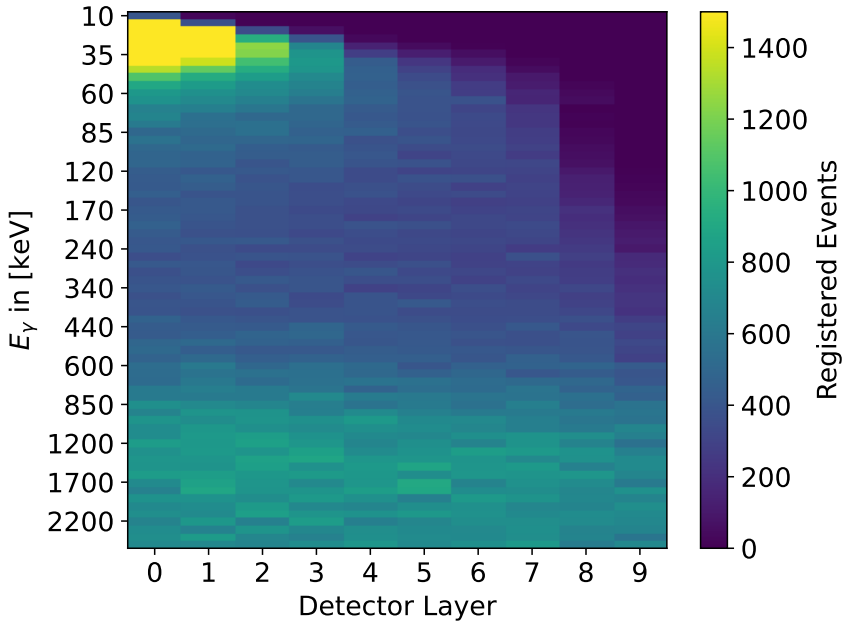

Figure 4.3.: Total number of registered signals of the Dosepix detectors within the spectrometer for all simulated monoenergetic photon spectra.

into deeper layers and deposit their energy there. As the electrons deposit more energy per unit length than a photon, this effect results in stronger signals in deeper layers.

The discussed behaviour is also reflected by the total number of registered events per detector for all energies, as visualized in Figure 4.3. The strongest signals are induced by low-energy photons in the front detectors, resulting from the large interaction cross-section for such photons. Electromagnetic radiation of higher energies is able to penetrate further into the spectrometer, but with weaker signals in each detector. Signal strengths start to increase again for photon energies $\geq 300\,\mathrm{keV}$ due to an increasing influence of dose build-up and induce more homogeneous signals throughout the detector layers. As there is almost no visible difference anymore for photon energies $\geq 1000\,\mathrm{keV}$, even a stronger absorbing filter might be required to distinguish and reconstruct those energies.

4.3.2. Mathematical Description of X-Ray Spectra

The development process for a model to reconstruct emission spectra starts by reconstructing typical X-ray tube spectra at low dose rates, as this represents the field of research with the largest expertise regarding Dosepix behaviour [17]. Spectra, emitted by X-ray tubes, are parametrized by their photon flux Φ, their maximum photon energy E_{max}, given by the kinetic energy of the accelerated electrons and, thus, the tube voltage, and the absorption by filters. The basic emission of an unattenuated X-ray spectrum $I_0(E_\gamma)$ is approximately described by Kramer's law [112]:

$$I_0(E_\gamma) \approx \Phi \left(\frac{E_{\mathrm{max}}}{E_\gamma} - 1 \right). \tag{4.2}$$

Quality	Al	Cu	Sn	Pb
N-500	4	0	6	15
N-1000	8	0	12	45
N-1500	8	0	12	60
N-2000	30	0	30	60
N-2500	30	0	30	100

Table 4.2.: Filter combinations of the newly invented X-ray spectra for testing the reconstruction of high photon energies. The filter thicknesses are stated in mm.

Then, X-ray spectra $I(E_\gamma)$ are retrieved by multiplying this term with the corresponding filter attenuation components

$$I(E_\gamma) = I_0(E_\gamma) \cdot \prod_f \exp(-\mu_f d_f), \tag{4.3}$$

where $\mu_f = \mu_f(E_\gamma)$ represent the attenuation coefficients and d_f the thicknesses of the filter materials. The attenuation coefficients for this analysis are taken from [113]. For the first simulation run, the filter elements Al, Cu, Sn, and Pb are selected, as those materials are used for all official spectra, listed in ISO 4037-1 [74]. Therefore, X-ray spectra are fully parametrized by Φ, $E_{\max}$, d_{Al}, d_{Cu}, d_{Sn}, and d_{Pb} in this model.

When the different deconvolution techniques, presented in subsection 4.3.3 and 4.3.4, are established, they are validated by applying simulations of the N-series spectra of ISO 4037-1 and evaluating the prediction of the spectrometer. The N-series ("Narrow") is a list of strong filtered spectra with tube voltages between 7.5 keV and 400 keV. Their strong filtration leads to a narrow spectral shape because photons of low energies are effectively absorbed. This makes the N-series spectra attractive for metrology and device performance evaluation because the narrow shape enables straightforward investigation of energy dependencies. Unfortunately, the official radiation qualities only cover photon energies up to 400 keV, which is not enough for an exhaustive test of the spectrometer. Therefore, additional high-energy spectra in conformity with the N-series are defined for this purpose. These were called N-500, N-1000, N-1500, N-2000, and N-2500, where the number again depicts the maximum photon energy in units of keV. The filter combinations of the new spectra are listed in Table 4.2, while the shapes of the spectra are shown in Figure 4.4. Similar to the true N-series, the energy bandwidth of the new spectra is relatively small, compared to, e.g., the W- and H-series [74]. In the following paragraphs, all radiation qualities of the true N-series from ISO 4037-1, as well as the newly invented spectra, are meant when referring to the N-series.

The shapes of the spectra are determined via simulations with the Python package *xpecgen* [75, 76]. Figure 4.5 shows the exemplary simulation results for N-80 and N-400. The spectra have been normalized to their maximum value. In addition, the normalized spectral representations for the selected energy intervals of the spectrometer are shown. As the N-series contains narrow spectra, they only span over a few energy intervals, affecting the accuracy of the spectral representation. This might also affect the relative precision of the reconstruction. That way, the N-series serves as a realistic but strict test of the deconvolution techniques.

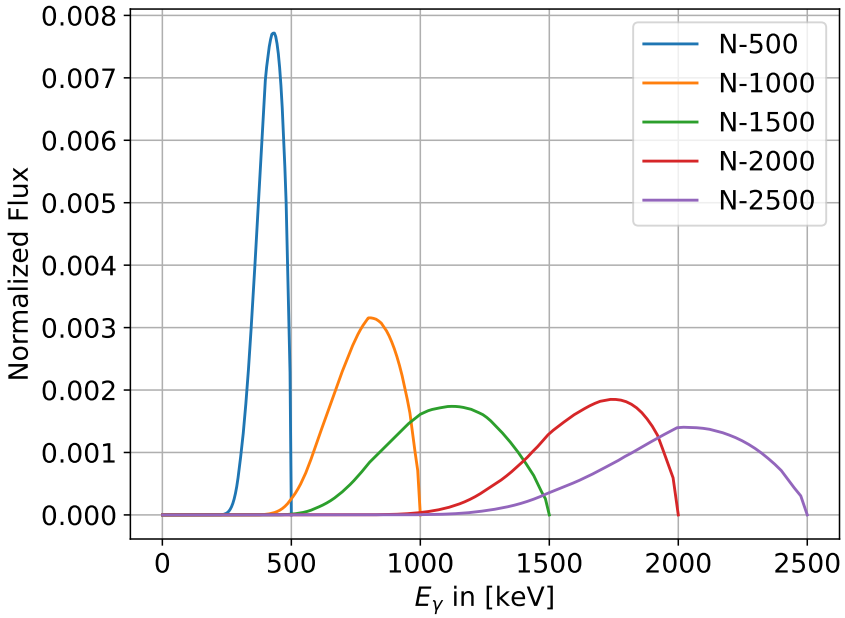

Figure 4.4.: Normalized shapes of the newly invented X-ray spectra for expanding the N-series with respect to the photon energy E_γ.

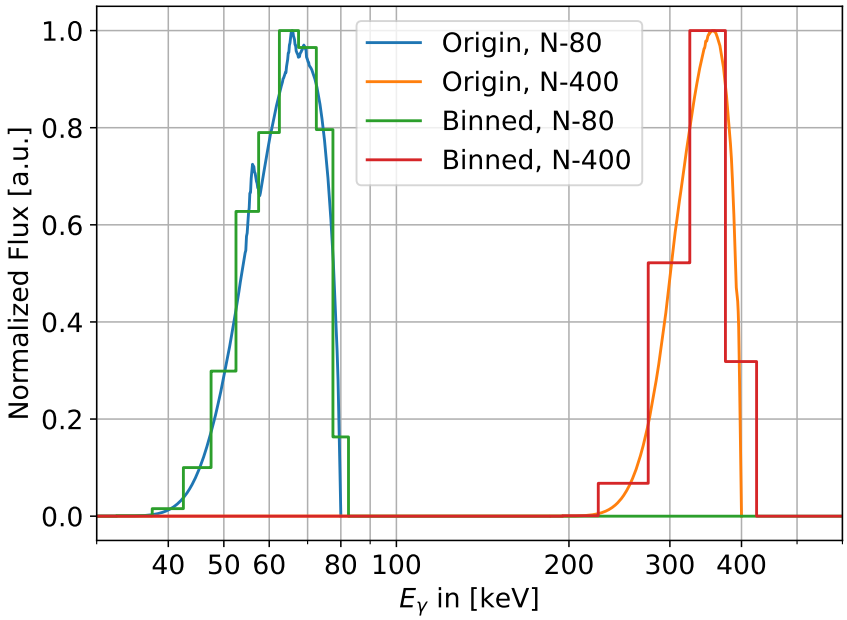

Figure 4.5.: Normalized simulated spectral shapes of N-80 and N-400, labeled as "Origin", with respect to the photon energy E_γ. The "Binned" curves show the representations of the spectra in the energy intervals of the spectrometer.

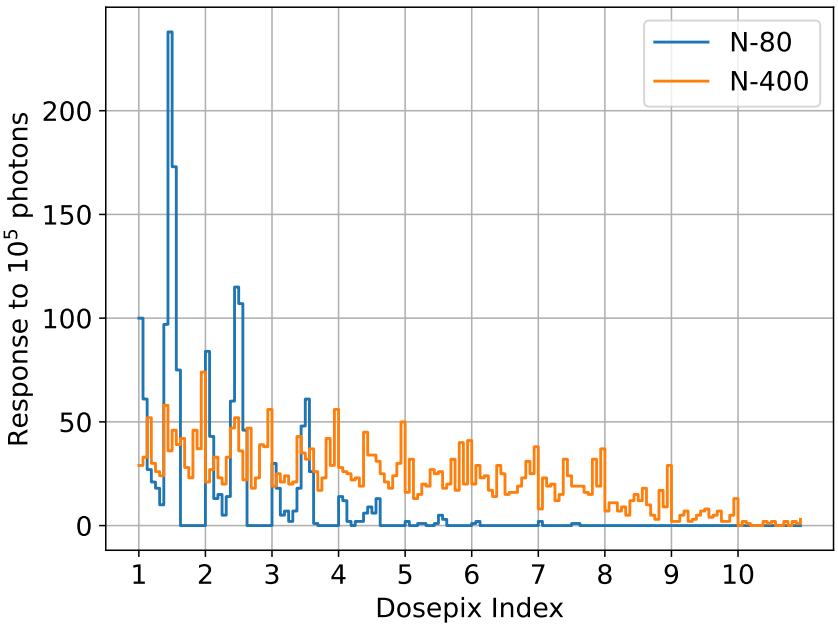

Figure 4.6.: Response of the simulated spectrometer to N-80 and N-400. 10^5 photons are simulated for each spectrum. The x-axis represents the 16 energy bins of the Dosepix detector in each layer.

The spectrometer response to the N-series spectra is simulated using Allpix^2, as in the simulations of the monoenergetic spectra. Results for all spectra are shown in section B.1. Those sets of initial emission spectra and corresponding detector responses serve as the validation of the spectral reconstruction methods presented in the following. The response to the two example spectra, N-80 and N-400, is shown in Figure 4.6. Similar observations to the response to the monoenergetic spectra can be drawn. The Dosepix detector of the first layer registers more events when exposed to N-80 than to N-400 due to the larger interaction cross-section. This ratio changes and turns around in deeper layers of the spectrometer, as the high-energy photons are less absorbed by the filter materials.

4.3.3. Pseudo-Inverse Response Matrix

The first approach to deconvolve the spectra is to directly determine the left-inverse response matrix M_{ij}^{-1}. As the mathematical invertibility of M_{ji} is not guaranteed, the pseudo-inverse matrix, according to Penrose, is determined instead [114]. This formalism is encoded in the *pinv* method of the Python package *scipy.linalg* [115]. Figure 4.7 shows exemplary reconstructed spectra for N-80 and N-400. Obviously, the results do not represent physically meaningful spectra. Both examples contain large amounts of negative entries and show very erratic behaviour throughout the observed energies. The non-zero contributions exceed the actual highest photon energies by far. Nevertheless, the response of the simulated spectrometer to those spectra, shown in Figure 4.8, still closely resembles the response to the actual N-80 and N-400, shown

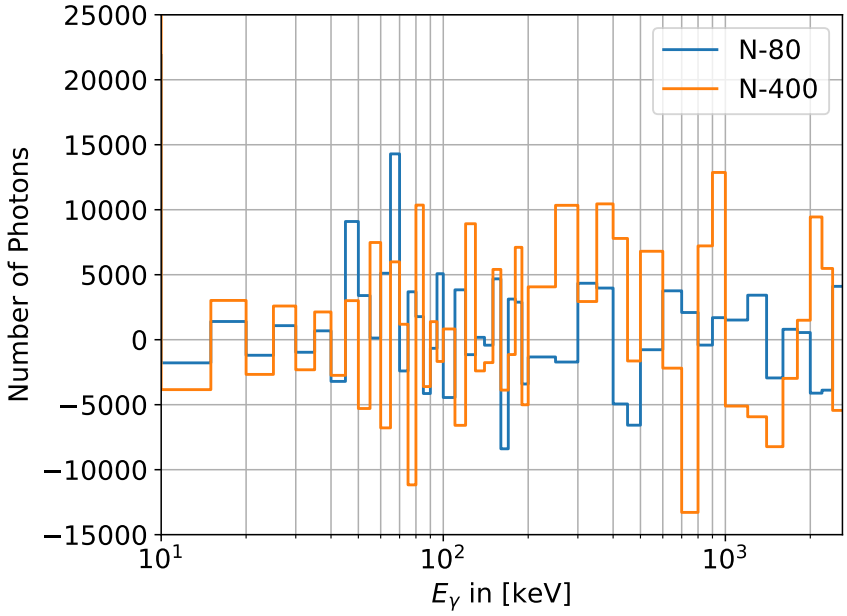

Figure 4.7.: Reconstructed spectra for N-80 and N-400 with respect to the photon energy E_γ, determined via the pseudo-inverse matrix M_{ij}^{-1}.

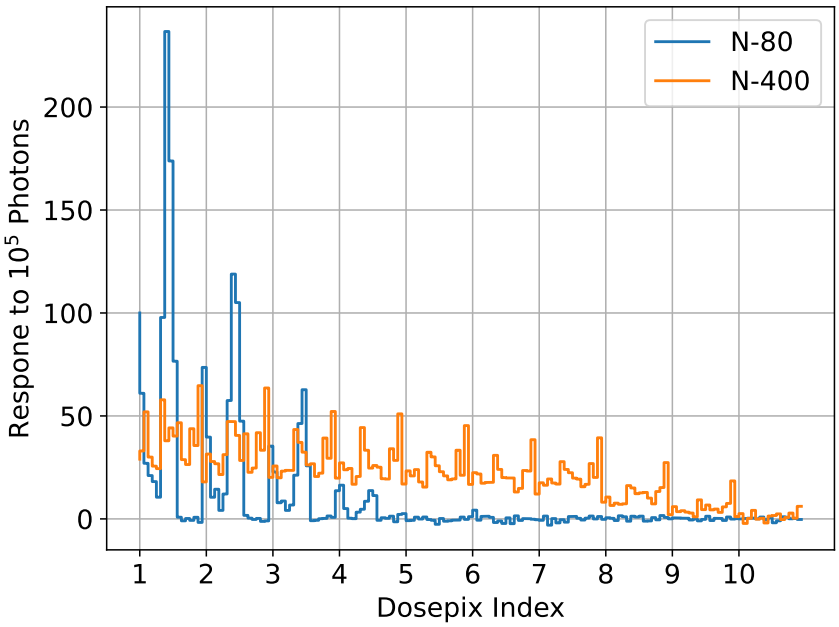

Figure 4.8.: Response of the spectrometer to exposition to the non-physical spectra, shown in Figure 4.7.

Spectra	Parameter	Φ	$E_{\max}$	d_{Al}	d_{Cu}	d_{Sn}	d_{Pb}
N-20 - N-400	start	10^5	95	3.0	0.0	0.0	0.0
	low	0	90	0.0	0.0	0.0	0.0
	up	10^8	1000	50.0	6.0	7.0	11.0
N-500 - N-2500	start	10^5	750	4.0	0.0	6.0	10.0
	low	0	400	0.0	0.0	0.0	0.0
	up	10^8	3000	400.0	400.0	400.0	400.0

Table 4.3.: Starting values, lower, and upper bounds (labeled "low" and "up") of the least-squares regression. $E_{\max}$ is given in units of [keV] and the filter thicknesses in units of [mm].

in Figure 4.6. Especially the front layers are well represented, and also the respective absorption in deeper layers is reflected. Negative responses only occur at energy bins, where the reference response is close to 0, i.e., for high energies for N-80 or in the deepest layers for both spectra. Therefore, the method of spectral reconstruction via the pseudo-inverse response matrix for photons is able to return mathematically conclusive results, but lacks physical meaning, deeming it worthless in the given context. However, follow-up studies might return to the basic idea of a direct matrix inversion, as the pseudo-inverse is not generally unique [114]. Therefore, there might be a physically meaningful pseudo-inverse matrix enabling direct calculation of the emission spectra for photons, as it is found for electrons, discussed in section 4.4.

4.3.4. Least-Squares Regression

The second tested method focuses on determining emission spectra via a least-squares fit to Equation 4.1. As the components of the energy deposition vector Ψ_j and the response matrix M_{ji} are known, the entries I_i may be adjusted until the resulting spectrometer output matches the originally simulated output. In this first attempt, not all components of I_i are adjusted independently, but only emission spectra of the basic shape, given by Equation 4.3, are considered. The parameters Φ, $E_{\max}$, d_{Al}, d_{Cu}, d_{Sn}, and d_{Pb} are adjusted with a trust-region reflective algortihm [116]. Equal starting values and parameter boundaries are provided for all spectra of the original N-series. For the extended N-series radiation qualities, the starting values and boundaries have to be adjusted to account for the extreme filter layers necessary to produce those spectra. The starting values, lower, and upper bounds are listed in Table 4.3. All models converged within a maximum number of 600 iterations.

The final deconvolved spectra are shown in Figure 4.9, 4.10, and 4.11 together with the true photon emission spectra. It is rather difficult to draw general conclusions as the various spectra show very different results. This is also apparent when looking at the absolute residuals of the estimated parameters, shown in Figure 4.12. As the residual represents the difference between the estimated and true parameters, divided by the true parameters, no value is drawn if the true parameter equals 0.

For the radiation qualities with the lowest energies up to N-40, the reconstructed spectra hardly represent the true spectra. While N-20 shows no convergence of the fit at all, the algorithm at least manages to estimate the energies of maximum flux for the other low-energy spectra, but significantly overestimates the width of the spectrum

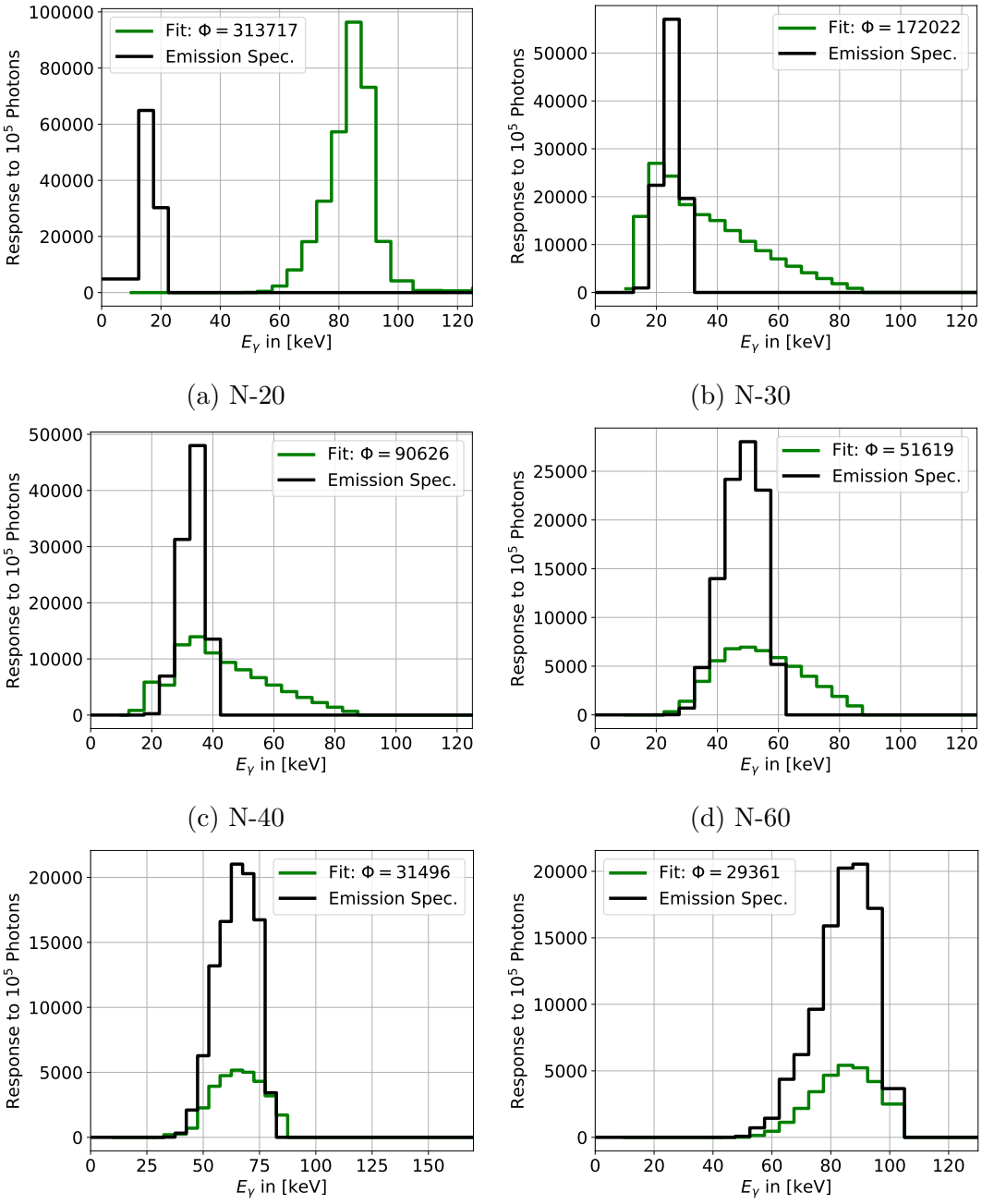

(a) N-20 (b) N-30

(c) N-40 (d) N-60

(e) N-80 (f) N-100

Figure 4.9.: Reconstructed N-series radiation qualities from least-squares fits with respect to the photon energy E_γ together with the original emission spectra from N-20 to N-100. The black line corresponds to the original emission spectrum. The green spectrum represents the least-squares fit result, with the number Φ in the caption being the total number of estimated photons.

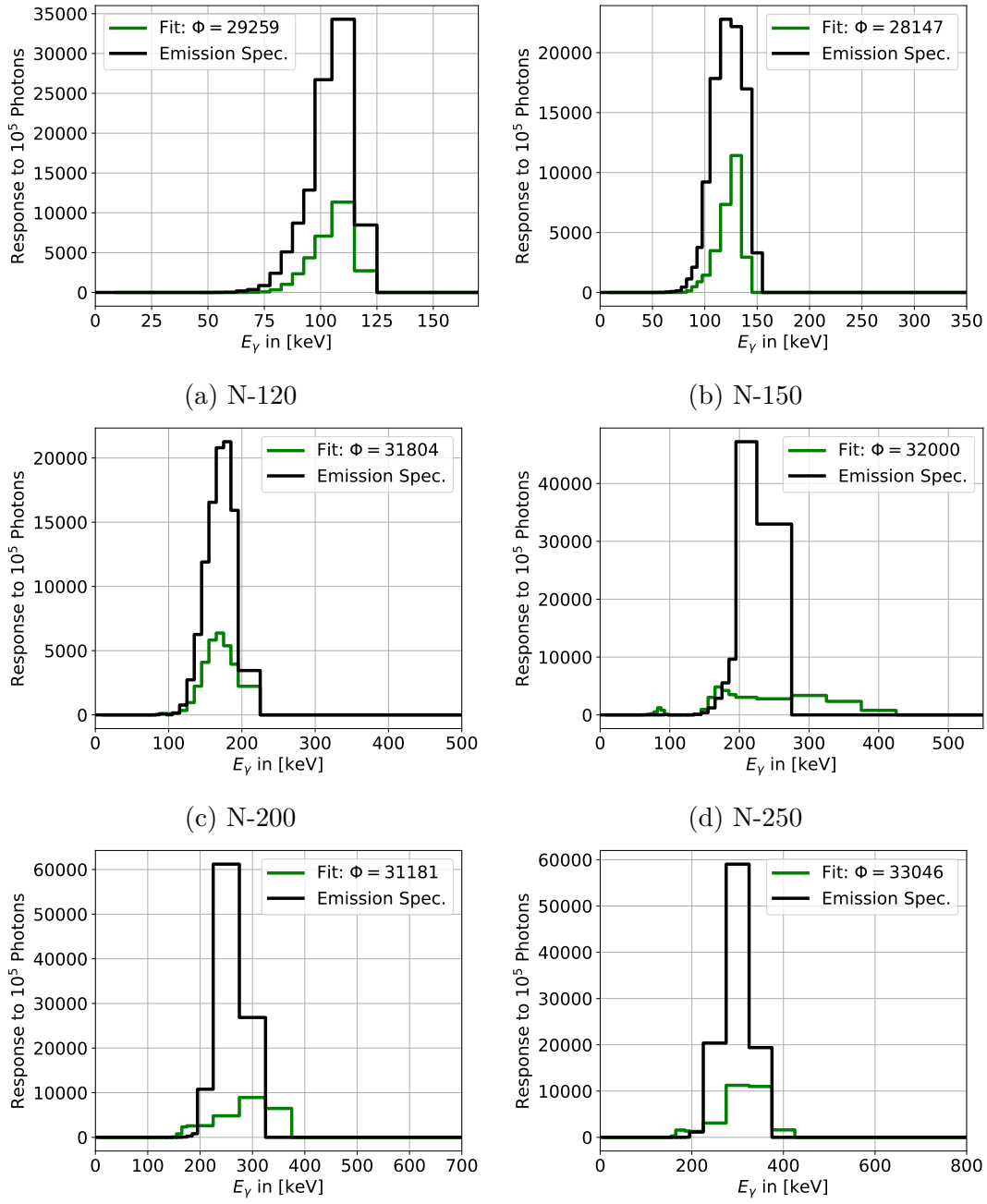

(a) N-120 (b) N-150

(c) N-200 (d) N-250

(e) N-300 (f) N-350

Figure 4.10.: Reconstructed N-series radiation qualities from least-squares fits with respect to the photon energy E_γ together with the original emission spectra from N-120 to N-350. The black line corresponds to the original emission spectrum. The green spectrum represents the least-squares fit result, with the number Φ in the caption being the total number of estimated photons.

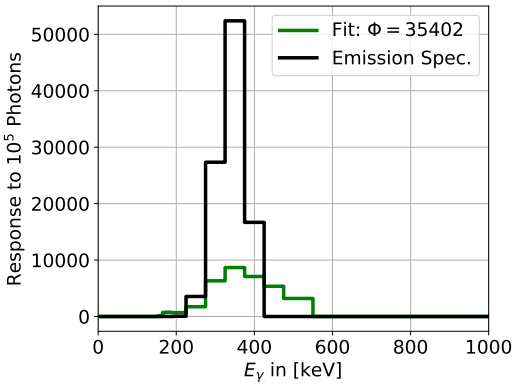

(a) N-400

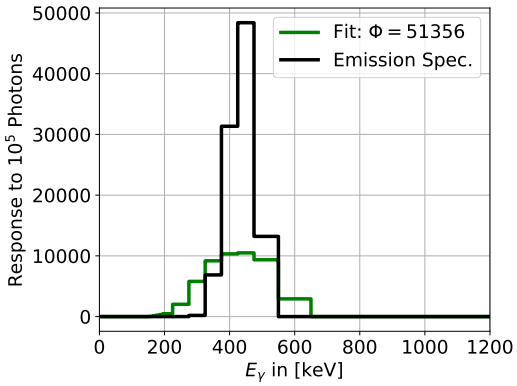

(b) N-500

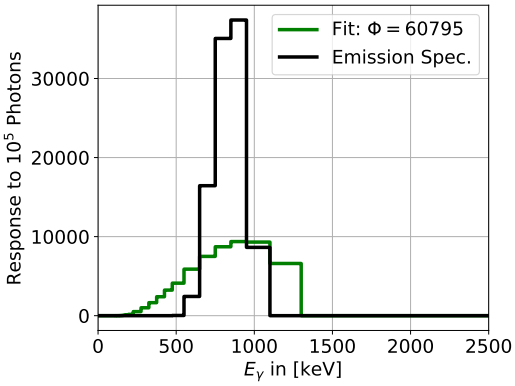

(c) N-1000

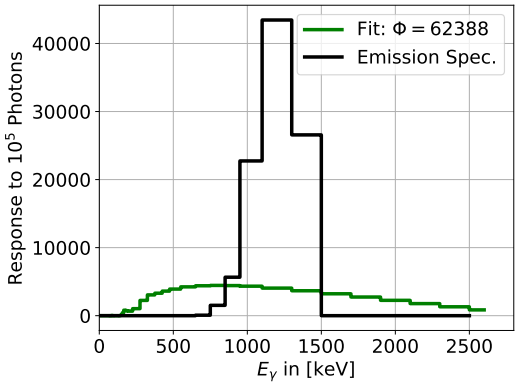

(d) N-1500

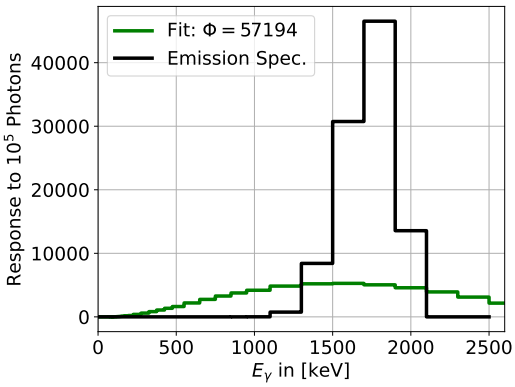

(e) N-2000

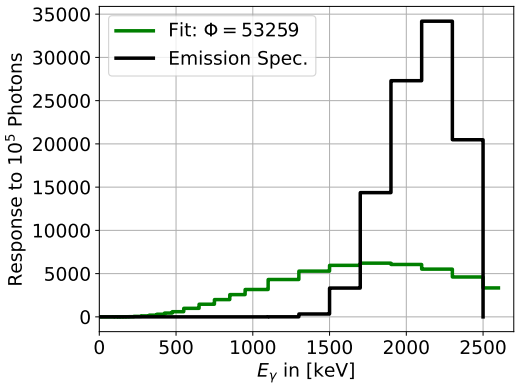

(f) N-2500

Figure 4.11.: Reconstructed N-series radiation qualities from least-squares fits with respect to the photon energy E_γ together with the original emission spectra from N-400 to N-2500. The black line corresponds to the original emission spectrum. The green spectrum represents the least-squares fit result, with the number Φ in the caption being the total number of estimated photons.

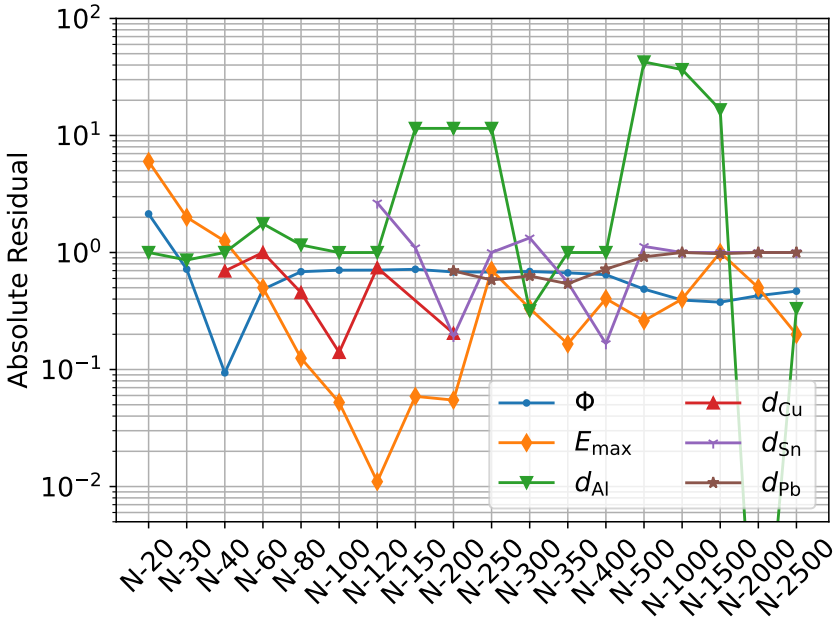

Figure 4.12.: Absolute Residual of the reconstructed parameters of the spectra, shown in Figure 4.9 to 4.11. The d_{Al} value for N-2000 equals $6.0 \cdot 10^{-5}$, but was not drawn to favour the visibility of the remaining points.

towards higher energies. The total photon fluence is approximately estimated. The least-squares algorithm possibly relies dominantly on the data of the front layers. There, the mathematical mode of the spectrum is most important, whereas the higher energies contribute less due to their smaller interaction cross-section. This behaviour flips for the deeper layers, where large amounts of the low-energy photons have already been absorbed, but this is not prioritized by the reconstruction algorithm. Those deviations between true spectra and the reconstructions reduce as the mean energy of the emission spectra increases. The best results, regarding the shape of the spectra, are achieved for N-80 and N-100. This energy range is still part of the optimal range for Dosepix detectors with silicon sensors, while the photon energy is also high enough to penetrate some of the filter layers of the spectrometer [16]. That way, the reconstruction can benefit from the layout of the spectrometer. As the mean photon energy further increases, the spectra begin to deviate from their original shape. The large ambiguity is likely due to the indistinguishability of the high energies in the detectors, resulting in very similar results in most layers of the spectrometer. On top of that, the low interaction probability of the silicon sensor regarding high photon energies likely causes the uncertain estimation of the total number of photons, but the details of that phenomenon remain ambiguous and require further research.

As a quantization of those discussed findings, the fitted spectra are compared with the binned reference spectra via a Kolmogorov-Smirnov test (see section 3.2 and [104]). The significance threshold for a significance level of $\alpha = 5\,\%$ and the 48 energy intervals is equal to 0.17302 [105]. The results are shown in Figure 4.13. As expected, the null hypothesis is unambiguously rejected for all radiation qualities. Therefore, the presented method is currently not suited to recreate the X-ray spectra of the expanded N-series.

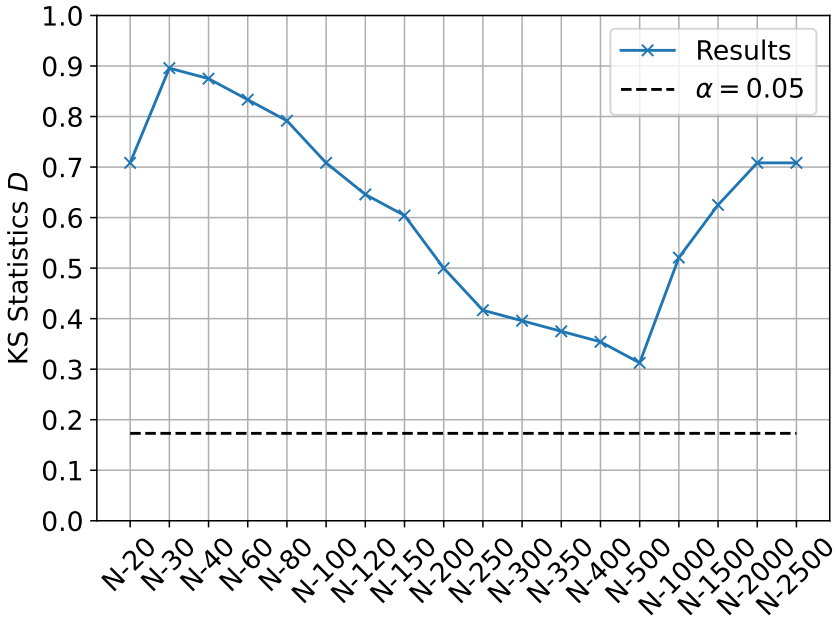

Figure 4.13.: Results of the Kolmogorov-Smirnov-tests D of the fit results for photons, shown in Figure 4.9 to 4.11. The black dashed line corresponds to the 5 % significance threshold.

4.4. Deconvolution of Low-Flux Electron Fields

In its final application, the novel spectrometer should be able to deconvolve mixed photon and electron spectra. After investigating the former in the limit of low particle fluxes, the same approach is conducted for pure electron spectra. The same ansatz of Equation 4.1 and the same deconvolution techniques are followed. That way, both reconstruction methods for photons and electrons may later be combined straightforwardly into a single framework. The range of simulated electron energies is set from 120 keV to 20 MeV (see Table A.2 and Table A.3 for the specific energy bins). These energies are chosen to account for the typical particle energies of medical electron energies between 7 MeV to 20 MeV, as well as the lower energies from decelerated and scattered electrons [41]. The lower limit of 120 keV is chosen heuristically as about 1 % of this typical medical energy range.

The response matrix for electrons M_{ji}^{e} is constructed in the same way as the response matrix for photons. Monoenergetic electron beams with 10^4 particles are sent directly onto the spectrometer. The number of simulated particles is reduced relative to photons to account for the longer computation time of electrons, as they interact more often with their surrounding material than photons. Exemplary energy deposition spectra, divided by the initial number of electrons, are shown in Figure 4.14. It is obvious that the low-energy electrons $\leq$ 1200 keV only produce a signal in the first detector layer before being stopped. Only the higher simulated energies manage to penetrate the PMMA layers and induce some signal in the back detectors. This exacerbates the reconstruction of the low electron energies, as they are perceived as very similar by the spectrometer. Despite the simulated higher energies, the energy bins of the Dosepix

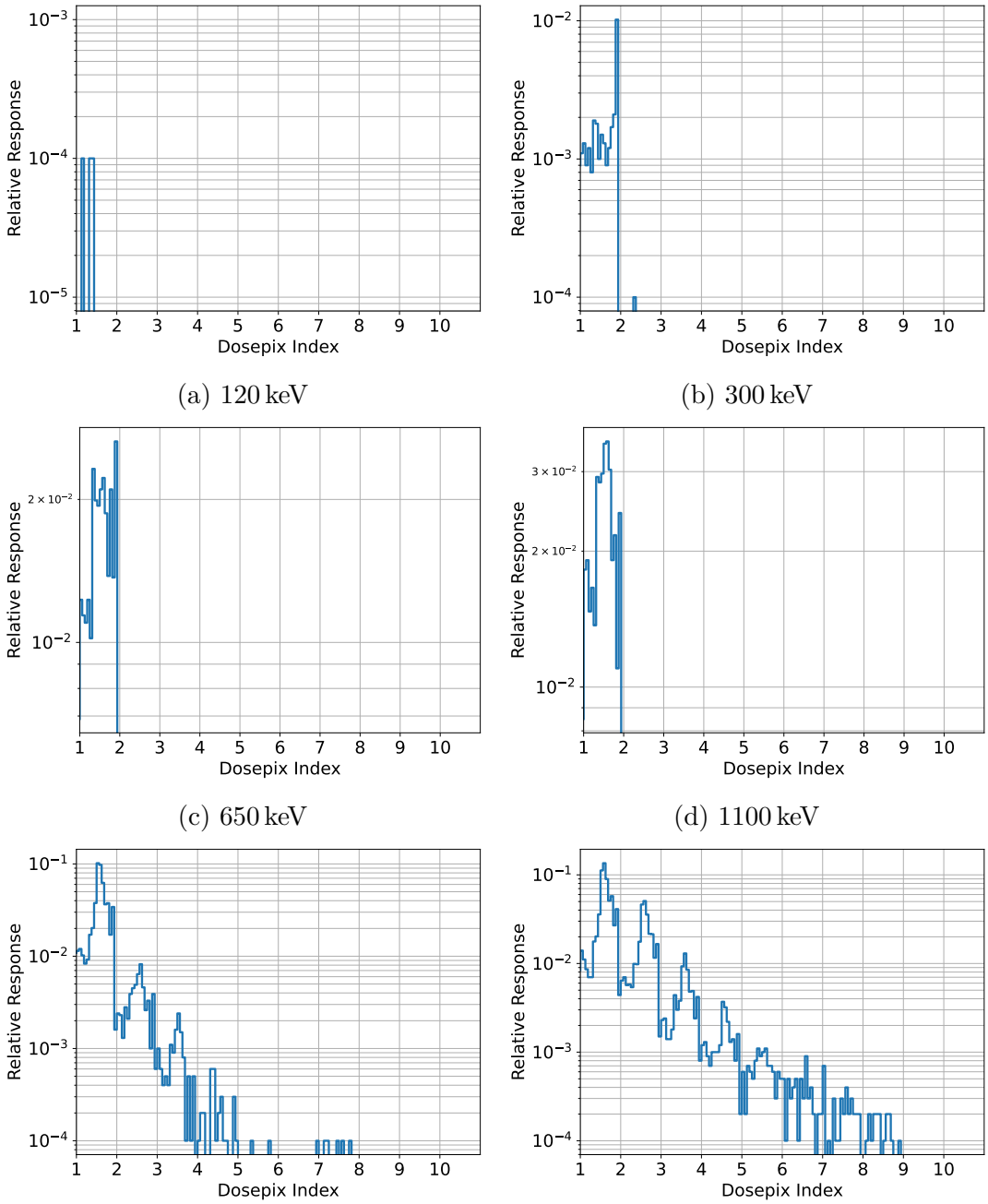

(a) 120 keV (b) 300 keV

(c) 650 keV (d) 1100 keV

(e) 6000 keV (f) 20 000 keV

Figure 4.14.: Detector response of all Dosepix detectors within the spectrometer, divided by the number of initial electrons. Each figure shows the response to a different primary monoenergetic spectrum, as indicated by the captions.

Spectrum	A in [10^4]	μ in [MeV]	σ in [MeV]
S1	6.265	3.106	2.479
S2	5.288	6.112	0.251
S3	7.723	8.858	2.503
S4	5.791	1.964	1.712
S5	8.439	10.636	2.022
S6	0.371	3.244	2.486
S7	1.660	2.432	3.891
S8	6.131	0.345	0.366
S9	7.600	8.568	0.743
S10	9.561	1.709	0.966
S11	5.394	1.242	4.672
S12	2.716	0.135	0.372

Table 4.4.: Values for A, μ, and σ (accoring to Equation 4.4) for the validation electron spectra.

detectors remain at the values between 12 keV and 150 keV, which have been chosen for the photons, because the electrons are not expected to deposit their entire energy in the sensor material, but rather ≈ 80 keV on average (see subsection 2.2.2).

Electrons for medical treatments are not expected to be emitted in the energetic distribution of X-ray spectra, but rather centered around a main energy, given by the respective accelerator. Therefore, the validation spectra for the deconvolution of the electron spectra are not generated by Equation 4.3, but by a Gaussian distribution

$$I_{\mathrm{e}}(E_{\mathrm{e}}) = \frac{A}{\sqrt{2\pi}\sigma} \exp\left(-\frac{1}{2}\left(\frac{E_{\mathrm{e}} - \mu}{\sigma}\right)^2\right) \tag{4.4}$$

with the electron energy E_{e}, the scaling parameter A, the mean energy μ, and the energy width σ. Twelve tuples of A, μ, and σ are randomly drawn to constitute the validation spectra. The parameters for all spectra are listed in Table 4.4.

Similar for the photon reconstructions, the pseudo-inverse response matrix, $(M^{\mathrm{e}})^{-1}_{ij}$, is calculated via the *scipy.linalg.pinv* method [115]. Figure 4.15 shows the binned validation spectra together with the calculated results from the inverted matrix. In contrast to the photon spectra, the reconstructed electron spectra excellently match the target spectra for numbers of particles, widths, and most mean energies except the lowest, e.g., S8 and S12. This proves that the purely mathematical approach of matrix inversion is capable of delivering physically meaningful results. For the lowest energies, the aforementioned similar electron behaviours and the short path lengths complicate a more precise reconstruction. However, those outstanding results remain a product of coincidence. Other mathematical solutions for the pseudo-inversion produce only physically meaningless results, and finding the desired solution is expected to become significantly more difficult when combining photons and electrons.

As the second deconvolution method, least-squares fits with trust-region reflective algorithms are used, as discussed in subsection 4.3.4. The parameters A, μ, and σ of Equation 4.4 are adjusted until the resulting spectrometer response match the response of the validation spectra. Similar to the photon spectra reconstruction, the starting

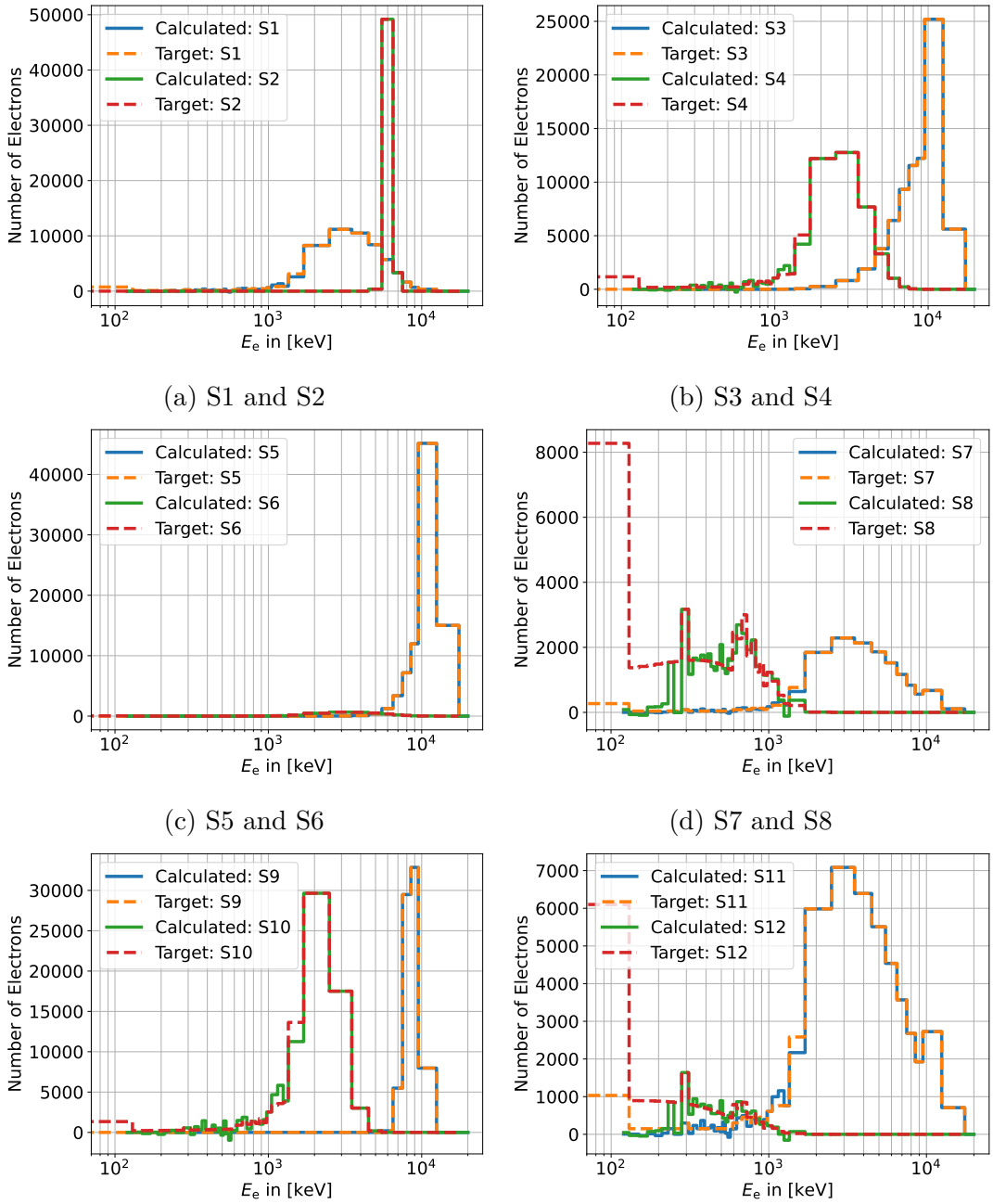

(a) S1 and S2

(b) S3 and S4

(c) S5 and S6

(d) S7 and S8

(e) S9 and S10

(f) S11 and S12

Figure 4.15.: Binned validation spectra for the electron reconstruction with respect to the electron energy E_e. The dashed lines show the original spectra, based on the parameters listed in Table 4.4 and labeled as "Target". The straight lines show the reconstructed spectra, calculated via the inverted electron response matrix, labeled as "Calculation".

Parameter	A	μ	σ
start	1	5100.0	1000.0
low	0	120.0	120.0
up	10^7	20000.0	5000.0

Table 4.5.: Starting values, lower, and upper bounds (labeled "low" and "up") of the least-squares regression for electrons. A is given in units of $\frac{1}{\mathrm{keV}}$ and μ and σ in units of [keV].

values and bounds are listed in Table 4.5. The minimization processes are carried out by a trust-region reflective algorithm [116]. The maximum number of iterations is set to $6 \cdot 10^4$. In the least-squares regression method, the absolute differences of the first Dosepix entered with a weighting factor of 1, the second with a factor of 6, the third with a factor of 16, and the remaining detectors again unmodified with a factor of 1. Those factors are chosen heuristically to compensate for lower signals in the deeper layers due to absorption [13]. After the third layer, almost no signal is expected for most of the observed energies, and a high regression weighting factor might lead to an overreaction of the algorithm to small background signals. All results are shown in Figure 4.16 and 4.17. Additionally, the absolute residuals of all fits are shown in Figure 4.18. Only the spectra S6, S8, and S12 accomplish a basic agreement between the original validation spectrum and the reconstruction. However, S8 and S12 still show a large absolute residual of the mean energy μ. Therefore, almost none of them correctly determine the initial spectral parameters, although the majority of the models converge. The ambiguity of the response explains that effect, as different electron energy distributions may cause a similar spectrometer response. This effect suggests a major flaw in the current spectrometer design. The absorption of the front layer is too high for any low-energy electrons with approximately $E_\mathrm{e} < 1100\,\mathrm{keV}$ to even reach the second detectors. This limit is partly given by the absorption of the Dosepix detectors themselves, i.e., constitutes a fundamental restriction on the setup if Dosepix detectors with silicon sensors are used [117]. When roughly assuming Dosepix as a 1 mm thick block of pure silicon, it completely absorbs electrons with about $E_\mathrm{e} < 400\,\mathrm{keV}$ (see subsection 2.2.2 and [117]).

On the other hand, the reconstruction of the high-energy electrons seems to be mainly limited by the sparseness of the energy bins, impeding an evaluation of the impact of small parameter changes. Especially, the spectra with higher energies (S2, S3, S5, S7, and S9) did not converge even after the maximum $6 \cdot 10^4$ iterations. All of them are stuck in estimations with small widths, spanning only over one energy bin, whereas the mean energy of the spectrum is better estimated. If the binning of the high energies were more subtle, the reconstructions would have possibly recognized the pattern of broader distributions more easily.

It is remarkable that, except for S7, every reconstruction underestimated the mean electron energy and the number of particles, represented by the parameter A. This also has an impact on the residuals being almost all < 1. The former might suggest that, despite the larger weights of the second and third detector layers, the reconstruction algorithm still focuses on the adjustment of the energy deposition in the first layer. Even when there are some entries also in the other layers, requiring a higher electron energy to occur, those events are mostly too few in number to become relevant for

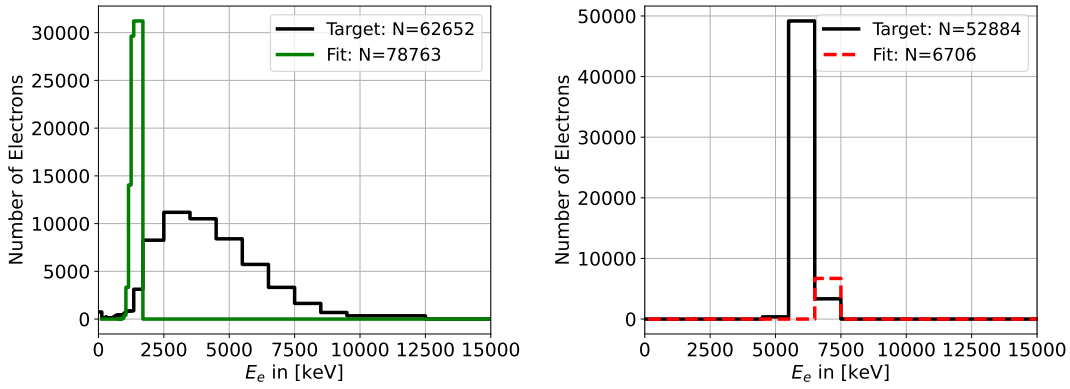

(a) S1

(b) S2

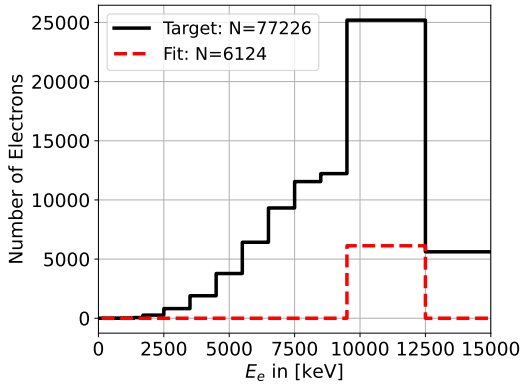

(c) S3

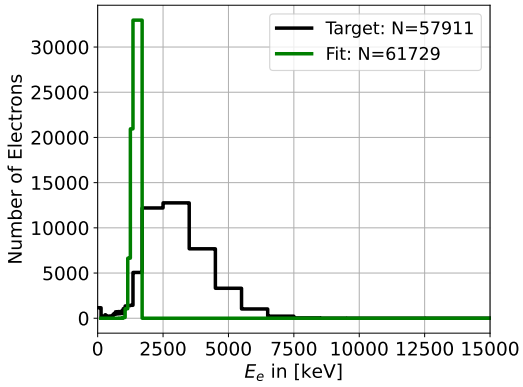

(d) S4

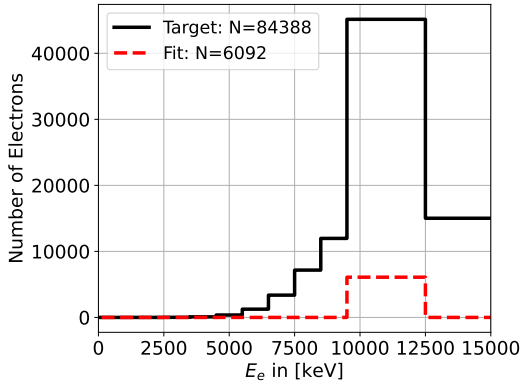

(e) S5

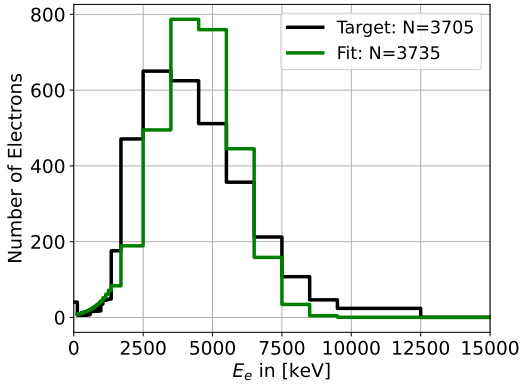

(f) S6

Figure 4.16.: S1 to S6 from the reconstructed Gaussian-shaped electron spectra from least-squares fits with respect to the electron energy E_e together with the original emission spectra from Table 4.4. If the fit converged within at least the $6 \cdot 10^4$ iteration, the curve is drawn as a straight green line, and otherwise as a dashed red line. N denotes the total number of particles.

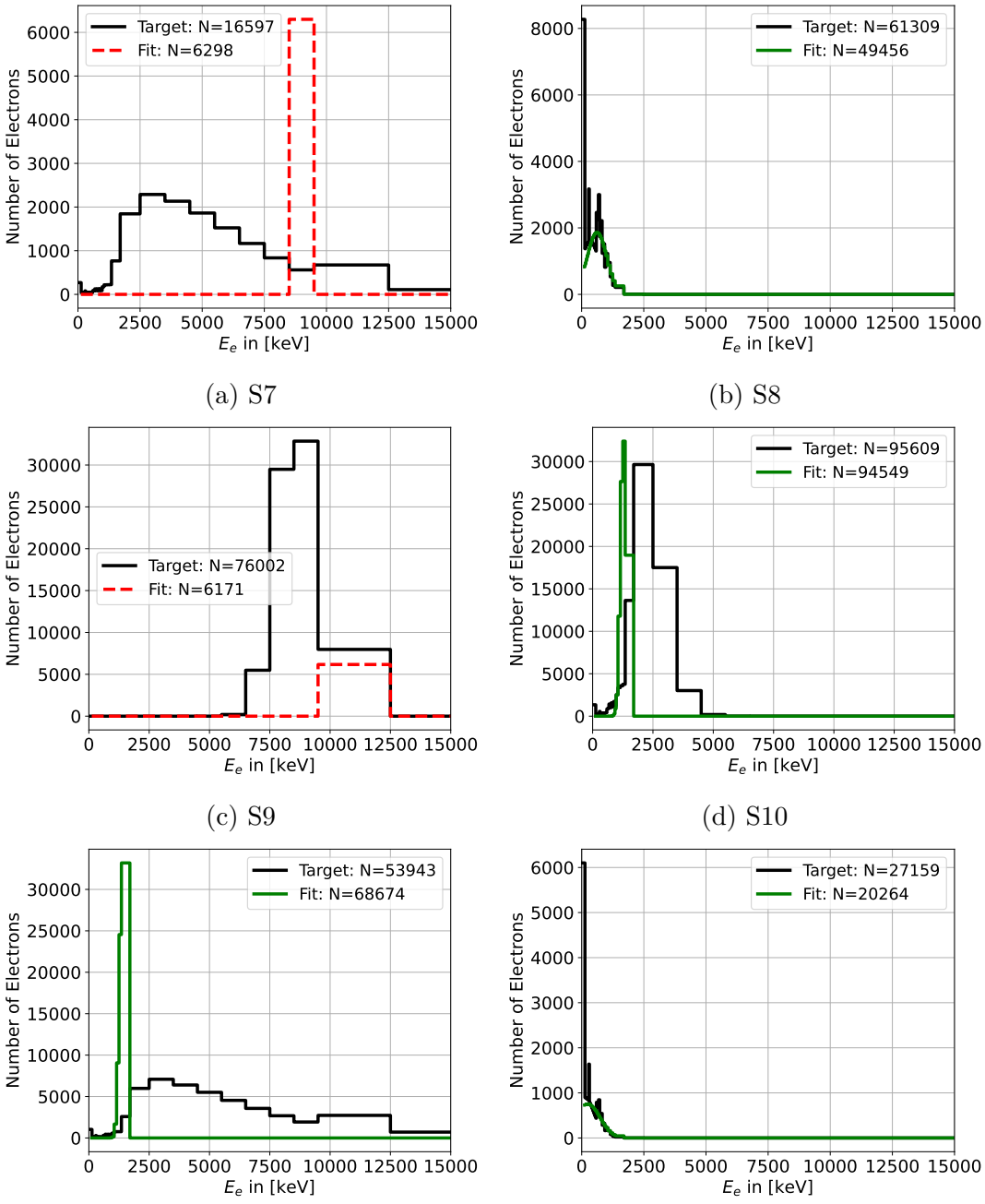

(a) S7 (b) S8

(c) S9 (d) S10

(e) S11 (f) S12

Figure 4.17.: S7 to S12 from the reconstructed Gaussian-shaped electron spectra from least-squares fits with respect to the electron energy E_e together with the original emission spectra from Table 4.4. If the fit converged within at least the $6 \cdot 10^4$ iteration, the curve is drawn as a straight green line, and otherwise as a dashed red line. N denotes the total number of particles.

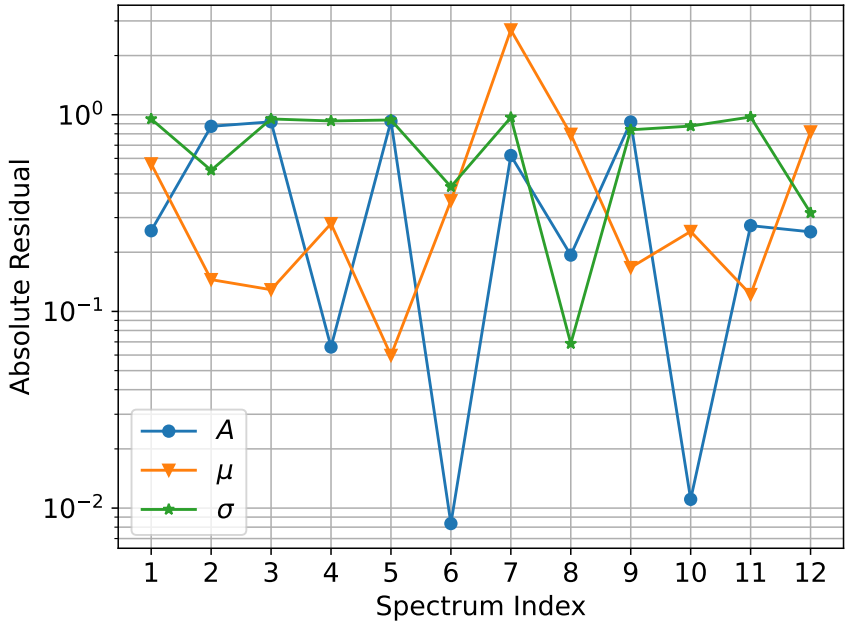

Figure 4.18.: Absolute Residual of the final parameters, corresponding to the spectra, shown in Figure 4.16 and Figure 4.17.

the least-squares algorithm. The underestimation of the number of particles originates from the small starting value for A. However, increasing the starting estimation for A led to worse results for the overall reconstruction. Similar to the photon spectra, the goodness of the fits is quantified via a Kolmogorov-Smirnov test, shown in Figure 4.19. As expected, the spectra S6 and S8 perform best. Only S8 is in accordance with the null hypothesis with an $\alpha = 5\,\%$ significance, emphasizing the large challenges of the current electron spectral reconstruction.

Actual electron energy spectra might comprise more degrees of freedom than the assumed basic Gaussian shape. Additionally, the current investigations do not include any particle-rate-dependent phenomena affecting the electron signal. In the extreme case of very high event rates, when the average time interval between two events per pixel becomes shorter than the typical event processing time of $\approx 1\,\mu s$, the energy deposition spectra are completely distorted by pile-up. In that case, any reconstruction has to rely on the sole absorption information over the different filter layers, which is not feasible with the current setup.

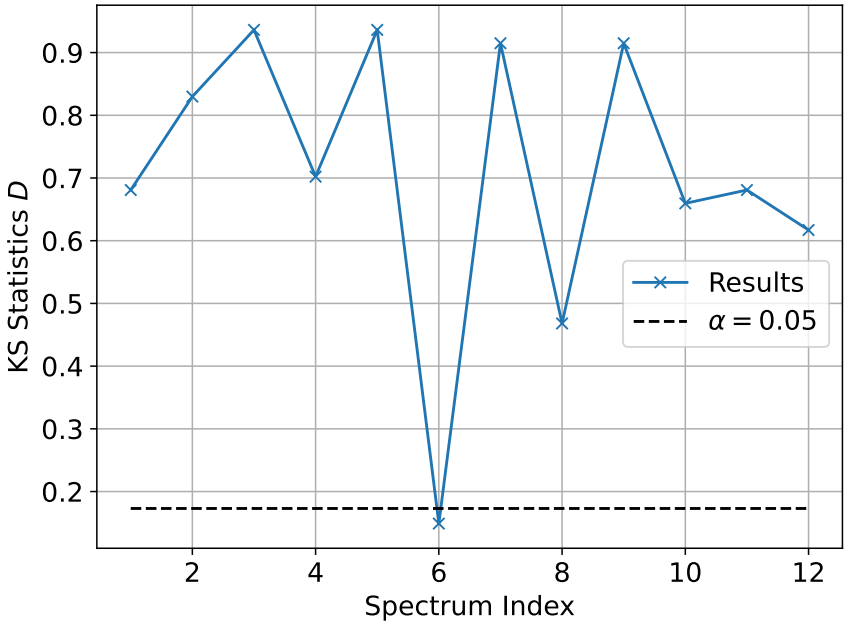

Figure 4.19.: Results of the Kolmogorov-Smirnov-tests of the least-squares results for electrons, shown in Figure 4.16 and 4.17. The black dashed line corresponds to the 5 % significance threshold.

4.5. Discussion and Conclusion

The previous sections present the achievements, challenges, and limitations of the proposed spectral reconstruction approaches for photon and electron spectra in low-flux environments. A novel spectrometer design comprising ten Dosepix detectors between filters of different thicknesses and materials is evaluated in simulations and compared with existing spectrometers. The accuracy of the photon spectra with the novel approach cannot compete with the existing Dosepix-based X-ray tube spectrometer, presented in [21]. Although a reliable comparison with the few-channel spectrometer is difficult, as no quantitative validation data are presented there, the few-channel spectrometer also seems to outperform the Dosepix spectrometer in terms of precise energy reconstruction [108].

All investigations so far have been limited to individual particles, impinging on the spectrometer without interfering with each other. This corresponds to the limit of low particle fluxes in the real world. However, this is not the intended use case of the spectrometer, as discussed in section 4.1. The fundamental purpose of FLASH radiation therapy, for which the spectrometer is designed, revolves around short irradiation times, often delivered by pulsed radiation with ultra-high dose rates of up to $10^{14}\,\frac{\mathrm{Gy}}{\mathrm{s}}$ [81]. Although Dosepix has been shown to function in comparable environments and deliver meaningful dose results, several new challenges, like total pile-up, are expected, further complicating the spectral reconstruction [20]. On top of that, the range of spectrum shapes must be opened up from the previous limitations to X-ray tube spectra and Gaussian electron distributions in order to work under various environments.

Several aspects of the current prototype design and analysis might be improved

to potentially receive more accurate results. Primarily, the filter composition across the layers might be adjusted to increase the amount of information in the detectors. Low-energy electrons ($< 400\,\mathrm{keV}$) require high transmission in the front layers to induce signals in not just the first detector. On the other hand, high-energy photons in the MeV-range might require even thicker and more absorbent layers to differentiate those energies. These, in some cases contradictary requirements to the spectrometer for different energies and particle types, impose a dilemma on the design. One way to work around this problem would be to introduce more filter layers to meet all needs. This approach was pursued by the few-channel spectrometer, which consists of 30 layers, with the first ten layers exclusively utilizing little absorbent PMMA filters [108]. However, applying this to the Dosepix spectrometer is not straightforward due to two reasons. First, the Dosepix detectors and read-out hardware require a much larger spacing of 2 cm between the layers than the thin TLDs do, which were used for the few-channel spectrometer and can be assembled almost densely. Therefore, the Dosepix spectrometer would drastically increase in length to over 60 cm and its weight to about 3.5 kg, affecting its mobility and usability. Second, the transmission of the filter layers is limited by the transmission of Dosepix itself, as discussed in section 4.4. This could be addressed by an offset arrangement of the detectors, such that no Dosepix would be directly covered by another. However, this would limit the spectrometer to homogeneous radiation fields at a scale of $> 1\,\mathrm{cm}^2$ (about ten times the surface area of Dosepix), which is not given for many FLASH-capable particle accelerators [80, 81].

Alternatively, the sensors of the Dosepix detectors could be changed to adjust the transmission and, simultaneously, take into account the different properties of the radiation expected in each layer, in terms of their induced signal. Thinner silicon sensors in the front layers would increase the transmission and also reduce the signal strength in the first detector layer, thereby presumably also addressing the dominance of the first layer over the spectrum reconstruction. The layers further back are mainly responsible for the higher energies and might profit from sensor materials with a higher atomic number Z and a higher photoelectric cross section, like GaAs or CdTe [113]. Therefore, an elaborate choice of sensor materials, which is the second general suggestion of improvement for the spectrometer, might increase the signal quality and, by producing full-absorption events throughout all detector layers and energies, contribute to the quality of the energy deconvolution.

Lastly, improved or different reconstruction algorithms may be utilized. As shown for electrons, the pseudo-inversion of the response matrix may produce physically meaningful results. A similar approach might work for photon spectra and high particle fluxes, too. Also, other reconstruction algorithms than least-squares methods might prove sufficient. For example, adjusted Richardson-Lucy algorithms have been successfully applied by Xie et al and Brodusch et al to reconstruct gamma and X-ray radiation fields [118, 119]. Moreover, Genetay et al. reconstructed X-ray tube spectra via measurements with Timepix4 and direct correction of charge sharing, Compton probability, and detector sensitivity, although this approach is limited to low-flux environments [120]. Furthermore, a neural network could enhance the accuracy of the results, since the limited information from the energy deposition spectra is one of the largest current challenges of the Dosepix spectrometer, and a neural network might be able to extract more information from the data. For example, a convolutional neural network has been successfully implemented for reconstructing X-ray tube spectra with three Dosepix

detectors and filter caps in 2021 [21]. A similar approach might also prove fruitful for this spectrometer.

In conclusion, many major challenges in the development process of a Dosepix-based spectrometer for high-flux mixed photon and electron spectra remain. Currently, such a prototype is not expected to outperform existing methods and devices, such as the TLD-based few-channel spectrometer [109] or the deconvolution of mixed fields from tokamak plasmas, presented by Patel et al. [121]. Therefore, the presented approach of a Dosepix spectrometer is not continued in this thesis.

5. Eye Lens Dosimetry with Dosepix in Clinical Practice

Contents

5.1. Eye Lens Dosemeter Prototype

Eye lens dosimetry has become an increasingly relevant field of study in the last decade, since the International Commission on Radiological Protection (ICRP) tightened its recommendations for occupationally exposed personnel in terms of annual eye lens dose in 2012 [6, 122]. Despite the necessity of eye lens dose monitoring systems [7], only two $H_p(3)$-dosemeters have been officially approved by the German National Metrology Institute (German: Physikalisch-Technische Bundesanstalt (PTB)) by March 2026 [123]. Both of them are passive dosemeters, i.e., they only provide information about the integrated dose they have been exposed to between two read-outs, typically performed monthly. Therefore, it is impossible to receive information about the origins and causes of high radiation exposure, complicating effective protective measures with passive dosemeters. In contrast, active dosemeters provide real-time dose monitoring, enabling immediate warning in cases of high dose rates as well as the ability to adjust behaviour or shielding installations directly. For that reason, a prototype of an active personal eye

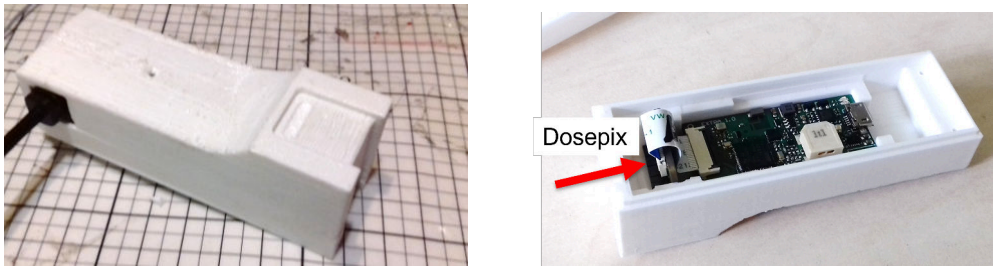

(a) close (b) open

Figure 5.1.: Prototype of an active personal eye lens dosemeter, based on Dosepix. a) shows the 3D-printed housing of the dosemeter, b) its electronics and the position of Dosepix. The pictures are taken from [85].

lens dosemeter based on the hybrid pixelated Dosepix detector has been developed by the Erlangen Centre for Astroparticle Physics (ECAP) as part of Friedrich-Alexander-Universität Erlangen-Nürnberg and PlatyPlatinen GmbH in 2022 [10]. Pictures of the dosemeter prototype are shown in Figure 5.1. A Dosepix detector at the front of the device is controlled by an STM32WB55RG V6 microcontroller [124]. Currently, the dosemeter is powered and read out via a PC connected to the prototype by UART. Autonomous operation, as well as a Bluetooth connection, are planned for the final product. The current housing has got a length of 8.9 cm, and a frontal surface of 3.0 cm × 2.8 cm. In [10], the performance of the eye lens dosemeter has been investigated under laboratory conditions to examine its response with respect to various dose-influencing quantities such as photon energy, angle of irradiation, dose rate, and reproducibility in both continuous and pulsed radiation fields. In that setup, the dosemeter was positioned in front of a water cylinder phantom according to ISO 4037-1 [74], which resembles the setup also used for legal approval of $H_\mathrm{p}(3)$-dosemeters.

However, that does not represent the intended use case of the dosemeter. In the practical application, it will be worn on the side of the head of occupationally exposed personnel during interventional medical procedures. Radiation fields of interest for such procedures are generated by X-ray tubes and scattered by the patient, room equipment, or the head of the monitored person before impinging on the eye lenses of the personnel [125]. Thus, the resulting radiation significantly differs from the unscattered, homogeneous radiation fields of laboratory conditions. Furthermore, the current dose-measuring procedure does not account for the shielding effects of radiation protection glasses, which are recommended for occupationally exposed staff [126, 127]. As shown in section 5.4, those radiation protection glasses are able to reduce $H_\mathrm{p}(3)$ in the eye lens for the relevant photon energies up to 95%. Thus, the dosemeter prototype would drastically overestimate the radiation exposure if those were not taken into account during the dose reconstruction.

The estimated dose is also affected by the temperature of the chip, as shown in [84]. Higher temperatures result in an underestimation of the deposited energies in the sensor layer. This temperature dependence of Dosepix can be reduced by increasing the leakage current compensating current I_Krum. An investigation of the effect of the temperature dependence on dose reconstruction in open setups and with Dosepix embedded in an eye lens dosemeter prototype is shown in section 5.2. After that, results

of measurements with the eye lens dosemeter prototype under realistic conditions at the Marienklinik Siegen are presented in section 5.3 before discussing custom-made lead glass pieces in front of the dosemeter housing to account for the shielding effect of radiation protection lead glasses. The chapter concludes by presenting a quantitative study of the reproducibility of the $H_\mathrm{p}(3)$ estimation process.

5.2. Temperature Dependence of Dosepix

5.2.1. Temperature Dependence of $H_\mathrm{p}(3)$

A severe temperature dependence of the functionality of the Dosepix detector has been shown in [84]. Especially, an increase in the chip temperature leads to a lower ToT with respect to the deposited energy. This is likely correlated with an insufficient leakage current compensation within the sensor layer, attached to Dosepix, increasingly disturbing the analogue pixel electronics of the detector. As the discharging current I_Krum is also responsible for leakage current compensation (see subsection 2.8.2), an increase of that parameter was shown to reduce the temperature-dependent ToT-shift [84]. However, the effect cannot be eradicated completely with this method, which is likely due to two reasons according to [85]. First, leakage current compensation of the Dosepix detector seems to be electronically flawed, as the theoretically designed maximum compensation of $I_\mathrm{Krum}/2$ per pixel is not achieved during operation. Second, other contributions have been shown to affect the temperature-dependent ToT-shift apart from leakage current, as shown in [85]. Therefore, it is crucial to complementarily investigate the effect of the temperature dependence on $H_\mathrm{p}(3)$-measurements specifically if Dosepix is used as part of the eye lens dosemeter prototype. In order to also examine the effect of different I_Krum, the following measurements are conducted with $I_\mathrm{Krum} = 2.2\,\mathrm{nA}$ and $I_\mathrm{Krum} = 11.0\,\mathrm{nA}$. The former value has been standard for most Dosepix experiments so far, e.g. [87]. The latter was shown in [84] to be the highest tested value, at which Dosepix's energy reconstruction is still functioning properly.

The tests are conducted with a Megalix Cat 125/35/80-121GW X-ray tube [77] and an eye lens dosemeter prototype. Figure 5.2 shows the setup used for the measurements. The ambient temperature within the fridge is tracked by a Leybold Sensor-Cassy 2 [128] readout system and a NiCr-Ni temperature sensor [129], similar to the setup used in [84]. The X-ray tube is put in a vertical position, radiating upwards. At a distance of 1 m, the eye lens dosemeter is positioned inside a fridge while facing the X-ray tube. Different combinations of tube voltage and filter layers, consisting of aluminum, copper, and tin, are used to attenuate the radiation. Although the filter combinations are chosen to represent radiation qualities of the N-series spectra, defined in ISO 4037-1 [74], the actual radiation fields differ from the listed ones due to the additional filtering effect of the fridge wall and the distance between tube and detector being smaller than 2.5 m as stated in the norm. For each measurement, an irradiation time of 20 s and an X-ray tube current of 1 mA are chosen to provide sufficient statistics while minimizing the influence of analog pile-up events.

Figure 5.3 shows the temperature, measured by the Cassy sensor, with respect to time. The blue and the green parts of the curve indicate the time intervals during which data is taken. Although the fridge is turned off during the warm interval, the temperature is not completely stable. Instead, a slight steady increase is visible, likely originating

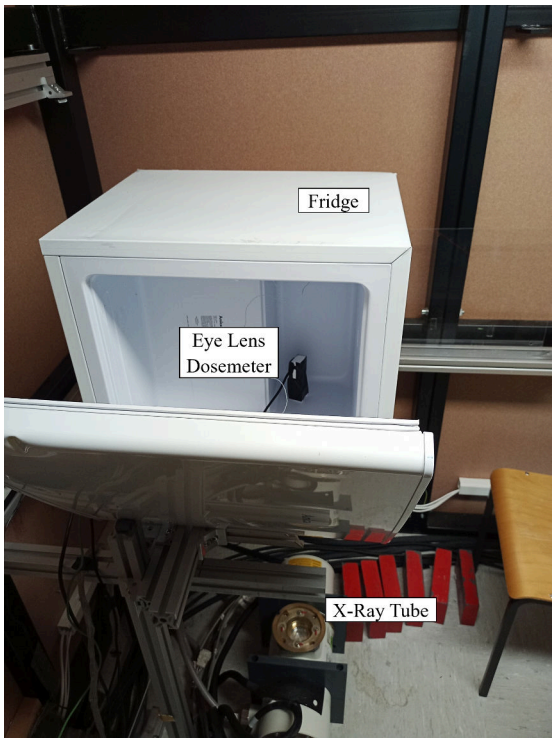

Figure 5.2.: Setup for the temperature-dependent dose measurements. The eye lens dosemeter prototype is located within a fridge above the X-ray tube.

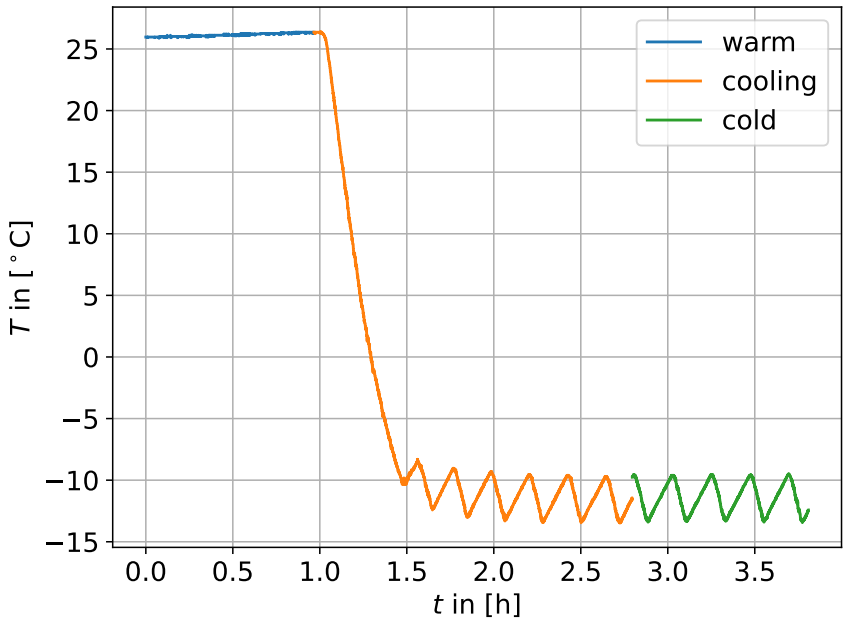

Figure 5.3.: Ambient temperature T within the fridge during the data taking process, measured by a NiCr-Ni temperature sensor with respect to time t. The blue and green curves represent the time intervals selected for analysis.

from the fridge approaching thermal equilibrium as it was brought to the location of the experiment only shortly before the experiment. An oscillating behaviour of the temperature is present during the cold phase. This is produced by the temperature regulator of the fridge being unable to keep such low temperatures constant. As data is taken throughout both temperature states, this oscillation is treated as an additional uncertainty of the actual temperature. The corresponding energy deposition spectra are shown in Figure 5.4 for large and in Figure 5.5 for the small pixels for $I_{\mathrm{Krum}} = 2.2\,\mathrm{nA}$ and 11 nA. As previously discussed, the measured deposited energy decreases with higher temperature. This effect becomes even more significant for higher energies. Similar shifts are visible for the small pixels. The effect significantly diminishes for the higher I_{Krum} in all energy ranges. Differences between the warm measurements with both I_{Krum} can be attributed to systematic uncertainties from the energy calibrations. Additionally, the total number of registered events is lower at cold temperatures for all investigated spectra. This results from some pixels being unable to process incoming events at such low temperatures [84].

To quantify the effect of the temperature dependence on the dose measurements, the corresponding $H_{\mathrm{p}}(3)$ is calculated for the warm and cold measurements. The ratios of the estimated $H_{\mathrm{p}}(3)$ for each radiation quality are shown in Figure 5.6. At lower photon energies, the $H_{\mathrm{p}}(3)$-ratio is larger than 1, especially for 11 nA, since the dose estimation is more affected by the reduced number of events at cold temperatures than by the temperature shift. In contrast, dose estimation is strongly affected by the temperature-dependent energy shift at higher photon energies since the effect is more prevalent by itself and the approximately exponential behaviour of the dose conversion factors with respect to the deposited energy amplifies the influence of the energy shift on the results. For the small pixels, the dose conversion factors for high energies are even larger (see Appendix A). Therefore, the described influence is even stronger, resulting in an even lower dose ratio compared to the large pixels. For both I_{Krum}, the relative temperature-dependent change of the dose is larger than ±20% for some radiation qualities. Because of that, the eye lens dosemeter prototype is not suited for usage at all temperatures. Therefore, the dosemeter will only be able to achieve official approval for indoor use. In [37], this is defined as an approved functionality of a device in environments with ambient temperatures of 15 °C to 30 °C.

5.2.2. Indoor-Use Regime

The measurements of this subsection have been previously published as part of Nico Kießl's Bachelor's thesis [86]. As the origins of the temperature dependence of Dosepix are not understood and might, therefore, also partly stem from the read-out electronics connected to the detector, all statements regarding the temperature behaviour of the dosemeter prototype must be investigated separately. The studies, presented in this subsection, examine the compatibility of the dosemeter with the official indoor-use requirements as stated in IEC 61526 [37]. This standard requires a relative dose fluctuation of less than +18% and -13% within an ambient temperature range of 15 °C to 30 °C. This is not fulfilled by the results shown in Figure 5.6. To check if this is similar for the eye lens dosemeter prototype, it is positioned inside a temperature chamber. Equal examinations are carried out with two free Dosepix detectors on the regular readout hardware without the specifics of the eye lens dosemeter. Those are

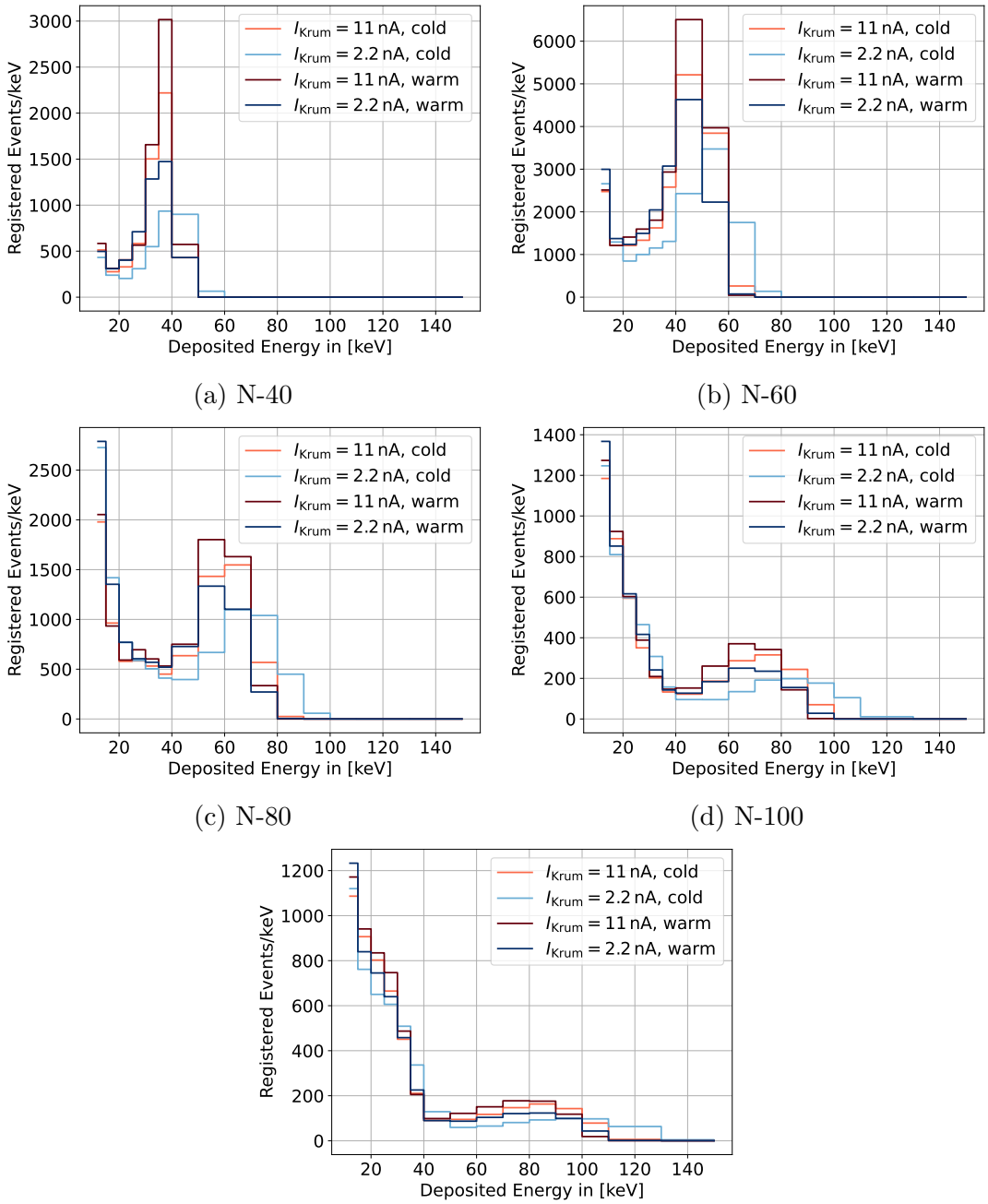

(a) N-40

(b) N-60

(c) N-80

(d) N-100

(e) N-120

Figure 5.4.: Binned energy deposition spectra, measured by the large pixels of the eye lens dosemeter prototype, in warm ($\approx 25°$) and cold ($\approx -15°$) environment with a low I_{Krum} of 2.2 nA and a high I_{Krum} of 11.0 nA.

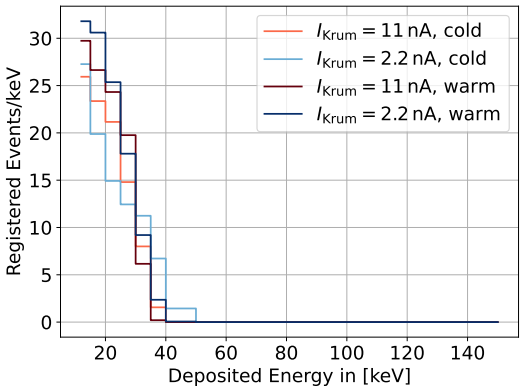

(a) N-40

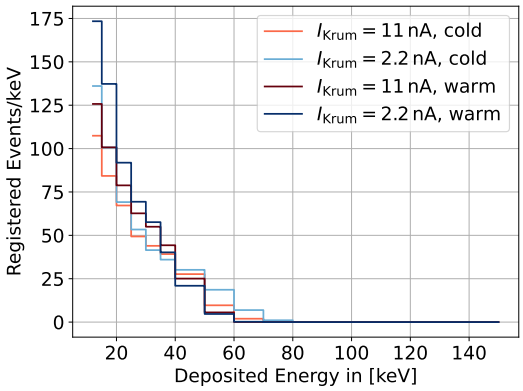

(b) N-60

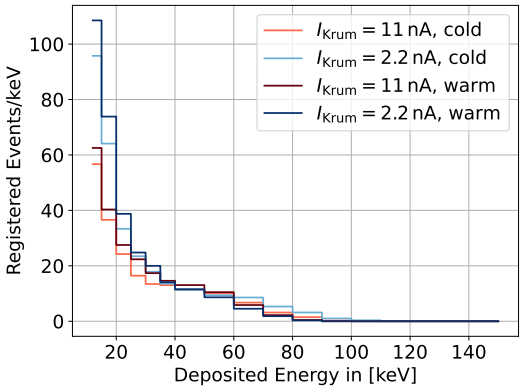

(c) N-80

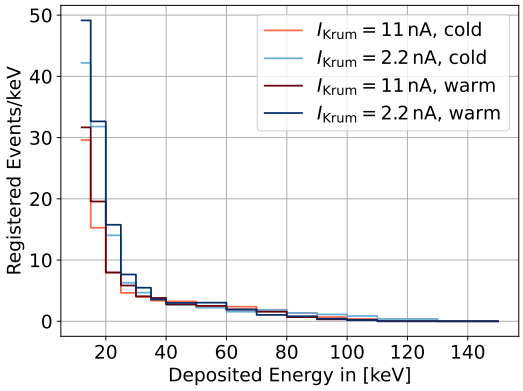

(d) N-100

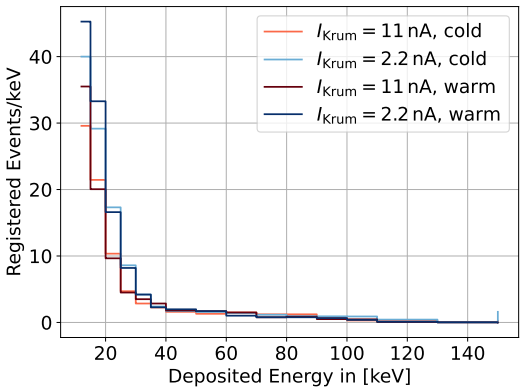

(e) N-120

Figure 5.5.: Binned energy deposition spectra, measured by the small pixels of the eye lens dosemeter prototype, in warm ($\approx 25°$) and cold ($\approx -15°$) environment with a low I_{Krum} of 2.2 nA and a high I_{Krum} of 11.0 nA.

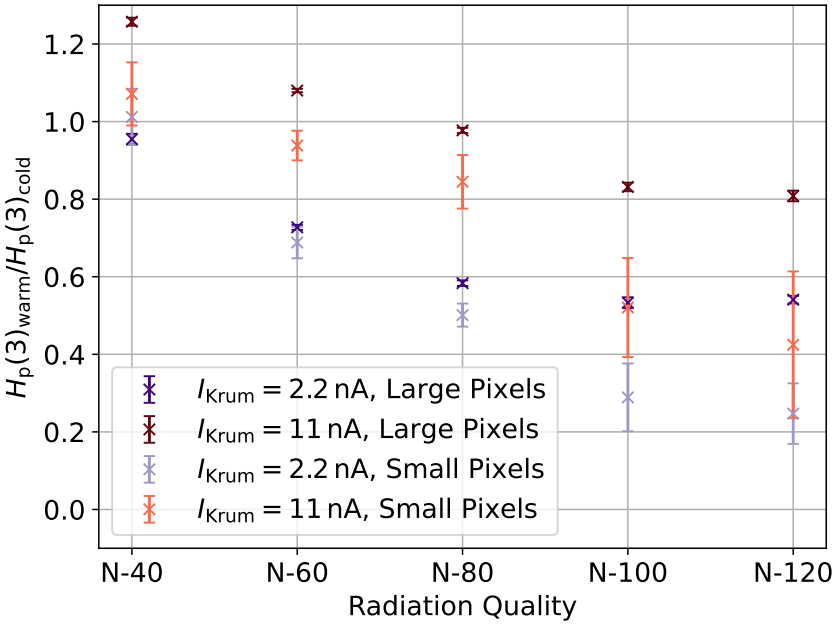

Figure 5.6.: Ratio of $H_p(3)$, estimated via Equation 2.23 in warm and cold environments for large and pixels.

referred to as "open" in the following. Constant temperatures from 5 °C to 35 °C with a step size of 5 °C are set and held steady for 20 min each. Afterwards, the dosemeter is removed from the temperature chamber and is immediately irradiated with an Ivario COMET iXRS-160/4.5 X-ray tube [130]. In separate measurements, all three Dosepix detectors are irradiated with radioactive sources of $^{241}_{95}$Am, $^{133}_{56}$Ba, and $^{137}_{55}$Cs inside a climate chamber. The entire irradiation lasts ≈ 16 h and is split into equal sections of constant temperature from 5 °C to 30 °C with a step size of 5 °C. All detectors are read out in energy-binning mode every 2.5 s. By also reading out the internal temperature chip of Dosepix during each data frame, the time intervals according to the different ambient temperatures can be assigned to the respective Dosepix data. In Figure 5.7, the temperature curves of two Dosepix detectors during the measurement are shown with respect to time. As the chip temperature of Dosepix is given in units of ADC values, it has to be calibrated first by utilizing the functions and parameters provided by [86]. However, this calibration has only been conducted with respect to the ambient temperature of a Cassy sensor because an independent chip temperature measurement could not be performed. Therefore, there might be some discrepancy between the actual temperature of the chip during operation and the temperature of its surroundings. Although the implications of this effect have to be addressed in further studies to quantify temperature dependence, it is expedient to use the ambient temperature as the reference for the scope of this work, since the official requirements of IEC 61526 also refer to the ambient temperature. The normalized estimated $H_p(3)$ with respect to temperature for all investigated detectors is shown in Figure 5.8. Here, normalization is performed with respect to the length of the time window of each data acquisition and the estimated $H_p(3)$ at 20 °C for each detector, pixel size, and radiation quality. Equation 2.24 is used to approximate the uncertainties of the normalized $H_p(3)$, depicted as error bars

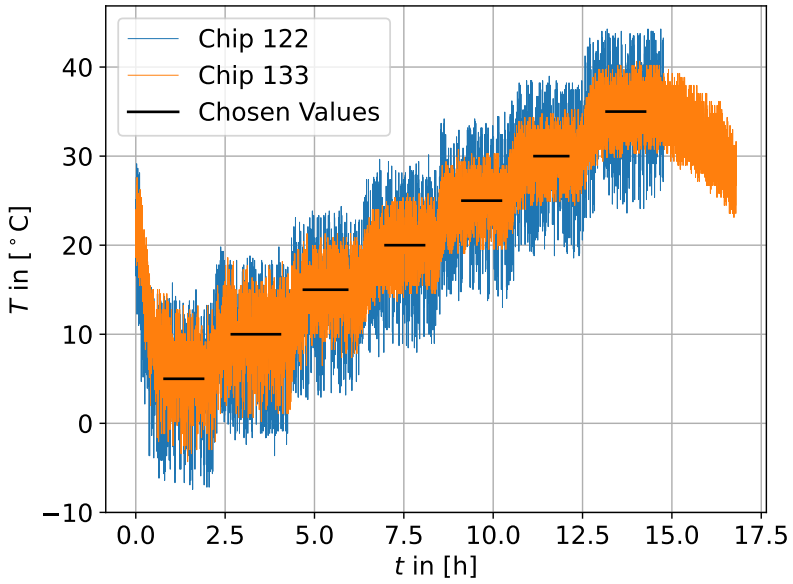

Figure 5.7.: Temperature of chip 122 (open) and chip 133 (eye lens dosemeter) with respect to time under constant irradiation with a $^{137}_{55}$Cs source. The calibration of the temperature has been conducted with the parameters given by [86]. The black line indicates time windows, during which the temperature is assumed to be constant.

in Figure 5.8. The horizontal error bars represent a temperature uncertainty $\pm 1\,^{\circ}$C. Red dashed lines indicate the indoor use requirements. Only the results of the large pixels of Doespix, integrated in the eye lens dosemeter, consistently fulfill the indoor use requirements. Both open detectors show steeper temperature dependencies leading to larger dose deviations, especially for higher mean photon energies, e.g., N-120. The small pixels occasionally show significant statistical uncertainties ($^{133}_{56}$Ba) as well as overall stronger temperature dependence. The former is caused by the smaller sensitive volume of the small pixels compared to large pixels, which results in fewer energy deposition events. The stronger temperature dependence of the estimated $H_{\mathrm{p}}(3)$ of the small pixels is explained by the dose conversion factors. As those depend heavily on the registered deposited energy in the pixel, the same temperature-induced energy shift results in a large dose variation. Therefore, the small pixels cannot be used autonomously to estimate $H_{\mathrm{p}}(3)$ in an officially approved eye lens dosemeter as they do not fulfill the requirements. On the other hand, the large pixels of the detector inside the eye lens dosemeter fulfill the indoor-use requirements. Their better performance in comparison with the open detectors 122 and 1001 could be due to temperature shielding by the dosemeter housing. Nevertheless, further research on that topic is necessary to draw finite conclusions because the better performance of Dosepix 133 compared to the other detectors might be merely coincidental regarding this particular Dosepix. To prove the hypothesis of the detector housing reducing temperature dependence, more eye lens dosemeter prototypes must be assembled and individual Dosepix detectors must be examined inside and outside of dosemeter housings.

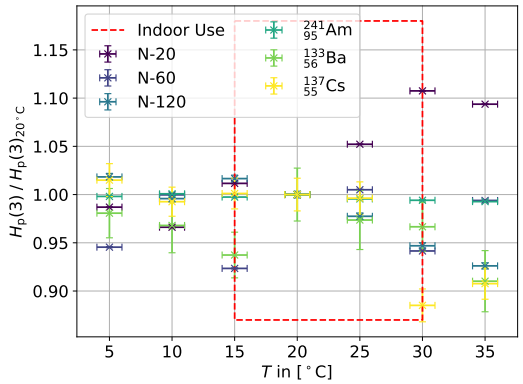

(a) Dosepix 133 (eye lens dosemeter), large pixels

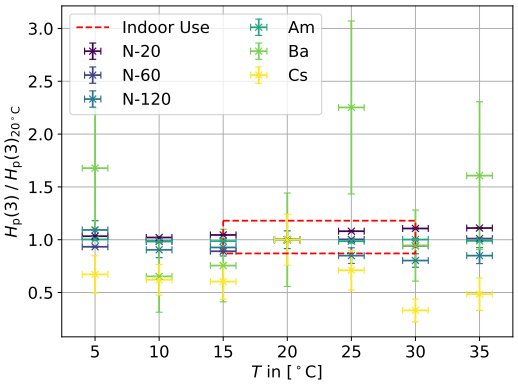

(b) Dosepix 133 (eye lens dosemeter), small pixels

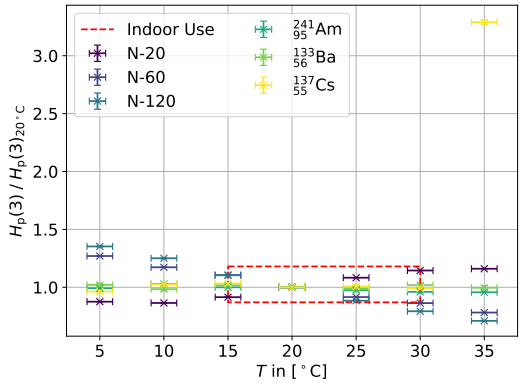

(c) Dosepix 122, large pixels

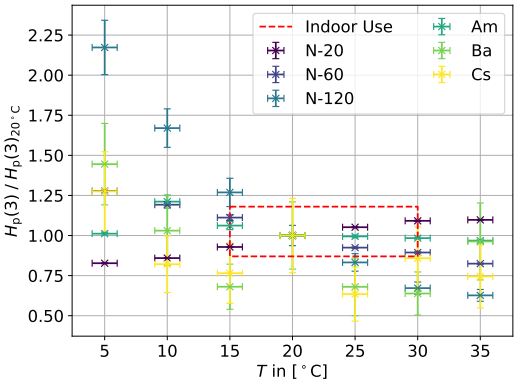

(d) Dosepix 122, small pixels

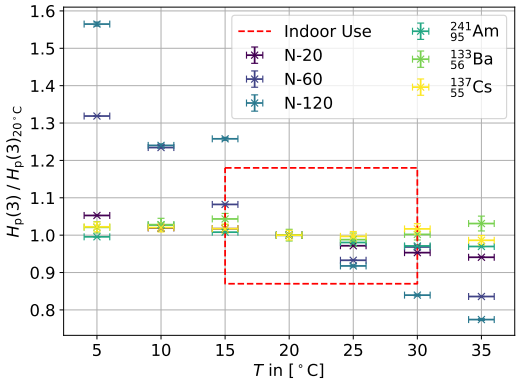

(e) Dosepix 1001, large pixels

Figure 5.8.: $H_p(3)$, measured by different Dosepix detectors from different radiating sources at different ambient temperatures, normalized to the $H_p(3)$, measured at 20 °C. The results are divided into the large and small pixels of the respective detector, with Dosepix 1001 not containing any small pixels. The error bars in the y-direction represent statistical uncertainties of the dose estimation, the error bars in the x-direction represent heuristically estimated uncertainties of the ambient temperature.

5.3. Measurements at Marienklinik Siegen

In order to investigate the performance of the eye lens dosemeter prototype under realistic conditions, measurements at the angiography department of Marienklinik Siegen were performed in November 2023. Figure 5.9 shows the setup, used for the measurements, presented in this section, if not stated otherwise. The experimental setup and results were part of Leonie Ullmann's Master's thesis, where a more detailed description of the measurement campaign is provided [98]. Irradiations are performed with a medical C-arm, which consists of a 120 kV X-ray tube and a pixelated imaging detector. The X-ray tube is located under the patient and irradiates upwards. In order to mimic the scattering behaviour of a patient, an Alderson phantom is placed on the patient table. The X-ray tube of the C-arm can be moved around the patient table to irradiate from different angles between $-30°$ and $30°$. Next to the C-arm, a plastic mannequin is positioned at five different positions. This mannequin is wearing the eye lens dosemeter prototype. The positions are chosen to represent typical locations of the occupationally exposed medical staff during the procedures to assess meaningful $H_\mathrm{p}(3)$. In Figure 5.10, a sketch of the different positions with respect to the patient table is provided. All irradiations are performed with ten repetitions of 20 s of beam and gaps of 10 s. As a result, the reproducibility of the $H_\mathrm{p}(3)$ measurements and automatic adjustments of the X-ray tube can be monitored.

In Figure 5.11, an exemplary measurement in the energy-binning mode is depicted. For each data frame, the dose of the large and small pixels is reconstructed separately according to Equation 2.23. The pixel columns of Dosepix are read out every 2.5 s to assure proper time resolution while simultaneously acquiring sufficient statistics per data frame to enable meaningful dose rate assumptions. Statistical uncertainties of the individual reconstructed $H_\mathrm{p}(3)$ are illustrated in the graph by the filled areas. Even though the $H_\mathrm{p}(3)$ at each data frame is $< 1\,\mu\mathrm{Sv}$, the results of the large pixels still enable meaningful dose assumptions due to their low coefficient of variation. On the other hand, the small pixels vary more significantly. Therefore, the latter are only used for validation purposes by checking whether their reconstructed mean dose roughly follows the mean of the large pixels. The results highlight the importance of statistical robustness due to the small dose contributions per read-out, leading to low statistics even for the large pixels.

5.3.1. Exposure of Medical Staff

As previously mentioned, $H_\mathrm{p}(3)$-measurements are performed at different positions and with different shielding modalities. All results, shown in this section, are received from measurements with the so-called "Körperstamm" mode, at which the central part of the Alderson phantom is irradiated (refer to [98] for a comparison with liver irradiation). If not stated otherwise, all measurements consisted of 10 individual irradiations of 20 s with gaps of 5 s in between. These settings are chosen by the medical personnel of the Marienklinik Siegen to roughly reflect the dose of a typical treatment. The dose results for different angles of the X-ray tube and positions of the mannequin are shown in Figure 5.12 for large and small pixels. Overall, the estimated eye lens dose decreases with higher distances. However, there are several exceptions to that general trend. All of them can likely be attributed to the complex geometry of the setup, with profuse scattering and absorbing objects like the patient table, the Alderson phantom, or the

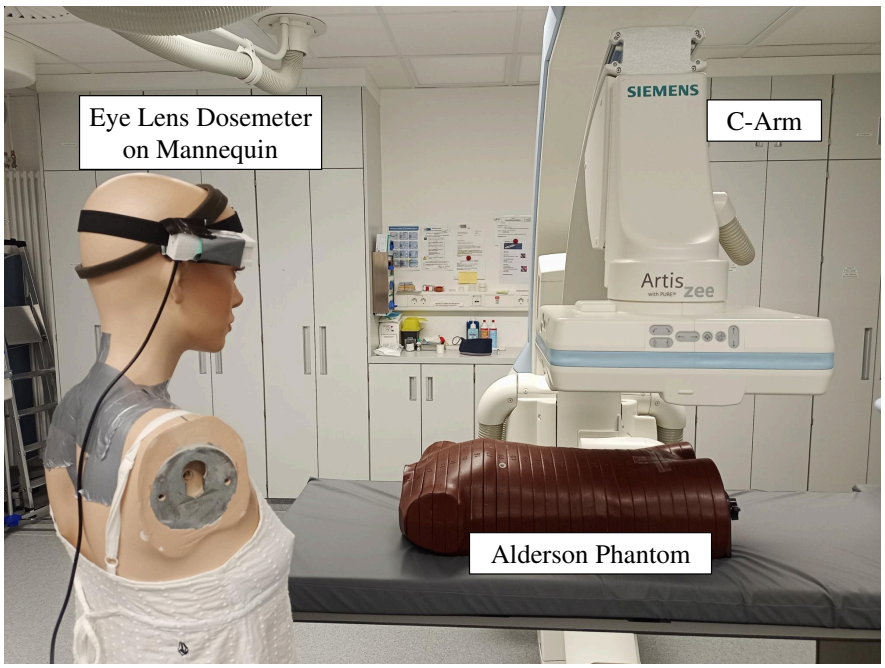

Figure 5.9.: Setup of the measurements at Marienklinikum Siegen. The eye lens dosemeter prototype is put on a plastic mannequin at different positions next to the patient table. Irradiations are performed with a medical C-arm onto an Alderson phantom.

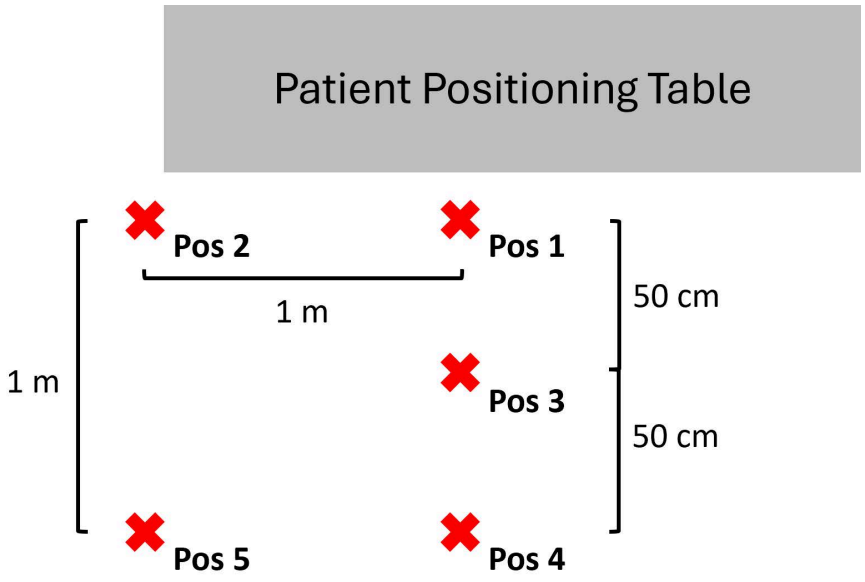

Figure 5.10.: Sketch of the different positions of the mannequin wearing the eye lens dosemeter prototype with respect to the patient table and the C-arm. The sketch is taken from [98].

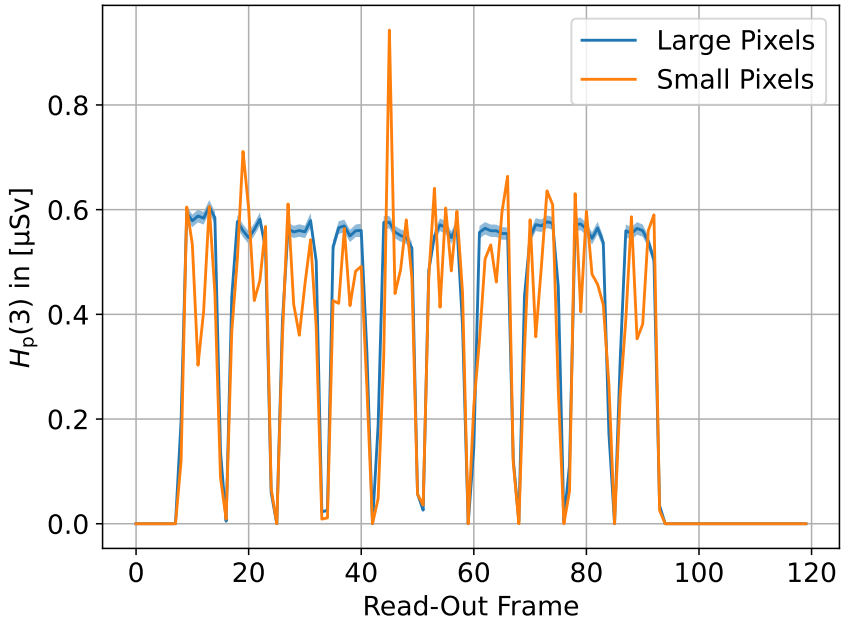

Figure 5.11.: Exemplary $H_p(3)$-measurement at the C-arm at the Marienklinikum Siegen. Every read-out cycle consists of 2.5 s of data. The lightly filled areas of the large pixels represent the statistical uncertainties of each individually reconstructed $H_p(3)$.

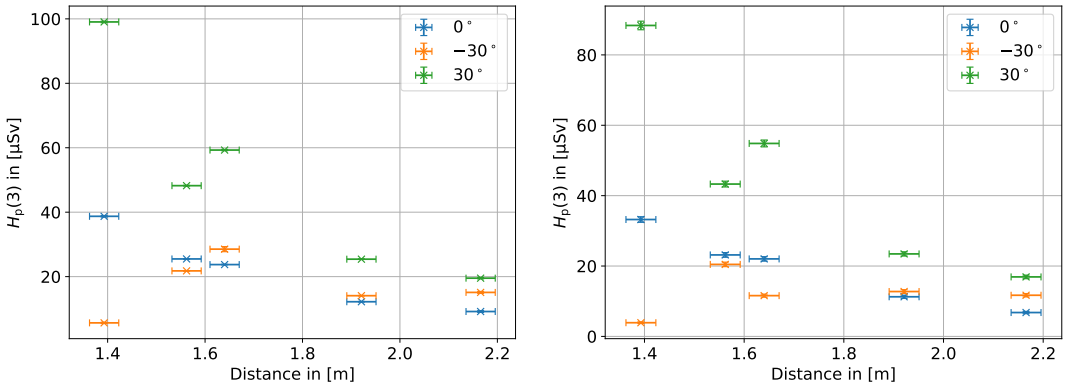

(a) Large pixels (b) Small pixels

Figure 5.12.: Measured $H_p(3)$ of the eye lens dosemeter prototype at the angiography unit of the Marienklinik Siegen with respect to the distance between the X-ray tube and the dosemeter. The colours indicate the position angle of the X-ray tube. Error bars in y-direction indicate the standard deviation of $H_p(3)$, error bars in x-direction an estimated position uncertainty.

Figure 5.13.: Setup of the measurements at Marienklinikum Siegen with additional radiation protection glasses. The eye lens dosemeter prototype is put on a plastic mannequin at different positions next to the patient table. Irradiations are performed with a medical C-arm onto an Alderson phantom.

walls of the treatment room. The data of the small pixels generally match the results of the large pixels, with the systematic differences in accordance with the discussions from [85]. In the scenario of 30° at the typical doctor's position (1), up to 100 µSv per treatment are reached. This would accumulate to the legal annual limit of 20 mSv for 200 treatments per year or about 4 treatments per working week. Therefore, exceeding the limit for occupationally exposed medical personnel poses a realistic threat without special radiation protection for the eye lens. These results are in accordance with previous findings in [7, 122].

To investigate the dose reduction of one of the most common eye-specific radiation protection gears, radiation protection lead glasses are positioned in front of the eye lens dosemeter prototype [126]. The adjusted setup is shown in Figure 5.13. The radiation protection glasses are put at the front face of the dosemeter to shield the Dosepix detector inside the dosemeter prototype as best as possible. Afterwards, irradiations were performed at the same positions and radiation modalities as for the unshielded measurements. Ratios of the reconstructed eye lens dose without and with lead glasses are depicted in Figure 5.14. The uncertainty bars in the y-directions are calculated by Gaussian error propagation from the standard deviations of the individual doses, whereas the uncertainty bars in the x-direction represent the same heuristic position uncertainties as in Figure 5.12. Depending on the position of the mannequin and the X-ray tube, dose reductions from factors of 5 to 33 are achievable. Absorption is comparatively low at position 1 (distance of 1.4 m) because most of the radiation reaches the detector from steep angles. Thus, many photons hit Dosepix by flying underneath the lead glasses. This effect decreased for positions 2 and 3, increasing the

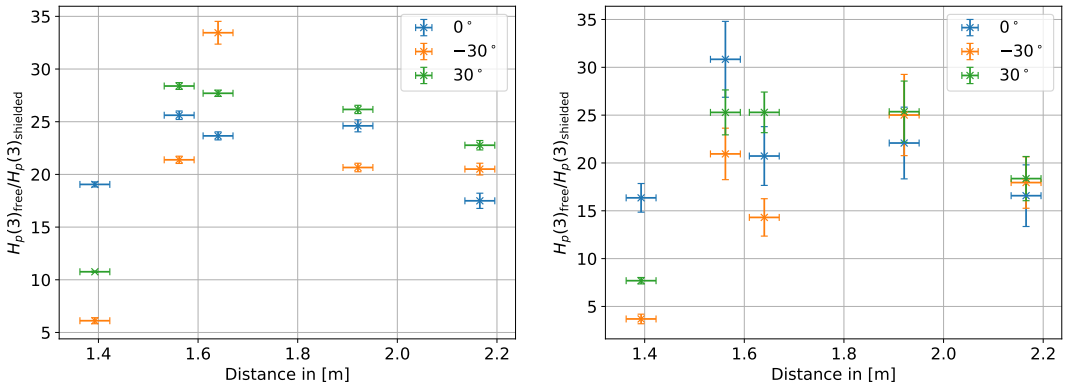

(a) Large pixels (b) Small pixels

Figure 5.14.: Ratio of $H_p(3)$, estimated by the eye lens dosemeter prototype without shielding compared to results with lead glasses in front of the prototype for large (a) and small pixels (b).

absorption capability of the lead glasses. At even larger distances, a larger percentage of the dose contributing photons stems from scattered radiation, thus the effect of the lead glasses starts to decrease again. Ultimately, lead glasses are able to reduce the eye lens dose significantly, enabling occupationally exposed medical personnel to safely work for the entire year. Complementary studies, conducted by Leonie Ullmann, showed that the eye lens dose can be reduced even further if lead glasses are combined with other radiation protection measures, like movable lead glass plates [98]. However, it is difficult to correctly estimate the actual dose reduction of lead glasses in front of the eyes, as the meaningfulness of the measurement position on the side of the head with regard to eye lens dose remains uncertain, especially with additional lead glasses. The first investigations regarding that topic are presented in section 5.4.

5.3.2. Distribution of Deposited Energies

Lastly, energy deposition spectra, as measured by the eye lens dosemeter prototype, are compared for scattered and direct beam radiation fields. When measuring the energy deposition spectra of the direct beam, the dosemeter is positioned face down on the patient table. The centre point of the X-ray tube is positioned such that it targets the dosemeter prototype directly. Different scattering objects are then placed next to the prototype to examine their different scattering behaviours as well as the influence of the automatic radiation regulation mechanisms of the C-arm. An exemplary photograph depicting the torso of the utilised Alderson phantom is shown in Figure 5.15. As the beam is targeted at the dosemeter, a significant part of the radiation reaches the detector by only traversing the patient table, but not the Alderson phantom.

The results are shown in Figure 5.16. In addition to the scattered beam, results from three different measurements in the direct beam of the C-arm are shown. The overall shapes of all energy deposition spectra are similar with a dominant peak-like structure at about 27 keV and a tail towards higher energies. For the small pixels, the spectra are dominated by charge-sharing events at lower energies. However, the exact shape differs between the measurements, especially the location of the peak and the maximum energy.

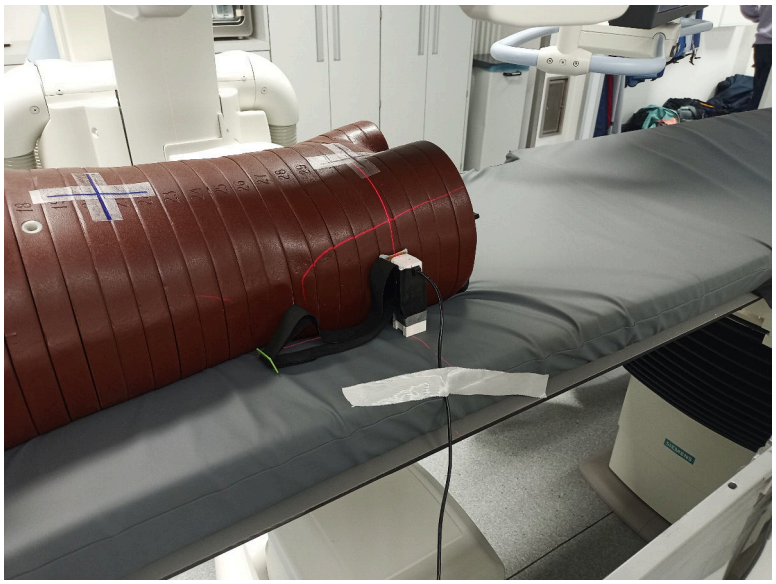

Figure 5.15.: Setup of the measurements of the direct beam at the angiography unit of Marienklinik Siegen. The eye lens dosemeter prototype is positioned on the patient table next to varying objects. The picture shows the torso of an Alderson phantom. The red laser cross indicates the centre of the X-ray beam.

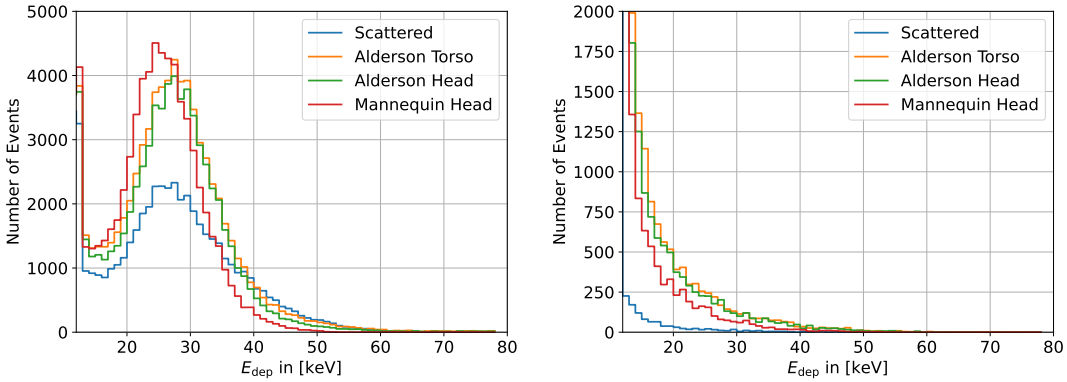

(a) Large pixels (b) Small pixels

Figure 5.16.: Measured ToT-spectra for the eye lens dosemeter prototype, calibrated to deposited energies for large (a) and small pixels (b). The blue curve is measured at the mannequin head at position 1 (see Figure 5.10), the other curves are measured in the direct beam of the C-arm with a respective additional absorbing body according to the legend. For those measurements, the centre of the beam is aimed at the centre of the front face of the dosemeter housing.

This originates mainly from the dose control system of the C-arm. In order to minimize the dose to a patient during an operation, the flux of the X-ray tube is controlled with respect to the measured flux of the imaging detector. Thereby, the amount of radiation is adjusted according to the patient's physical properties. However, in the here performed measurements, a large fraction of the emitted radiation reaches the detector almost unattenuated because the central point is at the position of the eye lens dosemeter prototype, not a human body or the Alderson phantom. Therefore, the tube current and voltage are reduced significantly by the C-arm. For the scattered results, the entire Alderson torso phantom is covered by the beam, resulting in the highest X-ray tube voltage of the presented measurements. For the direct beam measurements, the voltage is successively reduced, depending on the absorption properties and sizes of the objects. The lowest amount of attenuation is provided by the mannequin, since it is hollow and consists mainly of plastic. Unfortunately, the exact values for tube current, voltage, or measured flux could not be provided by the clinic, preventing a detailed analysis of the control effects. To better compare the scattering behaviour of the different objects, measurements in the same radiation field must be performed without automated flux control. Nevertheless, the results prove the functionality of the eye lens dosemeter prototype even in the most extreme environment (direct beam) within this clinical scenario.

Ultimately, the tests at the Marienklinik Siegen have proven the functionality of the eye lens dosemeter prototype, based on Dosepix, under realistic clinical conditions, as well as the necessity of eye lens dosimetry in terms of radiation protection. Nevertheless, radiation protection measures such as lead glasses must be correctly taken into account for meaningful eye lens dose monitoring of occupationally exposed personnel. One approach to do so is by applying special pieces of lead glass plates in front of the dosemeter, which is discussed in detail in section 5.4.

5.4. Consideration of Personal Radiation Protection Measures

5.4.1. Lead Glass Pieces in Front of the Eye Lens Dosemeter

Radiation protection lead glasses are one common method to protect the eye lenses of occupationally exposed medical personnel during operations [127]. Their usage reduces the dose to the eye lenses, as shown in clinical measurements in section 5.3. Such a dose reduction must also be acknowledged by the dose estimation method of the eye lens dosemeter prototype. Otherwise, it might overestimate the dose, resulting in no meaningful monitoring. Passive eye lens dosemeters, such as the EYE-D dosemeter, take this into account by directly measuring the radiation behind the radiation protection glasses. However, this is not feasible for the active dosemeter, based on Dosepix, as it is too large and lengthy to fit behind radiation protection glasses. Another approach would be to incorporate the absorption properties of the lead glasses into the dose conversion factors, but this would introduce two disadvantages. First, the dosemeter would be vulnerable to exploitation because dose estimation with additional absorption could just be activated without actually wearing eye lens protection. Second, many different types, shapes, and materials exist for lead glasses. A single set of dose conversion factors could only correctly account for the absorption of one specific lead glass model. For every other model, the estimated eye lens dose might be off. Therefore, the sparing effect of

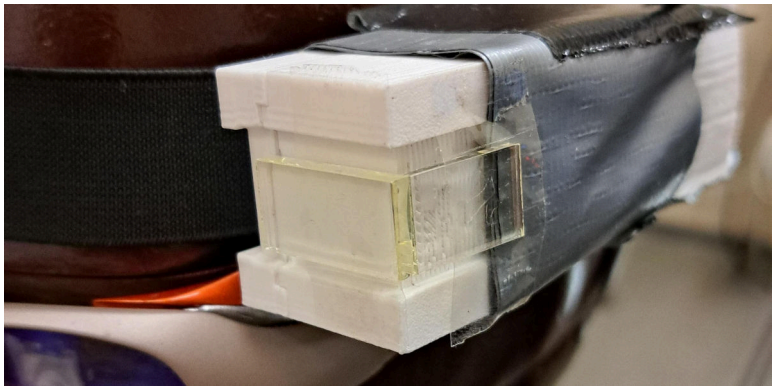

Figure 5.17.: Photograph of the lead glass pieces (batch 1) attached to the front and side of the dosemeter housing. The photograph is taken from [132].

Parameter	Front Glasses	Side Glasses
Height	11.30	11.25
Length	22.40	17.00
Thickness (batch 1)	2.50	1.95
Thickness (batch 2)	2.65	1.95

Table 5.1.: Dimensions of the lead glass pieces, used to resemble radiation safety glasses. All measures are given in mm with an uncertainty of 0.05 mm.

lead glasses should not be taken into account by software, but by physically resembling the absorption of the glasses also for the dosemeter.

For this purpose, special pieces of lead glass have been produced in order to correctly reflect the absorption of a certain kind of protective gear. These lead glass pieces are put in front of the eye lens dosemeter prototype. The radiation protection glasses Mavig BR126 are used for all measurements in this thesis [131]. Their eyeglass lenses have a height of 36 mm and a width at the broadest position of 55 mm. The distance between the eyeglass lenses and the human eye lenses is measured to equal about 18 mm. Accordingly, the lead glass pieces are designed to reflect these properties correctly, i.e., the angles of radiation incidence, under which the radiation protection glasses shield the eye lenses, should be the same angles under which the lead glass pieces shield Dosepix when put on the housing of the dosemeter. This is calculated via the intercept theorem, with a more detailed description of the calculation being provided in [132].

Figure 5.17 shows a photograph of the lead glass pieces, attached to the eye lens dosemeter prototype, and Table 5.1 the calculated dimensions of the lead glass pieces. Due to a measurement error of the eyeglass lenses of the radiation safety glasses, the first batch of lead glass pieces is ground to a thickness of only (2.50 ± 0.05) mm. Therefore, a second batch of lead glass pieces with a thickness of (2.65 ± 0.05) mm is commissioned.

First experiments with the lead glass pieces are conducted at the Materials Testing Office North Rhine-Westphalia (German: Materialprüfungsamt Nordrhein-Westfalen (short: MPA)) in November 2023. The prototype of an active eye lens dosemeter, based on Dosepix, is fixed at the side of an Alderson phantom [133]. Three passive thin-layer LiF thermoluminescence dosemeters (TLDs) [134] are calibrated with respect to $H_\mathrm{p}(3)$ and positioned in front of the eyes and the forehead of the Alderson phantom.

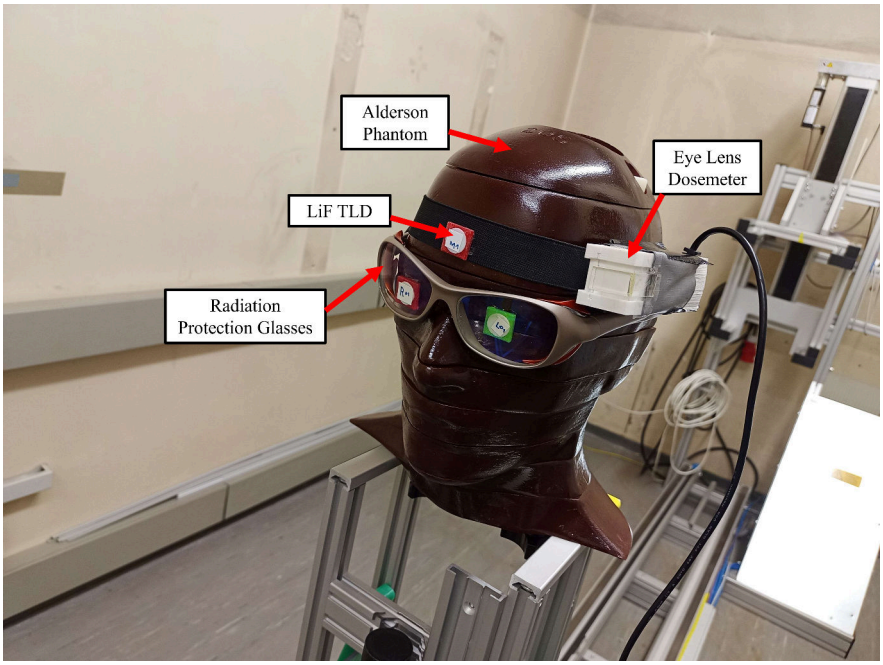

Figure 5.18.: Fully prepared Alderson phantom, as it is used for the measurements at the Materials Testing Office North Rhine-Westphalia. The red-white and green-white squares are LiF thermoluminescence dosemeters. The Alderson phantom directly faces the X-ray tube at a distance of 2 m.

Additionally, the output of the X-ray tube is validated via a transmission chamber. The radiation safety glasses are placed on the Alderson phantom in front of the TLDs. Dose results from the TLDs behind the glasses are compared with the estimated dose of the active eye lens dosemeter prototype with the attached lead glass pieces (batch 1). This allows for a comparison of measurement positions as well as the angle-dependent attenuation of radiation protection glasses and lead glass pieces. A photograph of the Alderson phantom with all dosemeters attached is shown in Figure 5.18.

A follow-up experiment is performed at the German National Metrology Institute (German: Physikalisch-Technische Bundesanstalt (PTB)) in February 2024. Figure 5.19 shows the setup with an Alderson phantom in front of an X-ray tube. There, four EYE-D TL-dosemeters are used as reference devices [135]. Two of them are positioned in front of the eyes of an Alderson phantom; the other two are placed adjacent to the former on the outside. Generally, only the inner TLDs are used for the analysis, whereas the outer ones are used for backup purposes in cases of technical issues, which happened once. The active personal eye lens dosemeter prototype is placed next to the Alderson phantom, such that Dosepix is in line with the nasal root of the phantom. If the setups adhered to ISO 29661 [136], their reference points in terms of rotations would be centered on the Dosepix detector. However, this would not apply to the scientific case of these measurements, as the movements of occupationally exposed personnel shall be approximated. Therefore, the reference point of the setup is placed at the nasal root of the Alderson phantom. Lead glass pieces from batch 2 are used to attenuate the radiation reaching Dosepix. The measurements at MPA are described in more detail in the Bachelor's thesis of Tom Tröltzsch [132], the measurements at PTB in the

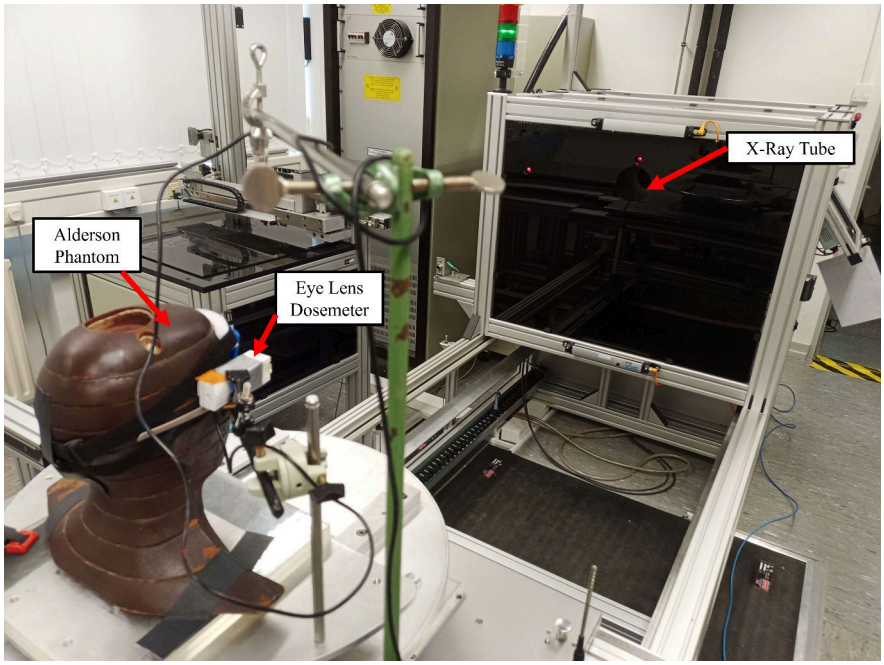

Figure 5.19.: Photograph of the setup at the German National Metrology Institute.

Master's thesis of Leonie Ullmann [98]. On top of that, the PTB data are also part of a publication from 2025 [137]. This applies to the underlying data of the results, shown in Figure 5.21, the PTB data of Figure 5.22, and Figure 5.25. Nevertheless, an independent analysis of the data is carried out for this work.

Different radiation qualities of the N-series of ISO 4037-1 [74] are irradiated homogeneously at the setups. The irradiation angles ranged from $-75°$ to $75°$ where positive angles refer to counter-clockwise rotation, as seen from the X-ray tube. Exemplary spectra of N-60, measured with the eye lens dosemeter prototype at MPA and PTB, with and without lead glass pieces, are shown in Figure 5.20. All spectra are normalized to 1 mSv of irradiated $H_p(3)$. The results from both measurement campaigns largely match within 25 % systematic difference, indicating the similarities and comparabilities of the setups. Especially the unfiltered spectra clearly show the main features of N-60 with a prominent narrow structure between 30 keV and 60 keV and a mean energy of 48 keV. Analog features are prevalent in the filtered spectra, too; however, the mean energy of the main structure is slightly shifted to lower energies, and the low-energy contributions are higher. This is contrary at first glance, since filtering leads to a relative increase of higher-energy contributions due to the energy-dependent absorption coefficients [117]. However, a significant part of the signal in this setup originates from scattered radiation from the Alderson phantom and the dosemeter housing [133]. As these lower-energy contributions are not affected by the lead glass absorption, their relative impact with respect to the signal from the direct beam increases. Overall, the installation of the lead glass filters results in a decrease of approximately 10 in the number of registered events.

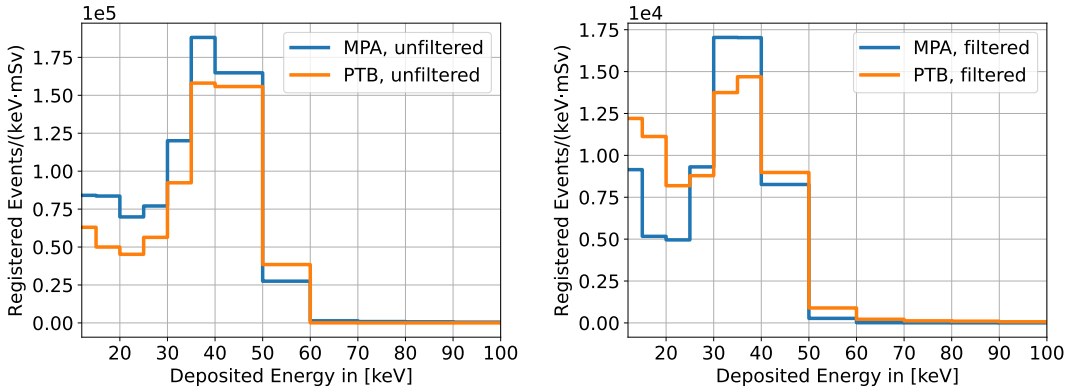

(a) N-60, unfiltered

(b) N-60, lead glass filters

Figure 5.20.: Measured energy deposition spectra of the radiation quality N-60 with 0° angle of radiation incidence. The eye lens dosemeter is positioned at the side of an Alderson phantom. In b), the lead glass pieces are attached at the dosemeter and the phantom wears radiation protection glasses.

5.4.2. Energy and Angular Dependence

In the following paragraph, the results of the active eye lens dosemeter and the TLDs are compared in terms of photon energy and angular dependence. The response of all dosemeters with respect to the mean photon energy with and without shielding is shown in Figure 5.21. All irradiated spectra are part of the N-series, except the spectrum from the MPA measurements with a mean photon energy of 28.1 keV. There, W-40 is used instead of N-40 (also from [74]), as the former enables higher maximum dose rates and resulting short measurement periods, which had to be resorted to due to the limited availability of the facility. For Dosepix, the response uncertainties are calculated via eq. Equation 2.24, the uncertainties for the LiF dosemeters are assumed to be 8% (relative) according to [134], and the difference between the TLDs on the left and the right eye approximate the uncertainty of the EYE-D dosemeters. Both experiments show similar results. When no radiation protection glasses are worn and no lead glass pieces are attached to the eye lens dosemeter prototype, the response of the active dosemeter prototype slightly decreases until a mean photon energy of 200 keV, but always stays in the officially allowed response range from 0.71 to 1.67, aligning with the results, presented in [10]. The unshielded thermoluminescence detectors roughly follow this behaviour, with only minor differences between the different eye and forehead positions. Only the EYE-D dosemeters show severe dose overestimation at lower photon energies $<$50 keV, but still within the official approval limits. These trends switch if lead glass shielding is installed. Firstly, the measured dose of all detectors decreases drastically at all energies. Only the TLD at the forehead during the MPA measurements only witnesses a slight decrease in the measured $H_p(3)$, because it is never shielded by lead glass. With that in mind, it is still remarkable that there are significant differences with regard to the presence of lead glasses, even at this position. This can only be explained by less radiation reaching the Alderson phantom due to the attenuation of the glasses, resulting in less radiation being scattered by the phantom into the dosemeter. For the shielded detectors, the measured dose increases with higher photon energies. This is

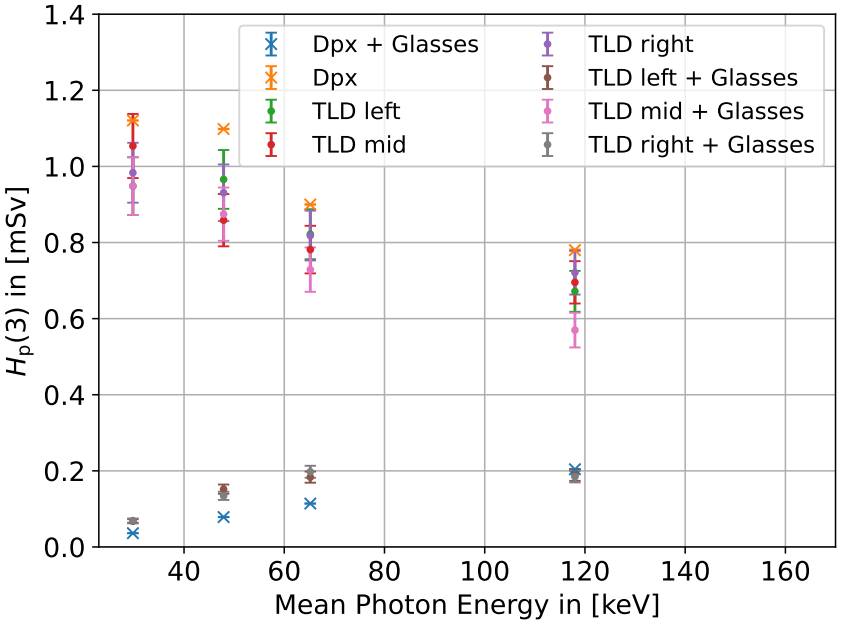

(a) MPA

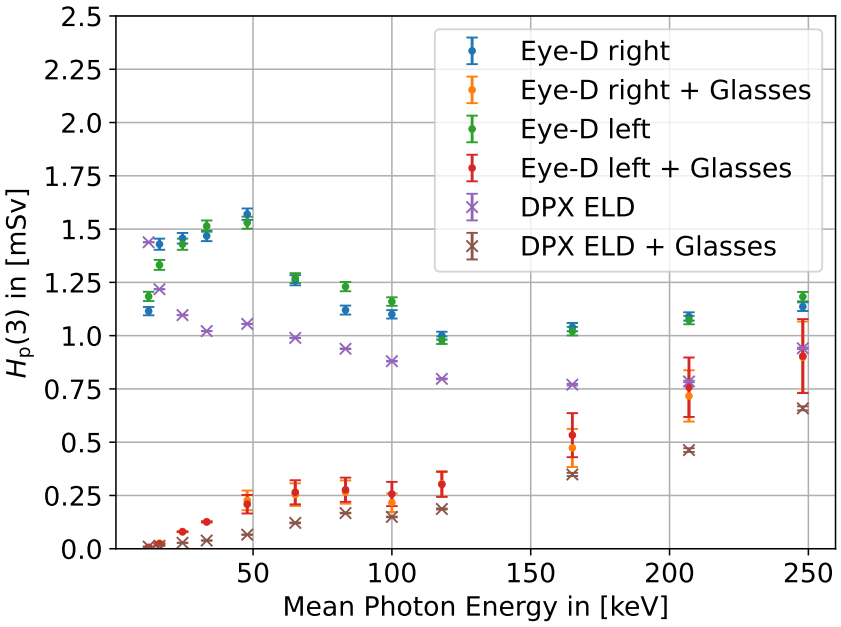

(b) PTB

Figure 5.21.: Response of the active eye lens dosemeter prototype, based on Dosepix, (Dpx) and thermoluminescence dosemeters (TLDs) with respect to mean photon energy. The measurements with radiation protection glasses and lead glass pieces are indicated with "+ Glasses"; otherwise, no glasses are present. For the results of the MPA data (a), thin LiF TLDs are used, whereas EYE-D dosemeters are used for the PTB data (b). All data points are normalized to 1 mSv of irradiated $H_p(3)$.

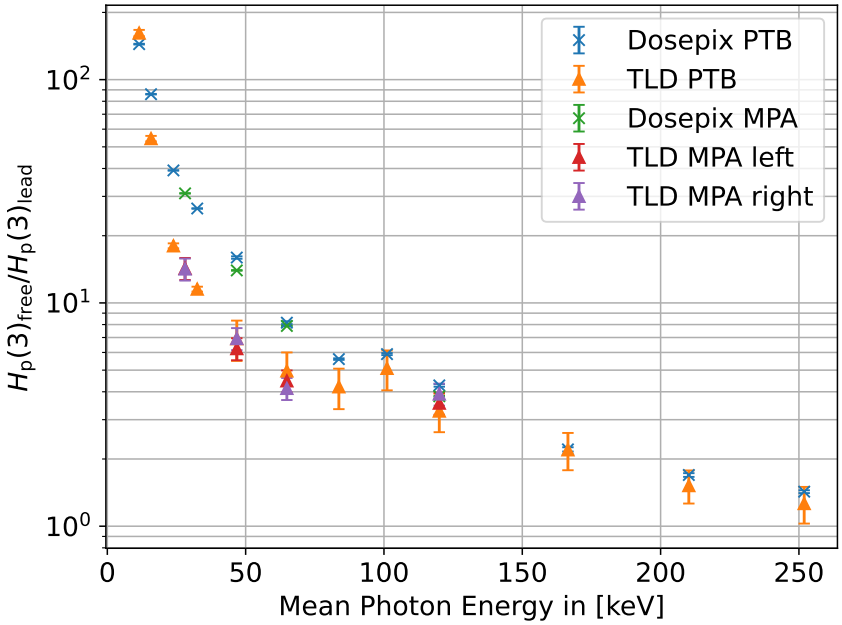

Figure 5.22.: Ratio of the $H_p(3)$, measured with thin-layer TLDs, EYE-D dosemeters, and the active eye lens dosemeter prototype, without and with lead glass shielding as a function of the mean irradiated photon energy.

primarily caused by the energy-dependent absorption properties of photons, resulting in higher absorption at lower energies.

In order to compare the absorption of the radiation protection glasses and the lead glass pieces, the ratio of the $H_p(3)$, measured without shielding and with additional glasses, is shown in Figure 5.22. Within the previosuly observed 25 % accuracy, there is no significant difference between the MPA and PTB measurements and their trends closely align with each other. Also, no significant difference between the lead glass plate batches can be extracted from that data, as the Dosepix results from both measurement campaigns agree very well, hinting at only negligible influences of the exact position of the dosemeter with respect to the Alderson phantom. The TLD data also agree well within the scope of their uncertainties, although different dosemeters are used. Thus, the slope of the data in Figure 5.22 appears to be predominantly determined by the absorption capabilities of the radiation protection glasses and the scattering behaviour of the Alderson phantom. According to that, the differences between Dosepix and the TLDs for mean photon energies $\leq 100\,\mathrm{keV}$ might also mostly originate from absorption and scattering. The local absorption maximum at $\approx 90\,\mathrm{keV}$ correlates to the K-edge of lead at 88.4 keV [117]. In conclusion, the $H_p(3)$ measurement position at the side of the head with attached lead glass plates offers a meaningful approximation of the eye lens dose equivalent for homogeneous head-on irradiations.

Nevertheless, the radiation exposure might significantly depend on the angle of irradiation if additional radiation protection glasses are present. To investigate this, many of the aforementioned radiation qualities ae also examined at different angles. At MPA, angular-dependent measurements are performed with and without lead glasses, whereas only experiments with shielding are conducted at PTB. The results from MPA

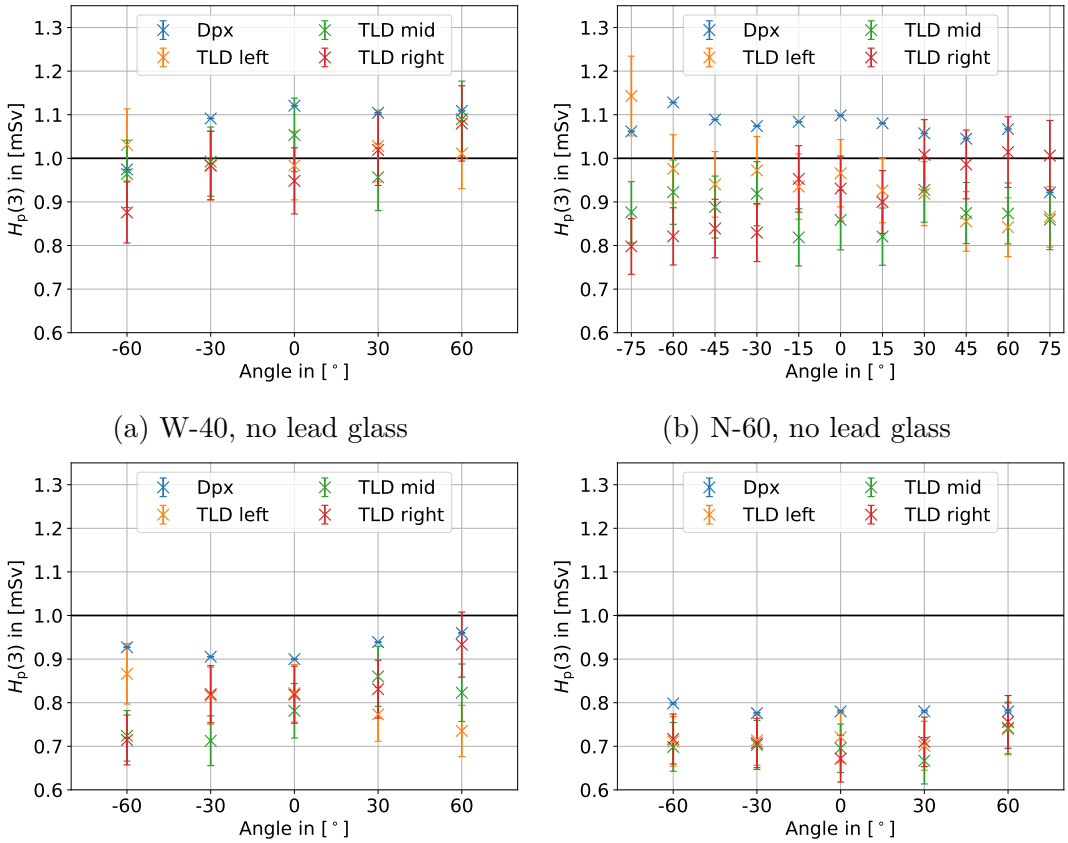

(a) W-40, no lead glass

(b) N-60, no lead glass

(c) N-80, no lead glass

(d) N-150, no lead glass

Figure 5.23.: Irradiation-angle dependent $H_p(3)$. The figures show the estimated dose by Dosepix and LiF-TLDs with respect to the angle of the irradiation for different X-ray spectra without lead glass shielding. The black line indicates the applied dose at 0° of 1 mSv.

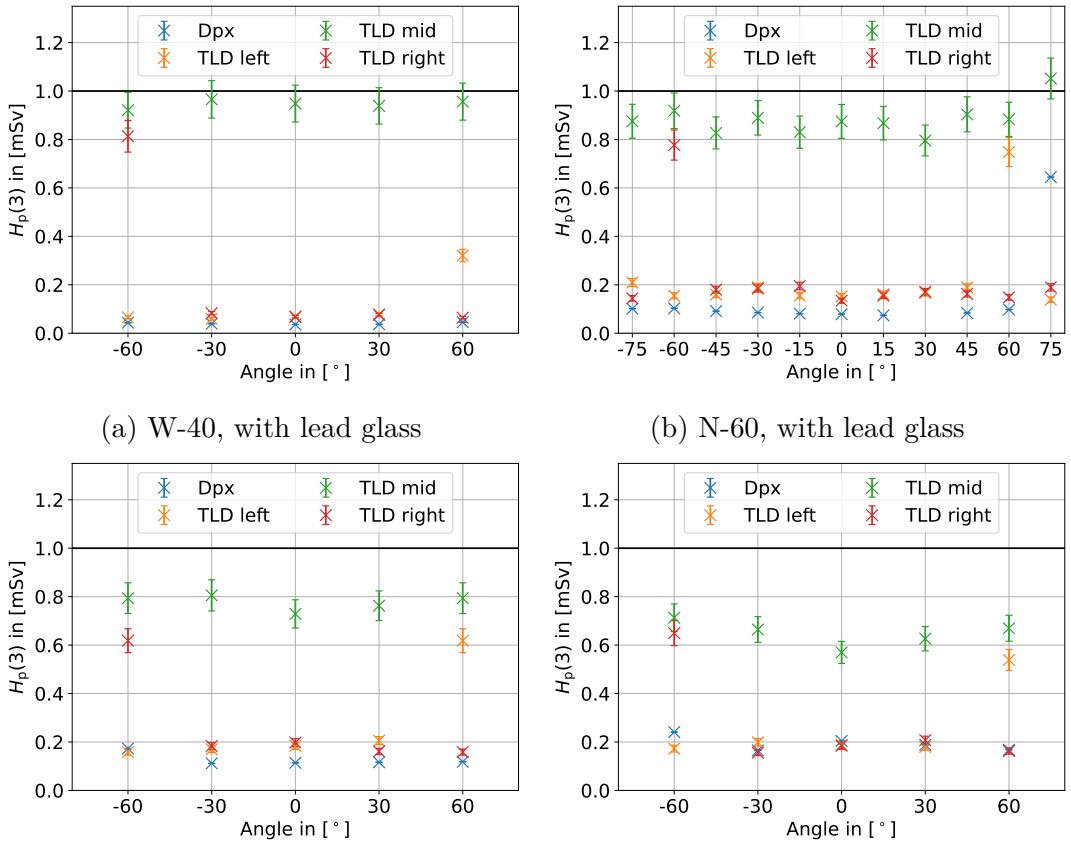

(a) W-40, with lead glass

(b) N-60, with lead glass

(c) N-80, with lead glass

(d) N-150, with lead glass

Figure 5.24.: Irradiation-angle dependent $H_p(3)$. The figures show the estimated dose by Dosepix and LiF-TLDs with respect to the angle of the irradiation for different X-ray spectra with radiation protection glasses in front of the eyes of the Alderson phantom and lead glass plates in front of the eye lens dosemeter prototype. The black line indicates the applied dose at 0° without lead glass absorption of 1 mSv.

without lead glass shielding are shown in Figure 5.23. Tube voltage, current, and irradiation time are set to correspond to 1 mSv $H_p(3)$ at 0° for each radiation quality. However, the actual relation between air kerma and $H_p(3)$, thus also fluence and $H_p(3)$, is angle-dependent [138]. This correction factor is taken into account by a subsequent correction of the $H_p(3)$-results of all detectors, which is reasonable due to the proven dose linearity of EYE-D and the active eye lens dosemeter prototype [85, 135]. The plots match the results for frontal irradiation. The active eye lens dosemeter prototype slightly overestimates the equivalent dose at the eye lens, compared to the TLDs, for almost all radiation qualities and angles by about 10 to 20 %, while still following the same overall trends. Furthermore, the TLDs at different positions show similar results, indicating approximately homogeneous scattering throughout the entire Alderson phantom.

In contrast, these relations change dramatically when the radiation protection glasses and the lead glass pieces are added. Figure 5.24 shows the reconstructed $H_p(3)$ with lead glass shielding for the MPA measurements, while Figure 5.25 shows the results for PTB. As expected, the results for the front TLDs do not change significantly, as

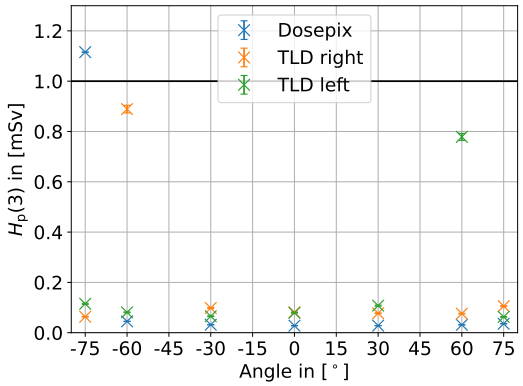

(a) N-30, with lead glass

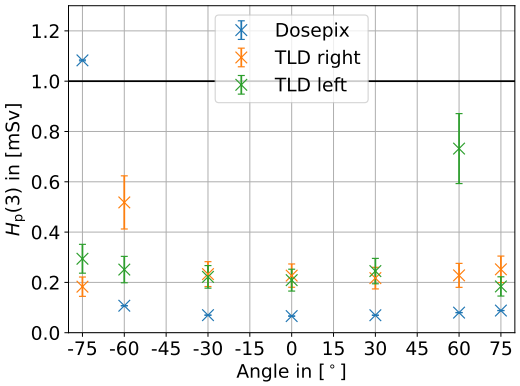

(b) N-60, with lead glass

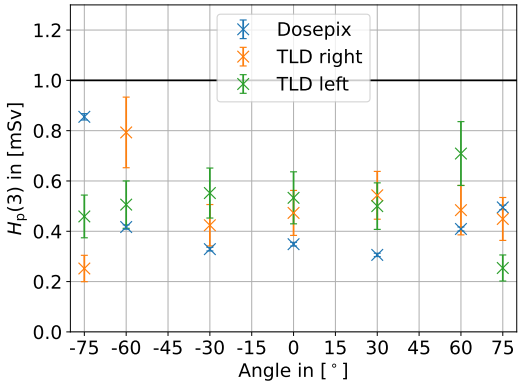

(c) N-200, with lead glass

Figure 5.25.: Irradiation-angle dependent $H_p(3)$. The figures show the estimated dose by Dosepix and EYE-D with respect to the angle of the irradiation for different X-ray spectra with radiation protection glasses in front of the eyes of the Alderson phantom and lead glass plates in front of the eye lens dosemeter prototype.

they are not shielded. For Dosepix and the eye-covering TLDs, the amount of radiation drops by up to two orders of magnitude. Here, the active eye lens dosemeter prototype measures lower eye lens doses compared to the TLDs at the eyes, which is contrary to the unshielded behaviour. This could be explained by two possible reasons. First, the lead glass pieces might absorb more radiation than the radiation protection glasses. Proving that would definitely require information about the composition of the lead glass inside the radiation protection glasses, but all information requests to the manufacturer are refused. While measuring the direct absorption of both would also solve the riddle, actually doing so comes with several major challenges, as all real X-ray setups are accompanied by radiation scattering. As this strongly depends on the shape and size of the examined materials, the small lead glass pieces and the larger curved radiation protection glasses will always produce incomparable results. This could only be solved by simulations, which would again require information about the material composition, or equally shaped samples of both materials. Second, the TLDs may be more affected by scattered radiation than Dosepix. Since scattering contributions are only insignificantly influenced by the presence of lead glass in the entire setup, $H_\mathrm{p}(3)$, estimated by the TLDs, decreases less when installing lead glasses. This explanation is reasonable because the TLDs are closer to the Alderson phantom and are placed more centrally. Follow-up measurements, performed by Leonie Ullmann in 2024, confirmed this hypothesis as being at least a major contribution to the observed effects [137].

Despite the overall agreement of the detectors for most angles of irradiation, there are some significant outliers. At 75° or −75°, depending on which side the dosemeter is worn, radiation is able to go past the lead glass pieces. Therefore, the estimated $H_\mathrm{p}(3)$ of the active eye lens dosemeter prototype is much higher than at other angles. At those angles, the utilised lead glass piece models are unable to correctly reflect the absorption properties of radiation protection glasses, since the TLDs do not witness a similar steep increase at $|75°|$. This issue could be solved by extending the side parts of the lead glass pieces. The other conspicuousnesses are the outliers of TLDs at ±60°, present during both measurement campaigns and all radiation qualities. As it is always only the detector that is rotated away from the X-ray tube, it seems like the X-rays could bypass the lead glass along the nasal root of the Alderson phantom and directly hit the TLD in front of the eye at this angle of radiation incidence. This is very unfortunate, as radiation monitoring is hardly capable of taking such contributions into account, leading to potentially underestimated radiation exposure.

However, some caution is necessary when interpreting these results. On the one hand, the TLDs are not exactly at the positions of the eye lenses themselves, but in front of them. Therefore, such delicately angle-dependent results might not reflect the effects regarding real eyes during occupational exposure. On the other hand, interchanging the model of the radiation protection glasses or changing the shape of the nose or cheekbones may also alter these results.

In summary, introducing lead glass pieces to reflect the absorption of radiation protection glasses is generally possible. For different photon energies, radiation qualities, and angles of irradiation, the response of the active eye lens dosemeter prototype, based on Dosepix, and passive thermoluminescence dosemeters match within the scope of the given uncertainties. Nonetheless, some differences between the detectors and measurement positions occur, which cannot be resolved within the scope of this work. Additionally, different types of radiation protection glasses may produce varying results,

even when their individual properties are considered by the measures of the lead glass plates. Thus, the presented measurements should be repeated with different glass models or other radiation protection gear. Additionally, the presented investigation is solely based on homogeneous radiation fields under fixed laboratory conditions. This does not reflect reality, as discussed in section 5.3, emphasizing investigations about the influence of the measurement position and lead glass pieces under inhomogeneous and more realistic radiation fields.

5.5. Reproducibility

5.5.1. Contributions to the Coefficient of Variation

The reproducibility of dose results under identical conditions is among the most crucial properties of dosemeters in general. The coefficient of variation v quantifies the stability of dose measurements and serves as the decisive parameter for the official approval procedure, according to IEC 61526 [37] (see section 2.4). The norm states a maximally allowed variation of 15 % for $H_\mathrm{p}(3) < 0.3\,\mathrm{mSv}$, $\left(16 - \frac{H_\mathrm{p}(3)}{0.3\,\mathrm{mSv}}\right)$ % for $0.3\,\mathrm{mSv} \leq H_\mathrm{p}(3) < 3.3\,\mathrm{mSv}$, and 5 % for $H_\mathrm{p}(3) \geq 3.3\,\mathrm{mSv}$. In 2024, these limits were slightly softened as the norm included the suggestions from [139]. The measured coefficient of variation of the active eye lens dosemeter prototype has been significantly lower in previous studies [10], ranging from 0.4% to 0.7%. Nevertheless, the pure variation of the active dosemeter prototype may be even lower because fluctuations of the X-ray tube also add to the total result.

In this section, measurements towards disentangling the individual components of the total coefficient of variation are presented. This may help to better understand the properties of the dosemeter prototype as well as to predict its behaviour, e.g., if the pixel size or read-out frequency were changed. As a suitable approximation for this analysis, the total standard deviation σ of n dose values is described by

$$\sigma^2 = \sigma_\gamma^2 + \sigma_\mathrm{F}^2 + \sigma_\mathrm{el}^2 + \sigma_t^2 + \sigma_T^2 + \sigma_\mathrm{Source}^2 + \sigma_\mathcal{O}^2 \tag{5.1}$$

with σ_γ the photon noise, σ_F the standard deviation due to the statistical uncertainty of the charge production inside the sensor material, described by the Fano uncertainty [13], σ_el the combined uncertainty due to electronics, σ_t the uncertainty due to a fluctuation of the actual exposure time per read-out cycle, σ_T the uncertainty due to temperature fluctuations, σ_Source all uncertainties, induced by non-constant behaviour of the radiation emitting source (e.g. X-ray tube, radioactive sample), and $\sigma_\mathcal{O}$ remaining influence terms, approximated as 0 in this work. In this entire section, σ_x refers to a certain standard deviation while $v_x = \frac{\sigma_x}{\mu_x}$ means the corresponding variation, i.e., the standard deviation, divided by its mean μ_x. σ_T has already been discussed in section 5.2. It only necessarily adds to the overall uncertainty if the temperature of Dosepix changes over time during a measurement series, because, otherwise, temperature-specific calibration may remove these contributions to the dose uncertainty for a given temperature. σ_el takes into account all contributions related to hardware-specific uncertainties, such as deviations of basic electronic components (resistances, capacitors, inductances) from their specified properties. This is mostly evident as differences between individual pixels, e.g., in terms of the energy threshold and the relation between ToT and E_dep. Although the

systematic parts of those differences are reducible by threshold equalization and pixel-specific energy calibration procedures, they are not completely eliminable [21]. They primarily manifest as energy uncertainties, which in turn affect the dose reconstruction procedure. They compose an unavoidable baseline for the coefficient of variation.

5.5.2. Fano Uncertainty

First, the dose uncertainty due to the fundamental Fano uncertainty is quantified. The Fano uncertainty describes the statistical fluctuations of the number of produced electron-hole pairs by a directly ionizing particle with energy E within a sensor layer. For the case of the Dosepix-based eye lens dosemeter prototype in medical X-ray environments, energy deposition occurs via primary photons with energy E_γ transferring a part of their energy $E_{\mathrm{dep}} \leq E_\gamma$ to an electron, which, subsequently, produces electron-hole pairs until it is stopped (see section 2.2). For medically relevant energy depositions with $E_{\mathrm{dep}} \leq 150\,\mathrm{keV}$, only a negligible fraction of these electrons is expected to leave a 300 µm silicon sensor, thus the entire deposited energy is contained [13]. In such cases, the relative statistical fluctuation of the number of produced electron-hole pairs $v_{N,\mathrm{F}}$ of a given energy is not given by pure Poisson statistics, but by a Poisson statistics, modified by the so-called Fano factor F to

$$v_{N,\mathrm{F}}^2 = \frac{Fw}{E_{\mathrm{dep}}},\ F < 1 \tag{5.2}$$

with $w = 3.63\,\mathrm{eV}$ the mean energy loss per electron-hole pair creation in silicon [27]. $v_{N,\mathrm{F}}$ is equal to the corresponding relative energy uncertainty $v_{E,\mathrm{F}}$. [13]

In reality, the Fano factor in silicon depends on the energy, thus $F = F\left(E_{\mathrm{dep}}\right)$, as measured in [140]. With the values from [140], $v_{E,\mathrm{F}}$ is calculated for a silicon sensor, with the results shown in Figure 5.26. If compared naively with typical total dose reconstruction variations of Dosepix, the presented values for $v_{E,\mathrm{F}}$ are in the same order of magnitude. However, the actual effect of the Fano uncertainty on $H_{\mathrm{p}}(3)$-results is much smaller than $v_{E,\mathrm{F}}$ because of the dose estimation process itself (see subsection 2.8.3). As $H_{\mathrm{p}}(3)$ is determined from a 16-channel energy deposition histogram with bin widths ranging from 3 keV to 20 keV, only deposited energies close to the bin edges potentially alter $H_{\mathrm{p}}(3)$ via wrong bin sorting. The magnitude of this effect is determined by the following calculation: The dose conversion factors $k\left(E_{\mathrm{dep}}\right)$, introduced in subsection 2.8.3, are given by

$$k\left(E_{\mathrm{dep}}\right) = k_1 + \sum_{i=2}^{16} \theta\left(E_{\mathrm{dep}} - E_i\right)\left(k_i - k_{i-1}\right) \tag{5.3}$$

with k_i the dose conversion factors of the individual energy bins, E_i the bin edges, and $\theta(x)$ the Heaviside function. However, the Fano uncertainty prevents an exact determination of the real deposited energy E_{dep}. Instead, the probability of measuring a deposited energy $E_{\mathrm{dep}}^{\mathrm{meas}}$ is approximately given by the Gaussian distribution

$$p\left(E_{\mathrm{dep}}^{\mathrm{meas}}\right) = \frac{1}{\sqrt{2\pi}\sigma_{E,\mathrm{F}}} \exp\left(-\frac{\left(E_{\mathrm{dep}}^{\mathrm{meas}} - E_{\mathrm{dep}}\right)^2}{2\sigma_{E,\mathrm{F}}^2}\right). \tag{5.4}$$

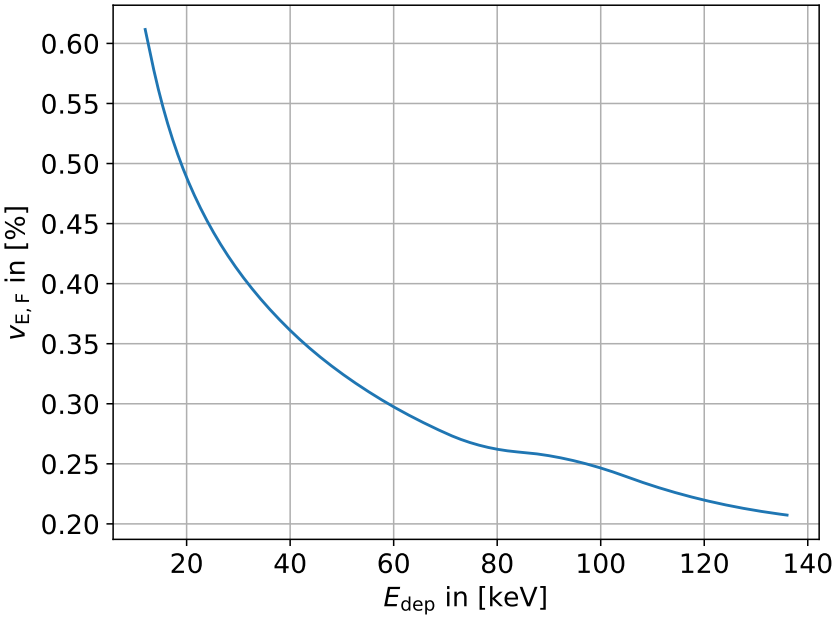

Figure 5.26.: Variation of energy due to Fano uncertainty $v_{E,\mathrm{F}}$ with respect to the deposited energy E_{dep} in silicon sensors. The values for F were taken from [140] and interpolated quadratically in between.

Then, the effective mean dose conversion factors of monoenergetic energy depositions, smeared out due to the Fano uncertainty, are given by the convolution of p and k:

$$\begin{aligned} &k^{\mathrm{mean}}\left(E_{\mathrm{dep}}\right) = \left(p * k\right)\left(E_{\mathrm{dep}}\right) = \\ &k_1 + \sum_{i=2}^{16}\left(\mathrm{erf}\left(\frac{E_{\mathrm{dep}}-E_i}{\sqrt{2}\sigma_{E,\mathrm{F}}}\right)+1\right)\left(k_i - k_{i-1}\right), \end{aligned} \tag{5.5}$$

where the Heaviside functions have been replaced by the Gaussian error function erf(x). Following that, the relative coefficient of variation for monoenergetic energy depositions due to Fano uncertainty $v_{\mathrm{F}}^{\mathrm{mono}}$ is given by

$$v_{\mathrm{F}}^{\mathrm{mono}}\left(E_{\mathrm{dep}}\right) = \frac{k^{\mathrm{mean}}\left(E_{\mathrm{dep}}\right) - k\left(E_{\mathrm{dep}}\right)}{k\left(E_{\mathrm{dep}}\right)}. \tag{5.6}$$

The results of Equation 5.6, applied on the active eye lens dosemeter prototype, are shown in Figure 5.27. For most energies, the Fano uncertainty does not affect the dose estimation process significantly, but substantial contributions of v_{F} even exceeding 80% are possible for certain energies just below the bin edges. This originates from the discontinuity of the dose conversion factors disproportionately amplifying energy misdeterminations at the bin edges.

However, such results do not occur in reality. The presented calculation only takes into account monoenergetic energy depositions but neither are monoenergetic emission spectra realized in typical clinical environments (see section 5.3) nor would even those result in monoenergetic energy deposition spectra due to Compton scattering and charge sharing (seesubsection 2.8.1). Therefore, a meaningful estimation on v_{F} is only given by

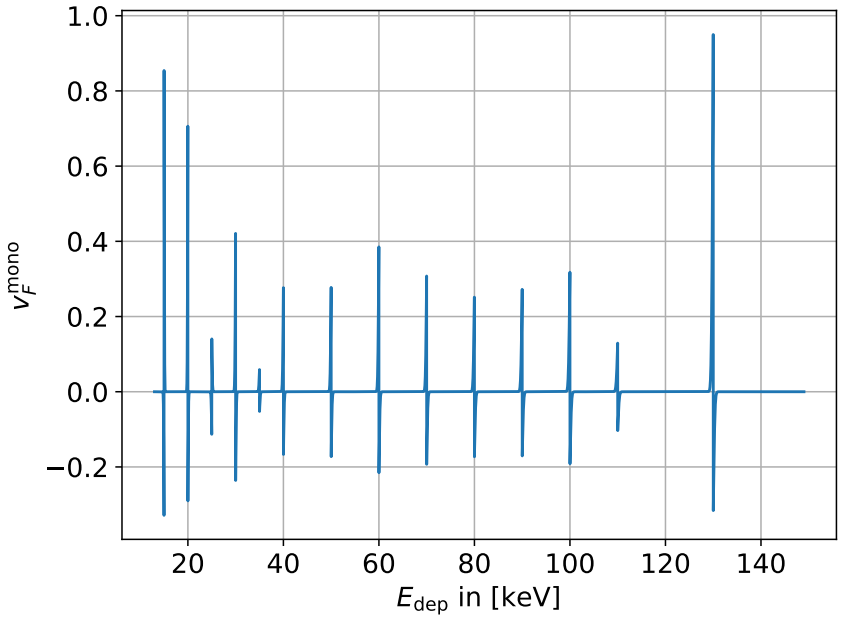

Figure 5.27.: Relative variation of $H_\mathrm{p}(3)$, estimated by the eye lens dosemeter prototype for monoenergetic energy depositions, due to Fano uncertainty $v_\mathrm{F}^\mathrm{mono}\,(E_\mathrm{dep})$ with respect to the true deposited energy E_dep.

a weighted integral of Equation 5.6 with a normalized represantative energy deposition spectrum $f\,(E_\mathrm{dep})$:

$$v_\mathrm{F} = \frac{\int_0^\infty (v_\mathrm{F}^\mathrm{mono} \cdot k \cdot f)\,\mathrm{d}E_\mathrm{dep}}{\int_0^\infty (k \cdot f)\,\mathrm{d}E_\mathrm{dep}}. \tag{5.7}$$

This cannot be analytically calculated, since a true spectrum of the deposited energies without any influence of the remaining data-taking process is fundamentally unobtainable and may only be drawn from simulations for a more exhaustive investigation of the Fano uncertainty. For this study, an energy-calibrated measured ToT-spectrum is used as an approximation for $f\,(E_\mathrm{dep})$. The spectrum, measured in the scattered radiation field in Marienklinik Siegen, shown in Figure 5.16, is used as a representation of typical radiation exposure of personnel. The spectrum is normalized and interpolated linearly between the stated values. Finally, Equation 5.7 for this case grants an estimate on v_F of

$$v_\mathrm{F} \approx 0.013\,\%, \tag{5.8}$$

which is orders of magnitude below the peaks of Figure 5.27 and also barely relevant in the scope of the total coefficient of variation. This results mainly from three factors. First, only deposited energies close to the bin edges result in a wrong estimation of $H_\mathrm{p}(3)$, as already mentioned. Second, the eye lens dose and also $H_\mathrm{p}(3)$ estimation is dominated by events with high energy depositions (see subsection 2.8.3), thus those events also dominantly contribute to v_F. For the tested spectrum, this corresponds to deposited energies from 35 keV to 60 keV, for which $v_\mathrm{F}^\mathrm{mono}$ is comparatively smaller. Third, a large part of the energy over- and underestimations cancel out and only a small fraction due to the slope of the spectrum produces an actual net variation.

5.5.3. Variation of the Read-out Time

v_t is expected to contribute to the total coefficient of variation independently of statistics. The total frame period consists of the externally set idle time, during which all pixel columns of Dosepix are collecting data, and the read-out time. The latter ranges from the call to read out Dosepix from the controlling PC until it has finished processing the incoming Dosepix data and is ready to start the next cycle. During this additional time, at least 15/16 of the pixels are still recording, as explained in subsection 2.8.2. To check the stability of the read-out period, one Dosepix detector is irradiated by a radioactive $^{241}_{95}$Am source for about 71 h. The idle part of the frame time is set to 30 s. Figure 5.28a shows the total measured read-out periods Δt with respect to time and their histogram. For the majority of read-outs, Δt shows statistical behaviour with constant variation. However, there are clustered outliers to smaller Δt, especially at about 32 h. This is reflected in the histogram as a main Gaussian-like structure, but with a tail of smaller values down to 31.97 s. In addition, only quantised values of Δt are realized, which is not natively understood from the behaviour of Dosepix. In order to quantify the features of the histogram, a function of the shape

$$f(\Delta t) = A \sin^2(\omega \cdot \Delta t + \varphi) \cdot \mathrm{e}^{-\frac{(\Delta t - \mu_t)^2}{2\sigma_t^2}} \tag{5.9}$$

with fit parameters $A, \omega, \varphi, \mu_t$, and σ_t is adjusted to the Gaussian part of the histogram from Figure 5.28b (32.2 s to 32.4 s) via a Levenberg-Marquardt algorithm of the python package *scipy.optimize* [141]. The final parameters are: $A = 194.0 \pm 1.7$, $\omega = (-1.42 \pm 0.06)\ \frac{1}{\mathrm{ms}}$, $\varphi = (9.5 \pm 0.6) \cdot 10^2$, $\mu = (32.2938 \pm 0.0027)$ s, and $\sigma_t = (26.3 \pm 1.9)$ ms. This model is not derived from any theoretical model, but chosen heuristically to extract the defining parameters of the distribution. The periodic structure most likely originates from internal frequencies from the operating system of the controlling PC, which hints at its periodicity of 15 ms [142]. Nevertheless, the spread of Δt provides the wanted information about the dose uncertainty due to read-out time variation. For time-invariant irradiation, the estimated $H_\mathrm{p}(3)$ is directly proportional to the data recording time. If only the Gaussian part of the Δt histogram is taken into account, v_t is simply given by

$$v_t^{\mathrm{Gauss}} = \frac{\sigma_t}{\mu_t} = (0.081571 \pm 0.000012)\ \% \tag{5.10}$$

with σ_t and μ_t from Equation 5.9 and the uncertainty calculated from Gaussian error propagation of the fit uncertainties. If all measured values of Δt are taken into account, v_t increases to

$$v_t = (0.1711 \pm 0.0014)\ \%. \tag{5.11}$$

The latter is calculated from the standard deviation and mean of all values, and the uncertainty derived $\frac{v_t}{2\sqrt{N-1}}$, with N the number of entries in the histogram according to [143].

5.5.4. Combined Coefficient of Variation

Some of the contributions from Equation 5.1 affect the number of registered events, others the energy resolution of the detector. Therefore, by comparing the variation of

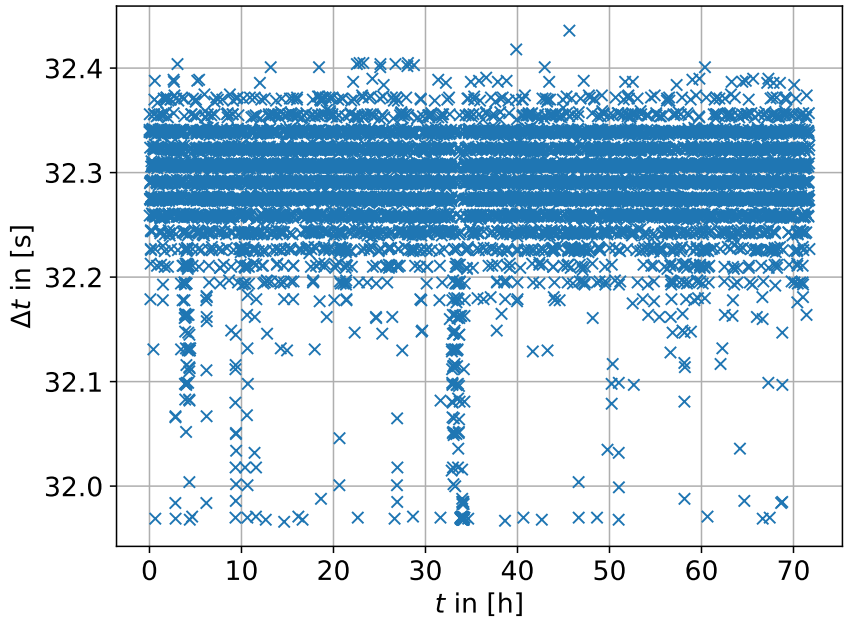

(a) Total readout period Δt with respect to time for a set idle time of data taking of 30 s.

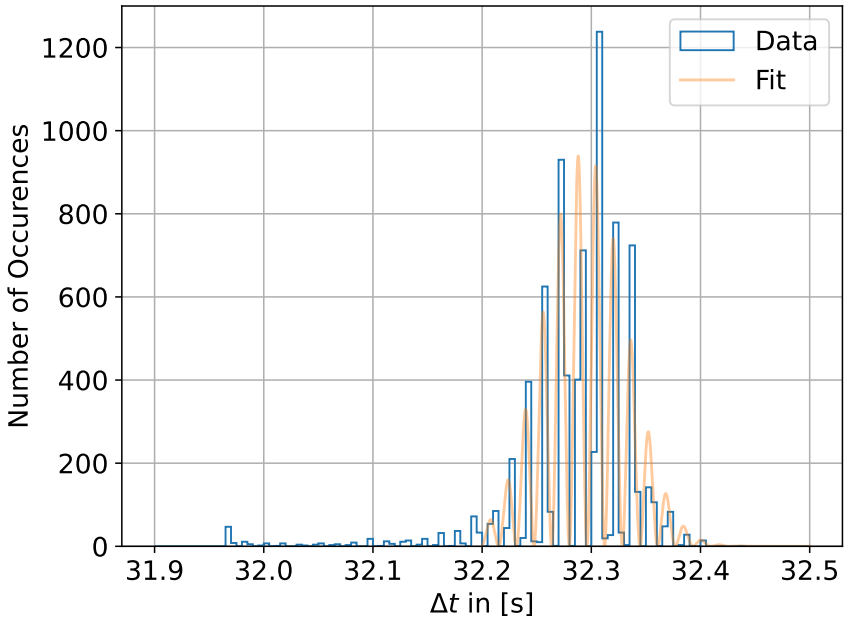

(b) Histogram of the read-out periods and fit.

Figure 5.28.: Raw values and histogram of the measured total read-out periods Δt of one Dosepix detector. The blue line respresents the measured values, the orange line a fit of Equation 5.9 to the data.

the histogram entries and the variation of the estimated energy, different aspects of the total variation can be disentangled. Additionally, by looking at data from different radiation sources, their influence encoded by σ_{Source} is estimated. Results for different radiation facilities are shown in Figure 5.29. All measurements are performed with the active eye lens prototype. The data, labeled as "GeSA-RQR8" and "400kV-Tube" were recorded at PTB in March 2022 [10]. GeSA is short for "Gepulste Strahlungsanlage (eng: Pulsed Radiation Facility), describing a facility capable of delivering high dose rates in short pulses. The utilized radiation quality RQR-8 is defined in [144] (Tube voltage 100 kV and Al filtration of 3.36 mm). The different data points are realized by varying the pulse duration from 4 ms to 10 s with a constant dose rate of 1 $\frac{\text{Sv}}{\text{h}}$. The "400kV-Tube" is another facility at PTB, capable of delivering radiation qualities from ISO 4037-1 [74] with high precision. For this experiment, radiation qualities from N-30 to N-300 are chosen with a constant dose of 167 µSv, delivered over 60 s. "Megalix" is a similar X-ray tube, used to test the variation via the radiation quality N-60 with a dose rate of 10 $\frac{\mu\text{Sv}}{\text{s}}$ and different irradiation times [77]. The relation between the reconstructed $H_{\text{p}}(3)$ and the irradiation time of Megalix is presented in Figure B.2 of section B.2. There is no linear dependence between the two, as would be expected, thus, either the dose rate of Megalix depends on the irradiation time or the actual irradiation time exceeds the set one. This should be investigated in the future by using detectors with time resolutions below 1 ms like Timepix3 [145]. Lastly, the first 25 h of the $^{241}_{95}$Am-measurement, which is discussed first in the context of Figure 5.28, is analysed under the label of "$^{241}_{95}$Am Sample". Additionally, the approximated value of σ_γ assuming linear independence of all registered events, i.e. (Number of Counts)$^{-0.5}$ is drawn as a purple line. Up until about 10^6 counts, the measured count variations follow the estimated Poissonian uncertainty; therefore, photonic noise is the dominant source for count variation $\geq 0.3\,\%$. According to the used mathematical model, none of the measured variations should lie below the purple line. However, many measured values, especially for the small pixels, do so, which is not covered by the theory underlying this work and is not understood. Although a systematic deviation from Poissonian behaviour for large count numbers would also be in line with the results for the small pixels, too few data points provide enough statistics to reliably draw this conclusion for both pixel sizes. Beyond 10^6 counts, the variation of counts is expected to be mainly determined by the variations of the recording time and the radiation source. For Megalix, this uncertainty equals 0.078 % whereas it is 0.121 % for GeSA.

To compare these values with the other contributions, these results must be correlated with the coefficient of variation of the dose reconstruction. Figure 5.30 shows the $H_{\text{p}}(3)$-related coefficients of variation for the same data as discussed before. Here, the variation baseline is in the regime of 0.4 % to 0.7 %, higher than for the count variation. This results from additional uncertainties due to the limited energy resolution of Dosepix affecting the dose estimation process. These uncertainties mainly encode σ_{el}, as σ_{F} is shown to be much smaller (see subsection 5.5.2). Therefore, the difference between these values and the previously determined baseline count variations serves as a rough approximation of

$$0.3\,\% \leq v_{\text{el}} \leq 0.6\,\%. \tag{5.12}$$

As visible in Figure 5.30, the variation also depends on the irradiated spectrum. This results from the histogramming of the events during energy-binning measurements, from which the dose is derived. For example, broader spectra like RQR-8 spread over multiple

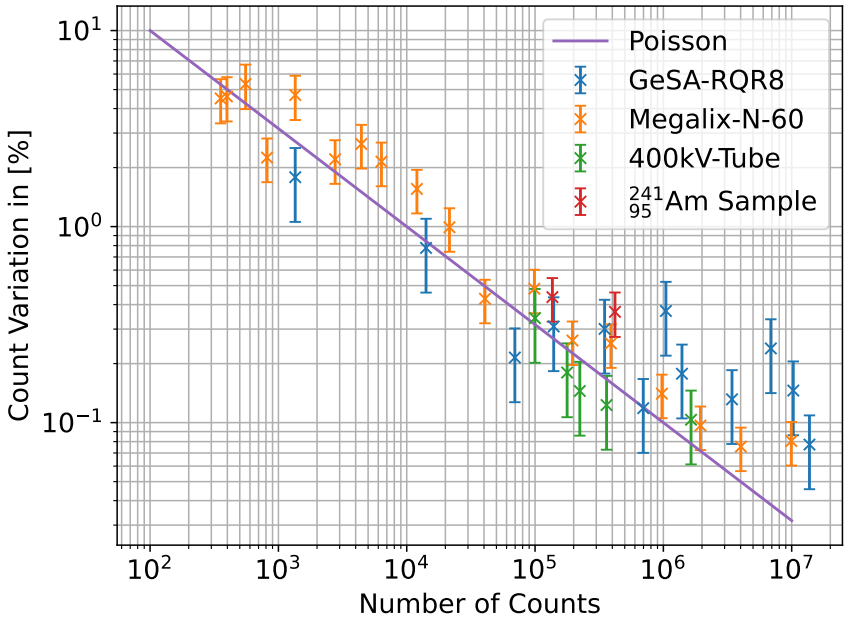

(a) Large pixels

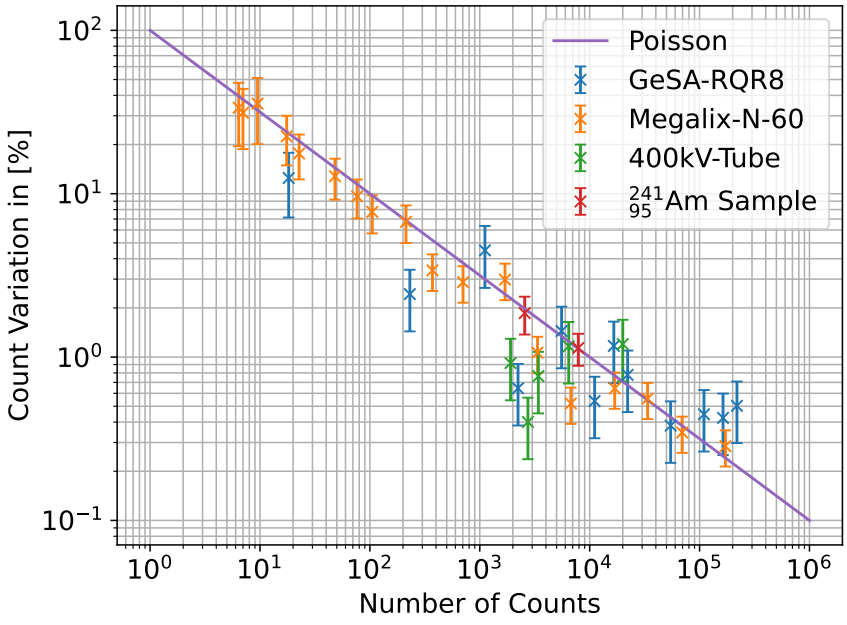

(b) Small pixels

Figure 5.29.: Variation of the number of registered events, measured at different radiation facilities, with respect to the mean number of events. "GeSA", and the "400kV-Tube" are X-ray tubes at PTB, "Megalix" is an additional X-ray tube, the $^{241}_{95}$Am sample is a radioactive probe with an activity of 1.1 GBq.

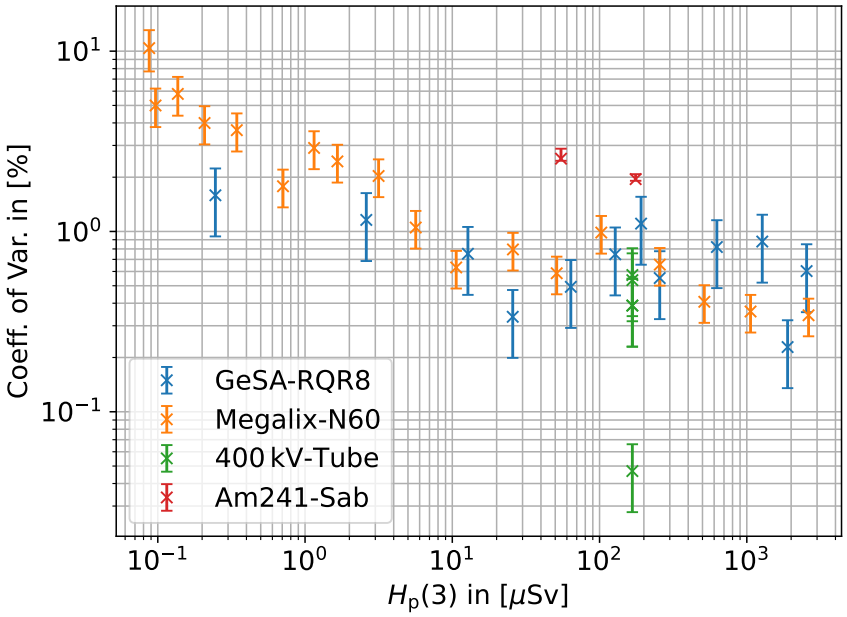

(a) Large pixels

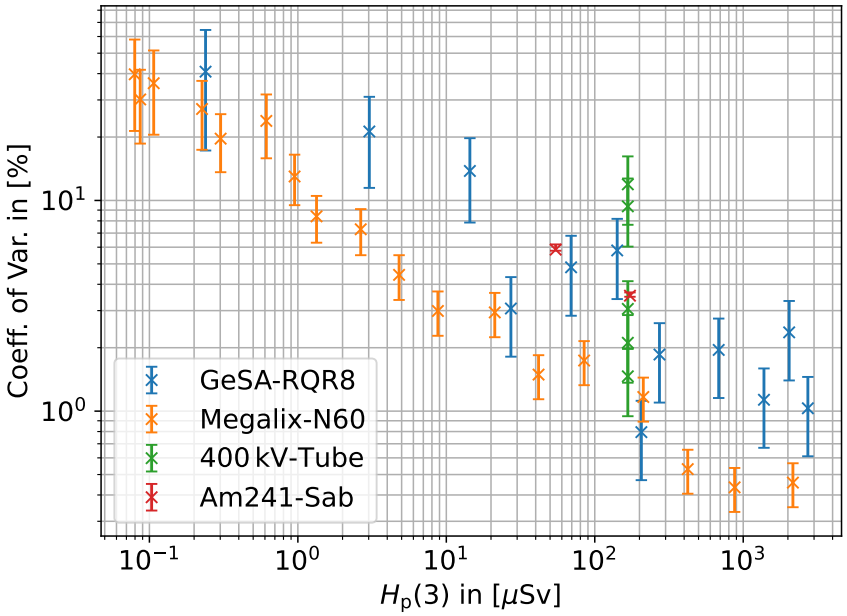

(b) Small pixels

Figure 5.30.: Measured coefficient of variation for different emission spectra with respect to the average estimated $H_p(3)$. "GeSA", and the "400kV-Tube" are X-ray tubes at PTB, "Megalix" is an additional X-ray tube, the $^{241}_{95}$Am sample is a radioactive probe with an activity of 1.1 GBq.

energy bins; thus, small energy misdeterminations cancel out. On the other hand, the $^{241}_{95}$Am-measurement serves as an approximation for the upper maximum of that effect, since the emitted spectrum mainly consists of monoenergetic photons with 59.5409 keV, which is very close to one of the bin edges at 60 keV (see Figure B.3). Therefore, even small errors in the energy estimation process significantly alter the final dose. Because of that, the coefficient of variation of the $^{241}_{95}$Am sample is higher than for the measurements at X-ray tubes, although σ_{Source} is expected to be negligible in the former case. One coefficient of variation of the 400kV-tube results falls significantly below all other results of the large pixels. This data point corresponds to N-80 and can only be explained by statistical coincidence due to only four measurements entering each estimation of the coefficient of variation. Repetitions of this measurement with higher statistics have already been performed, in which this outlier could not be reproduced [146].

5.5.5. Time-Dependent Influences

By now, the uncertainty of dose measurements has been examined only as a time-invariant quantity. However, additional studies suggest that the variation is also affected by time-dependent influences during and in between measurements [147]. This complicates comparisons between different studies. To look at such effects, the individual estimated dose values during constant irradiations and read-outs are investigated. This study is only performed for large pixels, as they provide better statistical stability and dose reconstruction than the small pixels. The radiation qualities W-30, W-60, W-80, and N-150 are irradiated at PTB in front of a water-filled cylinder phantom, according to [36] with reference $H_{\text{p}}(3)$ of 167 µSv, 3.4 mSv, 5.0 mSv, and 7.5 mSv. Exemplary results for W-60 are shown in Figure 5.31, the graphs for the other radiation qualities are shown in Figure B.4, B.5, and B.6. As is especially prevalent for the measurements of 167 µSv, the dose reconstruction is prone to some spikes and short-term outliers. Those can originate from various reasons, ranging from instabilities of the X-ray source to individual noisy pixels or background radiation impinging on the sensor layer. Events like this prevent a final robust determination of the pure statistical variation. This becomes evident when the coefficients of variation for the discussed data are determined, as shown in Figure 5.32. In order to calculate the coefficient of variation, each measurement is divided into four parts of an equal number of read-outs. Only the parts of the measurements with full irradiation are taken into account. Then, those four parts were treated as four individual measurements to calculate a standard deviation, average, and coefficient of variation. The aforementioned outlier events drastically affect the coefficient of variation. Because of that, immense coefficients of variation appear in Figure 5.32 that even reach the official approval limits [37]. Such effects are removable during post-processing, as noise signals appear in characteristic shapes and significantly differ from the signals of the pixels around them [16]. If background sources are known, those corresponding signals are also identifiable by their characteristic energies. However, such event reconstruction is impossible for an active dosemeter during monitoring, where no extensive analysis of the data is feasible, and dose results must be available after minimal delay to enable immediate radiation protection.

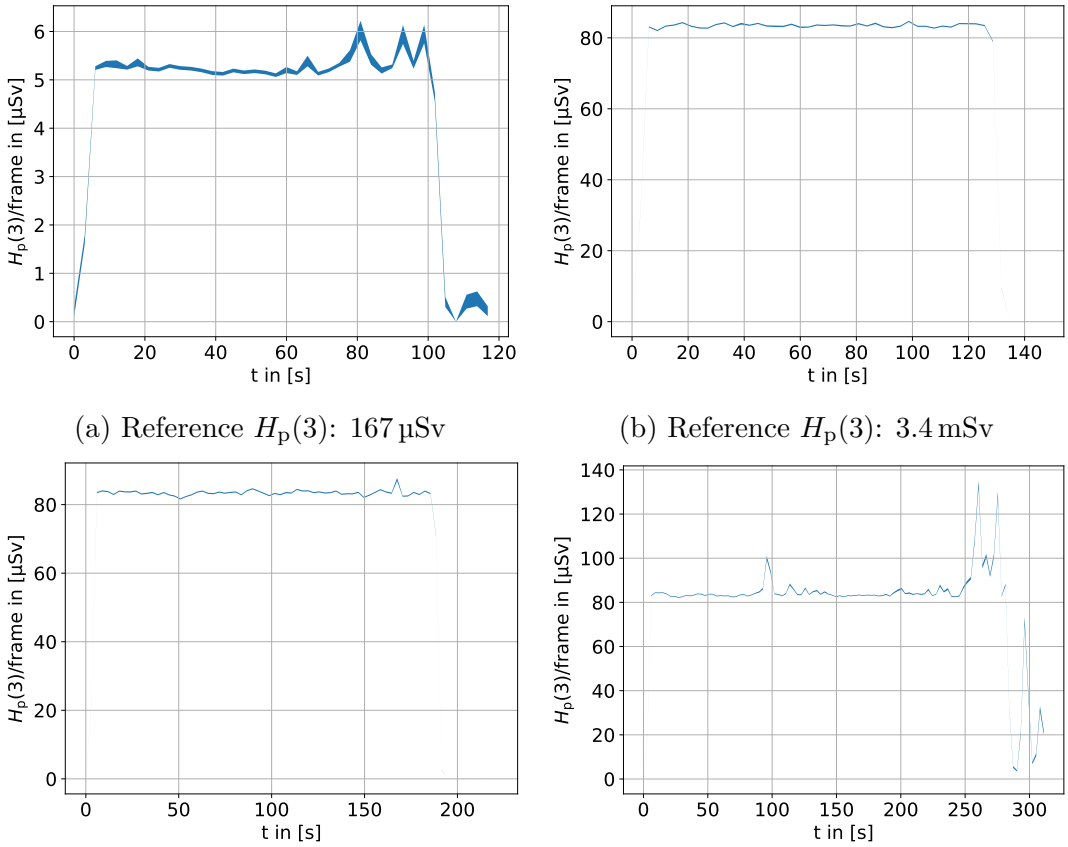

(a) Reference $H_p(3)$: 167 µSv

(b) Reference $H_p(3)$: 3.4 mSv

(c) Reference $H_p(3)$: 5.0 mSv

(d) Reference $H_p(3)$: 7.5 mSv

Figure 5.31.: Estimated $H_p(3)$ after each read-out cycle with respect to time for the radiation quality W-60. The thickness of the line represents the approximated standard deviation during each read-out.

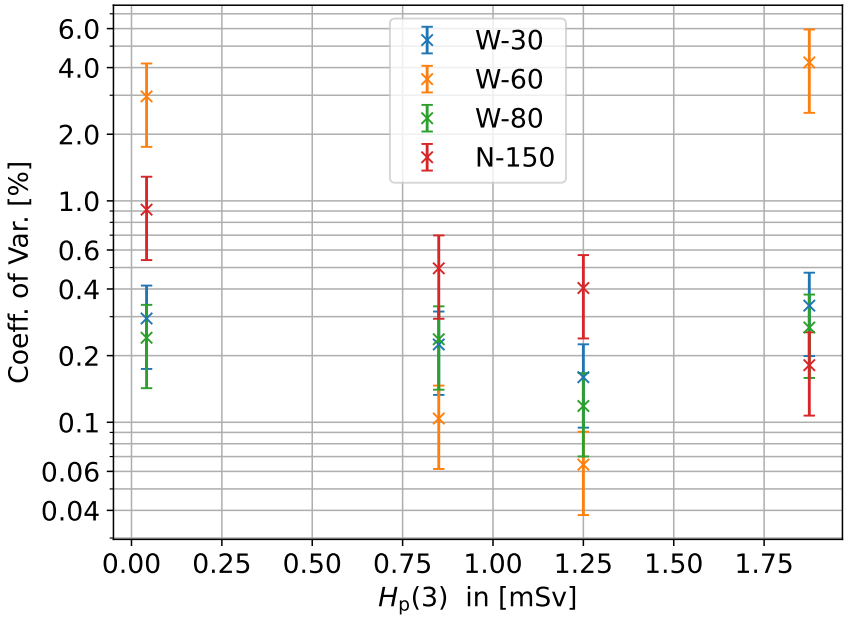

Figure 5.32.: Coefficient of variation for the measurements, presented in Figure 5.31, B.4, B.5, and B.6 for the large pixels with respect to the irradiated $H_p(3)$. The coefficient of variation is calculated by dividing each measurement into four equally long sections and treating them like individual measurements.

5.5.6. Summary

Many different quantities potentially influence the reproducibility of $H_p(3)$-measurements of the active eye lens dosemeter and Dosepix in general. For $H_p(3) \leq 10\,\mu Sv$, the Poissonian uncertainty of photonic noise dominates the coefficient of variation. Above that, several other contributions influence the reproducibility. While some of them can be estimated by the presented measurements, others highly depend on the individual setup or unpredictably disturb measurements on short time scales. A summary of the different components is given in Table 5.2. However, these results are only approximations, as the different components of the dose uncertainty can hardly be measured separately. Also, some of them change over time. In a follow-up study, presented in Linda Pfohlmann's

Parameter	Magnitude	Origin
v_γ	$1/\sqrt{N}$	photon noise
v_F	0.013%	electron-hole-pair production
v_{el}	$0.3\,\% - 0.6\%$	Dosepix
v_t	$0.08\% - 0.17\%$	control hard- and software
v_T	$< 15\%$	temperature dependence
v_{Source}	$0.078\% - 0.121\%$	source instability

Table 5.2.: Summary of the different uncertainty contributions to the overall $H_p(3)$-uncertainty σ. Here, N denotes the total number of registered events

Bachelor's thesis [147], such time dependencies were confirmed for an Ivario COMET iXRS-160/4.5 X-ray tube [130], too. Furthermore, the results in [147] showed time-dependent effects on various time scales up to several hours. In [146], a comparison of the coefficient of variation of two eye lens dosemeter prototypes was performed. The study found radiation qualities, where both prototypes differed significantly, although they behaved equally for the vast majority of irradiations, requiring complementary measurements with more dosemeter prototypes to draw robust conclusions. Ultimately, all the examined influences on the dose uncertainty except temperature dependence still fall well below the official approval limits of $\geq 5\,\%$, as stated in [37]. Only significant temperature changes or noise occurrences potentially affect the coefficient of variation strongly enough to conflict with the approval limits. Apart from that, a further reduction of the baseline variation could only be achieved by a redesign of Dosepix to decrease σ_{el} or the control hardware and software to decrease σ_t.

5.6. Conclusion and Outlook

The functionality of the Dosepix detector as part of a prototype of an active eye lens dosemeter prototype is tested under various aspects in this chapter. The prototype shows acceptable temperature stability for the planned indoor usage between 15 °C and 30 °C. Coefficients of variation consistently $< 1\%$ guarantee high reproducibility of dose results and low susceptibility to radiation monitoring errors. Combined with the results from [10], the active eye lens dosemeter prototype fulfills all specifications for an official dosemeter approval under laboratory conditions. Furthermore, it shows promising first results under realistic clinical conditions; however, follow-up measurements, including secondary standard dosemeters for reference purposes, are necessary to verify the accuracy of the results. Lead glass pieces at the front face of the dosemeter housing enable a decent consideration of radiation protection glasses that shield the eyes of occupationally exposed medical staff from ionizing radiation although delicate effects like gaps between the radiation protection glasses and the nose of the personnel cannot be taken into account that way. In summary, the concept of active eye lens dose monitoring with Dosepix is proven. Therefore, the next steps in the dosemeter development process should focus on the usability of the device within clinical workflows. This includes the communication of the device via Bluetooth and the removal of all cables and by-now necessary PC connections, as well as investigations about biologically meaningful dose and dose-rate thresholds for active warning purposes.

6. High-Dose-Rate VHE-Electron-Beam Monitoring

Contents

6.1. NitroFLASH Project

6.1.1. Overview

FLASH therapy with electron beams of energies from 50 MeV to 250 MeV is a promising candidate for next-generation radiation therapy as introduced in section 2.5. The ultra-high dose rates of FLASH treatments open up a larger therapeutic window compared to conventional radiation therapy, while the high-energy electrons enable the treatment of deep-seated tumors and enhance the robustness of treatment planning with respect to small system changes on mm-scales, such as breath-based movement [148]. FLASH beam deliveries usually last several milliseconds (see subsection 2.5.2). Whereas conventional treatments over the course of several minutes allow for the immediate response to some errors in the treatment planning or technical issues, FLASH radiation therapy potentially leads to much higher wrongly deposited doses due to its short treatment durations. Thus, FLASH therapy requires higher standards of beam monitoring in terms of precision, response time, and system stability. Beam monitoring includes the

dose per pulse, the average dose rate, the beam width, and the exact position of the electron beam behind the exit window of the particle accelerator.

The NitroFLASH collaboration was founded in mid-2023 to develop an electron beam monitoring device for the FLASH*lab* beamline at PITZ (see section 2.7 and [81]). It is a joint project of the Erlangen Centre for Astroparticle Physics (ECAP) as part of Friedrich-Alexander-Universität Erlangen-Nürnberg (FAU), the radiation protection group D3 of the Hamburg site of "Deutsches Elektronen Synchrotron" (DESY), the PITZ group of DESY Zeuthen site, and Berthold Technologies GmbH as an industrial partner. The underlying principle of the project is based on nitrogen fluorescence, which is emitted when the electron beam passes through air or pure nitrogen [23]. This UV light, with a dominant emission line at 337 nm [149], is measured by two photomultiplier tubes and a UV-sensitive camera. Additionally, the scattered radiation of the electron beam in air is measured by four Dosepix detectors. The camera and the Dosepix detectors are intended to determine the width and position of the beam. This work focuses on that part of the project. PMT signal analysis and dose reconstruction are carried out by the DESY Hamburg team. Ultimately, both components of the setup shall be integrated into a single beam-monitoring device.

6.1.2. Proposed Setup

Measuring the nitrogen fluorescence requires a dark environment shielded from ambient light. Apart from that, an online monitoring system depends on a non-destructive measurement technique in order to still use the monitored beam in cancer treatment. To realize that, the core element of the device is a cuboid with several ports, in which a dark environment is realized to enable imaging. Two of those ports serve as entrance and exit windows for the beam and are only covered by thin kapton foil to minimize beam interference. The different detector systems are attached to the remaining surfaces of the cuboid. A sketch of the original design is shown in Figure 6.1. As the nitrogen fluorescence photons are expected to be emitted isotropically [150], several detectors are positioned at the sides of the cuboid to enable parallel measurement of different quantities. Two UV-cameras facilitate a full 3D beam position and width reconstruction, while one or more photomultiplier tubes measure the integral fluorescence intensity to determine the charge of the electron bunches. On top of that, active pixel detectors measure the scattered radiation next to the beam to achieve cross-validation with the other detectors. By now, Dosepix detectors have served as the active pixel detectors, as they provide various measurement modalities to investigate the beam and have proven very resistant against high radiation fluxes (see subsection 2.8.2 and [20]). All investigations, regarding this thesis, are carried out with that original setup for the beam monitoring device in mind.

However, first studies during the project observed strong non-linearities of the PMT signals with respect to the bunch charges starting between 10 pC and 20 pC, as well as high disturbances of the signal from scattered radiation [151]. After those setbacks, this part of the project was not pursued any further and the PMTs were removed from the project. Without them, the entire beam monitoring is performed by the UV-cameras and the Dosepix detectors. The adjusted sketch is shown in Figure 6.2. Four Dosepix detectors are placed around the beam with 2.5 cm distance from the center on ring-shaped hardware, which enables synchronized clocks and read-out. For the

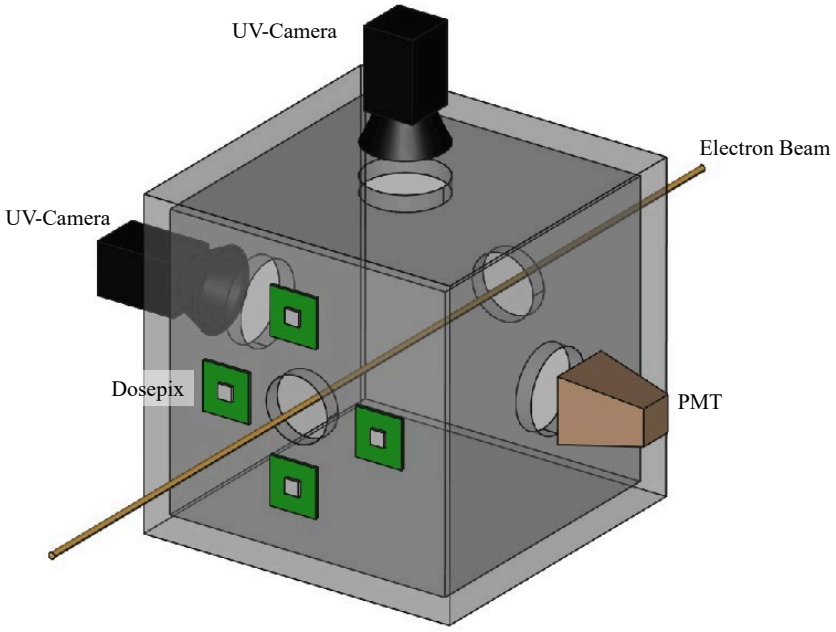

Figure 6.1.: Sketch of the originally proposed setup for the NitroFLASH project. The electron beam travels through a dark volume while producing nitrogen fluorescence photons, which are measured by cameras and photomultiplier tubes (PMTs). Additionally, Dosepix detectors measure scattered radiation.

imaging of the nitrogen fluorescence, a UV-sensitive camera is necessary. It should have a high quantum efficiency to account for the low expected intensities (see section 6.2) but should also be rather small and light to enable an easy mounting on the setup. These requirements are well fulfilled by Basler a2A2840-14gmUV cameras [152] with an IMX 487 UV sensor [153]. As shown in section 6.3, the influences of position, intensity, and beam width on the signal, measured by the Dosepix detectors, are strongly intertwined, and all three parameters must be determined in tandem. As two Dosepix detectors per spatial dimension are only sufficient to detect two of the three, camera and Dosepix detectors have to be used in a combined system for proper beam monitoring.

The setup is installed behind the exit window of the electron accelerator, thus enabling direct monitoring right before the beam enters the biological tissue. In contrast, other monitoring techniques rely on measurements along the beamline, making them blind to all potential influences on the particle beam that might occur between the measurement and the target volume [50]. Nonetheless, the results of the proposed setups still have to be calibrated to the eventual absorbed dose inside the target volume. For this purpose, additional detectors, calibrated to primary standards, must be used alongside the presented system before using it in clinical practice.

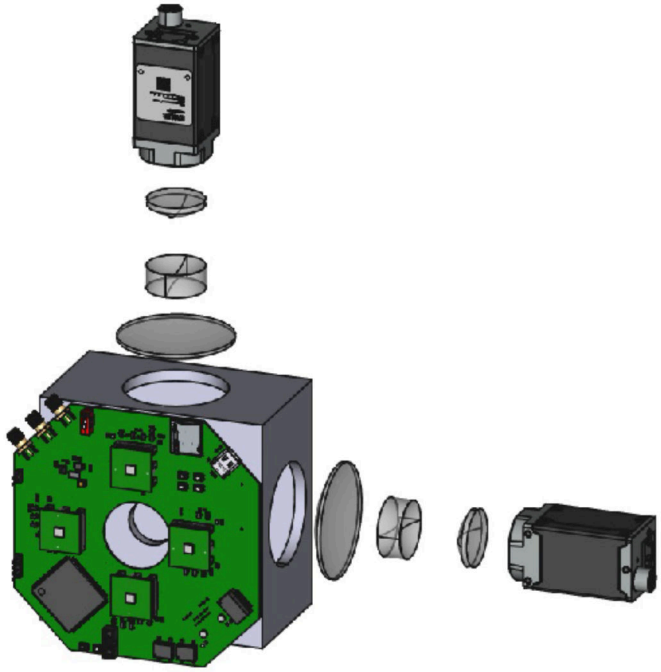

Figure 6.2.: Current design for the prototype of the NitroFLASH project. Two Basler a2A2840-14gmUV cameras are mounted at the sides of a 3D-printed cuboid. The fluorescence light is collected via three quartz glass lenses per camera (distances not to scale). Four Dosepix detectors are positioned around the entrance window of the beam to measure the scattered radiation.

6.2. Exploratory Simulations and Calculations

The NitroFLASH-project is the first occasion on which Dosepix detectors are operated at such ultra-high dose-rate electron environments. Only some pioneering experiments with Dosepix detectors inside water phantoms, irradiated by a medical linear accelerator, have been performed so far [30]. Therefore, some exploratory simulations are crucial in order to receive a first understanding of the detector's performance in idealized environments, as well as the behaviour of the beam itself when traversing air. The main deliverable of this simulation work is to propose optimal positions for the Dosepix detectors. On one hand, Dosepix and its silicon sensor must not saturate or even be damaged by too high energy deposition rates. On the other hand, the slope of the signal with respect to the distance between the detector and the beam should still be significant enough to reasonably estimate the distance. Additionally, an estimation of the expected fluxes of nitrogen fluorescence photons, usable for imaging, from first principles is presented to estimate light input of the camera.

6.2.1. Simulated Setup

The simulations are carried out with the Monte Carlo particle computer code Geant4, v10.07.03 [94]. Additionally, the specific analog signal produced in the pixelated sensor on top of Dosepix is examined. This is accomplished via the usage of the detector physics module Allpix^2 [99]. Otherwise, a theoretical ideal detector is positioned around the simulated setup. This detector yields the true energy, flight angle, and position of all particles when they first enter its volume. A sketch of the base setup is shown in Figure 6.3. All included materials are drawn from the standard Geant4 database [154]. The electrons are emitted from a square-shaped parallel beam with an edge length of 1.5 mm. At the time of the simulation runs, PITZ is intended as the target facility of the beam monitoring device; therefore, electron energies ≤ 20 MeV are simulated dominantly. The electrons traverse a volume of pure nitrogen, surrounded by an aluminum cube with an outer edge length of 10 cm and a wall thickness of 2.5 mm. The distance between the area of electron initiation and the wall of the cube is 5 cm. For the electrons to enter and exit the cube undisturbed, a square-shaped port with an edge length of 1.0 cm is cut in the center of the front and back face of the cube. Two more ports are left in the upper and side faces, also of square shape, but with a large edge length of 30 mm, representing the exit windows for the UV-cameras. Although some details about the setup (hole diameters and shapes) are later redesigned for the real setup due to technical feasibility, the simulations still provide valuable insight. The aluminum cube is surrounded by an ideal particle detector, as described before. Equal to the entrance and exit windows of the aluminum cube, two ports inside the detector allow the primary electrons to enter and leave the simulated volume. Therefore, only particles that have changed their direction of flight inside the cube are registered. This structure is located in the center of a $(15\,\mathrm{cm})^3$ world volume, consisting of air.

When the response of Dosepix is simulated, the ideal detector is removed. Instead, a simplified Dosepix model, attached to a 45 mm x 20 mm x 1.5 mm FR4 plate, is attached to the front face of the cube. A 20 mm x 20 mm x 1.8 mm plexiglass cover plate is put in front of Dosepix, similar to the plexiglass plates that are present to protect Dosepix mechanically during the actual measurements. The simplified Dosepix detector model consists of 12 x 16 quadratically shaped pixels with an edge length of

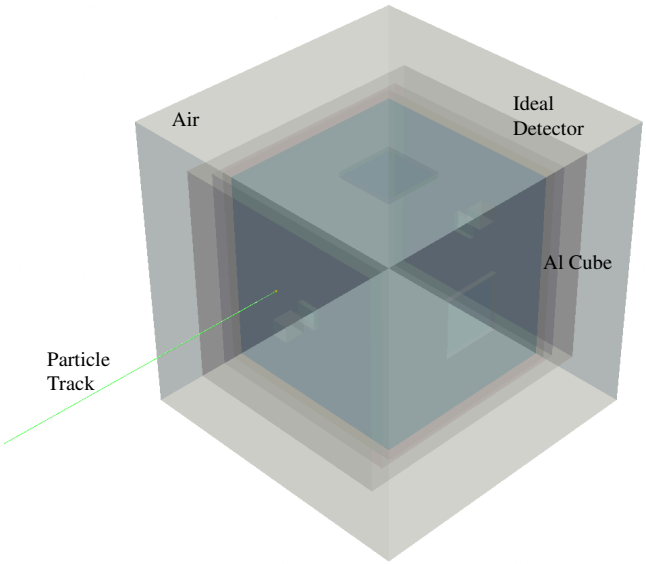

Figure 6.3.: Basic Geant4 simulation setup with an ideal detector without Dosepix. The vicinity of the setup itself is filled with air. The detection volume encloses an aluminum cube, filled with pure nitrogen.

220 µm and no gaps in between. Only the response of the large pixels is taken into account for the simulations, as the geometry of the small pixels with large intermediate electrically grounded areas could not be simulated by Allpix^2, all the more a combined sensor with both pixel sizes. The Dosepix ASIC is only taken into account in terms of scattering as a homogeneous block of 3.52 mm x 3.52 mm x 0.7 mm standard Allpix^2 ASIC material [99]. From this, the electron beam, equal to the description given for the simulations without Dosepix, is sent through the aluminum cube at different distances to the detector.

6.2.2. Energy and Position Dependence

As discussed in subsection 2.2.2, electrons traversing a medium scatter and transfer parts of their kinetic energy to their surroundings. This effect is investigated by simulating electrons with energies between 3 MeV and 15 MeV. The energies, registered by the ideal detector, which surrounds the hole cube except for the entrance and exit points, are shown in Figure 6.4. Only a small fraction of events enters the detector with the full primary energy, visible in the histogram as a small full-energy peak, since the majority of particles from the primary beam are only negligibly affected by the nitrogen and leave the observed volume undetected. Yet, there is a continuum of smaller energies ≤ 3 MeV, independent of the primary energy.

If the statistics are sufficiently high, the simulation also allows for a distinction between forward- and backward-scattered events. In a first draft of the NitroFLASH project, a positioning of the Dosepix detectors was considered, where the focus beam analysis reconstruction would have focused on the backward scattered data, e.g., next to the accelerator exit window. Therefore, backward-scattered electrons are also discussed

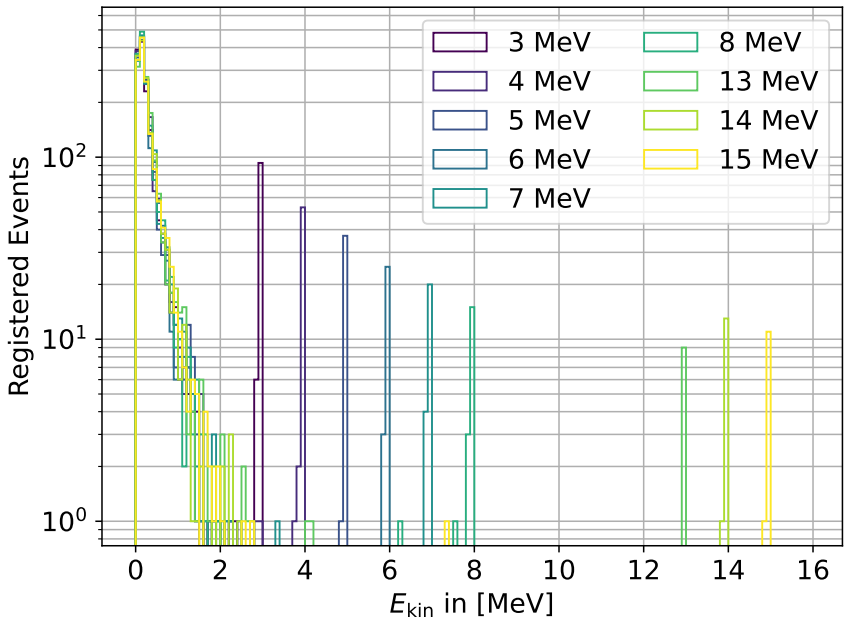

Figure 6.4.: Simulated particle energies E_{kin}, registered by the ideal detector surrounding the aluminum cube for different primary electron energies, as stated in the legend.

in the following paragraphs. Results for a 20 MeV and 20 pC total charge in the primary beam (i.e., 124,828,361 electrons) are shown in Figure 6.5. Significantly more particles are scattered into the front part of the detector, which is expected since smaller scattering angles are generally more likely than larger angles [13]. Also, events with higher energies close to the initial energy of 20 MeV primarily occur in the front detector. The backward detector part only registers few events with higher energies. There, the dominant part of the events is given by lower energy contributions.

Deciding where to put the Dosepix detectors in the final setup heavily depends on the distribution of the events with respect to their distance from the beam axis. The electron interaction cross sections also depend on the energy, wherefore this parameter must be taken into account in the evaluation, too [13]. Initial electron energies between 5 MeV and 100 MeV in 5 MeV increments are studied. The results for the lowest and highest energies and both directions are shown in Figure 6.6, the remaining energies are shown in Figure B.8 and Figure B.10. In the presented plots, the pixel size equals the total size of Dosepix; thus, the presented count numbers correspond to the number of events expected for Dosepix for 20 pC bunch charge. There are distinct differences between the individual images, again showing a strong energetic and directional dependence of the signal. As discussed previously, much higher event numbers are detected in the forward direction. Also, the slope of the number of events with respect to the distance is much steeper in the forward direction than in the backward direction, where an almost homogeneous distribution is observed. The latter is disadvantageous for a beam position reconstruction, as such benefits from a strong dependence of the signal intensity with respect to the distance to the beam. Therefore, a backward direction position of the Dosepix detectors is unsuitable for the intended use case of beam width and position monitoring. A frontal direction position of the detectors provides the

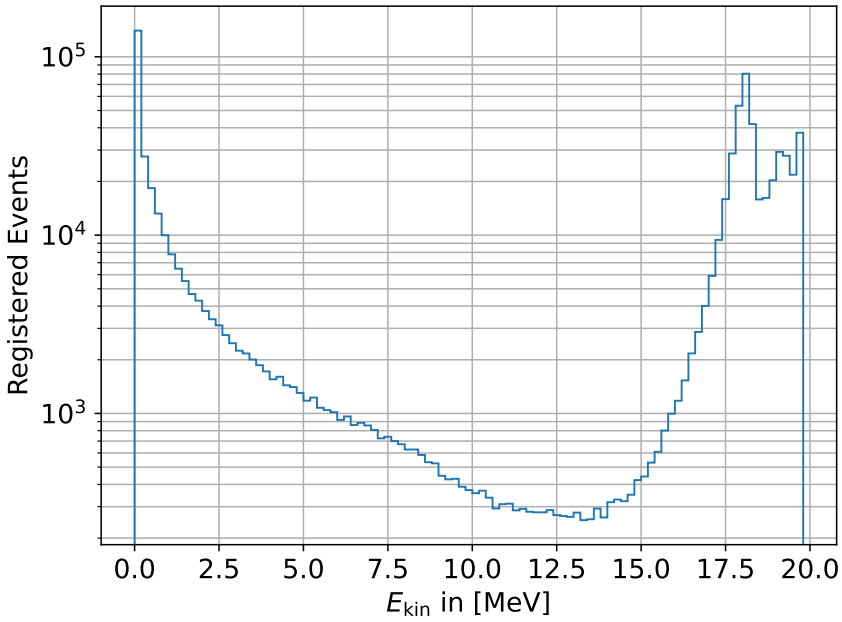

(a) Forward Scattering

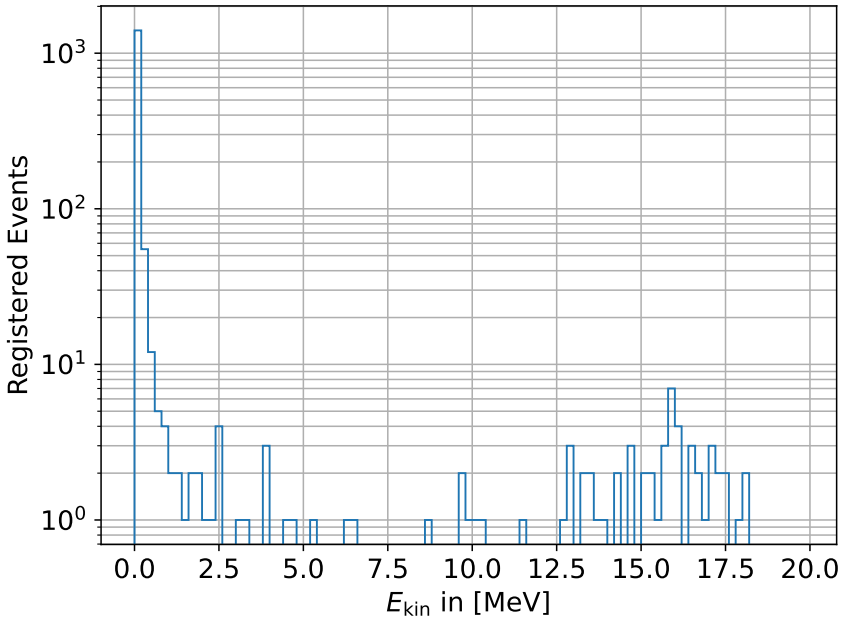

(b) Backscattering

Figure 6.5.: Simulated particle energies, entering the ideal detector. a) shows all events that entered the front surface of the detector, b) shows all events at the back surface. In total, 20 pC of primary electrons are simulated.

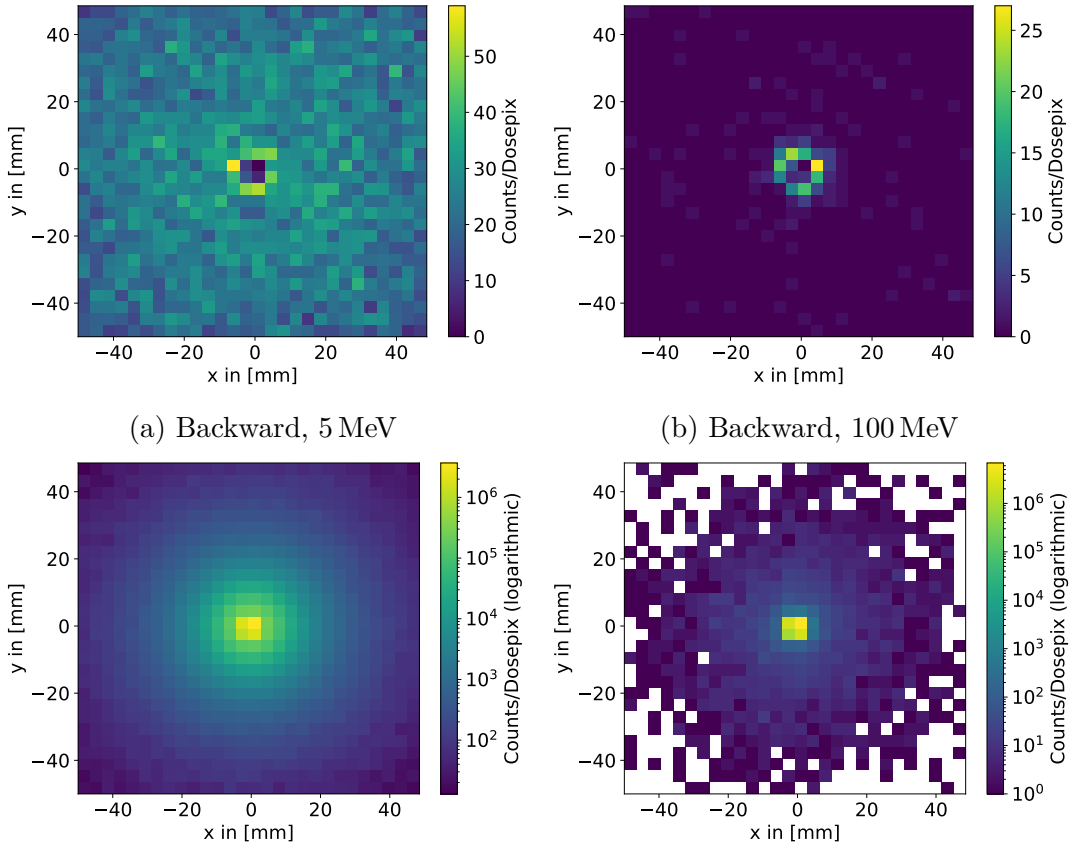

(a) Backward, 5 MeV

(b) Backward, 100 MeV

(c) Forward, 5 MeV

(d) Forward, 100 MeV

Figure 6.6.: Pixel Matrix of number of registered events for different primary electron energies and forward and backward direction. The color in c) and d) encodes a logarithmic representation of the number of counts.

necessary clear slope of the signal, but the specific relation mainly depends on the electron energy, too. A steeper slope, as present closer to the beam, would enable a better position reconstruction, but at the risk of saturating the detectors or potentially interacting with the direct beam itself. The latter could result in damaging the detector and compromising the beam, rendering it ineffectual for the intended radiation therapy. On the other hand, increasing the distance might result in insufficient signal rates, especially at higher electron energies, where larger scattering angles get increasingly suppressed. Heuristically, a distance between 1.5 cm and 2.5 cm is judged as optimal. To further investigate this, the response of the actual silicon pixels of Dosepix must be investigated for the different distances and electron energies.

6.2.3. Dosepix Response

The electron spectra, shown in Figure 6.4 and Figure 6.5, differ drastically from the expected energy deposition spectra, measured by a Dosepix detector, because electrons in the discussed energy range are only expected to deposit a small fraction of their kinetic energy in the sensor material. This is discussed in more detail in subsection 2.2.2. In the energy range relevant for this experiment, the thin-sensor approximation is valid because the absorption length of the electrons in silicon significantly exceeds the sensor thickness of 300 µm. For example, an electron with a kinetic energy of 22 MeV is expected to be stopped in silicon after ≈ 23 cm according to [28] (see subsection 2.2.2). For 100 MeV, the range in silicon increases to ≈ 79 cm. Results for the Dosepix model at different distances to the sensor are shown in Figure 6.7 for electron energies of 5 MeV and 100 MeV. The figures show histograms of the number of registered events in the entire sensor with respect to the deposited energy E_{dep}. As discussed, the typical deposited energies do not significantly depend on the primary energies of the electrons. This solidifies the approach of the thin-layer approximation, where the most likely deposited energy significantly depends only on the sensor thickness (see subsection 2.2.2). For the low energies of 5 MeV, there is a clear distance dependence of the number of registered events for forward and backward scattering. In contrast, this dependence vanishes for the backward scattering in the high-energy example, underpinning the advantage of the forward position. This is highlighted by looking at the total number of registered events with respect to the distance between the centers of Dosepix and the beam d, which is shown in Figure 6.8. Even in the most extreme case of the 5 MeV beam at the lowest distance of 1.5 cm, only 1200 events are registered in the simulation, corresponding to just about six events per pixel on average. This number decreases even further with higher electron energies, as the beam becomes narrower. Therefore, the Dosepix detector can and should be positioned close to the electron beam to maximise the signal output. Thus, a distance of 1.5 cm to 2.0 cm is recommended because placing Dosepix closer is impossible without potentially damaging the hardware around the detector and compromising the beam. The forward-scattered data at 5 MeV are statistically significant enough to extract the power-law exponent n of the data. For that purpose, a simple power law of the shape

$$N = \frac{a}{(d-b)^n} \tag{6.1}$$

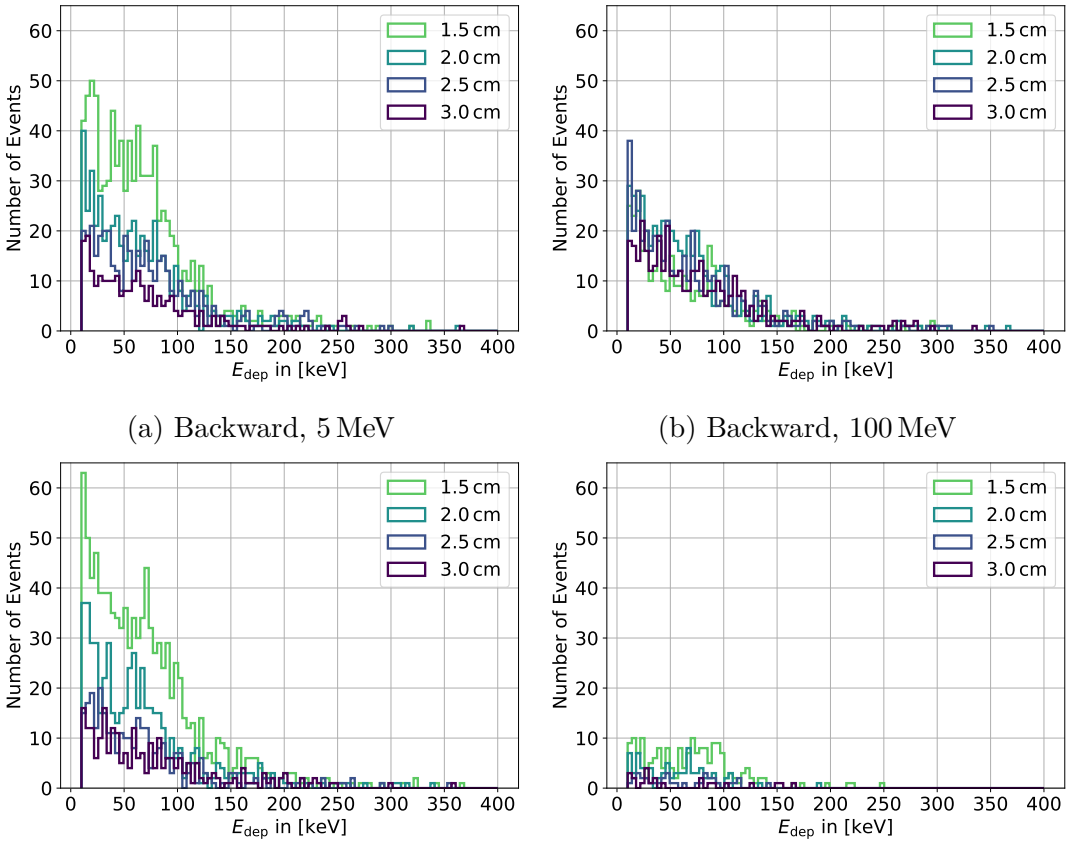

(a) Backward, 5 MeV

(b) Backward, 100 MeV

(c) Forward, 5 MeV

(d) Forward, 100 MeV

Figure 6.7.: Number of registered events of a simulated Dosepix detector with a 300 µm thick Si sensor layer. Only the large pixels of Dosepix are taken into account. Different electron energies, as well as the measurement of forward- or backward-scattered data, are simulated.

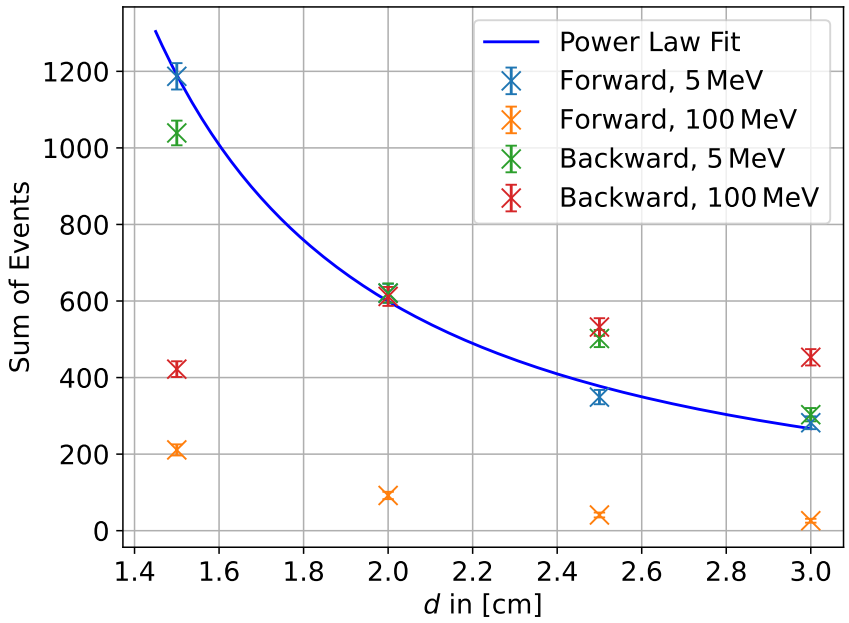

Figure 6.8.: Total number of simulated registered events in the silicon sensor with respect to the distance between the sensor and a 20 pC electron beam. The data points correspond to the histograms, shown in Figure 6.7. A power-law fit has been adjusted to the data for forward scattering at 5 MeV, since it contains higher statistics than the 100 MeV results.

with N the number of events, d the distance, and fit parameters a, b, and n, is adjusted to the data via a Levenberg-Marquardt algorithm. A power-law with an exponent between one and two is expected, since the fundamental distance dependence consists of $\frac{1}{d}$ and $\frac{1}{d^2}$ contributions, which becomes reasonable when looking at the two extreme models for the scattered radiation. If all events, detected by Dosepix at a certain position, originated from one upstream point along the beam axis, the system would behave like a point source, i.e. $\frac{1}{d^2}$ would dominate. If, on the other hand, the beam "emitted" scattered radiation isotropically, it would behave like a line source, and the signal would decrease like $\frac{1}{d}$. The results are: $a = (9 \pm 5) \cdot 10^2\,\mathrm{cm}^n$, $b = (0.7 \pm 0.4)$ cm, and $n = 1.4 \pm 0.5$. Although the results are quite imprecise due to the small number of data points, a decrease in the number of events, consistent with the first-principle expectation, is indicated. This result is needed for the distance reconstruction in subsection 6.3.2.

One major disadvantage of the simulations with Geant4 and Allpix^2 for this application is the separate simulation of each primary particle. That means that no simulation of dose rates is possible. However, the typical bunch durations at the accelerators PITZ and ARES are in the order of ≤ 30 ps [81], being even lower than a singular clock cycle of Dosepix (10 ns). Therefore, the entire charge per bunch is effectively deposited instantaneously, leading to behavioural changes of the sensor and the Dosepix hardware. Similar effects have been investigated previously in [20], but not for high-energy electron beams. Such effects can only be meaningfully investigated by measurements, performed in section 6.3, since even the framework, presented in section 3.2 uses 10 ns as its fundamental digital unit of time.

6.2.4. Calculations Towards Fluorescence Yield

Although there are some tools to simulate the nitrogen fluorescence yield, none of the tested ones proved suitable for the intended application. The simulation tool *fdsim* from the Pierre-Auger collaboration is optimized to simulate air showers in the upper atmosphere [155] and Geant4 simulations only yielded nonsensical results. Thus, calculations using the stopping power of electrons in air and the measured air fluorescence yield are performed to estimate the amount of nitrogen fluorescence photons produced by the electron beam.

The number of fluorescence photons emitted by traversing electrons is directly proportional to the deposited energy of the primary particles [156]. In [157], this proportionality factor y was calculated for electrons in air as $y = (4.05 \pm 0.14)\ \frac{\text{photons}}{\text{MeV}}$. The energy deposition of the electrons with respect to their kinetic energy is given by the stopping power $S(E)$ times the density of dry air at normal pressure and 20 °C, $\rho = 1.2041\ \frac{\text{kg}}{\text{m}^3}$ [158]. Figure 6.9 shows stopping power of electrons in air over a wide range of energies, taken from [28]. The energy loss per cm is several orders of magnitude lower than the total kinetic energy of the electrons. Therefore, the deposited energy in air is approximately given by the product of the stopping power, the air density, and the path length through air x. Thus, the fluorescence photon output $n(E)$ is determined by

$$n(E) = S(E)\,\rho\,x\,y. \tag{6.2}$$

Results for n for 20 MeV and 150 MeV, corresponding to typical electron energies at PITZ and ARES, are presented in Table 6.1. An observable path length of $x = 2$ cm is

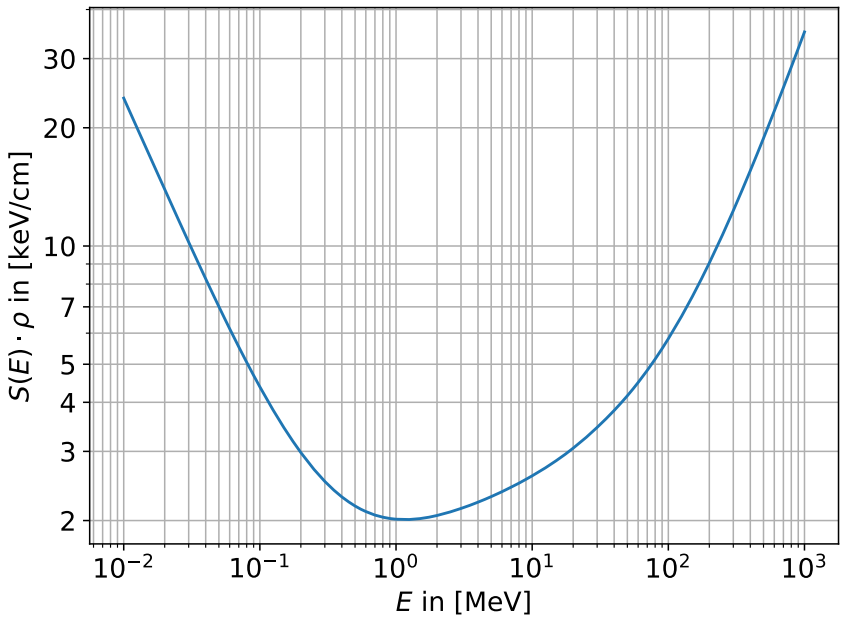

Figure 6.9.: Stopping power of electrons $S(E)$ times the density of air ρ with respect to their kinetic energy E. The data for $S(E)$ are taken from [28].

	20 MeV	150 MeV
n/e^-	$(2.48 \pm 0.09) \cdot 10^{-2}$	$(6.02 \pm 0.21) \cdot 10^{-2}$
$n/100\,\mathrm{pC}$	$(155 \pm 6) \cdot 10^{3}$	$(376 \pm 13) \cdot 10^{3}$
$n/100\,\mathrm{pC}$, exit window	$(9.7 \pm 0.4) \cdot 10^{3}$	$(23.5 \pm 0.9) \cdot 10^{3}$

Table 6.1.: Calculated number of fluorescence photons n for electron energies of 20 MeV and 150 MeV in 2 cm of air. The results for n/e^- and $n/100\,\mathrm{pC}$ point to the same calculation and are just rescaled. The uncertainties are determined from Gaussian error propagation of the uncertainty of the fluorescence yield y. The third row shows the number of fluorescence photons approximately usable for imaging in the proposed setup.

assumed, approximately resembling the final 3-lens setup, presented in subsection 6.4.2. In addition, the table shows an approximate number of expected photons at the exit window of the cube, at which the UV-camera is going to be installed. This is determined by multiplying the total number of photons by the ratio of the area of the exit window and the area of the sphere, with its radius given by the distance between the electron beam and the exit window, thereby assuming a perfect collectibility of all photons at the exit window. Ultimately, only a rather small number of fluorescence photons is expected to be available for imaging the beam for a typical bunch charge of 100 pC. Therefore, in order to image the beam, exposure times must include many bunches to increase the total fluorescence light in the camera sensor, and the utilized camera should be as sensitive as possible. These considerations lead to the setup and measurements, presented in subsection 6.4.2. Nevertheless, the fraction of collected photons should be increased significantly in future installments of the current setup to enable the possibility of single-bunch imaging and ensure a proper signal-to-noise ratio also for lower beam charges.

6.3. Dosepix

The following section presents the experiments performed with the hybrid pixelated detector Dosepix. Unfortunately, the Flash*lab* beamline at the *Photo Injector Test Facility at DESY, Zeuthen* (PITZ) was not available for most of the data-taking time, reserved for this work. Therefore, all measurements, presented here, are performed at the *Accelerator Research Experiment at Sinbad* (ARES), which is part of the Hamburg site of *Deutsches Elektronen-Synchrotron* (DESY) and is introduced in more detail in section 2.7. The first experiment in December 2024 focused on a single Dosepix detector and aimed to provide fundamental characterization of the detector's behaviour in high-dose-rate electron environments. All data-taking modes were tested and compared across different bunch charges and distances between Dosepix and the beam. It concluded by suggesting optimal modalities for succeeding ARES experiments. The follow-up experiments in June 2025 and August 2025 extended the setup to two detectors and established a first beam monitoring framework.

6.3.1. First Measurements at ARES

The first experiment with Dosepix in a high dose rate very-high energy electron (VHEE, see subsection 2.5.3) setting was performed in December 2024 at the ARES facility. A photograph of the setup is shown in Figure 6.10. A hardware extension of 18 cm length separates the readout hardware and Dosepix to reduce the risk of hitting critical parts of the hardware with the primary electrons. The entire setup is attached to an XYZ-stage to enable movements in all spatial directions. z refers to the axis, parallel to the beam, x to the horizontal, and y to the vertical direction. If not stated otherwise, the z-distance between the exit window of the accelerator and Dosepix is set to 50 cm. The physical presence of another experiment during the beamtime prevents a preferable closer positioning of the detector to the exit window. Different bunch charges from 12 pC to 127 pC are irradiated with 10 Hz repetition rate and a fixed electron energy of 153 MeV. Before any measurements are taken, the position and width of the beam are assured. For that, the beam is targeted at a luminescent screen, producing optical light

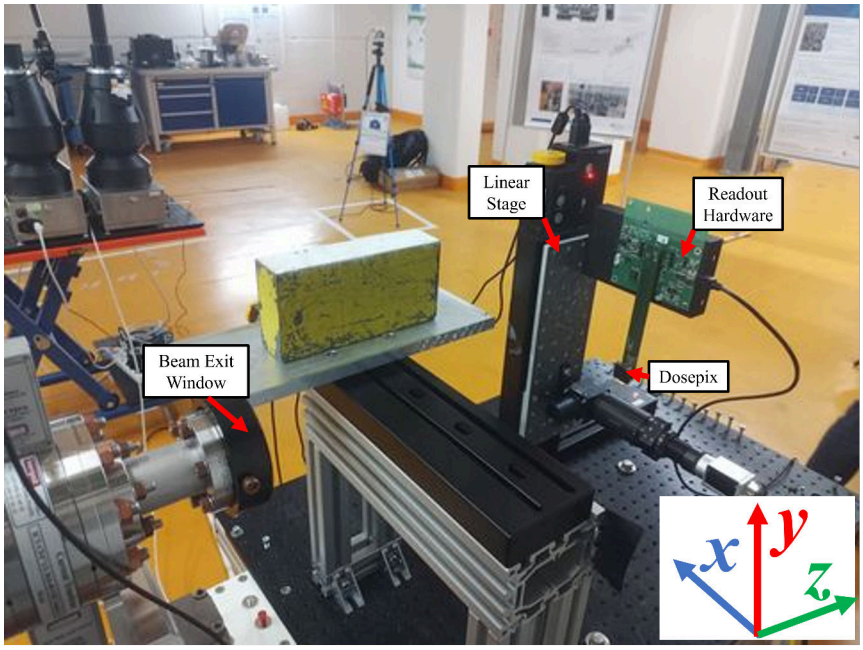

Figure 6.10.: Setup for the Dosepix measurements of the first experiment at ARES. Dosepix is connected to the read-out hardware via a 18 cm long extension.

that is directed at the sensor of a Basler acA2440-20gm camera [159]. The resulting pictures are used to control the beam parameters by manipulating the quadrupole magnets at the end of the beamline until the beam is spotted at the centre of the camera image. The beam width HWHM is measured as 2.9 mm due to the expansion of the beam during its flight through the air. Afterwards, the camera is interchanged with the Dosepix setup. This calibration procedure is repeated after each change of the bunch charge. Yet, this technique is not suited for online beam monitoring itself, since it is time-consuming, must be performed manually, and cannot take into account time-dependent changes of the system.

The following paragraphs present measurements of the signal from the ARES accelerator with all measurement modes of Dosepix (see subsection 2.8.2). The goals of that procedure are to extract as much information about Dosepix's behaviour in this novel environment as possible and to evaluate the best measurement mode for the intended use case.

ToT-Mode: In the ToT-mode, the last digitized energy deposition per pixel is read out after each data frame. This grants information about the shape of the prevalent energy deposition spectra. For that, ToT data is taken for 5 min at different x-distances to the beam with an electron bunch charge of 12 pC. Dosepix is read out roughly every 62 ms. Afterwards, the raw data are calibrated via the deep-learning-based procedure introduced in [21]. The results for the large and small pixels are shown in Figure 6.11. There is a large number of events with very low energies < 50 keV that are most probably an artifact of the readout and the bunch repetition rate. As both are similarly frequent, there are many Dosepix readouts with no bunch passing in between. Only the spectra of the large pixels at high distances ≥ 40 cm show a

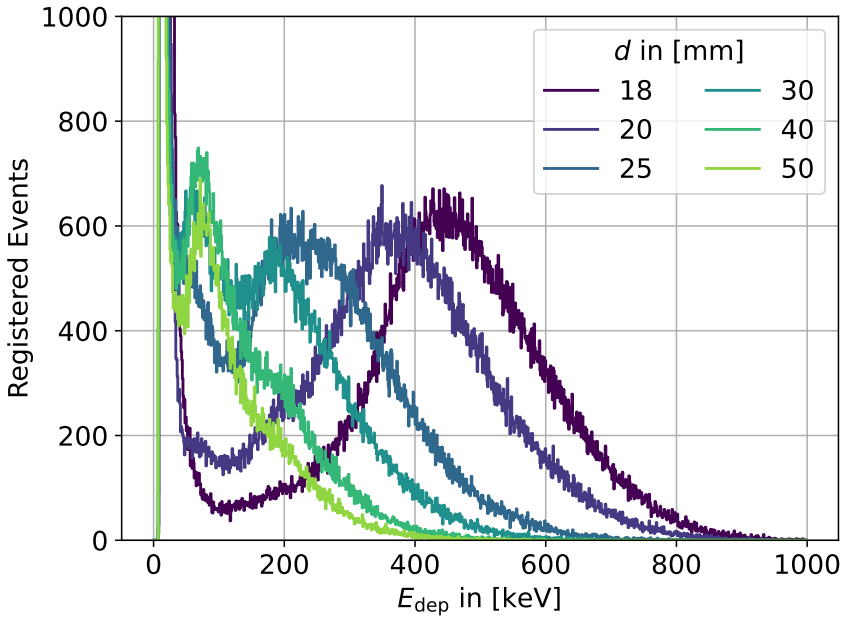

(a) Large Pixels

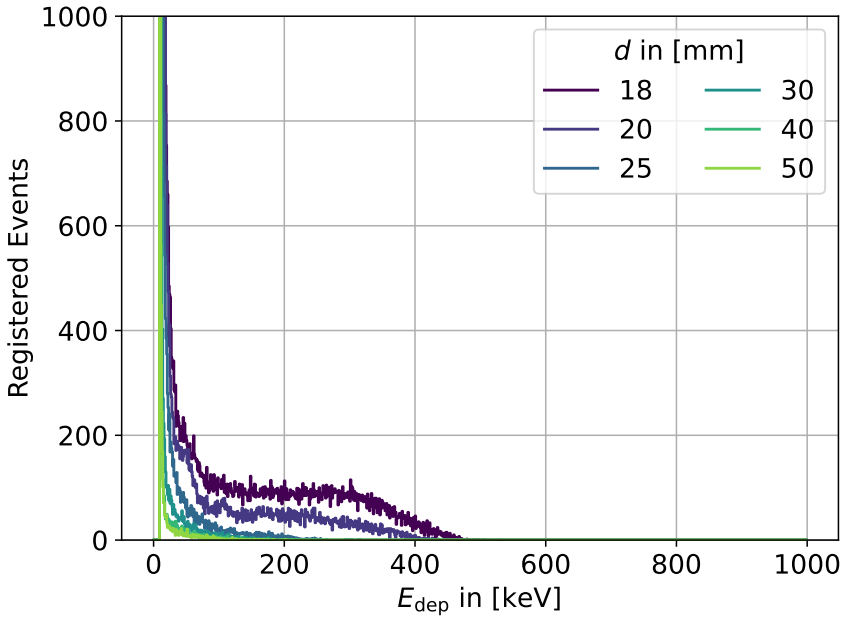

(b) Small Pixels

Figure 6.11.: Calibrated ToT-spectra, measured with one Dosepix detector at different distances d from the centre of the electron beamw with a bunch charge of 12 pC for large (a) and small pixels (b).

pronounced Landau peak at $\approx 80\,\mathrm{keV}$, equaling the previously measured most likely deposited energy for electrons in the silicon sensor [30]. Although a small equivalent structure might also be present in the spectra of the small pixels, it is overshadowed by the low-energy events and charge sharing. For smaller distances, the Landau peak is replaced by a broader Gaussian shape, with its mean energy increasing with decreasing distance. This is a sign of analog pile-up. The smaller the distance to the beam, the higher the probability for more particles to simultaneously interact with the same pixel, leading to overestimated energies. Statistically, this results in overlays of the pure energy deposition spectrum with its self-convolutions, leading to the Gaussian shape. Because of that, the mean detected energies in the small-pixel spectra are lower, since the probability for more particles hitting the detector is lower. Conclusively, no true energy deposition spectra, let alone electron energy spectra, can be measured with the ToT mode. Only information about the modal deposited energies could be determined at large distances or small bunch charges, while insights into the total fluence must be obtained from the other modes.

Photon-Counting and Energy-Binning Mode: Those two modes are the only ones to reveal information about the number of processed events per pixel. In photon-counting mode, the number of threshold passages is tracked on the individual pixel level. While this mode has been primarily used for the threshold equalization process at the pixel level, it may also support investigations into the signal-distance dependence and pile-up effects. Figure 6.12 shows pixel matrices of the number of threshold passages, measured for 200 s and a bunch charge of 12 pC, measured with the photon-counting mode. As the distance d increases, the pixel matrices become more homogeneous. At 18 mm and 20 mm, the relative deviation between the pixels is high due to outliers with a significantly higher number of measured threshold passages. This also holds for the small pixels, which detected an even slightly higher average number of events at those small distances. Such a behaviour could be, in general, explained by analog or digital pile-up, while the latter refers to an overflow and re-starting of digital counters. It is possible to qualitatively distinguish both types of pile-up by looking at the histogram of the read-out counts for one individual frame. This is done exemplarily for the fourth read-out frame of the measurement at 18 mm and is shown in Figure 6.13. Dosepix's ToT-counter, which also stores the photon-counting information, has a depth of just 8 bit when operated in photon-counting mode [16]. That means that every number of registered events above 255 is reset. This results in the two-fold distribution of events that is displayed in Figure 6.13a. Adding 255 to all small numbers of registered counts (the threshold is chosen visually as 120) results in the expected Gaussian shape of the data, shown in Figure 6.13b. Nonetheless, a meaningful correction of the digital pile-up is impossible within the scope of proper scientific practice, as crucial information, e.g., how often the counter overflew, is inaccessible and could only be guessed. For higher distances, the number of measured signals for the large pixels increases up to $d = 30\,\mathrm{mm}$ before decreasing again, when the digital pile-up effects do not overshadow the standard distance dependence of the event flux anymore. This effect is reflected by the small pixels, but with the turning point already at $d = 20\,\mathrm{mm}$, since the small pixels are less prone to pile-up.

The energy-binning mode provides 12-bit registers per energy bin and pixel, thereby significantly reducing the risk of digital pile-up. Therefore, the observed numbers of

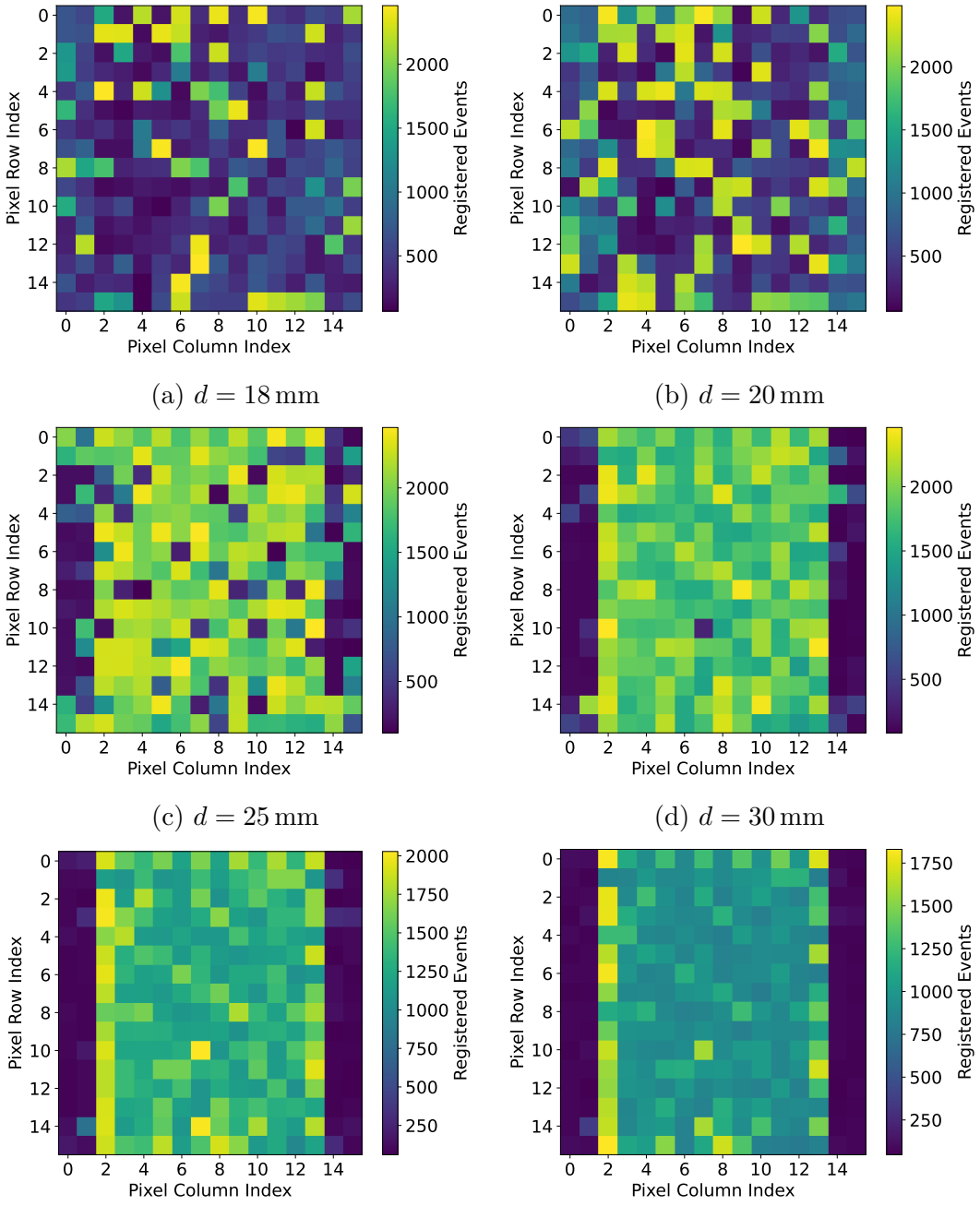

(a) $d = 18\,\mathrm{mm}$ (b) $d = 20\,\mathrm{mm}$

(c) $d = 25\,\mathrm{mm}$ (d) $d = 30\,\mathrm{mm}$

(e) $d = 40\,\mathrm{mm}$ (f) $d = 50\,\mathrm{mm}$

Figure 6.12.: Pixel matrices of the number of threshold passages, measured in photon-counting mode for different distances d between the primary electron beam and Dosepix and 200 s of data taking. The colorbar indicates the number of passages. The first and last two pixel columns correspond to the small pixels.

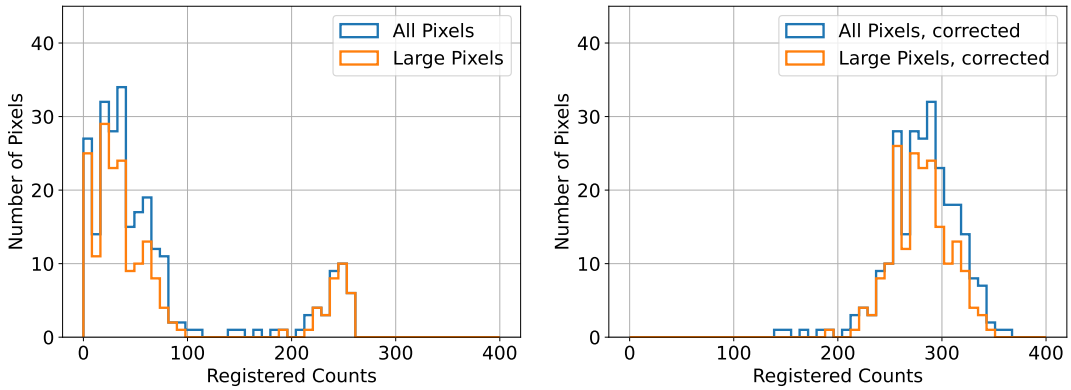

(a) Uncorrected (b) Corrected

Figure 6.13.: Histogram of the detected number of threshold passages for all pixels and only for all large pixels. The data corresponds to the fourth read-out frame at a distance of $d = 18\,\text{mm}$. a) shows the raw measurements. An offset of 255 was added to all registered counts < 120 as a correction in b).

registered events should better follow a steady decline with increasing distance. To test this hypothesis, energy-binning measurements with 87 s of data-taking and a bunch charge of 12.5 pC are performed. The corresponding energy deposition spectra are shown in Figure 6.14. Bin edges are chosen after examining the ToT-spectra to include the entire energy-deposition spectrum, but to exclude the lowest-energy events near the threshold, as had also been done in dosimetry experiments [10]. Therefore, equally spaced bin edges from 12 keV to 1050 keV are used. All numbers of registered events are normalized with respect to the number of bunches during the whole measurement. As expected, the general shapes of the energy deposition spectra are consistent with the ToT-measurements. Furthermore, the behaviour observed for the photon-counting mode regarding the number of registered events is not reproduced. This becomes even more prevalent when comparing the total number of registered events for both modes with respect to distance. Figure 6.15 shows the results for both modes and pixel sizes. The photon-counting measurements show the aforementioned strong digital pile-up effects, whereas the energy-binning results only experience some saturation effects for 18 mm. In this depiction, the differences between the two pixel sizes become obvious, with the large pixels showing digital pile-up already at larger distances than the small pixels.

Altogether, large counters are necessary for measurements with Dosepix at smaller distances in environments with high event rates. This disqualifies the photon-counting mode as the leading mode of data acquisition for the electron beam monitoring, as it already shows effects of full counters for the presented small bunch charge of 12 pC at intermediate distances. The energy-binning mode does not show similar effects and could be potentially used for beam monitoring. However, receiving the data in this mode with its rolling shutter takes about 1.0 s for the whole pixel matrix, which is too time-consuming for this purpose.

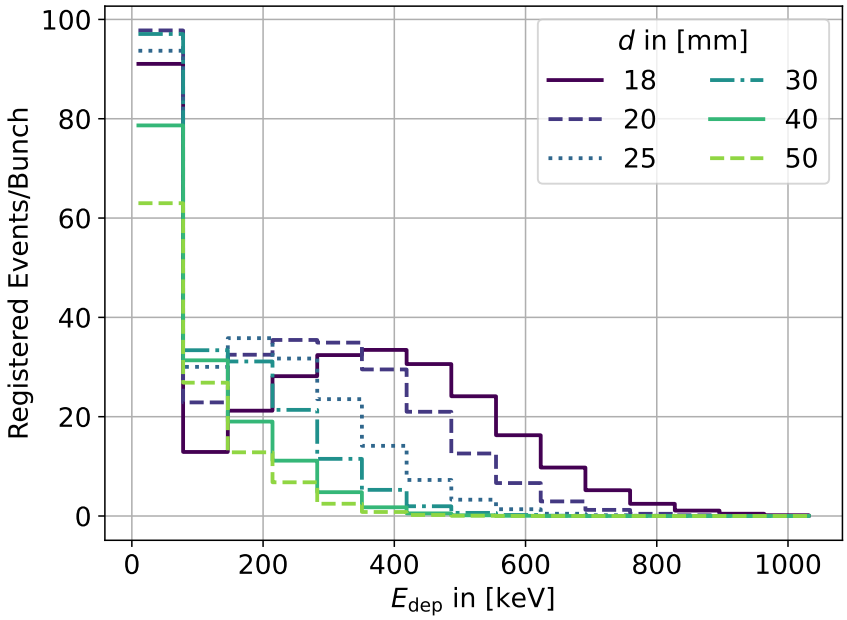

(a) Large Pixels

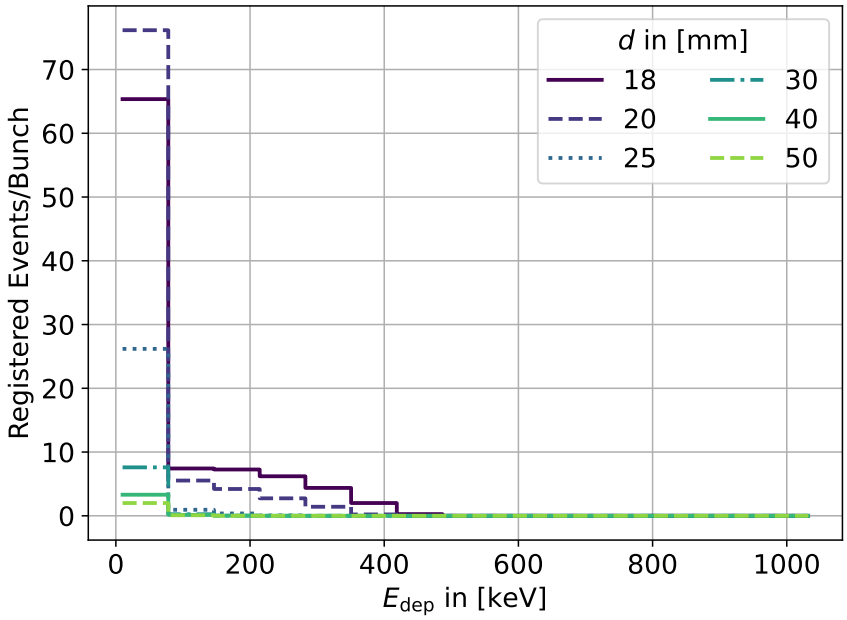

(b) Small Pixels

Figure 6.14.: Energy-Binning measurements at different distances d between the primary electron beam and Dosepix for a bunch charge of 12.5 pC and 87 s of data taking. a) shows the results for the large pixels, b) shows the results for the small pixels.

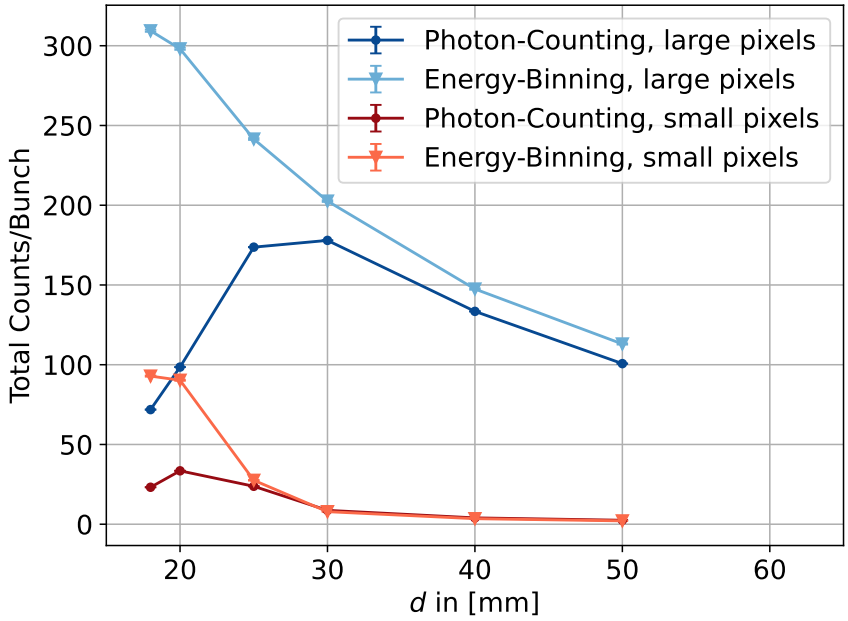

Figure 6.15.: Total number of registered events, measured with the photon-counting mode and with the energy-binning mode for large and small pixels with respect to the distance between the centre of the electron beam and Dosepix d.

Integration Mode: The last data-taking method of Dosepix records the integrated ToT, called $iToT$, of each pixel for a set amount of time. Therefore, there is no information about individual energy depositions, but only about an approximate expression of the integrated deposited energy. On the other hand, this makes the integration mode less susceptible to analog pile-up or any effects related to dose rate, while digital pile-up is also basically avoided due to the large $iToT$-register of 24 bits. Thus, integration mode is the best choice for the task of monitoring electron beams with high dose rates and is, therefore, investigated in more detail in the following paragraphs. This is in accordance with the findings from [20]. Measurements are performed at the previously discussed distances d, but also for different bunch charges ranging from 12 pC to 127 pC. If not stated otherwise, all measurements are performed via 10 read-out frames with an individual length of 20 s. Although this is much longer than typical FLASH treatment times (see subsection 2.5.2), the longer measurement durations are chosen to acquire proper statistics for the presented first evaluations. Histograms of the measured $iToT$, summed over all frames, are shown in Figure 6.16 for the large pixels and in Figure 6.17 for the small pixels. Smaller distances and higher bunch charges result in larger average $iToT$ and larger spread of the values. Especially for $d = 18$ mm and $d = 20$ mm in the case of higher bunch charges ≥ 50 pC, the increased $iToT$ spread results in a loss of the Gaussian shape. In these extreme scenarios, the different positions of the individual pixels and their distances to the beam start playing a role; thus, the pixels no longer contribute to the distribution in a purely statistical sense. Similar but less pronounced trends are present for the small pixels, too. For them, the measured distributions show significantly larger overlap regions for the individual distances, complicating a reliable beam position estimation from their $iToT$ data. Therefore and because of the large

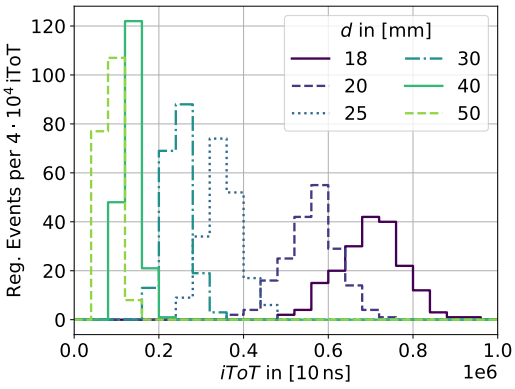

(a) 12 pC

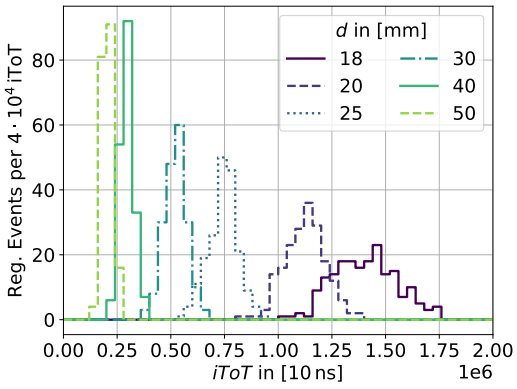

(b) 25 pC

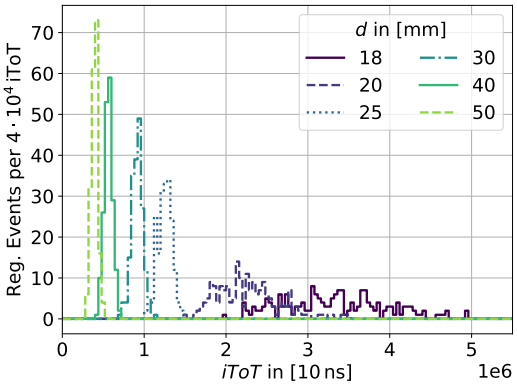

(c) 50 pC

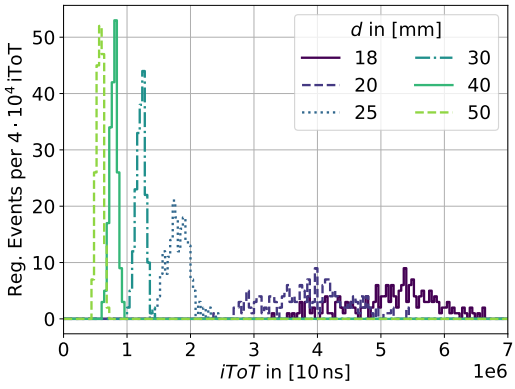

(d) 75 pC

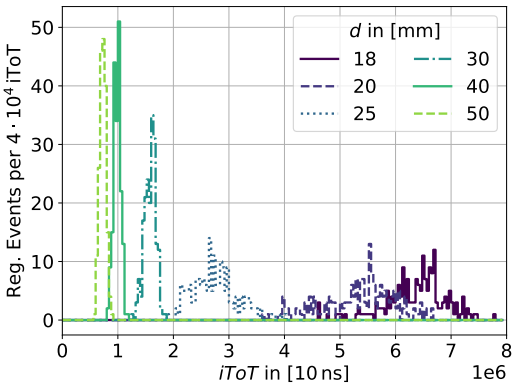

(e) 100 pC

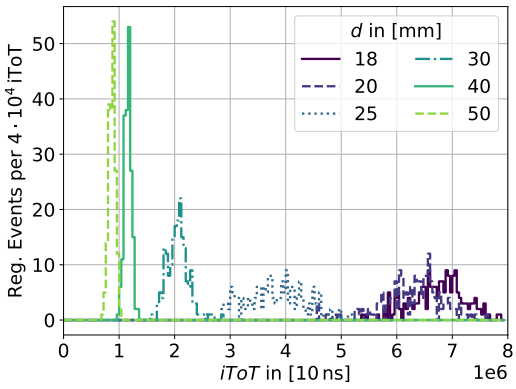

(f) 127 pC

Figure 6.16.: Histograms of the integrated time over threshold $iToT$, summed over all 10 readouts with a total measurement time of 200 s for different bunch charges. The histograms contain the data from the large pixels.

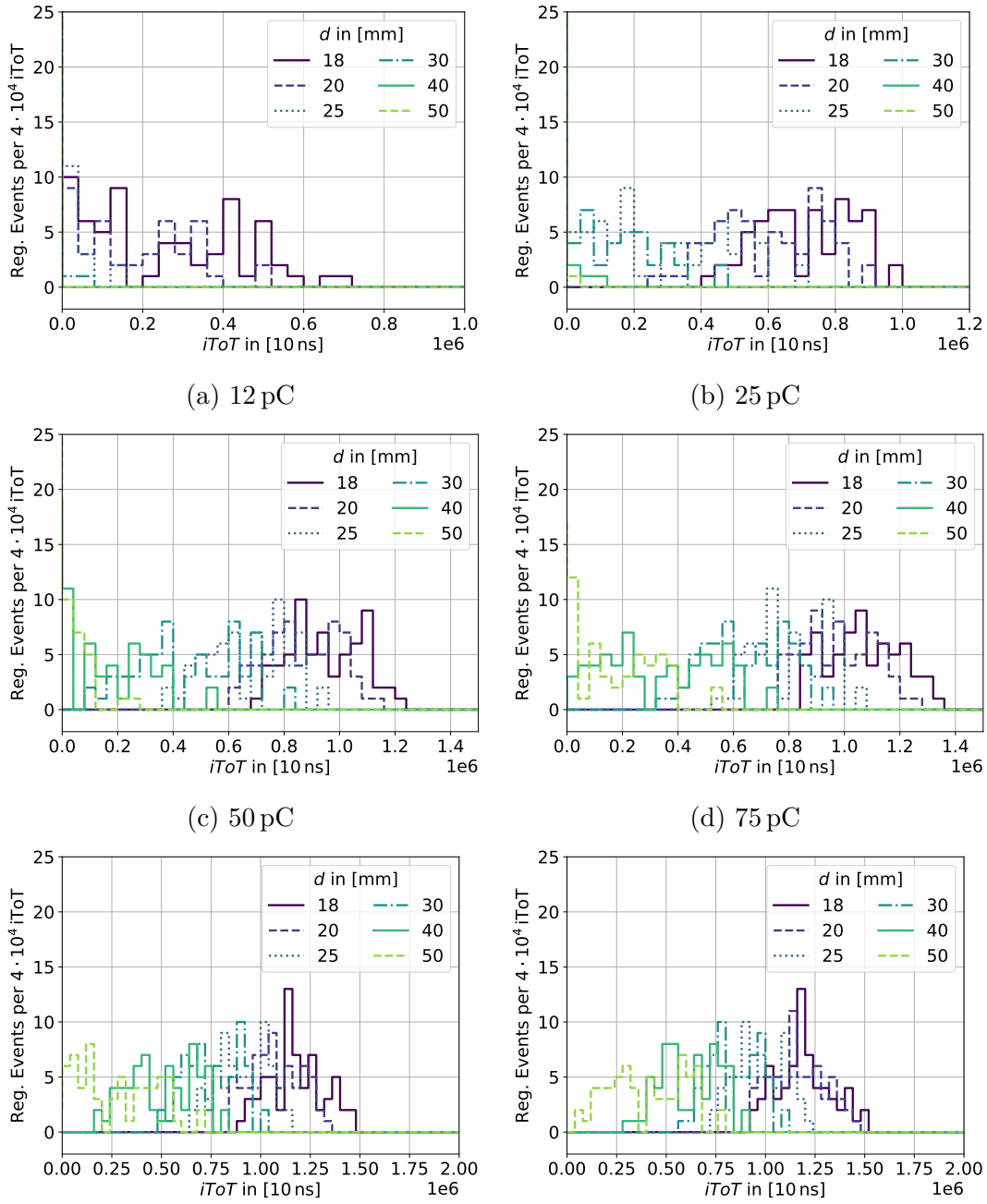

(a) 12 pC (b) 25 pC

(c) 50 pC (d) 75 pC

(e) 100 pC (f) 127 pC

Figure 6.17.: Histograms of the integrated time over threshold $iToT$, summed over all 10 readouts with a total measurement time of 200 s for different bunch charges. The histograms contain the data from the small pixels.

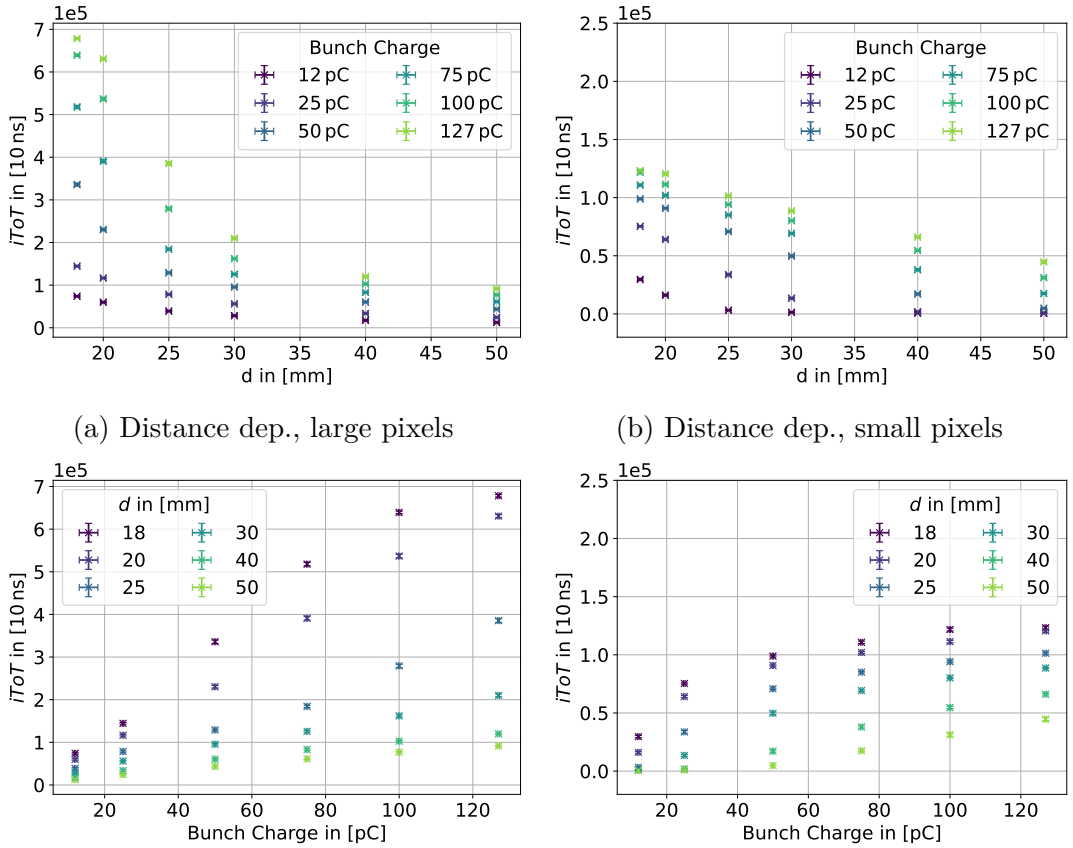

(a) Distance dep., large pixels

(b) Distance dep., small pixels

(c) Bunch charge dep., large pixels

(d) Bunch charge dep., small pixels

Figure 6.18.: $iToT$, averaged over all pixels and over all frames, with respect to distance d and bunch charge for large and small pixels. Figure 6.18a and 6.18c, or Figure 6.18b and 6.18d show the same data with just the x-axis and the legend interchanged. The error bars indicate the standard deviations with respect to the frames, averaged over all pixels.

difference in provided statistics, the large pixels are better suited for a reliable beam monitoring procedure.

The average $iToT$ results for all measurements and both pixel sizes are shown in Figure 6.18 with respect to the distance to the beam d and the bunch charge. A clear trend of increasing $iToT$ with decreasing distance and increasing bunch charge is observed for both pixel sizes. This strictly monotonic behaviour is the foundation of a later beam position reconstruction, since that depends on the inversion of the data in Figure 6.18a. On top of that, the measured signals with respect to the bunch charge show an excellent agreement with a linear behaviour, allowing also a potential bunch charge reconstruction. Merely the measurement under the most extreme conditions with 127 pC bunch charge and a distance of 18 mm shows some saturation effects, demonstrating the robustness of the integration mode concerning signal reconstruction effects related to high dose rates. These results serve as proof of principle for the beam monitoring capabilities with Dosepix detectors, but a quantitative analysis is only possible by taking into account external reference data about the distance, charge, and

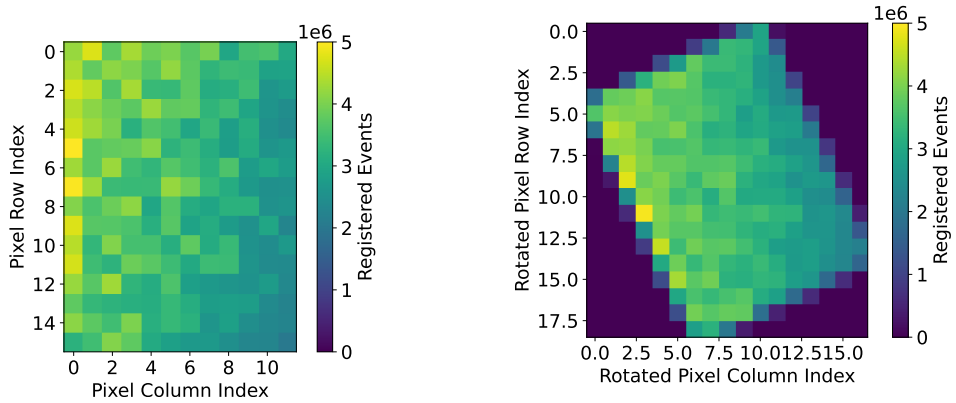

(a) Raw image (b) Rotated image

Figure 6.19.: Pixel matrix of the $iToT$ for the large pixels, summed over 2000 bunches with a charge of 50 pC at a distance of 18 mm. a) shows the raw image and b) the rotated image by 25 °C.

beam width. Such investigations including these reference values are conducted in the succeeding measurement campaign and are presented in subsection 6.3.2.

The statistical uncertainties in Figure 6.18 are estimated via the standard deviation of the signals of each frame. These standard deviations are then averaged over all pixels. This results in very small statistical uncertainties, compared to the absolute $iToT$, of 0.4 % to 8.8 % for the large pixels. Although this is advantageous for beam reconstruction, the precise numbers must be taken with care because these characterization measurements included 2000 bunches, leading to high statistics and, thus, small statistical uncertainties. That value is expected to increase in the case of single-bunch monitoring. Calculating the statistical uncertainty by just determining the standard deviation over all values, i.e., pixels and frames, would overestimate the uncertainty, since systematic influences from pixel deviations and the distance gradient between each pixel and the electron beam would also enter the calculation. This becomes evident when looking at an exemplary pixel matrix of the measurement with 50 pC at 18 mm, shown in Figure 6.19a. There, the signal maximum is - like the beam - on the left side of the detector. However, there is also some offset in the y-direction, due to some imprecision of the beam and Dosepix positions. In order to use the gradient information from the pixel matrices instead of constructing the entire beam monitoring on just one average value, those angular misadjustments must be considered in the analysis. For that purpose and to test its potential advantages, the presented image is rotated by 25°. The rotated image is shown in Figure 6.19b. The angle is determined heuristically to receive effective images, in which rows of pixels correspond to slices, parallel to the radial axis of the beam. From that, the correction angles for the other distances are determined geometrically. After that, the resulting effective pixel columns are projected onto the x-axis, and their summed $iToT$ is plotted with respect to the individual distance of each column. The results are shown in Figure 6.20. Generally, the trends within each pixel matrix align well with the overall trends across the different measurements. However, especially the regions with no strictly monotonic trends at small distances and high charges provide more detailed information on the distance

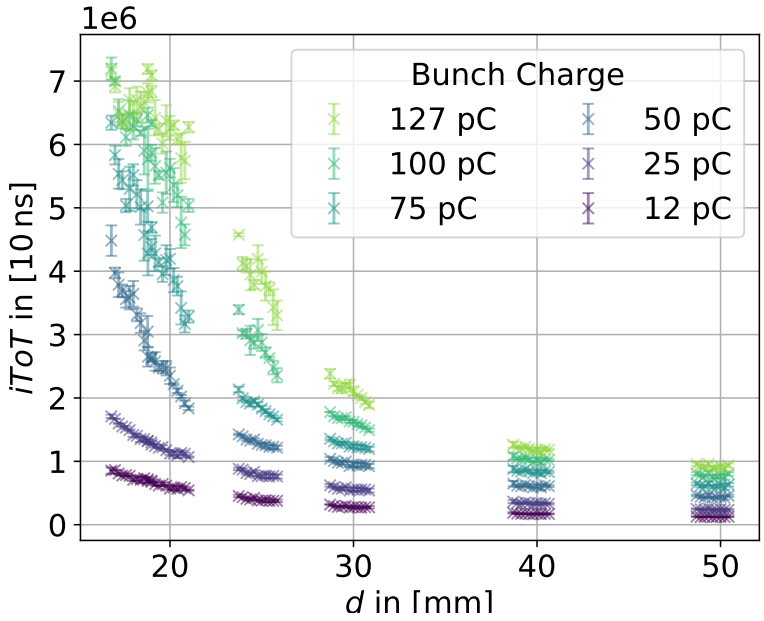

Figure 6.20.: $iToT$ of effective, rotated pixel columns of the large pixels with respect to the distance of each column for different bunch charges.

dependence of the saturation effects. In summary, the level of detail of the information increases when analysing Dosepix data, but no fundamental new insight is gained, and the amount of image processing required to remediate slight beam offsets is not feasible for the final application of in-time beam monitoring.

Lastly, the effect of the set integration time on the $iToT$-results is examined. The parameter space for the tested integration times ranges from 1 s to 20 s. Accordingly, the number of frames is adjusted to match the total data acquisition time of 200 s. Additionally, a measurement of 400 frames with an integration time of 0 s is appended, meaning opening and closing the shutter as quickly as technically possible (90 ms). The results are shown in Figure 6.21. For comparability reasons, the integrated time-over-threshold is normalized with respect to the frame time, yielding $i\dot{T}oT$. All data sets with equal total data acquisition time show the same results without significant deviations except for a small systematic offset for the data with 20 s of frame time, but that offset is attributed to an intensity drop of the ARES accelerator. Instabilities of the accelerator machine during those measurements are also most likely the reason for the slightly larger statistical uncertainties, compared to other results, presented in this chapter. Furthermore, the statistical uncertainty decreases with larger integration times, because the data show the standard deviation, not the mean error. The $i\dot{T}oT$ of the 0 s measurements are, as expected, much lower but still match the overall trends. Their standard deviations are comparatively high, resulting from the readout time being smaller than the repetition rate of the bunches. Therefore, there are entire readout cycles with and without irradiation. Nonetheless, real-time beam monitoring seems possible with short integration times. Still, characterization measurements and first evaluations may be conducted with higher integration times to benefit from better statistics, but remain applicable to the later case of short readout cycles.

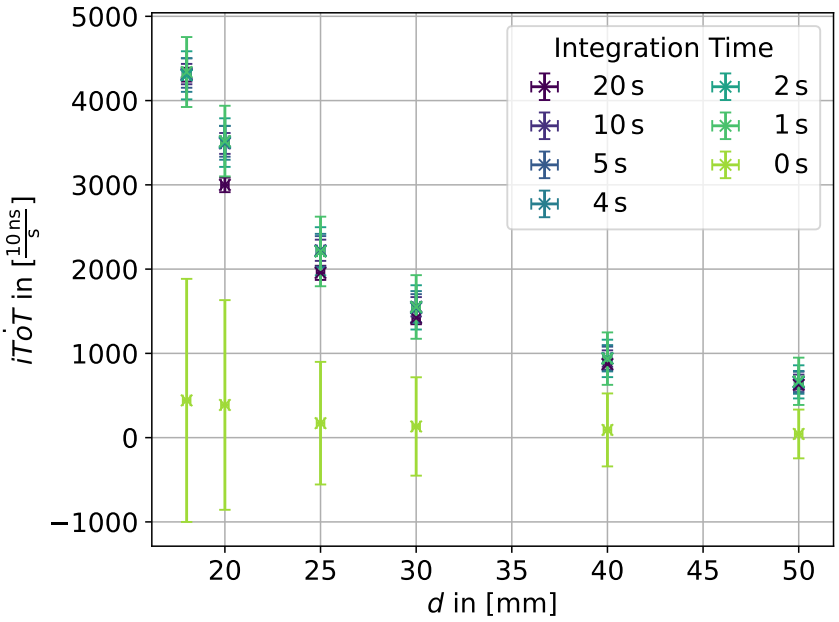

(a) Large pixels

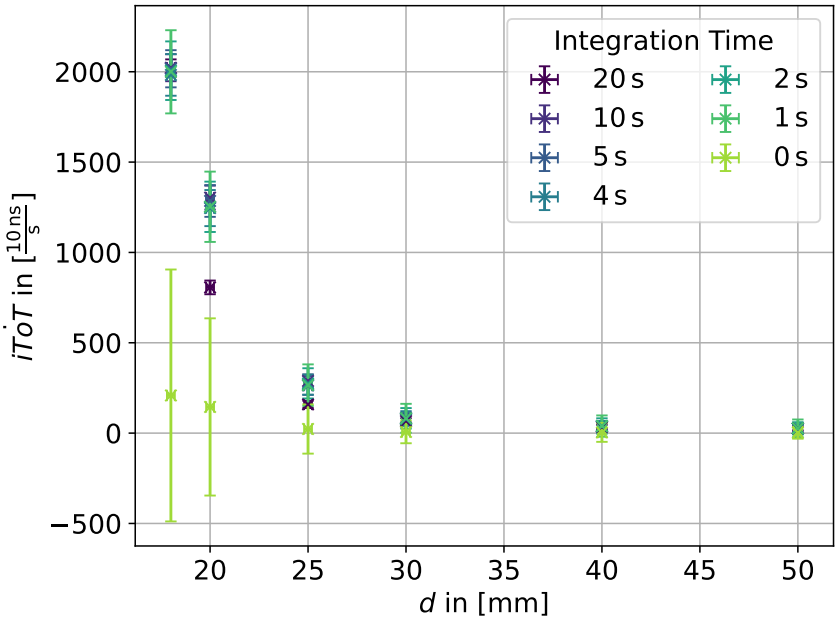

(b) Small pixels

Figure 6.21.: Average $i\dot{T}oT$ with respect to the distance between Dosepix and the electron beam d for different integration times per frame, but a fixed data acquisition time of 200 s, except for the measurement with 0 s. (a) shows the results for the large pixels, (b) the results for the small pixels.

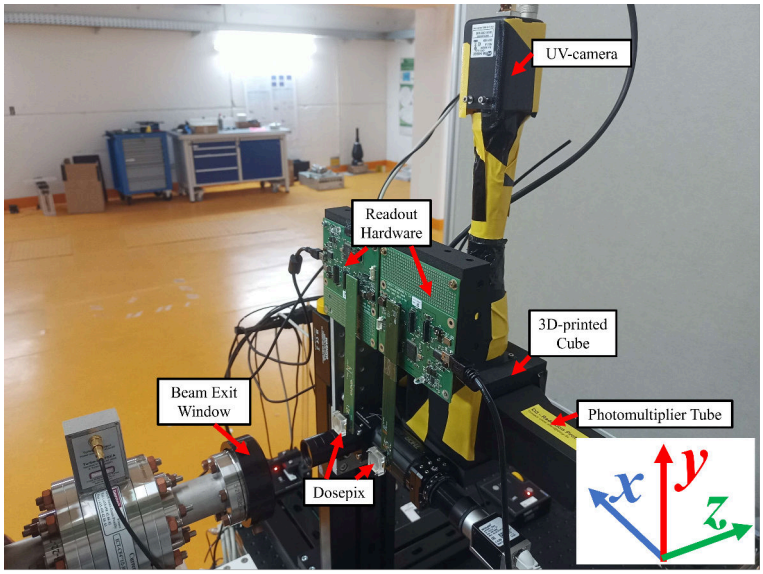

Figure 6.22.: Setup for the measurements of the second experiment at ARES. Two Dosepix detectors are separated by 5.8 cm (center to center) while the electron beam traverses the air between them at the same height. A 3D-printed cube with a UV-camera, PMT, and LED is positioned behind it and is used for the camera measurements, presented in section 6.4.

To summarize, the first measurement campaign, using one Dosepix detector to measure the scattered radiation of the ARES electron beam, yields promising results in terms of detector characterization and the intended application of beam monitoring. Invertible relations of the measured $iToT$ with respect to distance and bunch charge serve as proof-of-concept for the possibility of determining those parameters from measurements. However, only Dosepix's integration mode proves suitable for the intended use case, as all other modes cannot handle such high dose rates and fast readouts.

6.3.2. Extension to two Detectors

The pioneer measurement campaign of December 2024 is succeeded by the next set of measurements at the electron accelerator facility ARES in June and July 2025. This time, the beam monitoring system, described in subsection 6.3.1, is used to determine the position and the width of the beam. Developing a reconstruction procedure of the three main beam parameters (position, width, and bunch charge) is possible because reference detectors track all parameters independently during this beamtime. Also, a second Dosepix detector is added to the setup, taking one step towards the final combined setup, proposed for NitroFLASH (see section 6.2). The adjusted setup is shown in Figure 6.22. The Dosepix detectors are connected to two read-out boards to achieve a distance between the detectors of 5.8 cm while hardware extensions again physically separate the detectors from the controlling electronics. A black 3D-printed cube is positioned behind the Dosepix detectors for the first measurements, as will be explained later. That cube is attached to all components necessary for the nitrogen fluorescence measurements, presented in section 6.4.

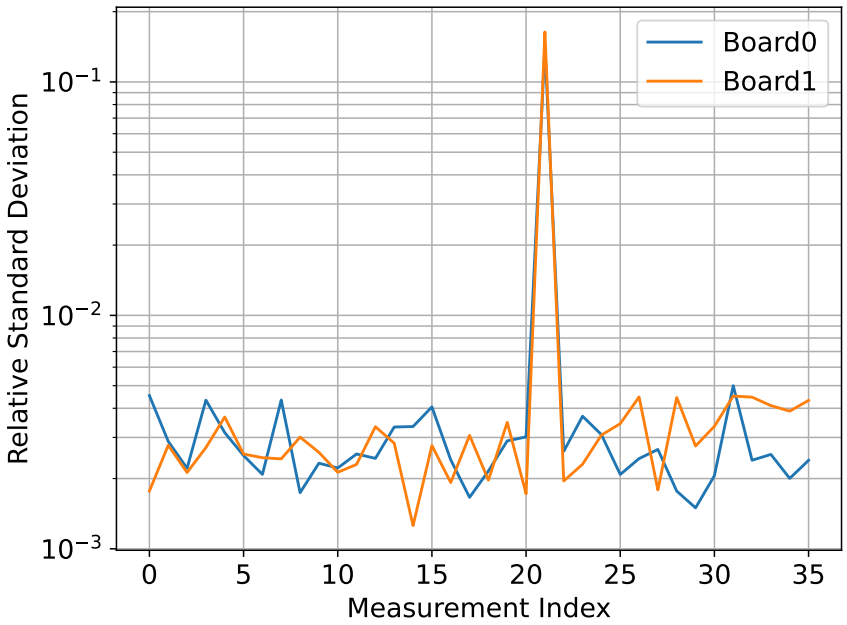

Figure 6.23.: Relative standard deviations for various positions in x- and y-direction with a bunch charge of 127 pC. An intermediate failure of the accelerator led to the large outlier at measurement 21.

Initially, the two Dosepix detectors are compared in terms of their statistical uncertainties because previous studies witnessed systematic differences between individual Dosepix detectors [85]. That determination utilizes data from 35 integration mode measurements, performed at various x- and y-positions with both coordinates reaching from -15 mm to 15 mm, while the coordinate (0,0) refers to the beam at the exact center and at the same height between both detectors. All measurements comprise 10 frames à 20 s of integration time and a bunch charge of 127 pC. Thereafter, the standard deviation of each pixel with respect to the frames is calculated and then averaged for both detectors. Figure 6.23 shows the relative standard deviation, normalized to the respective mean. Measurement 21 marks a large outlier that is caused by an intermediate failure of the ARES machine. All other relative standard deviations show decent stability and do not differ between the detectors. Hence, the statistical uncertainty of the subsequent measurements is approximately assumed to equal 0.3 %. Yet, other influences, especially due to inconsistencies of the accelerator, may cause larger deviations and uncertainties in individual measurements.

Another potential influence quantity is given by the aforementioned 3D-printed cube and its attachments. Its position in the close vicinity of the Dosepix detectors might affect the results due to backscattered events from the cube. This information is relevant to the project's further proceedings, specifically when the different components will be merged into a single prototype. For that purpose, measurements at different x-positions with a bunch charge of 127 pC are performed with and without the cube. In this and all following measurements, the two detector systems consisting of a Dosepix detector and its readout hardware are called "Board0" and "Board1". When referring to positions, it means the position of the whole detector system with respect to the electron beam,

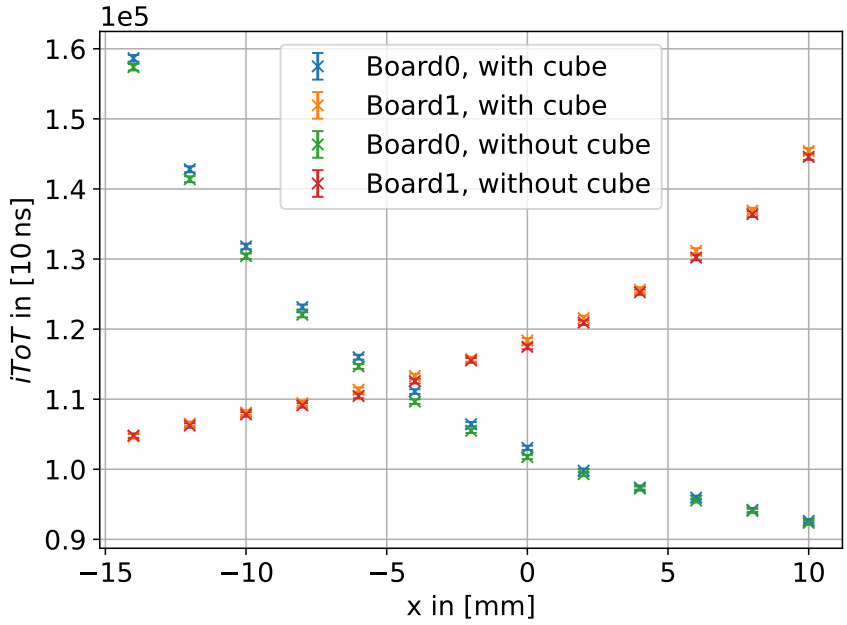

Figure 6.24.: Average $iToT$ with respect to the x-position for both Dosepix detectors with and without the camera setup behind the detectors.

or, in the case of the z-coordinate, the exit window of the accelerator. In contrast, the distance parameter d refers to the distance between the electron beam and the Dosepix detector of Board0. Figure 6.24 shows the average $iToT$ for different x-positions with and without the cube. Several aspects stand out. While the overall trend of position dependence remains distinctive, a clear asymmetry has emerged between the two detector systems. Especially, the crossing point of equal $iToT$ is distinctive of the geometric midpoint. This is likely caused by scattering asymmetries due to the surroundings of the setup, i.e., the linear stages, and systematic calibration differences of the individual Dosepix detectors, which have been known from previous Dosepix studies in dosimetry [10]. Such detector-related differences must be addressed by either taking them into account in the beam monitoring algorithm or by an intercalibration procedure of each Dosepix before its operation. The former is done for the analysis, presented in this thesis, yet it may turn out to be too cumbersome for a final product. On the other hand, the intercalibration would have to be performed under completely interchangeable conditions in the final radiation field to eliminate any other influences on the signal. The other aspect revolves around the influence of the cube. Both detectors acquire a slightly higher $iToT$ with the cube present, with ratios ≤ 1.015. Although this is a small effect, it nevertheless exceeds the measured statistical uncertainty. Furthermore, an unofficial limit of the dose resolution for dose monitoring systems in radiation therapy environments suggests a dose uncertainty of $\leq 1\,\%$ in order to comply with the official overall uncertainty limit of an entire radiation therapy procedure of $\leq 5\,\%$, stated in [160]. Therefore, the influence of the surroundings on the measured signals due to additional scattering contributions must not be ignored. For the remaining work of this study, the cube and its attachments are removed for the Dosepix measurements.

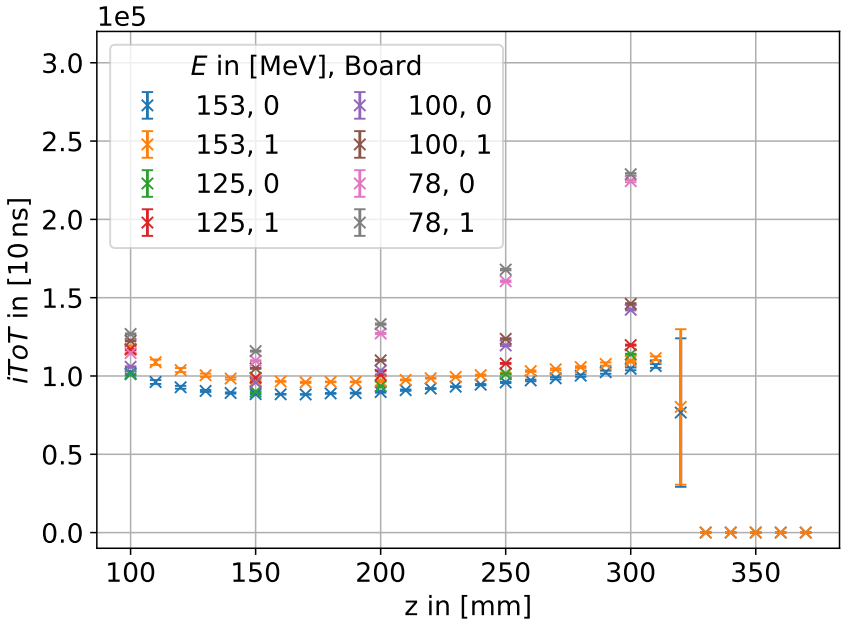

Figure 6.25.: z-dependence of the $iToT$, measured for both Dosepix detectors, for different electron energies E, indicated by the legend. The drop of the $iToT$ for 153 MeV at 32 cm is due to a complete failure of the accelerator.

The measured signal of the beam is also expected to be influenced by the z-position of the measurement and the kinetic energy of the electron. Therefore, both quantities are examined by taking measurements with energies of $E = 153\,\text{MeV}$, 125 MeV, 100 MeV, and 78 MeV at different z-positions parallel to the primary beam axis between 10 cm and 38 cm. A longer time window is available for the measurements of ARES' standard electron energy 153 MeV, thus, this scan is conducted with denser increments. There, each z is measured for 30 min with a frame time of 120 s. For the other energies, the standard procedure consisting of 10 frames with 20 s of integration time each, is conducted. The results are depicted in Figure 6.25. Unfortunately, the ARES accelerator crashed during the last measurements with $E = 153\,\text{MeV}$, and no meaningful data could be recorded for $z \geq 32\,\text{cm}$. All energies show a U-shaped behaviour with a global minimum at about 180 mm, yet the actual the beam waist is set to $z = 100\,\text{mm}$. This contrast originates from the method of measuring the beam via its scattered radiation. The majority of scattering happens at smaller angles; therefore, the signal at a certain position mostly contains information about the beam at upstream positions. Smaller energies lead to a stronger expansion of the beam, which is in accordance with the simulations, presented in section 6.2. The electron energy of PITZ is 22 MeV [81], which is even significantly lower than the lowest achievable energies at ARES, thus the beam expansion at PITZ is expected to prevail even more. As a consequence, the final prototype should be installed as close to the exit window as possible and should also be narrow, because, in order to use the beam for radiation treatment, the path length of the electrons through air should be minimal. Alternatively, the setup could be modified to operate in a low-pressure environment to reduce scattering, but that would also reduce

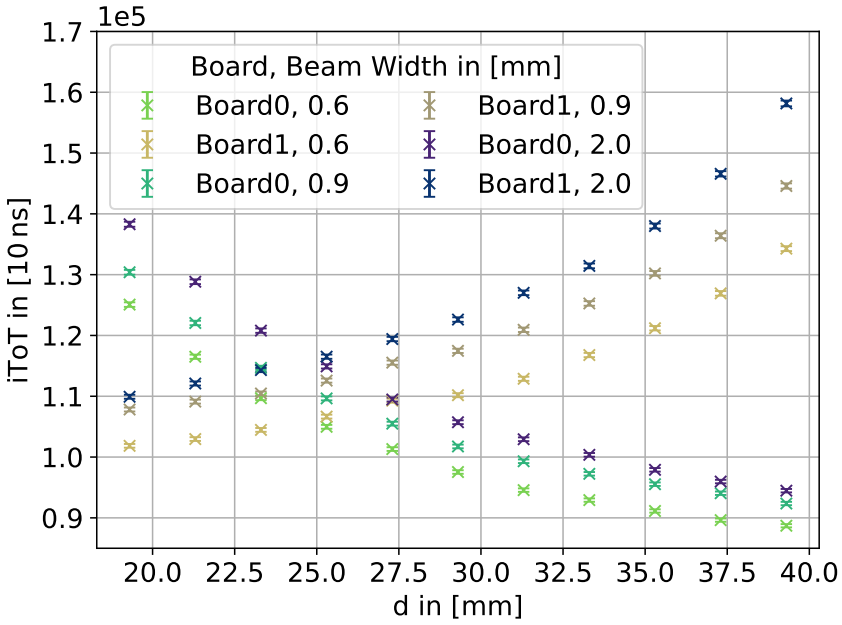

Figure 6.26.: Average $iToT$, measured for different distances d between the beam and Board0 and different beam widths, indicated in the legend by their HWHM.

the signal strength for the Dosepix measurements and the nitrogen fluorescence yield for the UV-camera measurements, as well as induce additional engineering challenges.

Ultimately, a beam monitoring method has to take into account several influencing quantities. The procedure, presented in the following, focuses on the beam position in x-direction and the beam width for an electron energy of 153 MeV and bunch charges of 127 pC. Figure 6.26 shows the underlying data for the reconstruction. There are $iToT(d)$-curves, as shown before, for both detectors. This time, the raw x-position is translated into the distance d, which always refers to Board0 and the beam. The two Dosepix detectors themselves are located 5.8 cm apart. The goal of this investigation was to establish and solve a set of equations for the distance d in x-direction between the electron beam and the Dosepix detector of Board0, which is translatable into an absolute x-position if the positions of the detectors are well-known, and the beam width w. Both quantities should depend only on the signals from both Dosepix detectors $iToT_0$ and $iToT_1$, i.e., the wanted equations are:

$$\begin{aligned} w &= w\left(iToT_0, iToT_1\right), \\ d &= d\left(w,\, iToT_0, iToT_1\right). \end{aligned} \tag{6.3}$$

As a first step, this procedure depends on the inversion of the curves from Figure 6.26 to receive relations d and $iToT_i, i \in \{0, 1\}$ for different w. Figure 6.27 shows the same data as before, but with interchanged axes. These trends shall be quantified for each detector and beam width. which is achieved by adjusting proper functions to the data via a Levenberg-Marquardt fit of the Python package *scipy.optimize* [141]. A superposition of $\frac{1}{iToT}$ and $\frac{1}{\sqrt{iToT}}$ contributions would be expected, since the fundamental distance dependence consists of $\frac{1}{d}$ and $\frac{1}{d^2}$ contributions, as discussed in subsection 6.2.3. In

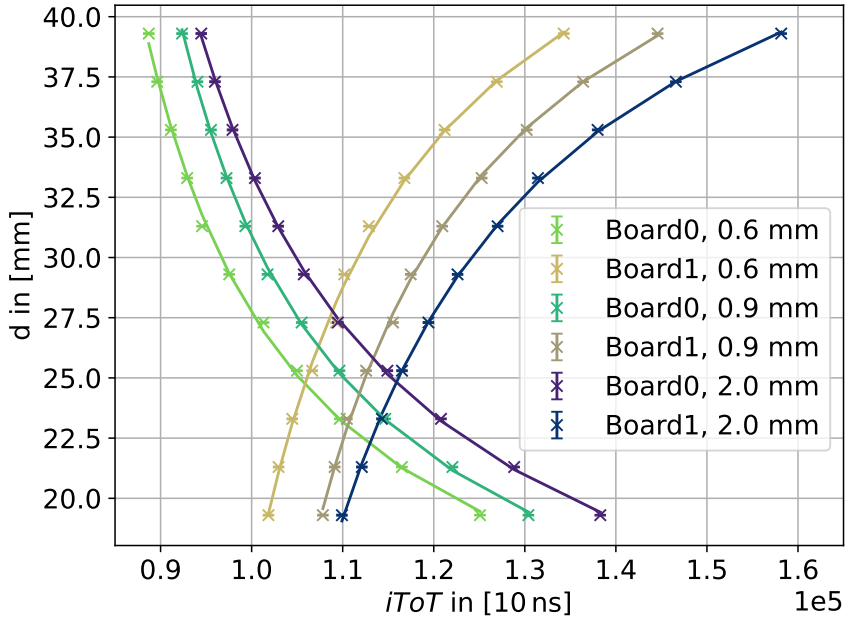

Figure 6.27.: Inversion of the data, shown in Figure 6.26, as well as reciprocal fits to the data of each detector and width.

order to simplify the following calculations, a pure $\frac{1}{d}$ is utilized as an approximation. Therefore, the fitted functions are of the shape

$$\begin{aligned} d\,(iToT_0) &= \tfrac{a_0}{iToT_0 - b_0} + c_0, \\ d\,(iToT_1) &= \tfrac{a_1}{b_1 - iToT_1} + c_1 \end{aligned} \tag{6.4}$$

with fit parameters a_i, b_i, and c_i, $i \in \{0, 1\}$. The adjusted functions are also shown in Figure 6.27. This yields two expressions for d, depending on which detector is referred to. Yet, each fit is still only valid for that specific beam width. In order to combine all the fits into one equation, the constant parameters a_i, b_i, and c_i are replaced by width-dependent functions $a_i(w)$, $b_i(w)$, and $c_i(w)$. For that purpose, all fit results are put in relation to their corresponding beam widths w, which is depicted in Figure 6.28. It is obvious that the three available data points per parameter are too sparse to meaningfully extract higher-level relations between the parameters and the beam width. For future investigations, more data curves at various beam widths are paramount to improve the model. The available data only suffice to adjust affine-linear relations. Whereas a and c seem to approximately follow such a trend, b shows no systematic behaviour. Thus, it is approximated by just its mean value for each detector. If not for the outlier at $w = 0.9\,\mathrm{mm}$, a constant behaviour might fit the data. During those specific measurements at $w = 0.9\,\mathrm{mm}$, the external beam width determination process was flawed, leading to a potential systematic error that might affect the results. Conclusively, the quantities are parametrized by

$$a_i = \alpha_i \cdot w + \beta_i,\ b_i = \overline{b_i},\ c_i = \gamma_i \cdot w + \delta_i \tag{6.5}$$

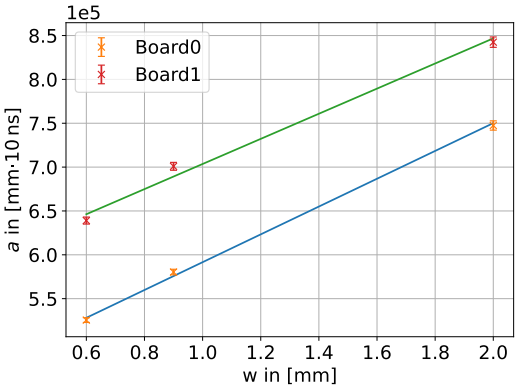

(a) Parameter a

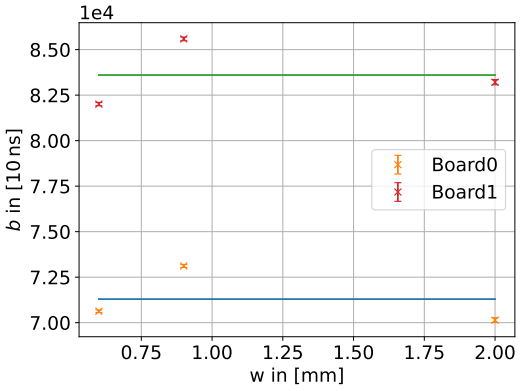

(b) Parameter b

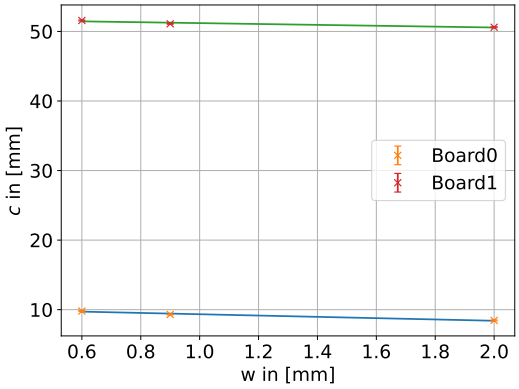

(c) Parameter c

Figure 6.28.: Results of the reciprocal fits of Equation 6.4, presented in Figure 6.27 for the three parameters a, b, and c with respect to the beam width w. The error bars represent the respective fit uncertainties.

Parameter	α in [10 ns]	β in [mm·10 ns]	b in [10 ns]
Board0	$(159 \pm 5) \cdot 10^3$	$(433 \pm 5) \cdot 10^3$	71294 ± 26
Board1	$(143 \pm 6) \cdot 10^3$	$(460 \pm 6) \cdot 10^3$	83603 ± 22
Parameter	γ in [1]	δ in [mm]	
Board0	-0.94 ± 0.06	10.28 ± 0.07	
Board1	-0.63 ± 0.07	51.83 ± 0.09	

Table 6.2.: Final values and fit uncertainties for the parameters, adjusted according to Equation 6.5 to the data, shown in Figure 6.28.

χ^2_{red}	a	b	c
Board0	1.6	672.7	6.0
Board1	5.3	679.7	5.4

Table 6.3.: Reduced χ^2_{red} results for the parameter fits, shown in Figure 6.28 for both detectors.

with the new parameters α_i, β_i, γ_i, and δ_i. The resulting parameters are listed in Table 6.2 and their corresponding graphs drawn in Figure 6.28. Additionally, Table 6.3 lists the reduced χ^2_{red} results of the fits. None of the models seems to correctly estimate the given data because none of the χ^2_{red} results is close to 1. However, there is still a large difference between the modeling of b, compared to a and c, which, at least, approximately represent the data points. Also, the symmetries in terms of the slopes α_i and γ_i hint at a basic quality of the utilized models.

Inserting Equation 6.5 into Equation 6.4 yields two functions for $d\,(w,\, iToT_i)$ corresponding to the two detectors. As an intermediate validation of the entire monitoring algorithm, those expressions for d are compared to the initial data, shown in Figure 6.27. That comparison is shown in Figure 6.29. The models reflect the main features of the data. Distinct differences between the model and the data are primarily induced by a shift in the $iToT$-direction, the most prevalent for the data with $w = 0.9\,\text{mm}$. This is a direct consequence of the low precision for the parameter b, as that represents the shift in that direction, highlighting again the importance of further measurements for different beam widths to refine the model. Nevertheless, the presented procedure is able to recreate the data apart from this systematic uncertainty and can function as a basis for beam monitoring.

Until this point, a system of two equations $d\,(iToT_0, w)$ and $d\,(iToT_1, w)$ exists. These equations are solved algebraically for the wanted equation $w\,(iToT_0, iToT_1)$, resulting after some calculation in:

$$w\,(iToT_0,\, iToT_1) = \frac{\frac{\beta_1}{b_1 - iToT_1} - \frac{\beta_0}{iToT_0 - b_0} + \delta_1 - \delta_0}{\frac{\alpha_0}{iToT_0 - b_0} - \frac{\alpha_1}{b_1 - iToT_1} + \gamma_0 - \gamma_1}. \tag{6.6}$$

If w is known, d is determined from Equations 6.4 and 6.5. The uncertainties are determined from the uncertainties of $iToT$ and the function parameters via Gaussian error propagation. This set of equations is validated first by applying it again to the initial data. The corresponding results are depicted in Figure 6.30 for w and in Figure 6.31 for d and the residuals in Figure 6.32. Especially, the results for the beam

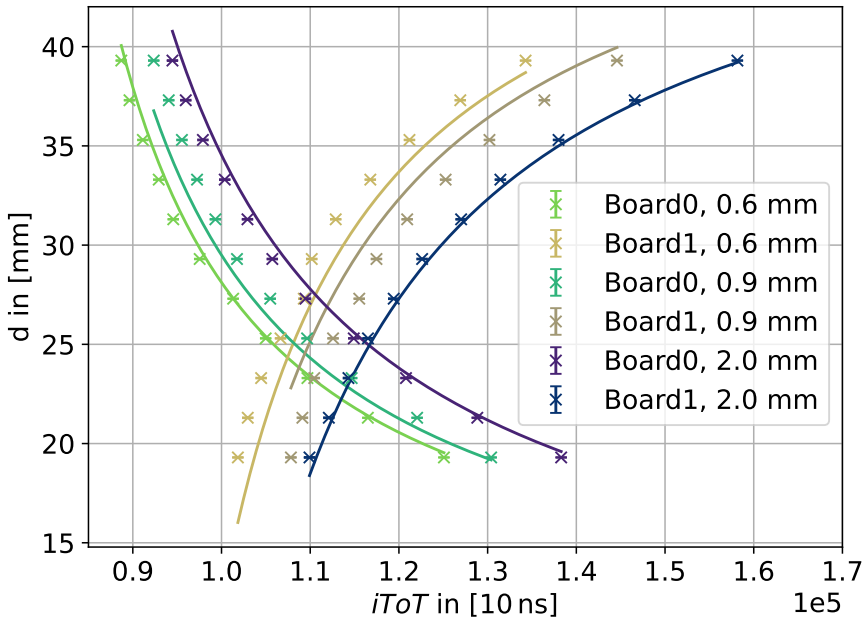

Figure 6.29.: Distance between the Dosepix detector of Board0 and the electron beam d with respect to the measured $iToT$ of each Dosepix. The crosses indicate measured data while the solid lines represent the models according to Equations 6.4 and refeq:NitroDpxSecondOrderFits.

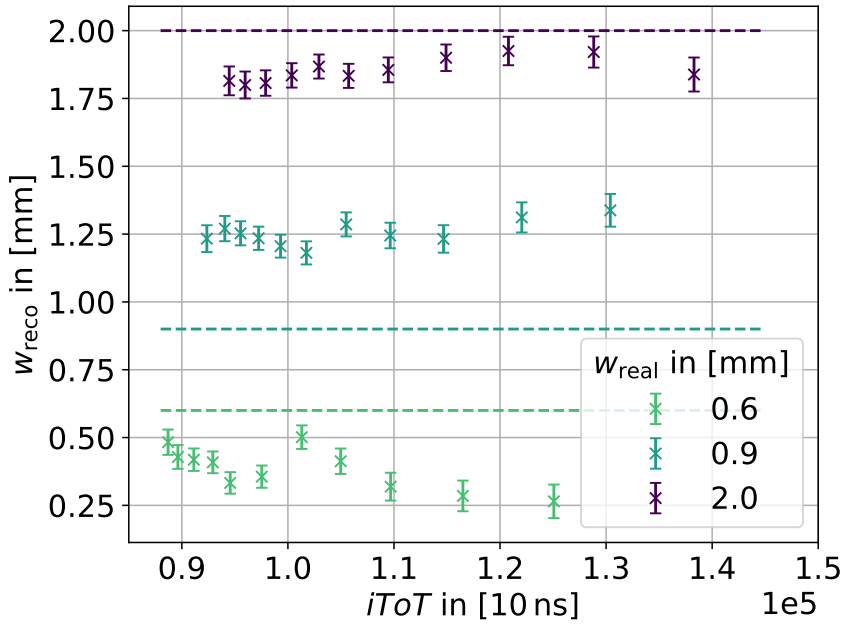

Figure 6.30.: Reconstructed beam width w_{reco} with respect to $iToT$, measured by the Dosepix detector of Board0. The crosses mark the reconstructed values from Equation 6.6 while the dashed lines indicate the reference values, extracted from the ARES beam diagnostics.

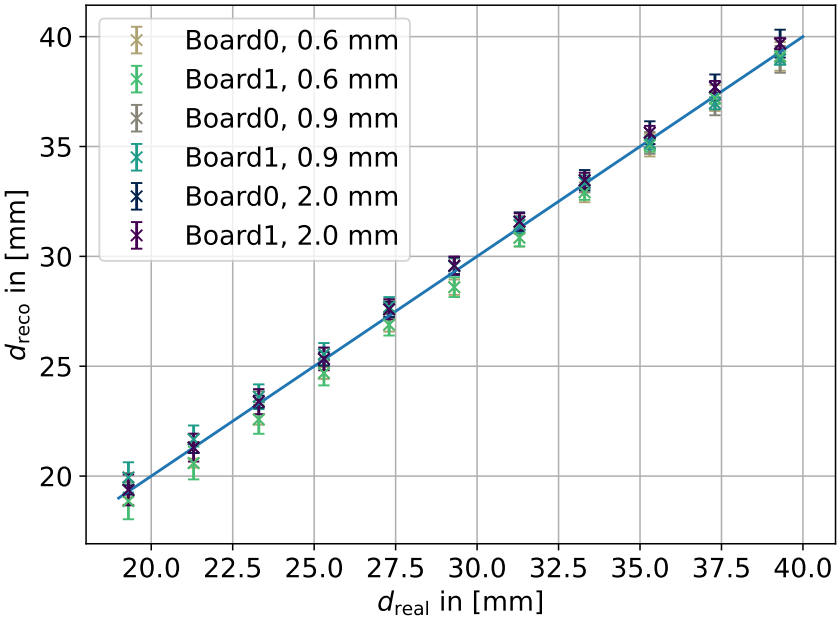

Figure 6.31.: Reconstructed distance d_{reco} between the electron beam and the Dosepix detector of Board0 with respect to the reference value d_{real}, acquired from the ARES beam diagnostics. The straight blue line marks the identity function, i.e., perfect distance reconstruction.

width w show significant systematic deviations from the reference values of up to 60 %. This is expected as a result of the previously observed systematic uncertainties of the method. The values for $w_{real} = 0.9\,\text{mm}$ stand out as the only data set to overestimate the actual beam width. It also comes with the largest absolute systematic deviations. In general, there is a clear link between the quality of the model describing each data set in Figure 6.29 and the ability to reconstruct the beam width. Although the reconstruction of d depends on the flawed results w, the results for the beam position better match the reference values. Most reconstructed values agree with the real distance, with the absolute residuals almost consistently $< 5\,\%$. In absolute numbers, this corresponds to errors in the position determination of $\leq 0.7\,\text{mm}$. In comparison, radiation therapy typically works with a spatial precision of about 1 mm [148]. Therefore, the achieved resolution is already promising but improving the accuracy would still benefit a potential radiation therapy procedure.

6.3.3. Model Validation

Nonetheless, the practical quality of the model must be evaluated via its predictive power on a distinct set of data that had not been used for its development. The measurements for that purpose were performed in August 2025 with the same method and setup, as described in subsection 6.3.2. The same two Dosepix detectors on the same readout hardware took data for 200 s at four different x-positions. Again, an electron energy of 153 MeV and a bunch charge of 127 pC are chosen. However, those measurements can only be used for a basic sanity check because the external beam

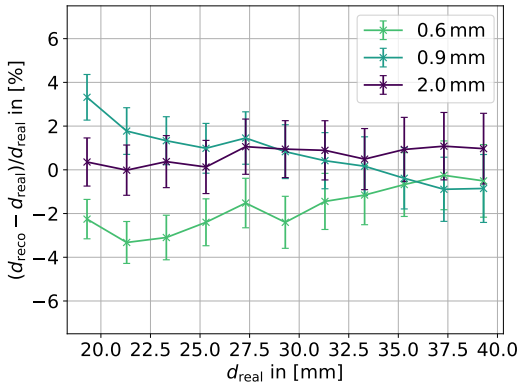

(a) Beam position, Board0

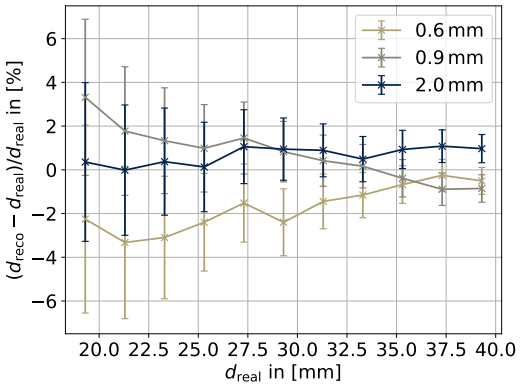

(b) Beam position, Board1

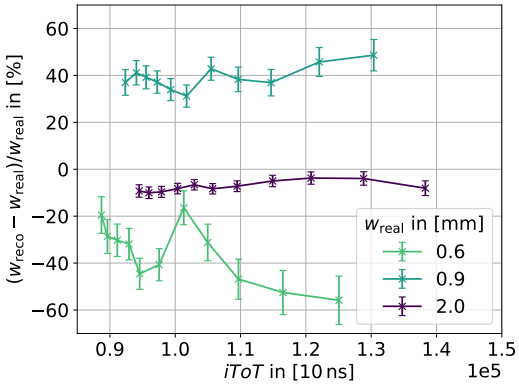

(c) Beam width

Figure 6.32.: Residuals of the reconstructed distance d_{reco} and the beam width w, corresponding to the data of Figure 6.30 and 6.31.

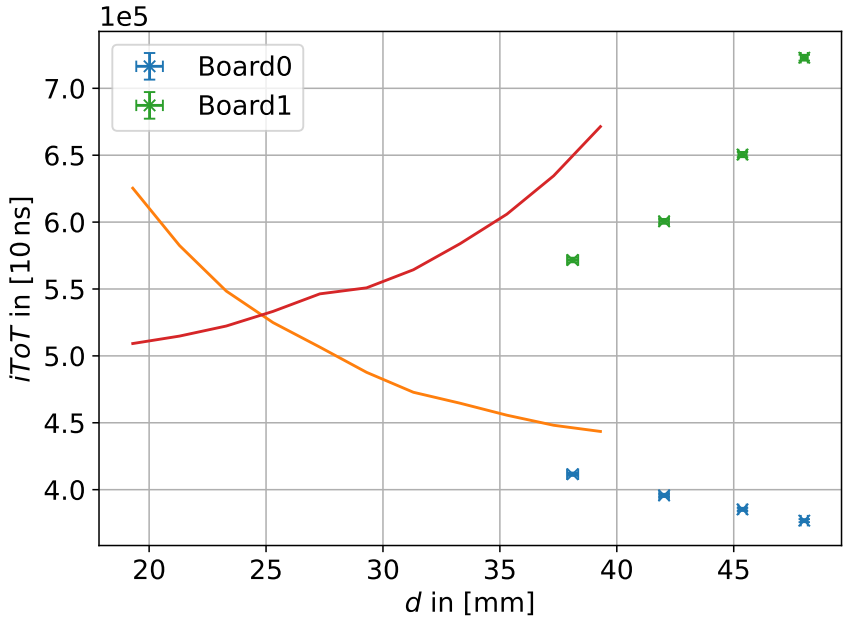

Figure 6.33.: Measured $iToT$ with respect to the reconstructed distance between the electron beam and the Dosepix detector of Board0. The red and orange lines represent the fit data for $w = 0.6\,\text{mm}$, shown in Figure 6.26.

monitoring system of ARES did not function properly, leading to an unreliable reference width and position. The beam width is approximately determined to equal about $w_{\text{real}} = (1.0 \pm 0.2)\,\text{mm}$, while the absolute distance could not be extracted due to an unknown absolute shift of the linear stage position. Only the step size between the four performed measurements is known to equal 2.0 mm. The reconstruction of the width results in a value of $w = (-1.3 \pm 0.4)\,\text{mm}$, which is unphysical, with only its absolute value being in accordance with the reference. The reconstructed distances are shown in Figure 6.33 together with the old fit data, marked as red and orange curves. The data points are ordered in the expected way although the reconstructed differences of the data points are larger than the reference ((3.9 ± 0.4) mm, (3.35 ± 0.28) mm, and (2.64 ± 0.24) mm).

The results indicate that Dosepix detectors measuring the scattered radiation of an electron beam are usable for beam monitoring, in particular, beam position monitoring, but the current model noticeably lacks additional data for defining and validating. Currently, the amount of available data simply does not fulfill the requirements for more sophisticated models that are likely to decrease the systematic reconstruction uncertainties. Also, the presented results show that the system is better at determining positions than widths, while the beam intensity, which is closely linked to the beam width in terms of expected signal strength, has been excluded from the analysis so far. Therefore, the thorough beam monitoring must include the additional information, provided by the UV-fluorescence imaging, presented in section 6.4. Those might specifically perform the beam width determination, as it is naturally received from imaging. That might improve the beam position reconstruction as well as release one degree of freedom in the Dosepix reconstruction usable for bunch charge monitoring.

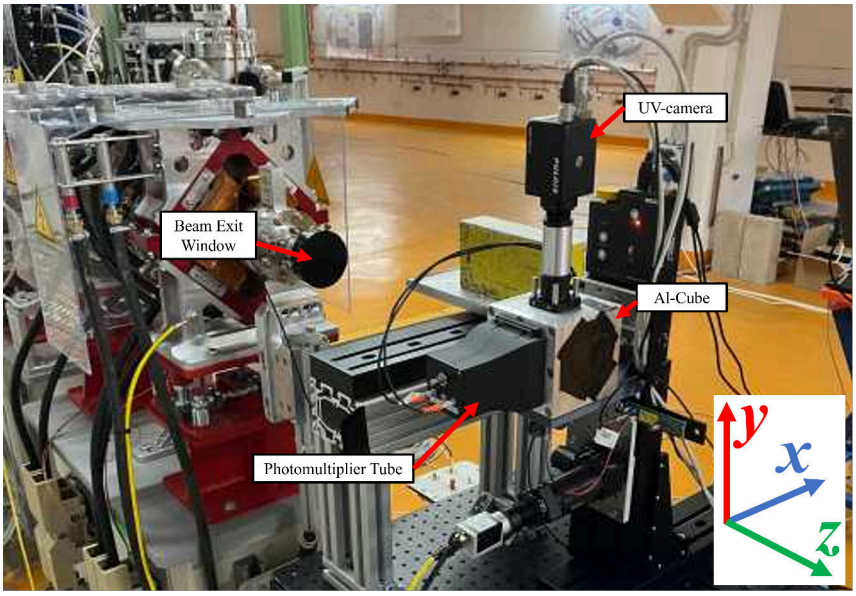

Figure 6.34.: Photograph of the first iteration of the UV-camera setup at the ARES facility. The Jai UV-camera on top is attached to an Al-cube with an outer edge length of 10 cm. The imaging optics is given by one convex lens in front of the camera.

6.4. UV-Camera

The other pillar of the electron beam monitoring process is based on the imaging of the nitrogen fluorescence light, emitted by the electrons as they traverse air. This light enables a direct determination of the position and width of the beam in the imaged plane. As the excitation of the nitrogen molecules by the electrons follows a statistical process, the amount of emitted light should be proportional to the number of electrons, i.e., the bunch charge. Yet, there might also be some intensity-dependent effects due to quenching that may disturb the basic proportionality [151]. Therefore, a system of two cameras surveilling the beam from two axes would be capable of monitoring the 3D-position as well as x- and y-coordinates of the beam while possibly also determining the intensity profile. The following section presents the development of the first two iterations for the UV-fluorescence-imaging setup using different cameras from Jai and Basler. Results for both setups at the electron accelerator facility ARES in Hamburg and the *European X-Ray Free-Electron Laser Facility* (EuXFEL) in Schenefeld are presented.

6.4.1. Simple Imaging Setup

The first experiments are conducted with the camera model Jai TM-1405GE [161] at the ARES electron accelerator facility. A photograph of the first setup is shown in Figure 6.34. The setup is positioned ≈ 50 cm behind the exit window of the accelerator. A hollow cube of aluminum serves as the core element, painted matte black from the inside, minimizing reflection. It has an outer edge length of 10 cm and a wall thickness of 1.25 cm, resulting in an inner volume of 420 ml. The cube is constantly flooded with pure nitrogen at normal pressure to repress oxygen and increase the nitrogen

fluorescence output. Two round ports with a diameter of 20 mm at the front and back of the cube serve as entrance and exit windows for the electron beam. They are covered with kapton foil to shield the inside of the cube from ambient light. Another port with the same diameter is cut in the bottom surface to enable a UV LED to illuminate the cube. The LED is mounted on a custom adapter to keep ambient light out of the cube. A larger port with a diameter of 25 mm is cut in the opposite surface, where the camera and its optics are attached. Lastly, a photomultiplier tube is attached to another port with 25 mm at the side of the cube. In this first iteration, a single convex lens is used to image the emitted light inside the center of the cube. The nitrogen fluorescence spectrum is dominated by UV light with wavelengths between 300 nm and 400 nm [149]. Thus, all optical components must not include standard glass, as this absorbs the UV light. Instead, quartz glass is used as a UV-transmissive material. The utilized lens has a diameter of 25 mm and a focal length of 40 mm [162]. It is positioned at a distance of 1.4 cm behind the outer surface of the cube and 9.7 cm in front of the camera sensor, resulting in a magnification of 1.7. The sensor itself consists of 1392 x 1040 square-shaped pixels with an edge length of 4.65 µm, resulting in a total sensitive area of 6.47 mm x 4.84 mm [161]. All standard glass components have been removed from the camera to enhance its spectral sensitivity into the UV-range.

The camera and the LED are connected to two machine triggers, enabling synchronization with the electron bunches and facilitating a validation of the timing of all devices. The PMT is capable of measuring signals from the LED and from the beam-emerging fluorescence light. This feature is used as a time calibration technique by adjusting the trigger of the LED until it is synchronized with the fluorescence signal. Then, the timing of the camera is modified until light from the LED is perceived, meaning the camera is also timed correctly to detect signals from the beam. An exemplary average image of the LED (1025 individual shots), where it operates with a voltage of 4 V and 100 µs of illumination time, is shown in Figure 6.35. A blurred image of the LED is visible on the right side of the picture because the sharp object plane of the setup is set to the center of the cube, where the beam is expected, while the LED is positioned 3.5 cm behind the center to avoid any interference with the beam. Small mechanical instabilities cause a slight off-center position of the LED. However, the observed effect corresponds to just ≈ 1 mm of shifted field of view in the object plane. Unfortunately, some dirt settled on the lens, leading to image artifacts, especially on the right side of the pixel matrix.

After the correct timing was ensured, images of the ARES beam with an electron energy of 153 MeV and a bunch charge of 117 pC are recorded. 4682 images with an individual illumination time of 30 ms are acquired, each image containing one electron bunch. The average image is shown in Figure 6.36. There is no distinct signal of nitrogen fluorescence light. The only visible structures in the raw image (Figure 6.36a) are broad vertical stripes. An average background image is recorded to investigate whether those structures originate from the beam or from general sensor artifacts. The background-subtracted net signal is shown in Figure 6.36b. The previously observed structures are replaced by smaller signal inconsistencies of individual pixel columns. None of the effects can be attributed to the electron beam. Therefore, only noise is be recorded with this setup.

The most probable hypothesis about the failure of the first iteration of the fluorescence light imaging setup revolves around the too low photon flux per pixel at the sensor

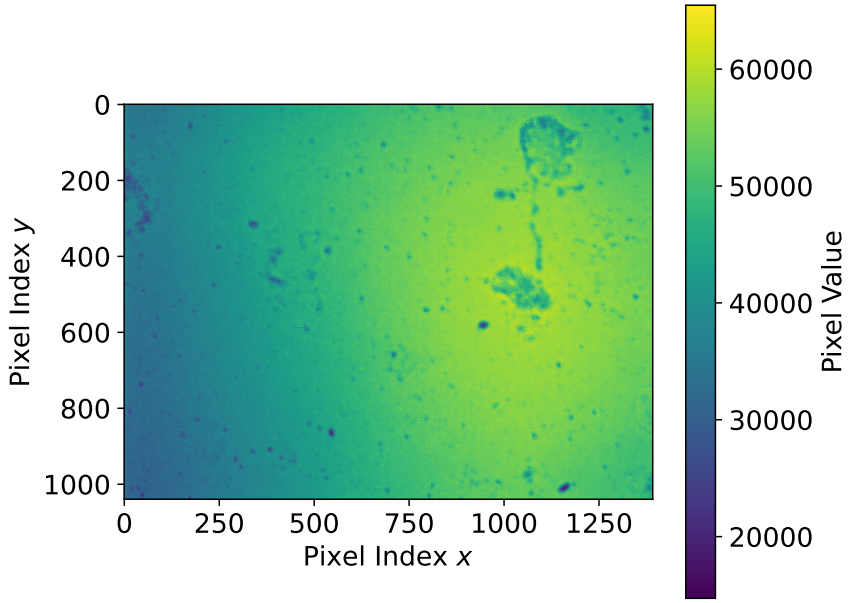

Figure 6.35.: Average over 1025 images, taken by the UV-enhanced Jai 1405 camera, showing the reference LED with a lumination time of 100 µs and an operation voltage of 4 V.

matrix. The order of magnitude of the missing intensity is determined by analyzing the output signal of the reference photomultiplier tube with respect to the LED. The latter is operated with different voltages and duty cycles to produce a set of different integral light outputs. The PMT and the camera then record those signals. Figure 6.37 shows the median pixel value of the camera for the different settings with respect to the integrated PMT signal. The expected linear dependence for stronger signals starts to break down at about $-2\,\mu\mathrm{V\,s}$ to $-1\,\mu\mathrm{V\,s}$, where the camera is no longer sensitive enough to receive a median signal different from the background. In contrast, the PMT signals, induced by the electron beams, are weaker than the breakdown signal of the camera, explaining the absence of the beam in the camera images. A missing sensitivity of the beam of about one order of magnitude may be concluded from the results; however, this estimation may only serve as a lower limit of the actual missing factor because the PMT signal does not exclusively originate from nitrogen fluorescence light, but is also induced by scattered radiation of the electron beam.

In conclusion, a simple setup of a UV-enhanced camera and one convex lens is insufficient to observe the ARES beam via its emitted nitrogen fluorescence light. Therefore, a different camera with native UV-sensitivity is used for the next experiments. Also, a larger lens ensemble with better light collection capabilities is installed.

6.4.2. Characterization of the Advanced 3-Lens Setup

The main objective of the advanced setup is to significantly increase the signal intensity of the camera, which depends on the amount of fluorescence light at the camera sensor and the quantum efficiency of the sensor. As the previously utilized Jai camera is

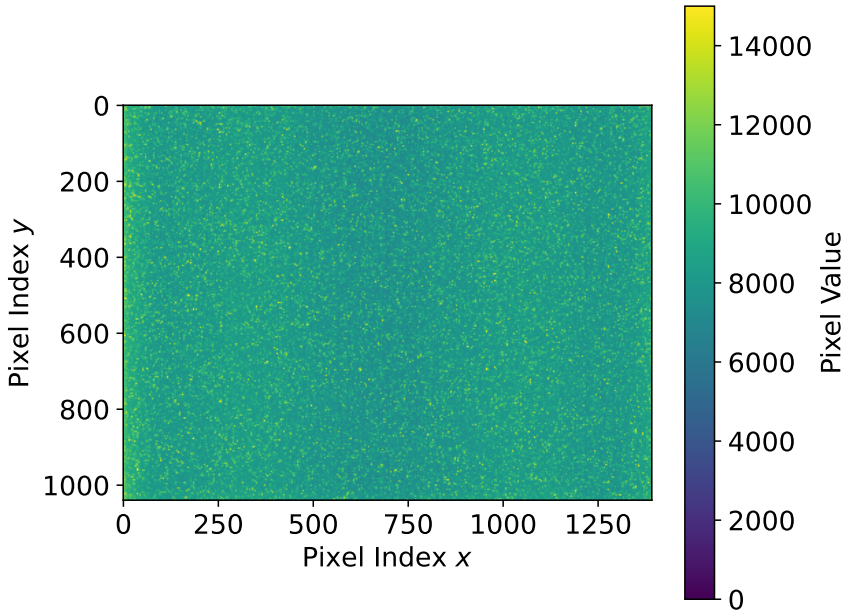

(a) Raw average image

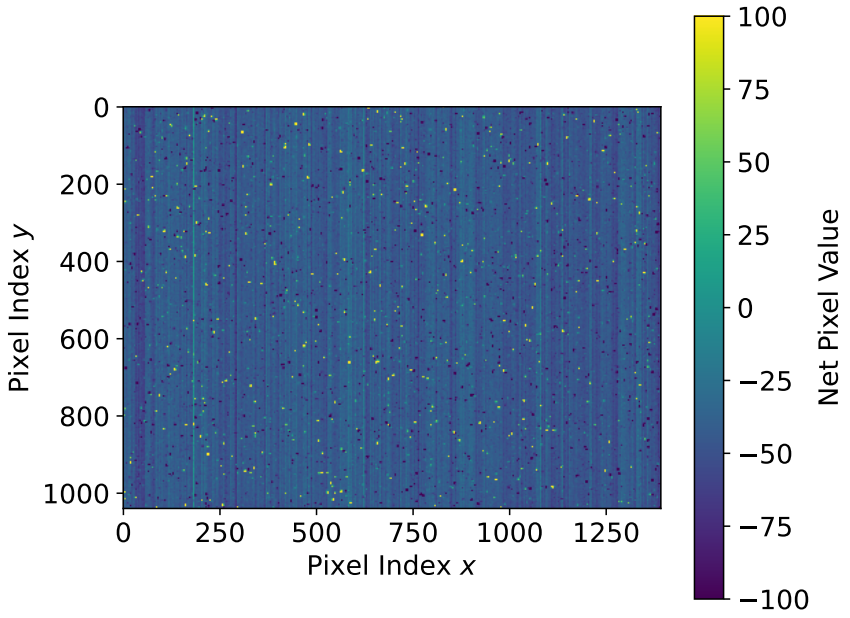

(b) Background-subtracted average image

Figure 6.36.: Average image of 117 pC electron bunches, recorded with the Jai 1405 camera. a) shows the raw average image, while an average background image has been subtracted in b).

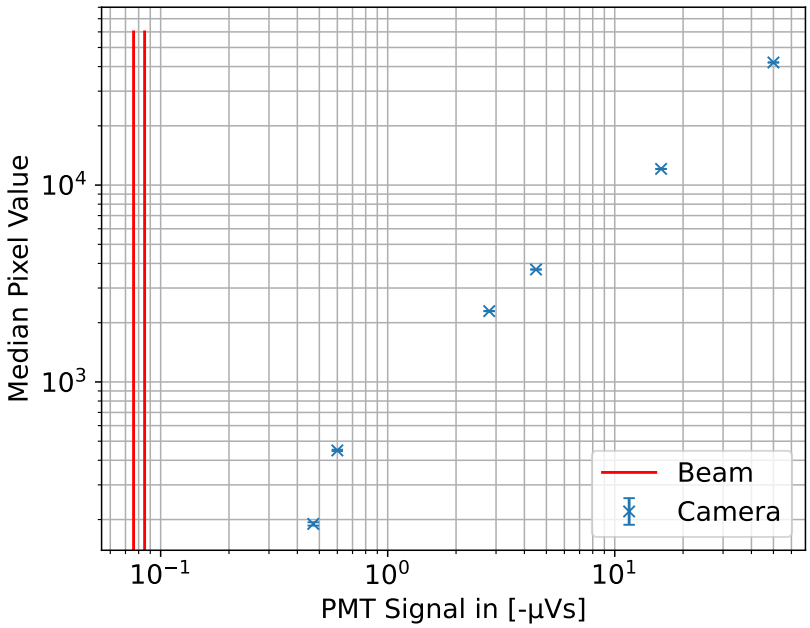

Figure 6.37.: Median pixel value of the Jai 1405 camera after background subtraction, receiving different light intensities from the LED, with respect to the PMT signal, resulting from the same LED settings. The red lines indicate the PMT signals from the ARES electron beam with bunch charges 114 pC and 140 pC.

not natively designed for UV-light, its respective properties in the relevant wavelength are hardly documented, complicating any analysis and optimization. Therefore, other camera models are used from now on, which are specifically designed to handle the relevant radiation. The main experiment is performed with a Basler a2A2840-14gmUV camera [152], as motivated in section 6.2. Thus, the following simulations and calculations are performed with respect to this camera model. The camera comes with a Sony IMX 487 sensor, which is divided into 2840 x 2840 pixels with an individual size of $(2.74\,\mu m)^2$, resulting in a total size of $(7.78\,mm)^2$.

The advanced lens setup consists of three quartz glass lenses and is designed to collect more light than the previous setup, while maintaining adequate spatial resolution and avoiding excessive size. Figure 6.38 shows the sketch of the reiterated setup. A large convex lens with a diameter 50 mm and a focal length of 100 mm is positioned at a distance of 85 mm from the center of the cube, where the electron beam is expected [164]. It is followed by a bi-concave lens with a focal length of −25 mm [165]. The distance between the edges of the lenses is 59 mm. A third lens is located 45 mm behind the bi-concave lens. It is the same convex lens used in the 1-lens setup, with a focal length of 40 mm [162]. Behind that, the light is guided towards the image plane containing the sensor, located at 60 mm behind the last lens.

That system is characterized via simulations with the Python-based raytracing tool KrakenOS [163]. All lenses are inserted into the framework, and rays at different positions and under different angles are simulated. To test the imaging capabilities of the system, the starting positions of the rays are set on a square-shaped grid with an edge length of 28 mm and 10 x 10 knots. At each position, 9 rays are initiated with

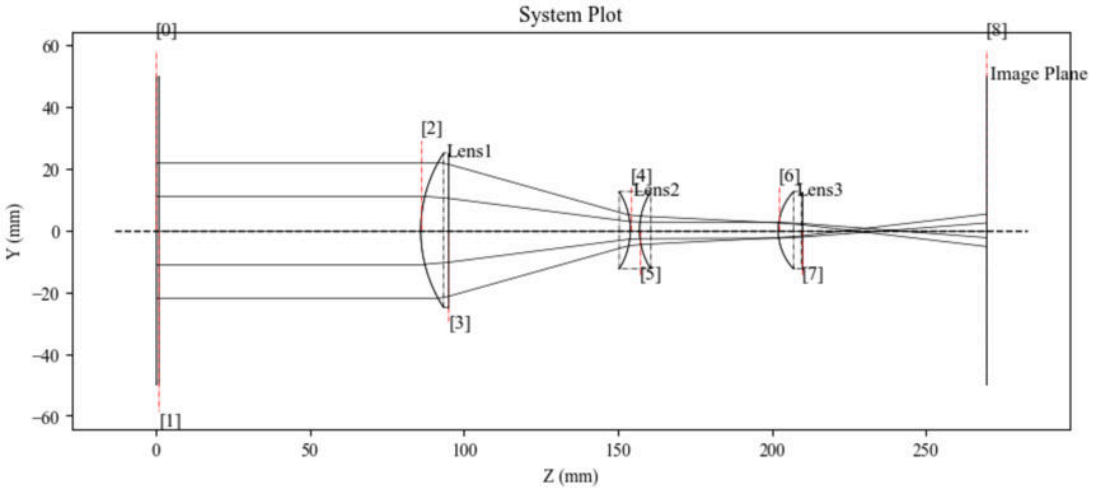

Figure 6.38.: Sketch of the advanced lens system. [0] and [1] indicate the position of the beam, [2] and [3] the large convex lens with a focal length of 100 mm, [4] and [5] the concave lens with a focal length of −25 mm, [6] and [7] the last convex lens with 40 mm focal length, and [8] the image plane at the camera sensor. Five exemplary parallel beams at $y = 0\,\text{mm}$, $\pm 10\,\text{mm}$, and $\pm 20\,\text{mm}$ are drawn as black lines. The figure is exported from [163].

varying initial horizontal and vertical angles between 0° and ±1°. Figure 6.39 shows the initial and final coordinates of all simulated rays. The grid-like shape of the initial coordinates is maintained throughout the optical setup, but some of the light that had been sent off under non-zero angles at the edges of the grid arrives outside of the sensor and does not contribute to the image. That effect indicates that the spatial positioning of the lenses is not yet ideal; thus, small readjustments are made for the real setup to minimize imaging artifacts. Those adjustments are applied empirically by visually optimizing the image quality. Apart from that, no significant distortions of the image are observed. The data also enables determining the expected magnification and, thus, the depictable area. By calculating the ratio of the initial and final coordinates of the rays with initial angles of 0°, the magnification is calculated to equal 0.26. Therefore, an area of 29.9 mm x 29.9 mm can be potentially projected onto the camera sensor.

The biggest disadvantage of KrakenOS is given by its long computation times if the number of simulated rays increases. Because of that, the following estimation of the collection efficiency of the three-lens system is performed via matrix optics calculations instead of raytracing [166]. However, matrix optics does not take into account lens abberations or the lenses' limited expansions. Therefore, this analysis should be repeated with a raytracing tool, e.g., by utilizing high-performance computing, to receive more accurate results. In this estimation, translation and refraction matrices are used to approximately determine the collection efficiency of the system with regard to light emitted at the center of the field of view. A ray of light is encoded by a two-component vector $\vec{x}$, which includes the distance of the ray from the central axis of the system and the angle of movement with respect to that axis θ. Translation matrices T encode the straight travel of a ray in a constant medium for the distance d while lens matrices M describe a refraction, caused by a thin lens with a focal length f. With

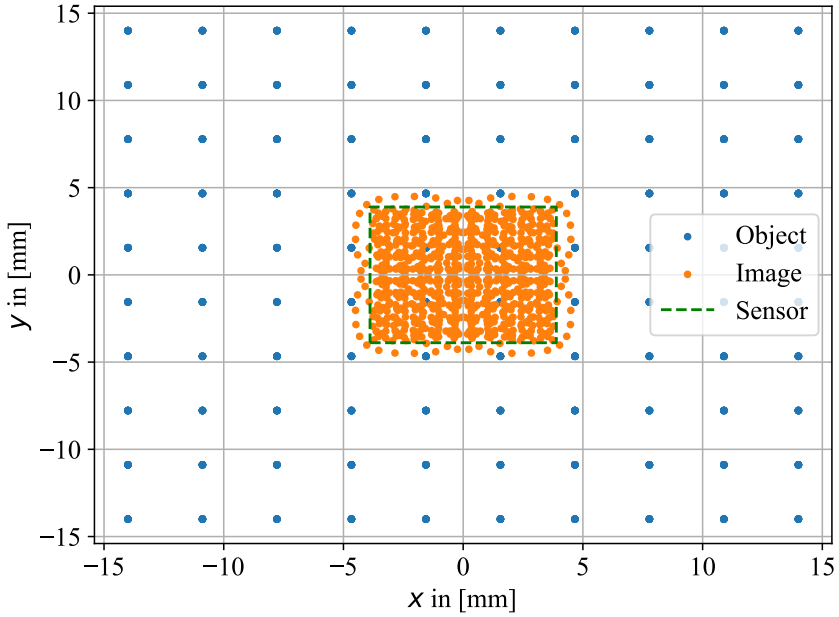

Figure 6.39.: Raytracing results of the simulated advanced 3-lens setup. The dots indicate the starting and end positions of the rays, which are initiated with starting angles between $-1°$ and $1°$ in horizontal and vertical direction. The green dashed line indicates the size of the camera sensor.

that formalism, light propagation through media and refractions can be calculated by multiplying the corresponding matrices and vectors. The aforementioned components are mathematically given by [166]:

$$\vec{x} = \begin{pmatrix} x \\ \theta \end{pmatrix}, \; T = \begin{pmatrix} 1 & d \\ 0 & 1 \end{pmatrix}, \; M = \begin{pmatrix} 1 & 0 \\ -\frac{1}{f} & 1 \end{pmatrix}. \tag{6.7}$$

This parametrization may only serve as a rough approximation of the real behaviour of the system, since it incorporates many assumptions like small-angle approximation and ideal lenses without any aberrations [166].

Initial ray vectors with $x = 0$ but different starting angles from 0 rad to $\theta_{\text{max}} = 0.46$ rad are mathematically sent through the lens system. θ_{max} corresponds to the largest possible angle at which rays still touch the first lens. Some exemplary rays are visualized in Figure 6.40 with respect to their position inside the lens tube. It is obvious that the bi-concave lens at a depth of 13 cm causes the light to bend away from the center. Therefore, light with larger absolute starting angles may not actually reach the image plane but impinge on the lens tube. To calculate the collection efficiency, the critical angle θ_{crit}, under which the light barely passes the walls of the lens tube at the position of the third lens, is determined. The relation between the largest distance of the rays from the center of the tube x_{max} and the initial θ is presented in Figure 6.41. $\theta_{\text{crit}} = 0.066$ rad is given by the intersection of the blue and the red line. If this is compared to θ_{max}, only 14 % of the light that hits the first lens actually contributes to the image at the sensor. This number is difficult to put in perspective, as there

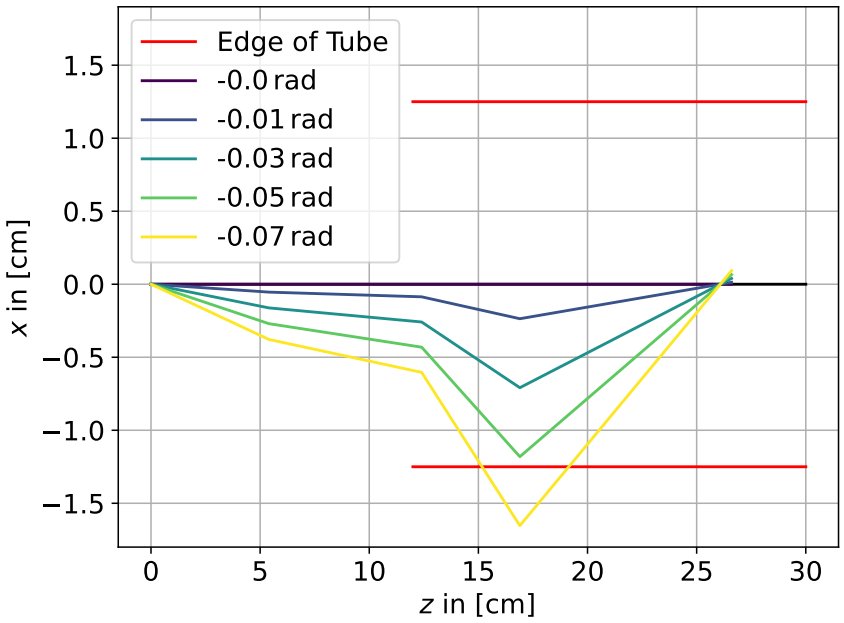

Figure 6.40.: Exemplary ray positions, calculated via matrix optics, throughout the utilized setup along the light propagation axis z. All rays start at $x = 0$ with different initial angles, indicated by the legend. The red lines indicate the edge of the lens tube from the second lens.

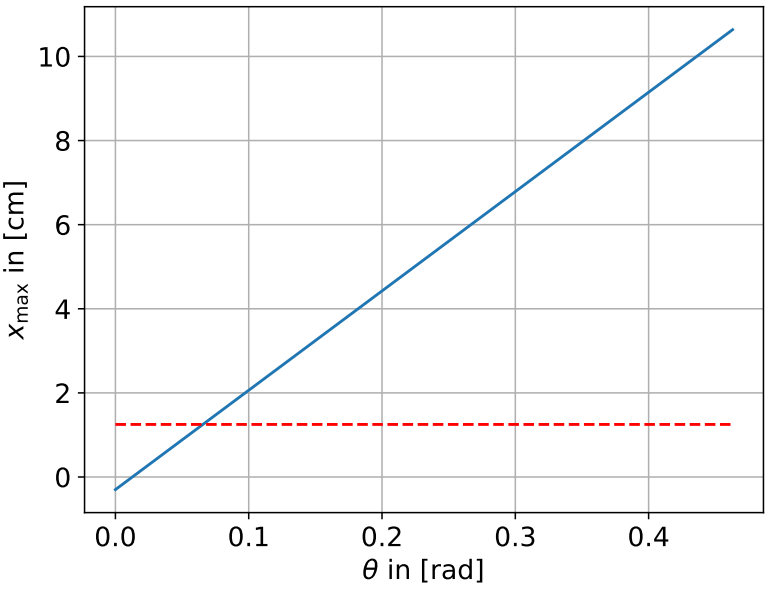

Figure 6.41.: Maximum distance from the central axis of the lens tube $x_{\max}$ for rays, starting at $x = 0$ with respect to their initial angle θ. The red dashed line indicates the radius of the lens tube.

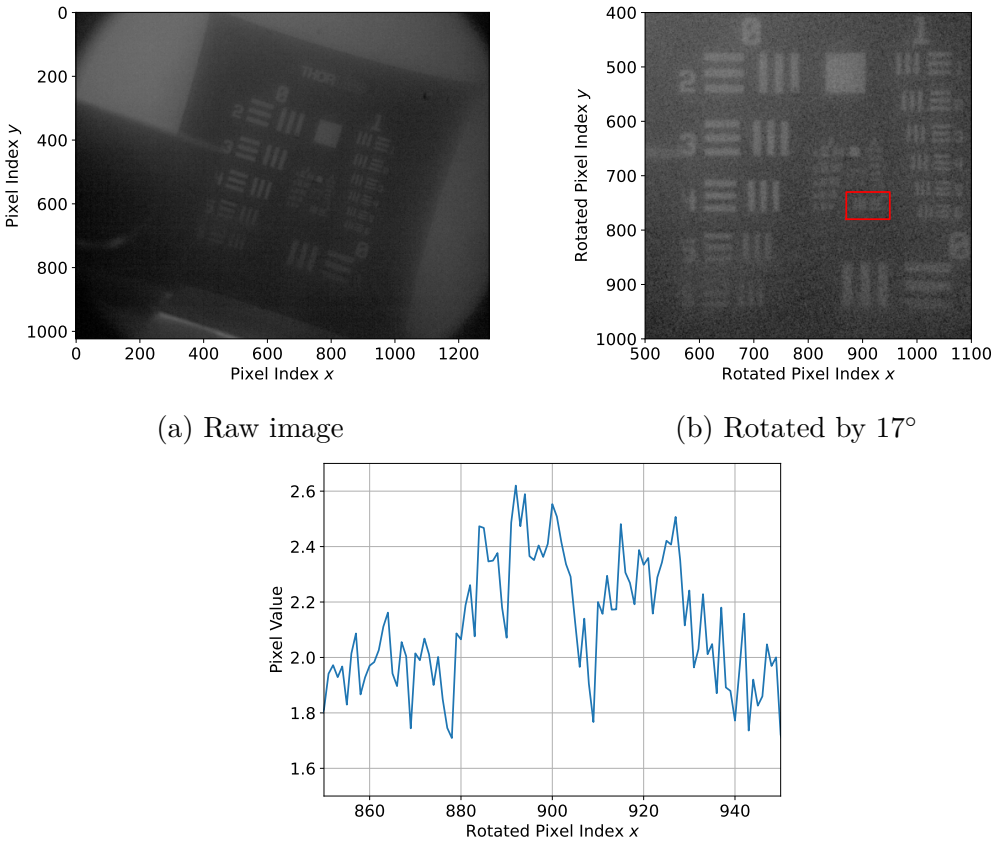

(a) Raw image

(b) Rotated by 17°

(c) Summed lineouts

Figure 6.42.: Images of a resolution target, recorded by a Basler acA2500-60uc camera, attached to the presented lens system. (a) shows the raw recorded image, (b) a zoom-in of the image, rotated by 17° with the determined resolution limit indicated in red, and (c) the summation of the lines of pixel row 745 to 760.

is a very limited number of comparable systems regarding typical object distances, magnification, and setup sizes. If compared to microscopes, which are among the closest fitting comparisons, the system would behave very poorly. The numerical aperture $na = \sin\frac{\theta_{\text{crit}}}{2}$ is an important parameter for the quantization of the light collection efficiency for microscopes. While na equals 0.066 for the presented system, much higher values of 0.1 to 0.9 are possible for microscopes [167]. However, those are designed to depict small volumes at high magnification, which imposes different optical requirements and optimization possibilities.

The last investigated parameter of the characterized system is its spatial resolution. This examination is performed experimentally by taking optical images with an optical Basler acA2500-60uc camera model that was available at that time [168]. Pictures of a resolution target [169] are used to determine the spatial resolution of the lens system. The blue pixels of the optical Basler camera are used because blue light behaves closest to the UV-light of the final application. Figure 6.42a shows the unprocessed recorded image next to a rotated and zoomed-in version of the same image, which is shown in Figure 6.42b. The spatial resolution is calculated from the smallest element of the

resolution target, on which the individual lines may still be distinguished. This limit is given by element 1 of group 2 of the line pairs of the resolution target [169]. The sum of the corresponding rotated pixel rows, which contain this element, is shown in Figure 6.42c. For this specific resolution target, this element corresponds to a spatial resolution of $4.0\,\frac{\text{line pairs}}{\text{mm}}$. This is smaller than the typical beam diameters seen for ARES in subsection 6.3.2 and similar to the simulated ideally achievable spot sizes of the planned upgrade of PITZ of $\approx 200\,\mu\text{m}$ [81]. Therefore, the presented new system for imaging the nitrogen fluorescence light of electron beams is expected to deliver physically meaningful results.

6.4.3. Advanced 3-Lens Setup at EuXFEL and ARES

The new setup is tested at the *Accelerator Research Experiment at SINBAD* (ARES) and the *European X-Ray Free-Electron Laser Facility* (European XFEL). The latter provides very high X-ray intensity pulses of up to $10^{12}\,\frac{\text{photons}}{\text{bunch}}$ with a photon energy of 9 keV and a base bunch repetition rate of 10 Hz, but larger trains of up to 2700 bunches are also possible [170]. All presented results from EuXFEL were acquired during a parasitic beamtime at the FXE experiment of EuXFEL in June 2025 with 10 bunches per train, i.e., only the mentioned set of fixed parameters was available. Fluorescence intensities at FXE drastically exceed the intensities at ARES (see Table 6.1). Although the photons interact less with the surrounding air and only 0.1593 % of them are expected to undergo a photoelectric interaction within the central 2 cm of the cube [171], this still results in a total deposited energy per bunch train of about 143 TeV. If the same fluorescence ratio of $4.05\,\frac{\text{photons}}{\text{MeV}_{\text{dep}}}$ is assumed as for electrons, this results in $5.8 \cdot 10^8$ photons, emitted isotropically for each bunch train. Such a high intensity even enables optical cameras and instruments to detect the fluorescence light via its optical tail [149]. Therefore, a Basler a2A4505-5gmBAS camera is used for this experiment [172]. That camera has been used previously by the EuXFEL facility for beam stability monitoring. The setup is shown in Figure 6.43. The photon beam enters the 3D-printed cube from the left side. Emitted fluorescence photons are imaged with the camera attached to the lens setup on top of the cube. Alternatively, the camera is also tested with a standard bought lens system at a distance of 15 cm from the cube. A dark environment is established by switching off the light in the entire laboratory.

Unfortunately, severe technical issues regarding the EuXFEL servers prevented the saving of any raw camera data, and only screenshots of the processed images remain available. The resulting images for both tested optics are shown in Figure 6.44. Both show a clear signal of the fluorescence beam. As mentioned, no quantitative analysis of those results is possible due to the lack of the corresponding raw data, limiting the interpretation to qualitative statements. The pixel intensities are significantly higher for the standard optics at the cost of potential spatial resolution.

For the measurements at ARES in August 2025, a similar setup is utilized as for the 1-lens system, described in subsection 6.4.1. A photograph is shown in Figure 6.45. The camera timing is again adjusted using the same LED and photomultiplier tube as before. The advanced lens system and the Basler a2A2840-14gmUV camera are attached to the 3D-printed cube. All measurements are carried out with a camera gain of 48. A heat sink surrounds the camera to improve thermal stability. Measurements with bunch charges of 102 pC and 127 pC and two different camera integration times of 10 µs and 10 s are

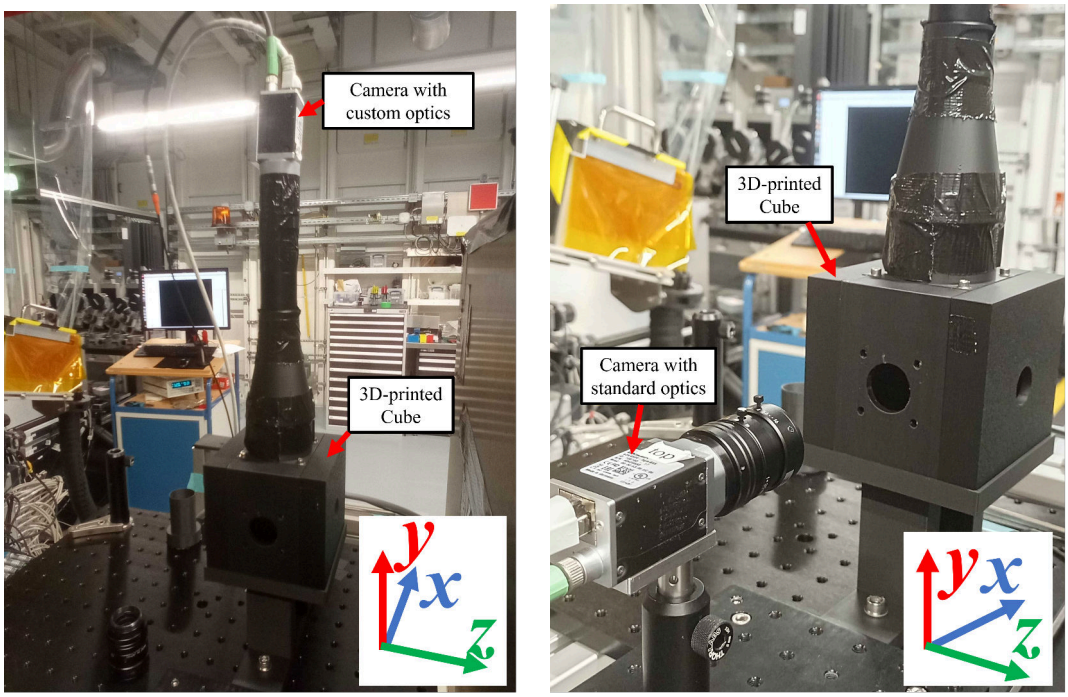

(a) Custom Lens Setup (b) Bought Optics

Figure 6.43.: Setup of the nitrogen fluorescence monitoring setup at the EuXFEL. (a) shows the custom lens system, characterized in subsection 6.4.2, (b) the same camera with a standard off-the-shelf lens system.

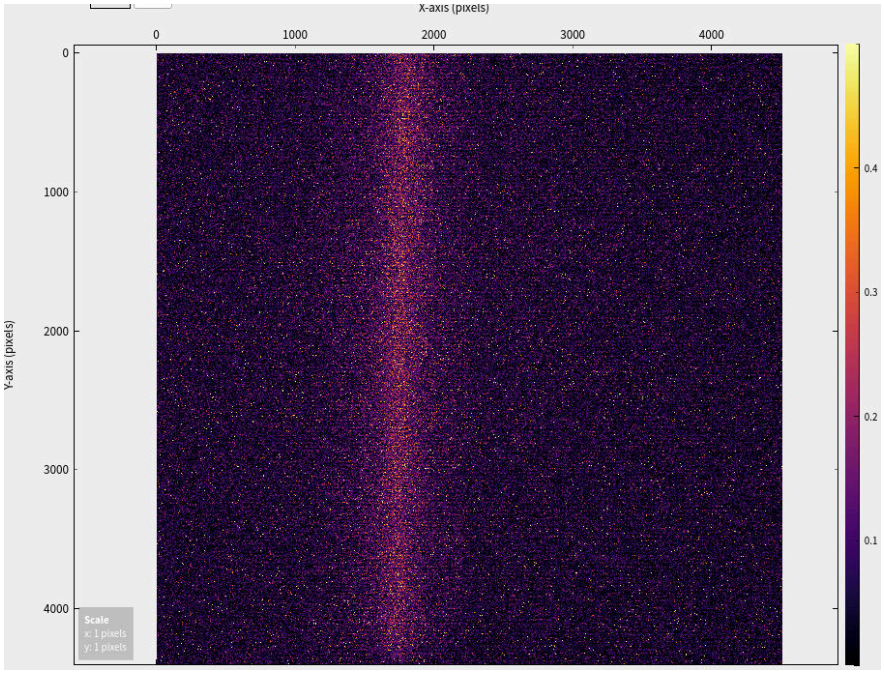

(a) Custom Lens Setup

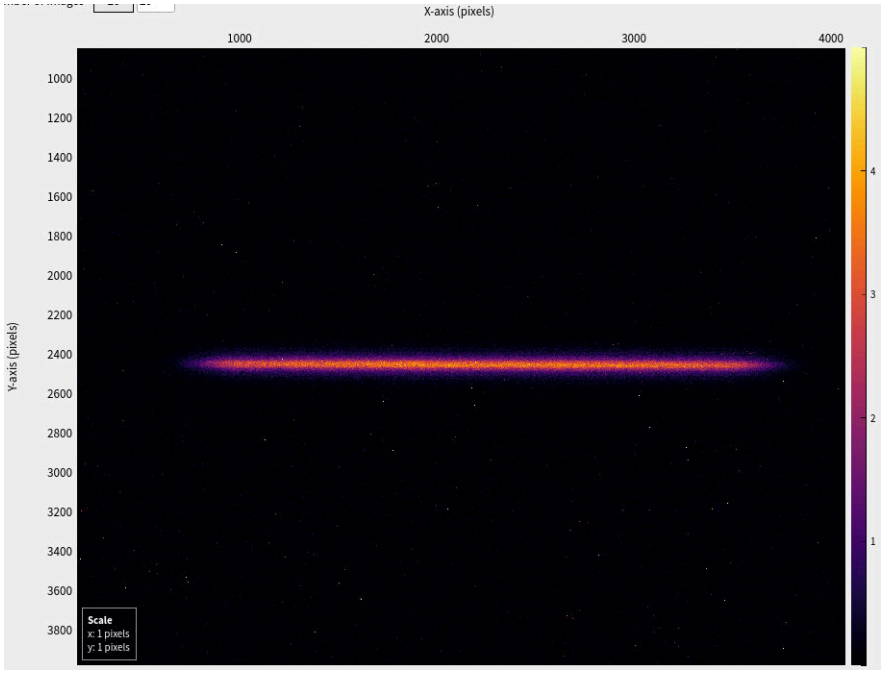

(b) Off-the-shelf Optics

Figure 6.44.: Images of the nitrogen fluorescence of the EuXFEL beam, recorded with the custom lens system, characterized in subsection 6.4.2 (a) and with standard off-the-shelf optics (b).

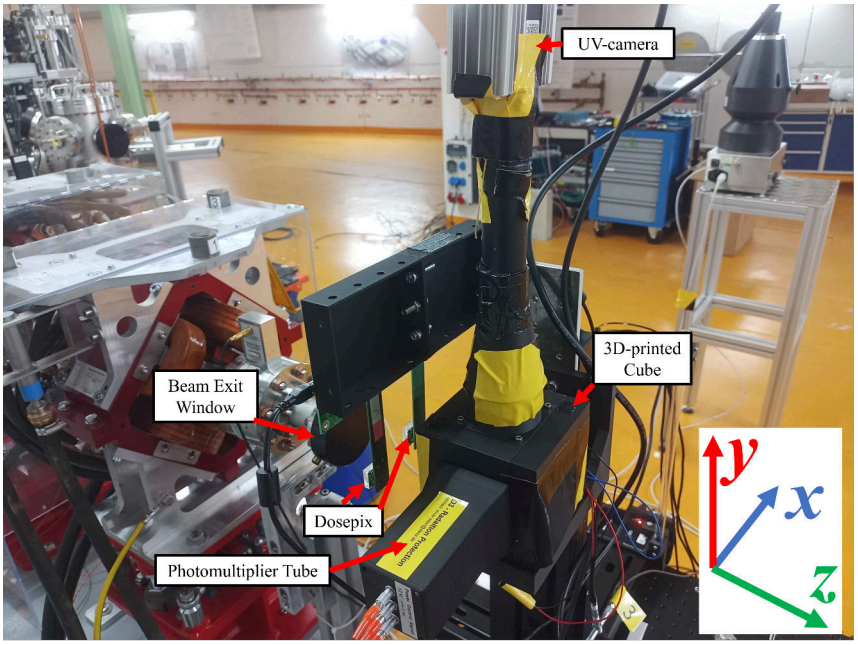

Figure 6.45.: Setup of the nitrogen fluorescence imaging setup, used at ARES in August 2025.

performed. For all settings, ten images are recorded and averaged in post-processing to increase the significance of the results. The average pictures for the different settings, as well as exemplary background images, are shown in Figure 6.46. If a beam were visible, it would manifest as a vertical line throughout the central columns of the pixel matrix, similar to the results for EuXFEL. No such structure is visible in any of the pictures, independent of the integration time or bunch charge. There is no distinct difference between the pictures under radiation and the background images, where the particle acceleration laser is shut down. However, background and radiation images show a significant horizontal gradient in their measured signal. This trend may originate from ambient light coupling into the system from the experimental hall and is otherwise not understood. The effect becomes even more apparent when looking at the projections of the images onto the x-axis, which are shown in Figure 6.47. The aforementioned general trend of a decreasing pixel value along the x-axis is observed for all tested settings of the beam and the camera, reinforcing the hypothesis of an external origin. Yet, the absolute values of the offset, as well as the differences between the offsets with and without irradiation, significantly change over the different settings. The background level even exceeds the baseline of the signal of the irradiated measurements in two cases. Therefore, either the intensity profile of the ambient light, which is still able to impinge on the camera sensor despite the performed darkening measures, changes over the course of the measurements, or the response of the camera varies due to temperature or other instabilities. In either case, this effect requires further investigation and is not yet understood from the available data. Consequently, the absolute pixel values cannot be meaningfully compared. Only the trends of the differences between irradiated and background measurements are worth analysing. As the statistical fluctuations of the samples over the pixel columns are too large to extract significant results, the

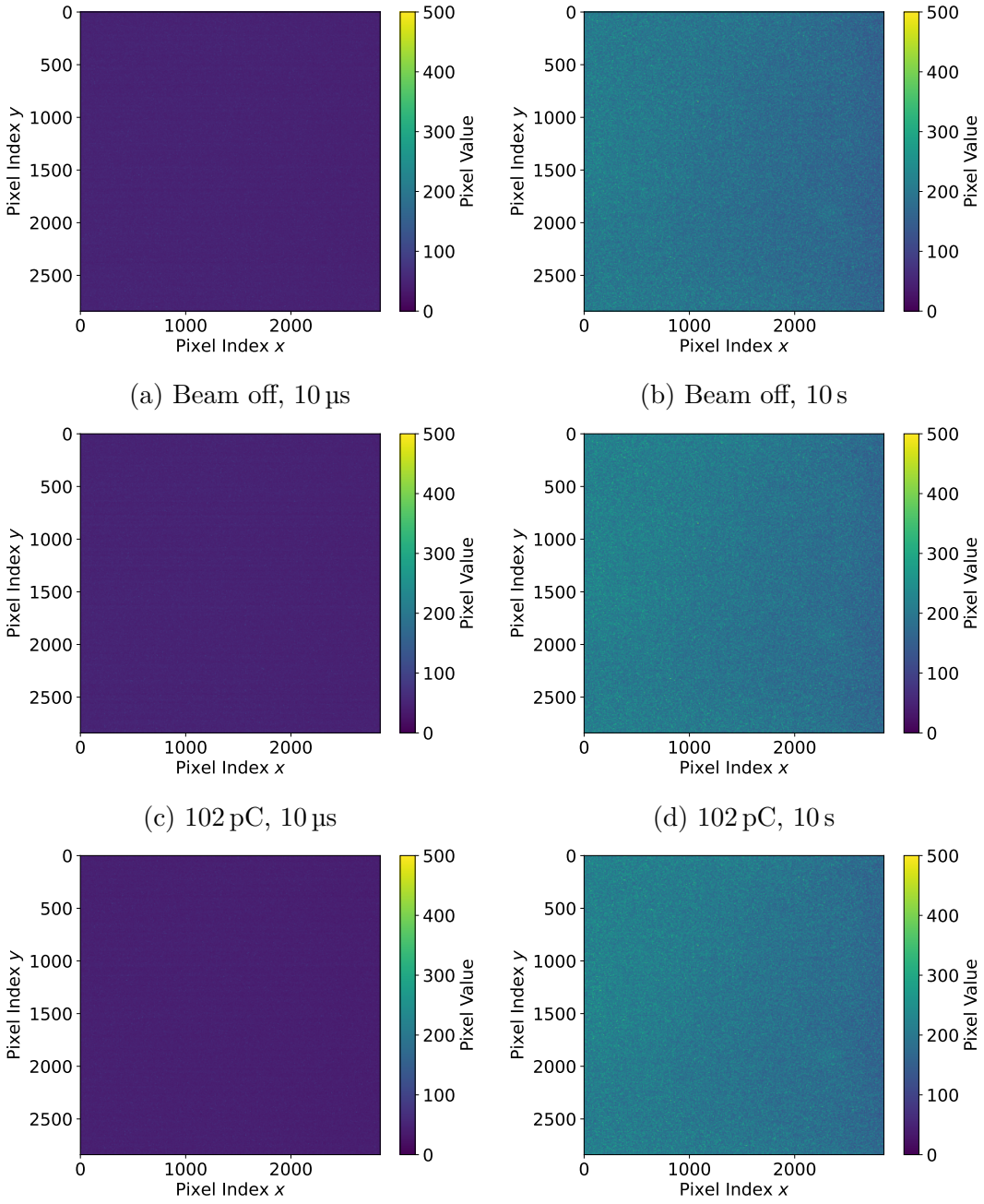

(a) Beam off, 10 µs

(b) Beam off, 10 s

(c) 102 pC, 10 µs

(d) 102 pC, 10 s

(e) 127 pC, 10 µs

(f) 127 pC, 10 s

Figure 6.46.: Average over ten camera images for different bunch charges and integration times, as indicated in the respective captions.

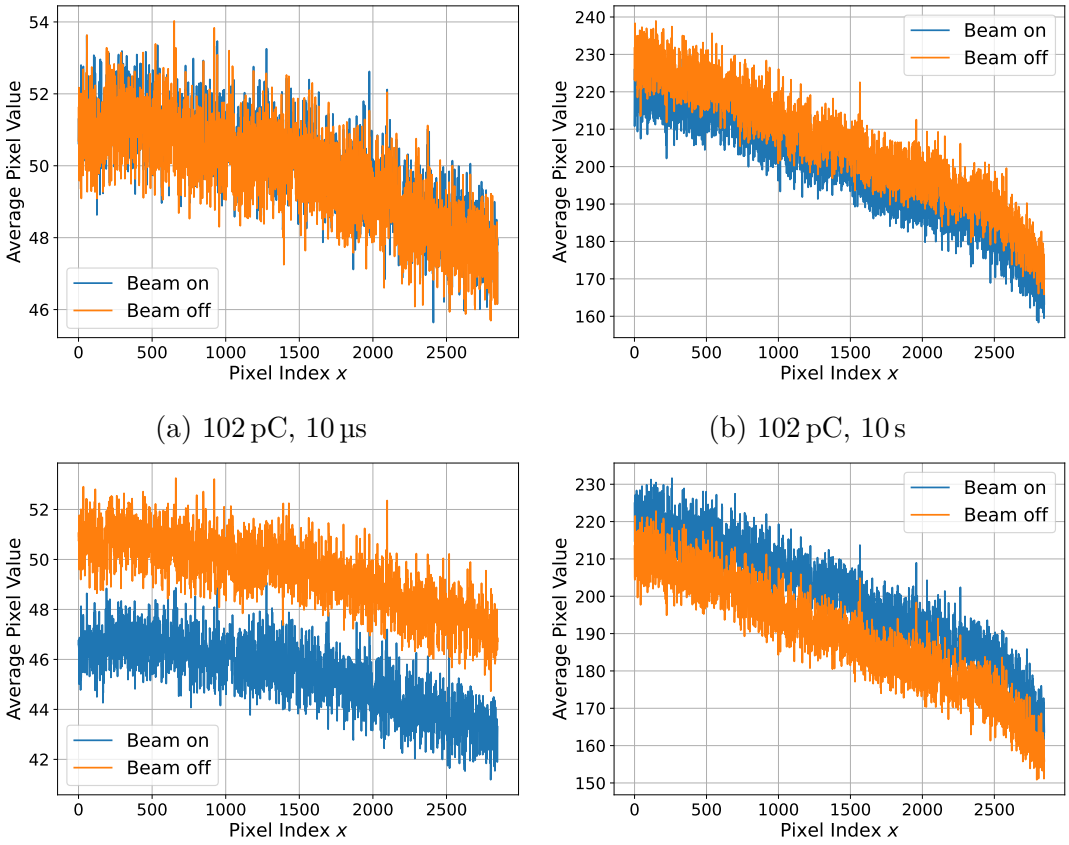

(a) 102 pC, 10 µs

(b) 102 pC, 10 s

(c) 127 pC, 10 µs

(d) 127 pC, 10 s

Figure 6.47.: Projections of the average camera images, shown in Figure 6.46 onto the x-axis for different bunch charges and integration times.

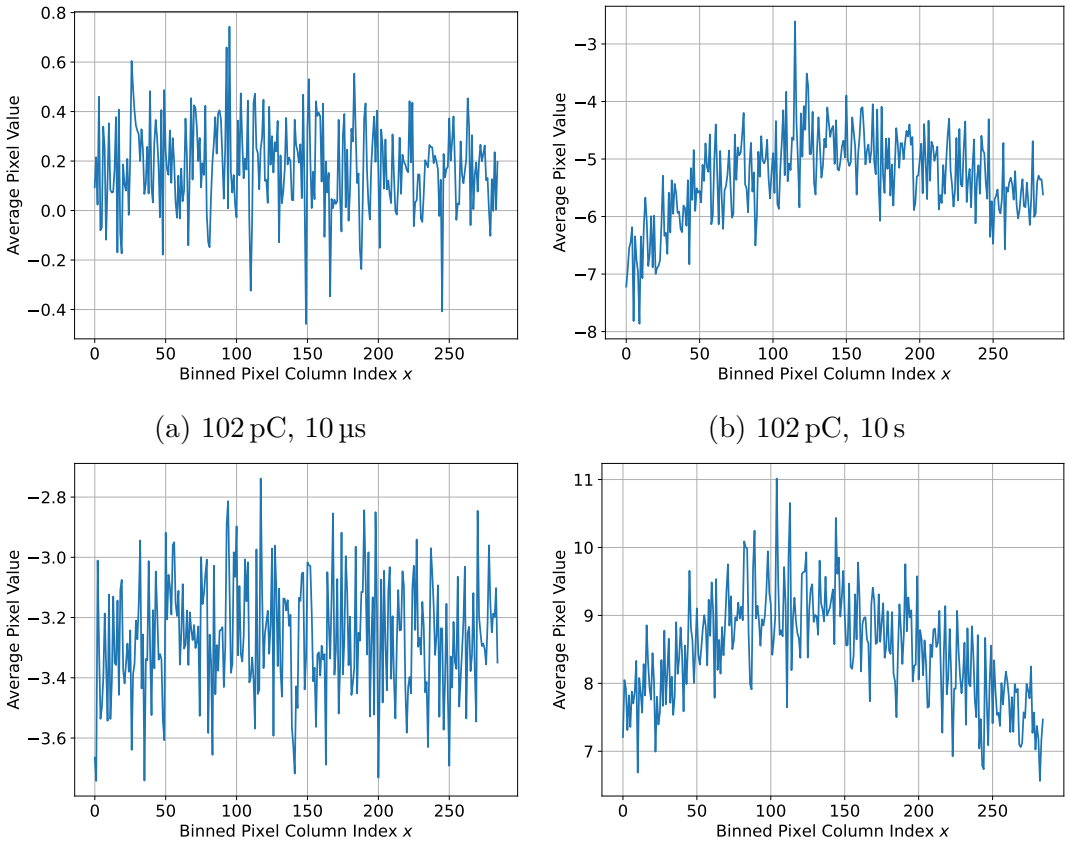

(a) 102 pC, 10 µs (b) 102 pC, 10 s

(c) 127 pC, 10 µs (d) 127 pC, 10 s

Figure 6.48.: Average difference of the pixel values with and without accelerated electrons, projected on the x-axis, with respect to the binned pixel index for different bunch charges and integration times, as indicated by the captions.

data is smoothed by combining each ten pixel columns into one average value. The term "Binned Pixel" refers to this data reduction in the following. Figure 6.48 shows the differences between the images with and without irradiation with respect to the binned pixel index. This is the first step in the analysis chain, in which a possible sign of the nitrogen fluorescence light emerges. No net signal is observed for the short integration time of 10 µs, independent of the tested bunch charge, but a clear structure with a maximum at about 130 binned pixels develops for 102 pC and 127 pC after 10 s of integration time. This is an indication of the presence of light when the beam is turned on, potentially resulting from nitrogen fluorescence. However, the significance of the results is very low, even though 10^4 bunches entered the data of ten images with 10 s of integration time.

The last investigation evolves around the possibility of building a fundamental beam monitoring procedure on such low-statistics data. For that purpose, electrons with a bunch charge of 80 pC are recorded ten times 10 s. This measurement is conducted for different beam positions in x-direction with respect to the cube (0 mm, 2 mm, 4 mm), which are realized by moving the entire setup via a linear stage. The binned projections of the camera images after background subtraction are shown in Figure 6.49.

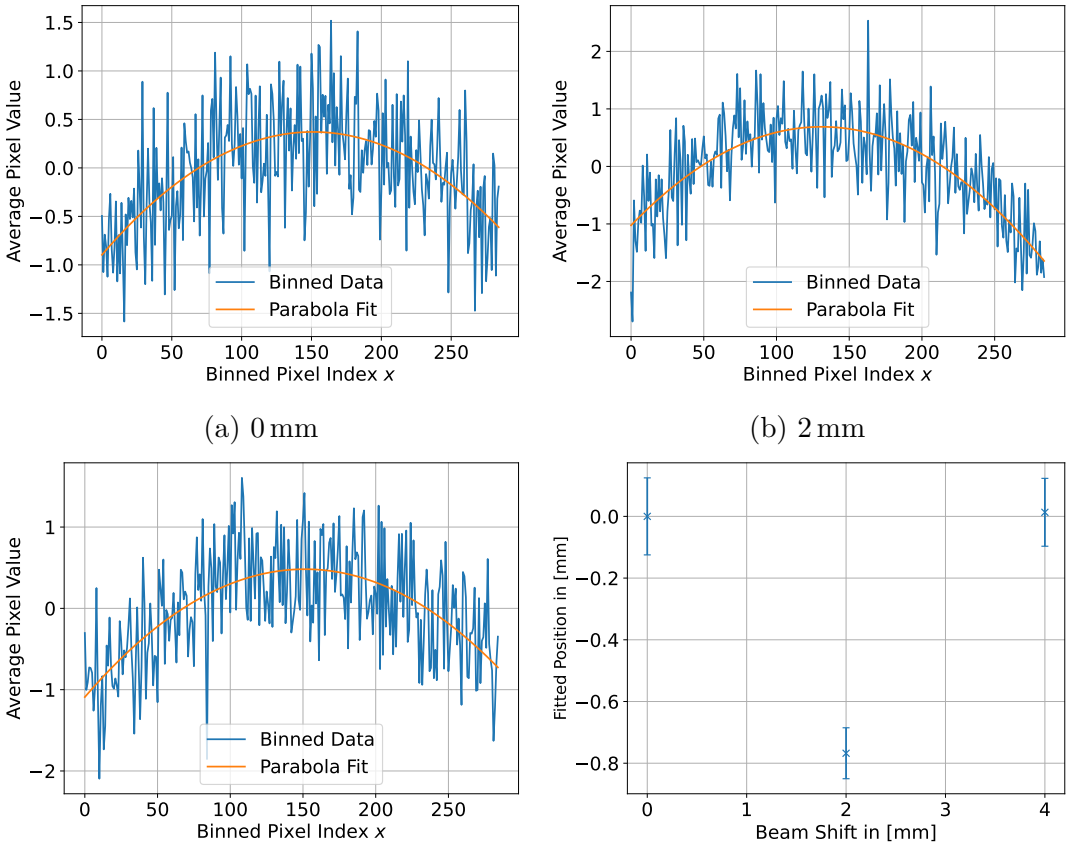

(a) 0 mm (b) 2 mm

(c) 4 mm (d) Fit results

Figure 6.49.: Average pixel value with respect to the binned pixel index for a bunch charge of 80 pC for different relative positions of the center of the camera to the electron beam in x-direction, indicated in the captions (a-c), as well as quadratic fits to that data. (d) shows the vertex points of the adjusted parabolae with respect to the actual relative beam position. The error bars represent the fit uncertainties.

All measurements show the previously observed hill-like structure, but with slightly different vertex positions. To quantify the shape of the data, parabolic functions of the shape

$$f(x) = a\ (x - b)^2 + c \tag{6.8}$$

with fit parameters a, b, and c are adjusted by a Levenberg-Marquardt to the data, performed via the python package *scipy.optimize* [141]. The resulting graphs are also shown in Figure 6.49. As the parabola is adjusted in vertex shape, the parameter b directly corresponds to the central point of the graph. The results and fit uncertainties, converted from binned pixels into a physical distance on the beam plane, are shown in Figure 6.49d. There is no agreement between the determined positions and the actual beam position shifts.

Therefore, beam monitoring for the tested bunch charges is impossible with the current iteration of the setup due to a significant lack of statistics. Neither the measured positions nor the large measured widths, spanning over the entire field of view, may be directly related to actual beam properties. A proof of concept for the intended imaging technique could only be delivered for the high-intensity photon pulses of EuXFEL, while only some weak beam-related signal is observed for the electron beam at ARES. However, the broad shape of the signal and its independence from beam position shifts might also indicate an origin from scattered electrons or dark current, interacting with the camera sensor directly.

6.5. Conclusion

The simulations and measurements of this chapter examine the possibilities and challenges of an active beam monitoring system for FLASH-capable electron beams utilizing Dosepix detectors and UV-cameras. Measurements of the scattered radiation with the integration mode of Dosepix show promising results, regarding the linearity of the integrated time-over-threshold with respect to bunch charge, and strictly monotonously decreasing signals with respect to higher distances between the beam and the detector. A beam position and width monitoring system for a fixed bunch charge of 127 pC at ARES has been established, but is lacking a reliable set of validation data, so far. The core framework of the monitoring procedure may also apply to other environments, but the specific parameters will require re-determination for other accelerators like PITZ, as the measured trends heavily depend on the bunch charge, electron energy, and distance of the setup from the exit window. Thus, the current version of the setup, comprising two Dosepix detectors, is, by itself, insufficient to independently monitor bunch charge, position, and beam width. Furthermore, the position and width have only been monitored in one dimension, with the second dimension, monitored by a perpendicular set of another two Dosepix detectors, is scheduled in a future iteration of the setup. An evolving setup may also address the timing limitations of the monitoring process, induced mainly by the readout duration of Dosepix. The currently achieved 90 ms are already close to the train repetition rate of the discussed accelerators, but far from the requirements needed for monitoring individual bunches within a train at PITZ, requiring time resolutions in the order of 1 µs [81].

The second component of the setup is planned to monitor the electron beam by imaging the nitrogen fluorescence photons emitted by the electrons as they traverse

air. As shown, using a UV-sensitive camera and three quartz glass lenses only works for high intensities, provided by EuXFEL, whereas only a weak signal is observed for ARES. Therefore, a proof-of-concept for the intended electron beams is still missing and requires additional beamtime. Measurements at PITZ with an up to $3 \cdot 10^4$ times higher beam intensity (see section 2.7) would be highly beneficial, as the much higher bunch charges and the possibility of bunch trains would reveal a much larger range of the charge dependence of the system. Nevertheless, the sensitivity of the setup requires significant improvement by increasing the light collection or switching to cameras with higher quantum efficiencies or even image intensifying capabilities.

By now, the setup has only been tested in terms of monitoring bunch charge, not actual patient dose. Calibrating the setup to dose would require external reference measurements of FLASH-capable detector systems, which had to be performed simultaneously. However, very few detectors currently fulfill those requirements [50].

7. Summary and Conclusion

Different aspects in the general field of the characterization of ionizing radiation are investigated in the previous chapters. Most investigations are based on the hybrid pixelated Dosepix detector, which is used to detect photons, electrons, and α-particles from 10 keV to 153 MeV. Yet, a deviation of the hitherto energy calibration of Dosepix is shown in section 3.1 for measurements with 5.6 MeV α-particles. The relation between ToT - Dosepix's internal measure of deposited energy - and the true energy in units of keV loses its linearity at (567 ± 6) keV. For higher deposited energies per pixel, Dosepix should be used with care, as a bijective mapping of ToT and deposited energies can no longer be guaranteed. In section 3.2, a Python-based framework for the simulation of ToT-spectra, taking analog pile-up at different dose rates into account, is presented. The framework is currently able to reconstruct ToT-data at low dose rates, yet significantly underestimates the influence of pile-up for higher dose rates. This presumably dominantly depends on the lack of precise knowledge about the exact CSA output of Dosepix, especially below the threshold. In addition, events that are too low to be registered by Dosepix but may still influence other events are currently not taken into account.

Chapter 4 explores the deconvolution of photon and electron spectra from the combined data of 10 Dosepix detectors in between filter layers of different materials and thicknesses. This study is based on Monte Carlo simulations with Geant4 and Allpix^2 to determine the response of the setup for both particle types and different energies. 10 keV to 2.5 MeV of photon energies and 120 keV to 20 MeV of electron energies are simulated. Spectra with a limited number of degrees of freedom (6 for photons, 3 for electrons) are used as a pioneering test of the simulated spectrometer. The two deconvolution methods of matrix pseudo-inversion and least-squares regression are compared for both particle types. Only the matrix pseudo-inversion of the electron spectra yields excellent results, while all other test cases fail to determine proper and physically meaningful spectra. Therefore, the Dosepix-based photon and electron spectrometer cannot even compete with other spectral deconvolution techniques in the basic tests involving a single known particle type and low dose rates. Many aspects of the current design may still be improved, e.g., the filter compositions or the sensor materials of the Dosepix detectors. Additionally, other deconvolution procedures, such as machine-learning approaches, may be employed to improve the quality of the results. Yet, the present difficulties of quickly absorbed electrons in the first layers and indistinguishable high-energy photons might even aggravate in the intended use case of the spectrometer in high-dose-rate environments, potentially suitable for FLASH radiotherapy. Therefore, the Dosepix-based spectrometer is not further developed in this work.

In contrast, Dosepix showed excellent usability as the key component of an active eye lens dosemeter prototype, as investigated in chapter 5. Although the dose results are affected by the ambient temperature, the deviations are shown to stay within the official limits of indoor devices. However, this result must be validated for other prototypes

to exclude beneficial coincidences. Measurements with the active eye lens dosemeter prototype under realistic clinical environments are performed at the Marienklinikum Siegen. During the investigated interventional operations, the eye lenses of medical personnel are exposed to severe radiation, potentially exceeding the annual limits of 20 mSv. Specialized radiation protection lead glasses can reduce the applied dose by a factor of 5 to 33, making them a very potent tool of dose reduction. Consequently, the influence of such radiation protection glasses must also be taken into account by the eye lens dose estimation of the active prototype. An approach utilizing pieces of lead glass in front of the dosemeter prototype is tested and compared to the dose results of thermoluminescence dosemeters at the positions of the eyes on an Alderson phantom. Both detectors show similar general trends within the achieved accuracy of the experiment. However, some special cases such as radiation surpassing the radiation protection glasses at certain angles are currently not represented by this setup and require further optimization. Furthermore, these investigations have only been performed for one model of radiation protection glasses so far. A comprehensive study of the reproducibility of the $H_\mathrm{p}(3)$-results of the active personal eye lens dosemeter prototype reveals the photon and electronics noise as the largest contributions to the overall uncertainty. However, the total variation of $< 1\,\%$ for most radiation fields stays well below the official limits.

Lastly, Dosepix detectors and UV-sensitive cameras are used to determine the position and width of electron bunches at the ARES accelerator, presented in chapter 6. Backed by Monte Carlo simulations, the electron beam position and width are determined from the scattered radiation in air, measured by two Dosepix detectors next to the beam. Especially, the width determination shows significant residuals of up to 50 %, possibly resulting from the small set and quality of the available reference data. Nevertheless, this work provides a proof-of-concept for an electron beam parameter reconstruction with Dosepix detectors. More sets of high-quality reference and validation data are essential to improve the reconstruction algorithm and validate it on independent results. Furthermore, the presented framework should also be established at alternative electron beam facilities like PITZ to test its applicability in other radiation environments. In the next steps, this setup should be extended to four Dosepix detectors to encompass both spatial dimensions of the position and width of the beam. As the second pillar of electron beam monitoring, UV-cameras are used to image the fluorescence light emitted by the nitrogen fluorescence as the electron beam traverses the air. Unfortunately, a distinct track of the beam could only be witnessed at the European XFEL facility, where the fluorescence intensity exceeds that of ARES by two orders of magnitude. Therefore, although a general proof of concept of the method is provided, the functionality of this beam monitoring technique for electron beams is still under investigation. Some net signal in the camera is also present for ARES, but with too low statistics to exclude an origin of scattered electrons or dark current. To follow up on these results, the setup should be tested with higher electron intensities at the PITZ facilities, where the fluorescence can match XFEL, to definitely test the concept of fluorescence-based electron beam monitoring.

Ultimately, the hybrid pixelated Dosepix detector has shown the ability to function in medical applications of radiation protection dosimetry with X-rays and beam monitoring of FLASH-capable electron accelerators. Yet, it can also limit the achievable success of some experiments, e.g., due to its own absorption in the spectrometer or its limited

time resolution for beam monitoring. Additionally, some of its capabilities like counting of individual events cannot be effectively utilized for electron beam imaging at high dose-rates. In such applications, moving on to other detector types should be considered.

A. Bin Edges and Dose Conversion Factors

Low	High	Large Pixels	Small Pixels
12	15	$1.49 \cdot 10^{-4}$	$1.44 \cdot 10^{-2}$
15	20	$5.03 \cdot 10^{-5}$	$2.40 \cdot 10^{-3}$
20	25	$1.27 \cdot 10^{-4}$	$1.27 \cdot 10^{-2}$
25	30	$9.75 \cdot 10^{-5}$	$8.76 \cdot 10^{-3}$
30	35	$1.86 \cdot 10^{-4}$	$1.23 \cdot 10^{-2}$
35	40	$2.09 \cdot 10^{-4}$	$3.08 \cdot 10^{-2}$
40	50	$3.26 \cdot 10^{-4}$	$2.67 \cdot 10^{-2}$
50	60	$5.11 \cdot 10^{-4}$	$6.45 \cdot 10^{-2}$
60	70	$9.17e \cdot 10^{-4}$	$1.37 \cdot 10^{-1}$
70	80	$1.51 \cdot 10^{-3}$	$1.69 \cdot 10^{-1}$
80	90	$2.31 \cdot 10^{-3}$	$3.07 \cdot 10^{-1}$
90	100	$3.57 \cdot 10^{-3}$	$8.64 \cdot 10^{-1}$
100	110	$5.89 \cdot 10^{-3}$	1.04
110	130	$7.45 \cdot 10^{-3}$	4.24
130	150	$2.16 \cdot 10^{-2}$	12.9
150	–	$5.07 \cdot 10^{-2}$	26.2

Table A.1.: List of low and high limits of energy bin edges in [keV] (1st and 2nd column) and $H_{\mathrm{p}}(3)$ conversion factors for large and small pixels (3rd and 4th column) in [µSv] determined in [85] and used throughout this thesis.

Index	Lower Limit	Upper Limit	Lower Limit	Upper Limit
1	0.0	12.5	0.0	130.0
2	12.5	17.5	130.0	150.0
3	17.5	22.5	150.0	170.0
4	22.5	27.5	170.0	190.0
5	27.5	32.5	190.0	210.0
6	32.5	37.5	210.0	230.0
7	37.5	42.5	230.0	250.0
8	42.5	47.5	250.0	280.0
9	47.5	52.5	280.0	310.0
10	52.5	57.5	310.0	330.0
11	57.5	62.5	330.0	350.0
12	62.5	67.5	350.0	370.0
13	67.5	72.5	370.0	390.0
14	72.5	77.5	390.0	410.0
15	77.5	82.5	410.0	430.0
16	82.5	87.5	430.0	450.0
17	87.5	92.5	450.0	470.0
18	92.5	97.5	470.0	490.0
19	97.5	105.0	490.0	510.0
20	105.0	115.0	510.0	530.0
21	115.0	125.0	530.0	550.0
22	125.5	135.0	550.0	570.0
23	135.0	145.0	570.0	590.0
24	145.0	155.0	590.0	625.0
25	155.0	165.0	625.0	675.0
26	165.0	175.0	675.0	725.0
27	175.0	185.0	725.0	775.0
28	185.0	195.0	775.0	825.0
29	195.0	225.0	825.0	875.0
30	225.0	275.0	875.0	925.0
31	275.0	325.0	925.0	975.0
32	325.0	375.0	975.0	1050.0
33	375.0	425.0	1050.0	1150.0
34	425.0	475.0	1150.0	1250.0
35	475.0	550.0	1250.0	1350.0
36	550.0	650.0	1350.0	1700.0

Table A.2.: Part 1 of the energy intervals, chosen for the description of the emission spectra. The left lower and upper limits correspond to the desciption of photon spectra, the right columns to the electron spectra. All quantities ar given in [keV].

Index	Lower Limit	Upper Limit	Lower Limit	Upper Limit
37	650.0	750.0	1700.0	2500.0
38	750.0	850.0	2500.0	3500.0
39	850.0	950.0	3500.0	4500.0
40	950.0	1100.0	4500.0	5500.0
41	1100.0	1300.0	5500.0	6500.0
42	1300.0	1500.0	6500.0	7500.0
43	1500.0	1700.0	7500.0	8500.0
44	1700.0	1900.0	8500.0	9500.0
45	1900.0	2100.0	9500.0	12500.0
46	2100.0	2300.0	12500.0	17500.0
47	2300.0	2500.0	17500.0	22500.0

Table A.3.: Part 2 of the energy intervals, chosen for the description of the emission spectra. The left lower and upper limits correspond to the description of photon spectra, the right columns to the electron spectra. All quantities are given in [keV].

B. Auxiliary Figures

B.1. Spectrometer Response

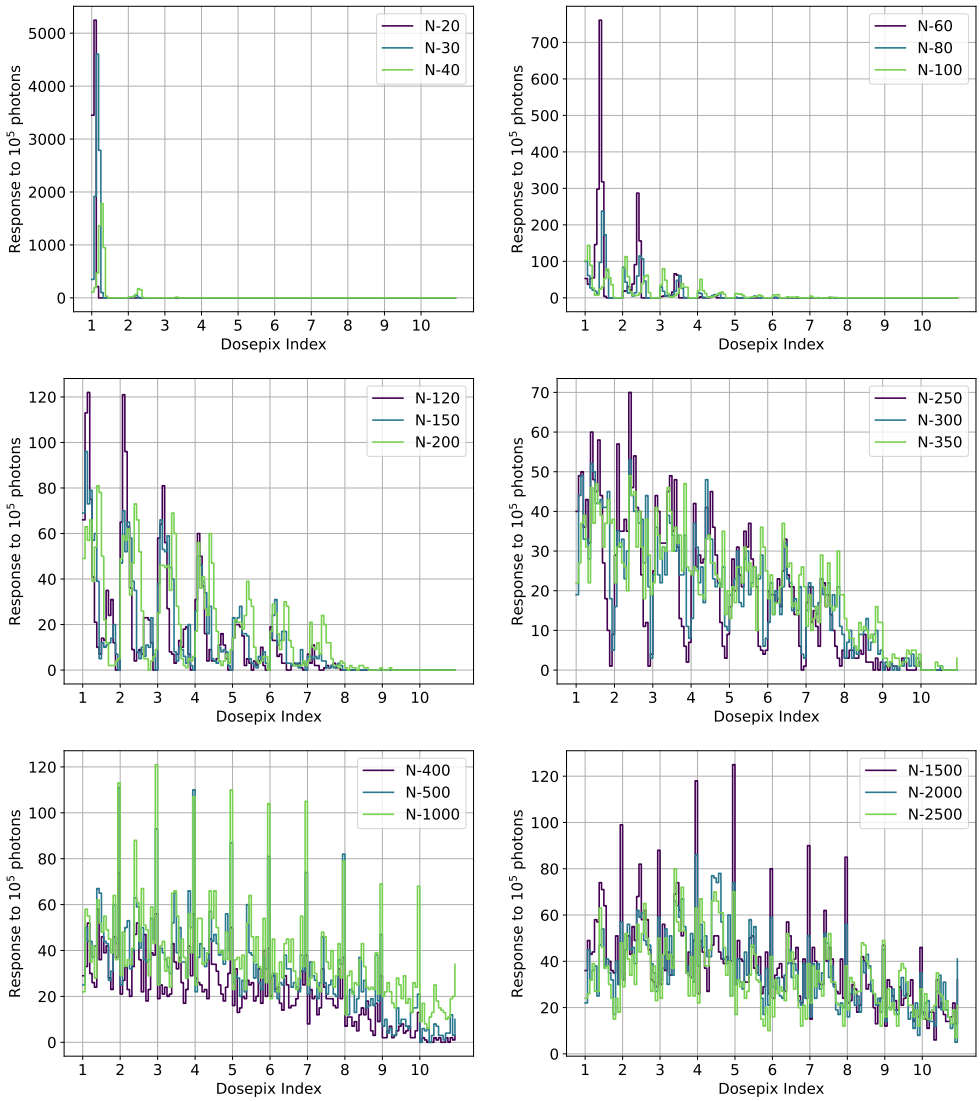

Figure B.1.: Response of the simulated spectrometer to the N-series spectra. 10^5 photons are simulated for each spectrum. The x-axis represents the 16 energy bins of the Dosepix detector in each layer.

B.2. Dosepix' Reproducibility

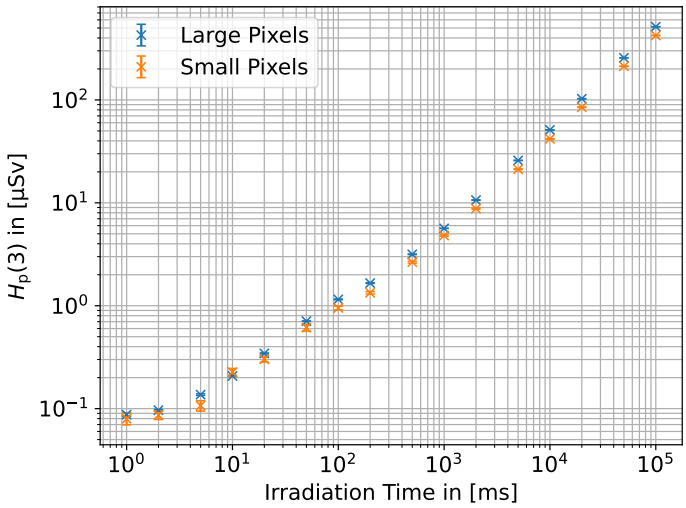

Figure B.2.: $H_p(3)$, reconstructed by the large and small pixels of an active eye lens dosemeter prototype, based on Dosepix, from the radiation of a Megalix CatPlus X-ray tube with respect to the irradiation time.

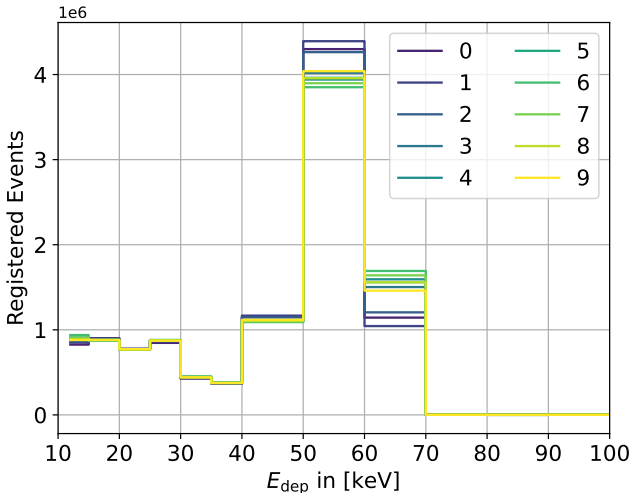

Figure B.3.: Exemplary energy deposition spectra of a radioactive $^{241}_{95}$Am sample, measured by the active eye lens dosemeter prototype with 32.3 s total irradiation time

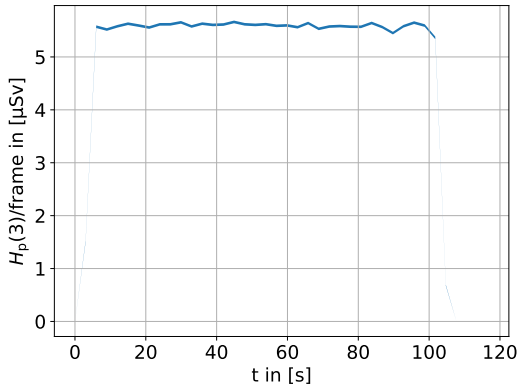

(a) Reference $H_p(3)$: 167 µSv

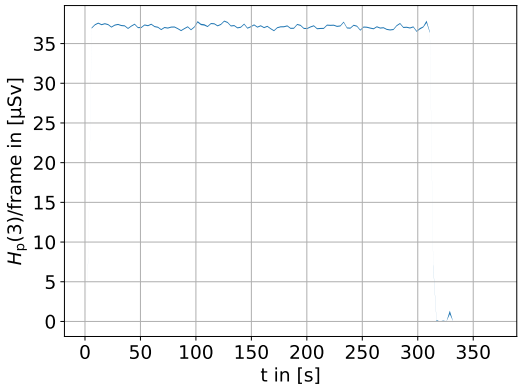

(b) Reference $H_p(3)$: 3.4 mSv

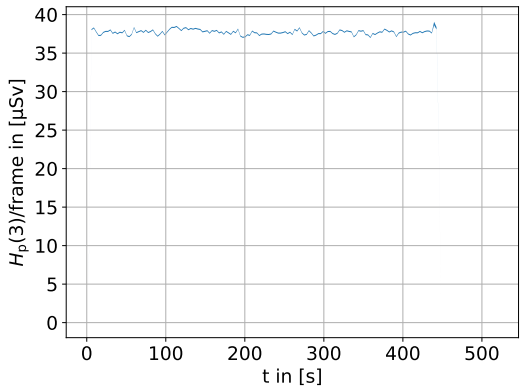

(c) Reference $H_p(3)$: 5.0 mSv

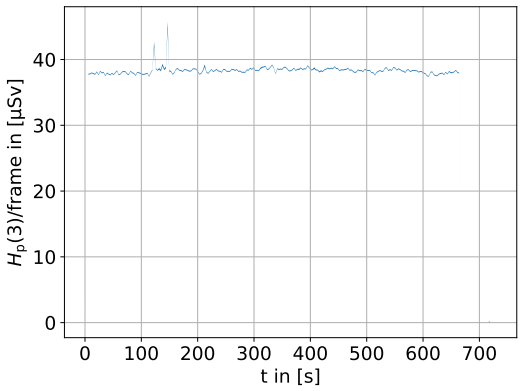

(d) Reference $H_p(3)$: 7.5 mSv

Figure B.4.: Estimated $H_p(3)$ after each read-out cycle with respect to time for the radiation quality W-30. The thickness of the line represents the approximated standard deviation during each read-out.

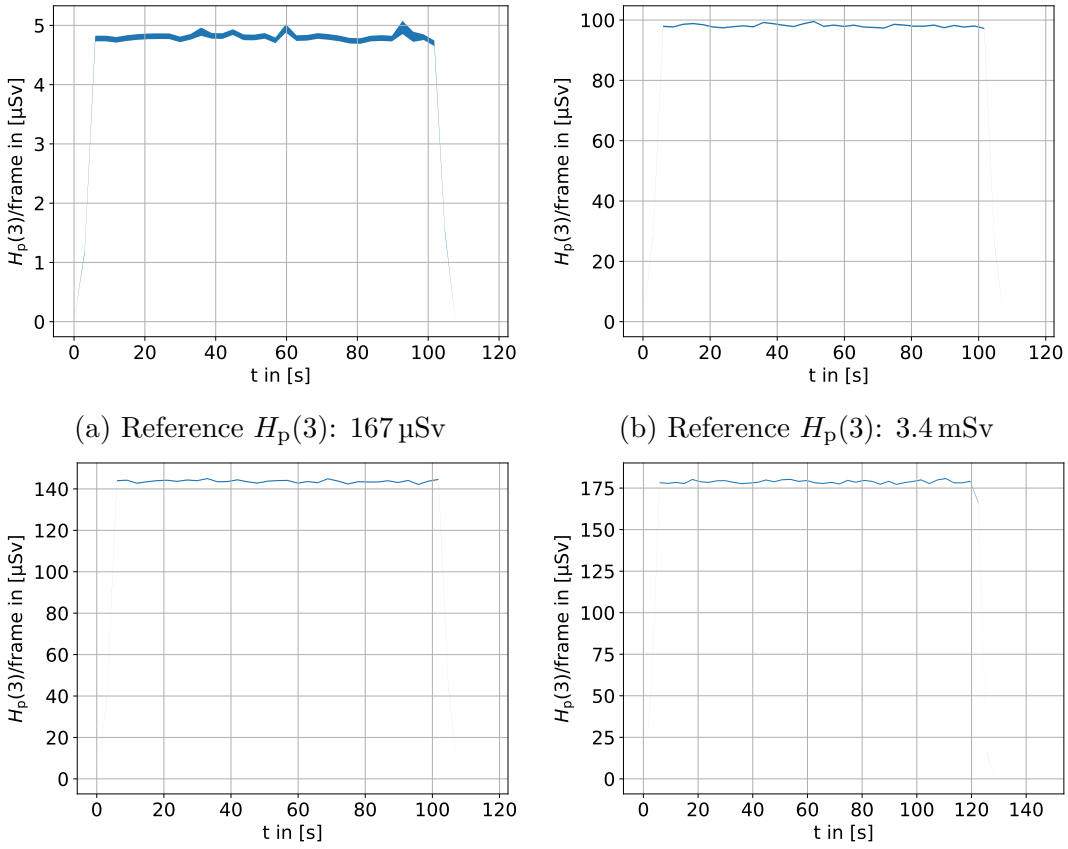

(a) Reference $H_p(3)$: 167 µSv

(b) Reference $H_p(3)$: 3.4 mSv

(c) Reference $H_p(3)$: 5.0 mSv

(d) Reference $H_p(3)$: 7.5 mSv

Figure B.5.: Estimated $H_p(3)$ after each read-out cycle with respect to time for the radiation quality W-80. The thickness of the line represents the approximated standard deviation during each read-out.

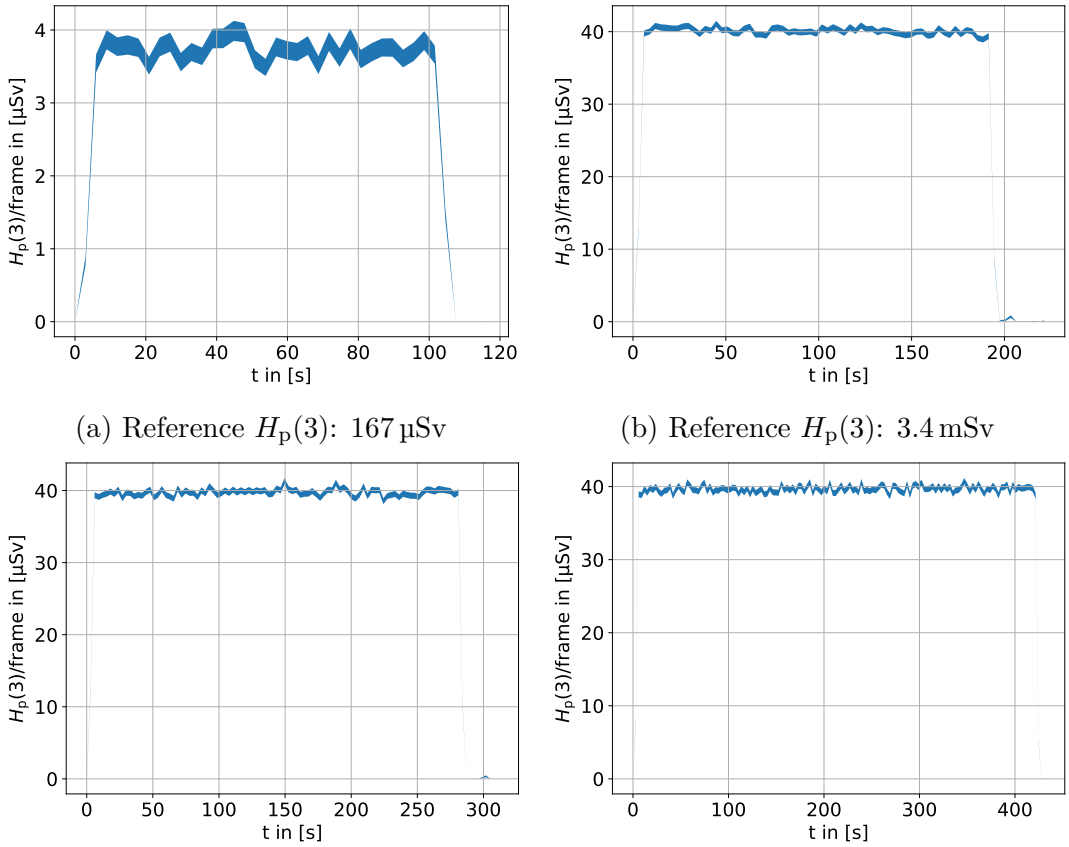

(a) Reference $H_p(3)$: 167 µSv

(b) Reference $H_p(3)$: 3.4 mSv

(c) Reference $H_p(3)$: 5.0 mSv

(d) Reference $H_p(3)$: 7.5 mSv

Figure B.6.: Estimated $H_p(3)$ after each read-out cycle with respect to time for the radiation quality N-150. The thickness of the line represents the approximated standard deviation during each read-out.

B.3. Beam Monitoring Simulations

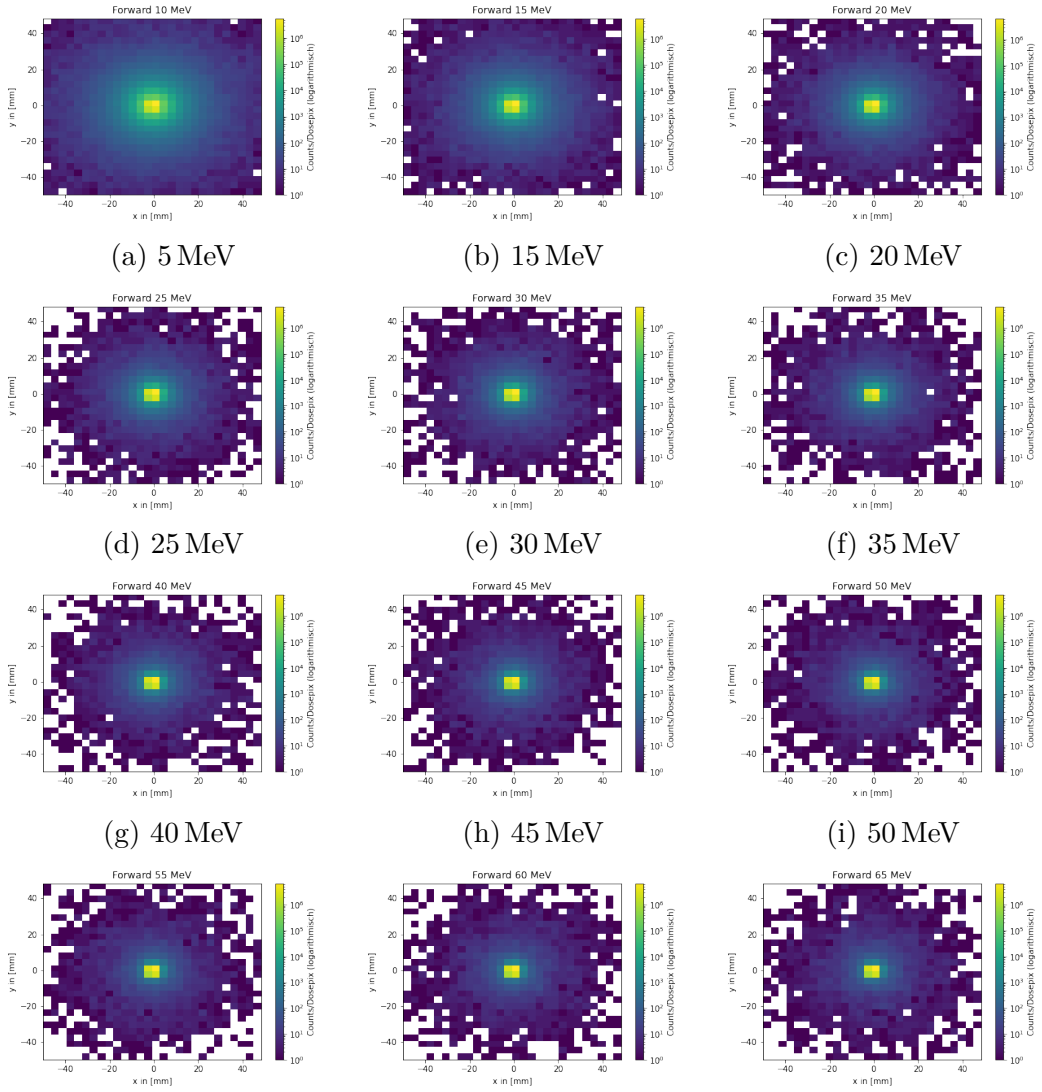

(a) 5 MeV (b) 15 MeV (c) 20 MeV

(d) 25 MeV (e) 30 MeV (f) 35 MeV

(g) 40 MeV (h) 45 MeV (i) 50 MeV

(j) 55 MeV (k) 60 MeV (l) 65 MeV

Figure B.7.: Registered events in forward direction.

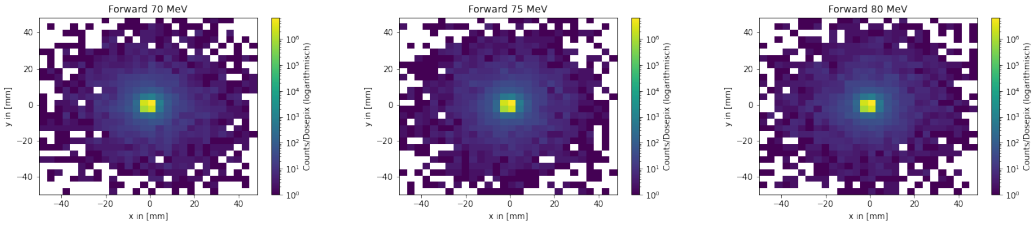

(a) 70 MeV (b) 75 MeV (c) 80 MeV

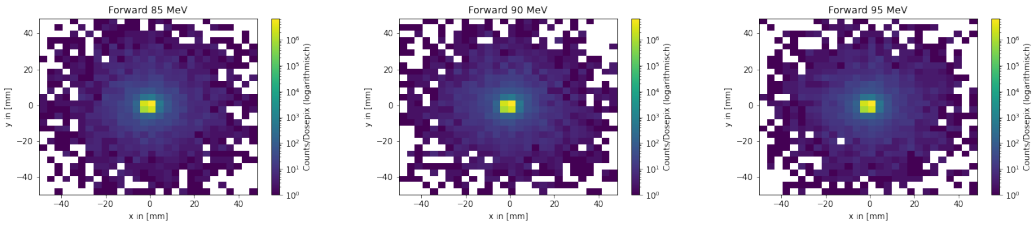

(d) 85 MeV (e) 90 MeV (f) 95 MeV

Figure B.8.: Registered events in forward direction.

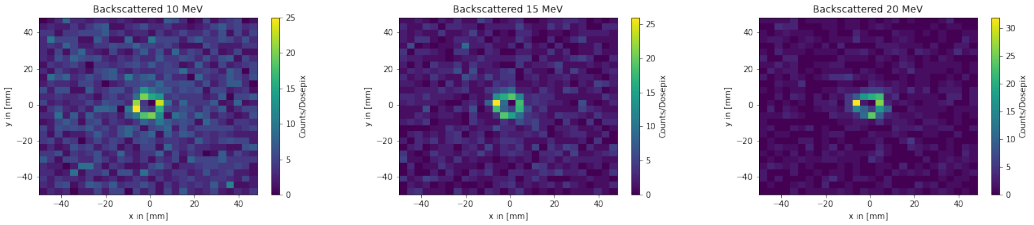

(a) 5 MeV (b) 15 MeV (c) 20 MeV

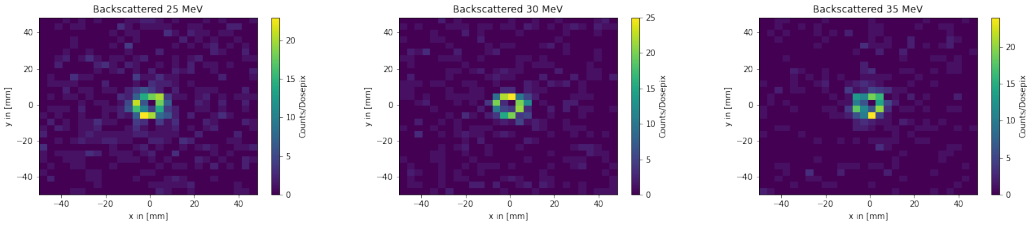

(d) 25 MeV (e) 30 MeV (f) 35 MeV

Figure B.9.: Registered events in backward direction.

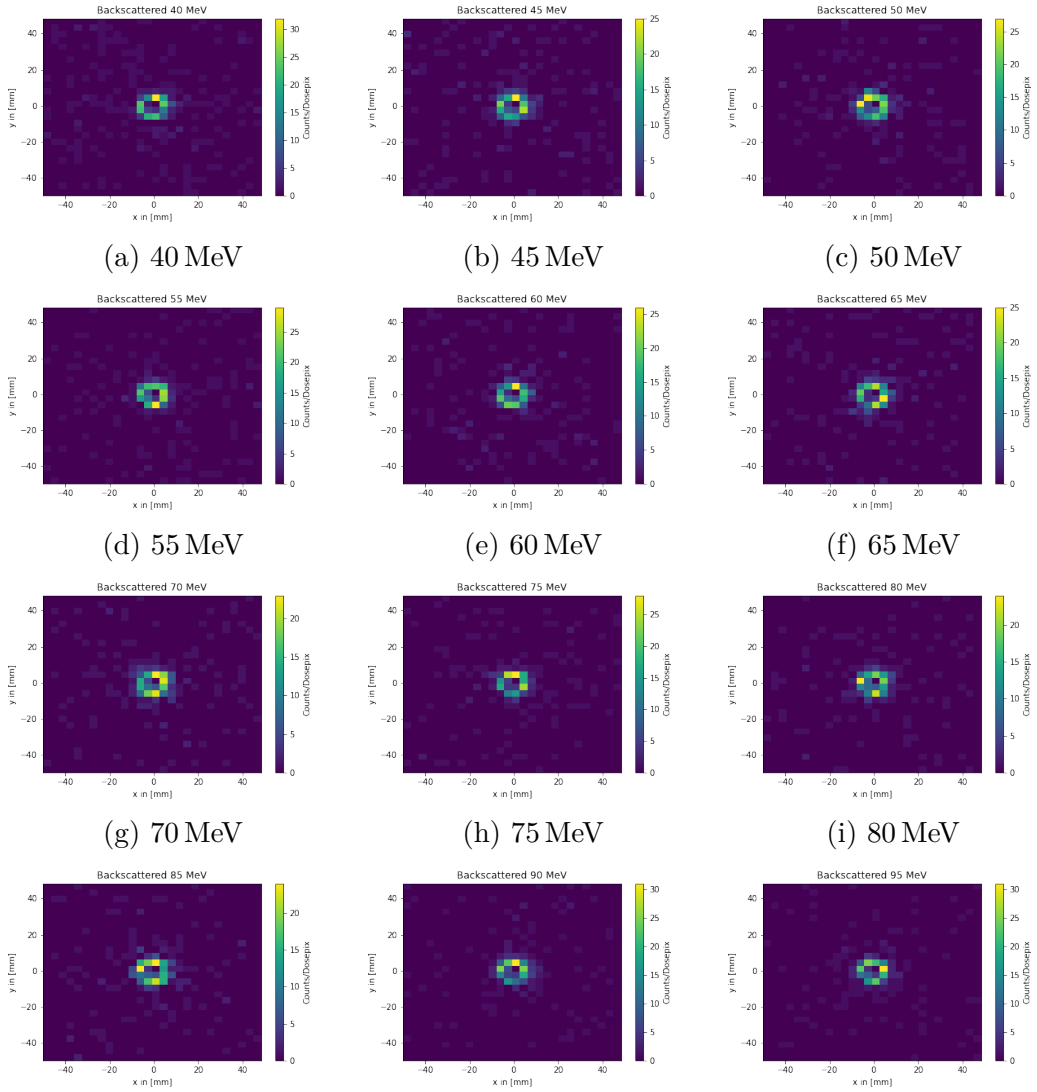

(a) 40 MeV (b) 45 MeV (c) 50 MeV

(d) 55 MeV (e) 60 MeV (f) 65 MeV

(g) 70 MeV (h) 75 MeV (i) 80 MeV

(j) 85 MeV (k) 90 MeV (l) 95 MeV

Figure B.10.: Registered events in backward direction.

Bibliography

[1] Isabelle Thierry-Chef et al. “Medical applications of ionizing radiation and radiation protection for European patients, population and environment”. In: *EPJ Nuclear Sci. Technol.* 8 (44 2022). URL: https://doi.org/10.1051/epjn/2022044.

[2] World Health Organization. *Ionizing radiation and health effects, accessed at 16.03.2026.* 2023. URL: https://www.who.int/news-room/fact-sheets/detail/ionizing-radiation-and-health-effects.

[3] Leslaw Gorniak et al. “A Practical Classification Approach for Chemical, Biological, Radiological and Nuclear (CBRN) Hazards Based on Toxicological and Situational Parameters”. In: *Applied Sciences* 15.19 (2025). ISSN: 2076-3417. DOI: 10.3390/app151910421. URL: https://www.mdpi.com/2076-3417/15/19/10421.

[4] D J Shah, R K Sachs, and D J Wilson. “Radiation-induced cancer: a modern view”. In: *British Journal of Radiology* 85.1020 (2014), e1166–e1173. ISSN: 0007-1285. DOI: 10.1259/bjr/25026140. eprint: https://academic.oup.com/bjr/article-pdf/85/1020/e1166/54539856/bjr_25026140.pdf. URL: https://doi.org/10.1259/bjr/25026140.

[5] A D Wrixon. “New ICRP recommendations”. In: *Journal of Radiological Protection* 28.2 (2008), p. 161. DOI: 10.1088/0952-4746/28/2/R02. URL: https://doi.org/10.1088/0952-4746/28/2/R02.

[6] F.A. Stewart et al. “2012 ICRP Statement on Tissue Reactions / Early and Late Effects of Radiation in Normal Tissues and Organs – Threshold Doses for Tissue Reactions in a Radiation Protection Context. ICRP Publication 118”. In: *ICRP 41(1/2)* (2012).

[7] Gabriel Chodick et al. “Risk of Cataract after Exposure to Low Doses of Ionizing Radiation: A 20-Year Prospective Cohort Study among US Radiologic Technologists”. In: *American Journal of Epidemiology* 168.6 (2008), pp. 620–631. ISSN: 0002-9262. DOI: 10.1093/aje/kwn171. eprint: https://academic.oup.com/aje/article-pdf/168/6/620/201598/kwn171.pdf. URL: https://doi.org/10.1093/aje/kwn171.

[8] Eiji Nakashima, Kazuo Neriishi, and Atsushi Minamoto. “A Reanalysis of Atomic-Bomb Cataract Data, 2000–2002: A Threshold Analysis”. In: *Health Physics* 90 (2 2006), pp. 154–160. DOI: 10.1097/01.HP.0000175442.03596.63. URL: https://journals.lww.com/health-physics/abstract/2006/02000/a_reanalysis_of_atomic_bomb_cataract_data,.6.aspx.

[9] Kazuo Neriishi et al. “Postoperative Cataract Cases among Atomic Bomb Survivors: Radiation Dose Response and Threshold”. In: *Radiation Research* 168.4 (2007), pp. 404 –408. DOI: 10.1667/RR0928.1. URL: https://doi.org/10.1667/RR0928.1.

[10] Florian Beißer et al. “Active Personal Eye Lens Dosimetry With the Hybrid Pixelated Dosepix Detector”. In: *IEEE Transactions on Radiation and Plasma Medical Sciences* 7.8 (2023), pp. 879–887. DOI: 10.1109/TRPMS.2023.3301503.

[11] Sandrine Pereira et al. “The Normal, the Radiosensitive, and the Ataxic in the Era of Precision Radiotherapy: A Narrative Review”. In: *Cancers* 14.24 (2022). ISSN: 2072-6694. DOI: 10.3390/cancers14246252. URL: https://www.mdpi.com/2072-6694/14/24/6252.

[12] Bundesamt für Strahlenschutz. *Radiotherapy treatment planning, accessed on 09.03.2026*. URL: https://www.bfs.de/EN/topics/ion/medicine/radiotherapy/planning/planning_node.html.

[13] William R. Leo. *Techniques for Nuclear and Particle Physics Experiments: A How-to Approach*. Springer- Verlag Berlin Heidelberg GmbH, 1994.

[14] W.S. Wong et al. “A pixel detector asic for dosimetry using time-over-threshold energy measurements”. In: *Radiation Measurements* 46.12 (2011). Proceedings of the 16th Solid State Dosimetry Conference , September 19-24 , Sydney , Australia, pp. 1619–1623. ISSN: 1350-4487. DOI: https://doi.org/10.1016/j.radmeas.2011.06.061. URL: https://www.sciencedirect.com/science/article/pii/S1350448711003209.

[15] W S Wong et al. “Electrical measurements of a multi-mode hybrid pixel detector ASIC for radiation detection”. In: *Journal of Instrumentation* 7.01 (2012), p. C01056. DOI: 10.1088/1748-0221/7/01/C01056. URL: https://doi.org/10.1088/1748-0221/7/01/C01056.

[16] Winnie Sze-Wing Wong. “A Hybrid Pixel Detector ASIC with Energy-Binning for Real-Time Spectroscopic Dose Measurements”. PhD thesis. Mid Sweden University, 2012.

[17] Dennis Haag et al. “Personal Dosimetry in Continuous Photon Radiation Fields With the Dosepix Detector”. In: *IEEE Transactions on Nuclear Science* 68.5 (2021), pp. 1129–1134. DOI: 10.1109/TNS.2021.3068832.

[18] Dennis Haag et al. “Personal Dosimetry in Direct Pulsed Photon Fields With the Dosepix Detector”. In: *IEEE Transactions on Nuclear Science* 69.12 (2022), pp. 2330–2334. DOI: 10.1109/TNS.2022.3222544.

[19] E. Fröjdh et al. “Spectral response of the energy-binning Dosepix ASIC coupled to a 300μm silicon sensor under high fluxes of synchrotron radiation”. In: *Nuclear Instruments and Methods in Physics Research Section A: Accelerators, Spectrometers, Detectors and Associated Equipment* 804 (2015), pp. 43–49. ISSN: 0168-9002. DOI: https://doi.org/10.1016/j.nima.2015.09.018. URL: https://www.sciencedirect.com/science/article/pii/S0168900215010700.

[20] Patrick Hufschmidt. “Dosimetry with the Dosepix detector in pulsed high dose rate photon fields”. PhD thesis. Friedrich-Alexander-Universität Erlangen-Nürnberg, 2022.

[21] Sebastian Schmidt. "Dosimetry and X-ray spectroscopy with the photon counting pixel detector Dosepix". PhD thesis. Friedrich-Alexander-Universität Erlangen-Nürnberg, 2021.

[22] Klaus Bethge, Gertrud Walter, and Bernhard Wiedemann. *Kernphysik: Eine Einführung, 3rd edition*. Springer, 2008.

[23] Wolfgang Demtröder. *Experimentalphysik 3: Atome, Moleküle und Festkörper*. Springer Spektrum, 2016.

[24] V.P. Chechev and N.K. Kuzmenko. *Am-241*. Tech. rep. International Atomic Energy Agency.

[25] NIST National Measurement Laboratory. *X-Ray Mass Attenuation Coefficients, physics.nist.gov/PhysRefData/XrayMassCoef/ElemTab/z14.html, accessed at 21.02.2026*.

[26] Wolfgang Demtröder. *Experimentalphysik 4: Kern-, Teilchen- und Astrophysik*. Springer Spektrum, 2017.

[27] Jingtian Fang et al. "Understanding the Average Electron–Hole Pair-Creation Energy in Silicon and Germanium Based on Full-Band Monte Carlo Simulations". In: *IEEE Transactions on Nuclear Science* 66.1 (2019), pp. 444–451. DOI: 10.1109/TNS.2018.2879593.

[28] NIST National Measurement Laboratory. *Stopping-Power & Range Tables for Electrons, Protons, and Helium Ions: NIST Standard Reference Database 124, https://www.nist.gov/pml/stopping-power-range-tables-electrons-protons-and-helium-ions, accessed at 12.01.2026*.

[29] V.M. Grishin and G.I. Merson. "A simple method for realistic estimation of the most probable energy loss in thin gas layers". In: *Nuclear Instruments and Methods in Physics Research Section A: Accelerators, Spectrometers, Detectors and Associated Equipment* 274.3 (1989), pp. 551–556. ISSN: 0168-9002. DOI: https://doi.org/10.1016/0168-9002(89)90190-3. URL: https://www.sciencedirect.com/science/article/pii/0168900289901903.

[30] Markus Schneider. "Investigation of Dosimetry for FLASH Radiotherapy with the Photon-Counting Pixel Detector Dosepix". MA thesis. Friedrich-Alexander-Universität Erlangen-Nürnberg, 2023.

[31] M. Ave et al. "Spectrally resolved pressure dependence measurements of air fluorescence emission with AIRFLY". In: *Nuclear Instruments and Methods in Physics Research Section A: Accelerators, Spectrometers, Detectors and Associated Equipment* 597.1 (2008). Proceedings of the 5th Fluorescence Workshop, pp. 41–45. ISSN: 0168-9002. DOI: https://doi.org/10.1016/j.nima.2008.08.052. URL: https://www.sciencedirect.com/science/article/pii/S016890020801276X.

[32] D.E. Shemansky and A.L. Broadfoot. "Excitation of N2 and N+2 systems by electrons—II. Excitation cross sections and N21PG low pressure afterglow". In: *Journal of Quantitative Spectroscopy and Radiative Transfer* 11.10 (1971), pp. 1401–1439. ISSN: 0022-4073. DOI: https://doi.org/10.1016/0022-4073(71)90106-3. URL: https://www.sciencedirect.com/science/article/pii/0022407371901063.

[33] R.F. Wuerker et al. “Lifetime measurements of the excited states of N2 AND N2+ by laser-induced fluorescence”. In: *Chemical Physics Letters* 150.6 (1988), pp. 443–446. ISSN: 0009-2614. DOI: https://doi.org/10.1016/0009-2614(88)80434-2. URL: https://www.sciencedirect.com/science/article/pii/0009261488804342.

[34] Wolfgang G. Alberts et al. “New dose quantities in radiation protection”. In: (1995). DOI: https://doi.org/10.7795/110.2020417EN. URL: https://oar.ptb.de/resources/show/10.7795/110.20200417EN.

[35] International Commission on Radiation Units and Measurements (ICRU). “Tissue Substitutes in Radiation Dosimetry and Measurement. ICRU Report 44”. In: *ICRU 23* (1989).

[36] Deutsches Institut für Normung. *Strahlenschutz – Röntgen- und Gamma-Referenzstrahlungsfelder zur Kalibrierung von Dosimetern und Dosisleistungsmessgeräten und zur Bestimmung ihres Ansprechvermögens als Funktion der Photonenenergie, Teil 3: Kalibrierung von Orts- und Personendosimetern und Messung ihres Ansprechvermögens als Funktion von Energie und Einfallswinkel (ISO 4037-3:2019); Deutsche Fassung EN ISO 4037-3:2021*. 2021.

[37] International Electrotechnical Commission. *DIN IEC 61526 (VDE 0492-1): 2020-08 Strahlenschutz-Messgeräte, Messung der Tiefen- und der Oberflächen-Personendosis Hp(10), Hp(3) und Hp(0,07) für Röntgen-, Gamma-, Neutronen- und Betastrahlung – Direkt ablesbare Personendosimeter (IEC 45B/960/CD:2020); Text Deutsch und Englisch*. 2020.

[38] S. McAleer. “A history of cancer and its treatment: Presidential Address to the Ulster Medical Society. 7th October 2021”. In: *The Ulster medical journal* 91 (3 2022), pp. 124–129. URL: https://pubmed.ncbi.nlm.nih.gov/36474852/.

[39] Stefanos Diamantopoulos et al. “Treatment plan verification: A review on the comparison of dose distributions”. In: *Physica Medica* 67 (2019), pp. 107–115. ISSN: 1120-1797. DOI: https://doi.org/10.1016/j.ejmp.2019.10.029. URL: https://www.sciencedirect.com/science/article/pii/S112017971930479X.

[40] Siyer Roohani et al. “Update on Dosing and Fractionation for Neoadjuvant Radiotherapy for Localized Soft Tissue Sarcoma”. In: *Current Treatment Options in Oncology* 25 (4 2024), pp. 543–555. DOI: 10.1007/s11864-024-01188-2. URL: https://doi.org/10.1007/s11864-024-01188-2.

[41] Natalia Matuszak et al. “FLASH radiotherapy: an emerging approach in radiation therapy”. In: *Reports of Practical Oncology and Radiotherapy* 27.2 (2022), pp. 343 –351. ISSN: 2083-4640. DOI: 10.5603/RPOR.a2022.0038. URL: https://journals.viamedica.pl/rpor/article/view/RPOR.a2022.0038.

[42] Rui Tang et al. “FLASH radiotherapy: A new milestone in the field of cancer radiotherapy”. In: *Cancer Letters* 587 (2024), p. 216651. ISSN: 0304-3835. DOI: https://doi.org/10.1016/j.canlet.2024.216651. URL: https://www.sciencedirect.com/science/article/pii/S0304383524000454.

[43] Roger J. Berry et al. “Survival of mammalian cells exposed to X rays at ultra-high dose-rates”. In: *British Journal of Radiology* 42.494 (2014), pp. 102–107. ISSN: 0007-1285. DOI: 10.1259/0007-1285-42-494-102. eprint: https://academic.oup.com/bjr/article-pdf/42/494/102/54228458/0007-1285-42-494-102.pdf. URL: https://doi.org/10.1259/0007-1285-42-494-102.

[44] Vincent Favaudon et al. “Ultrahigh dose-rate FLASH irradiation increases the differential response between normal and tumor tissue in mice”. In: *Science Translational Medicine* 6.245 (2014), 245ra93–245ra93. DOI: 10.1126/scitranslmed.3008973. eprint: https://www.science.org/doi/pdf/10.1126/scitranslmed.3008973. URL: https://www.science.org/doi/abs/10.1126/scitranslmed.3008973.

[45] Marie-Catherine Vozenin et al. “The Advantage of FLASH Radiotherapy Confirmed in Mini-pig and Cat-cancer Patients”. In: *Clinical Cancer Research* 25.1 (2019), pp. 35–42. ISSN: 1078-0432. DOI: 10.1158/1078-0432.CCR-17-3375. eprint: https://aacrjournals.org/clincancerres/article-pdf/25/1/35/2049875/35.pdf. URL: https://doi.org/10.1158/1078-0432.CCR-17-3375.

[46] Andrea Borghini et al. “FLASH ultra-high dose rates in radiotherapy: preclinical and radiobiological evidence”. In: *International Journal of Radiation Biology* 98.2 (2022). PMID: 34913413, pp. 127–135. DOI: 10.1080/09553002.2022.2009143. eprint: https://doi.org/10.1080/09553002.2022.2009143. URL: https://doi.org/10.1080/09553002.2022.2009143.

[47] Andreas Schüller et al. “The European Joint Research Project UHDpulse – Metrology for advanced radiotherapy using particle beams with ultra-high pulse dose rates”. In: *Physica Medica* 80 (2020), pp. 134–150. ISSN: 1120-1797. DOI: https://doi.org/10.1016/j.ejmp.2020.09.020. URL: https://www.sciencedirect.com/science/article/pii/S1120179720302362.

[48] Jean Bourhis et al. “Treatment of a first patient with FLASH-radiotherapy”. In: *Radiotherapy and Oncology* 139 (2019). FLASH radiotherapy International Workshop, pp. 18–22. ISSN: 0167-8140. DOI: https://doi.org/10.1016/j.radonc.2019.06.019. URL: https://www.sciencedirect.com/science/article/pii/S0167814019329597.

[49] Marie-Catherine Vozenin et al. “All Irradiations that are Ultra-High Dose Rate may not be FLASH: The Critical Importance of Beam Parameter Characterization and In Vivo Validation of the FLASH Effect”. In: *Radiation Research* 194.6 (2020), pp. 571 –572. DOI: 10.1667/RADE-20-00141.1. URL: https://doi.org/10.1667/RADE-20-00141.1.

[50] Magdalena Bazalova-Carter et al. “Balancing innovation and safety in FLASH radiotherapy”. In: *Nature Reviews Physics* 7 (12 2025), pp. 682–695. DOI: 10.1038/s42254-025-00881-x. URL: https://doi.org/10.1038/s42254-025-00881-x.

[51] Qixian Zhang et al. “Absence of Tissue-Sparing Effects in Partial Proton FLASH Irradiation in Murine Intestine”. In: *Cancers* 15.8 (2023). ISSN: 2072-6694. DOI: 10.3390/cancers15082269. URL: https://www.mdpi.com/2072-6694/15/8/2269.

[52] Kevin Liu et al. “Discordance in Acute Gastrointestinal Toxicity between Synchrotron-Based Proton and Linac-based Electron Ultra-High Dose Rate Irradiation”. In: *International Journal of Radiation Oncology*Biology*Physics* 122.2 (2025), pp. 491–501. ISSN: 0360-3016. DOI: https://doi.org/10.1016/j.ijrobp.2025.01.007. URL: https://www.sciencedirect.com/science/article/pii/S0360301625000586.

[53] Till Tobias Böhlen et al. “Effect of Conventional and Ultrahigh Dose Rate FLASH Irradiations on Preclinical Tumor Models: A Systematic Analysis”. In: *International Journal of Radiation Oncology*Biology*Physics* 117.4 (2023), pp. 1007–1017. ISSN: 0360-3016. DOI: https://doi.org/10.1016/j.ijrobp.2023.05.045. URL: https://www.sciencedirect.com/science/article/pii/S0360301623005357.

[54] Konrad P. Nesteruk et al. “Commissioning of a clinical pencil beam scanning proton therapy unit for ultra-high dose rates (FLASH)”. In: *Medical Physics* 48.7 (2021), pp. 4017–4026. DOI: https://doi.org/10.1002/mp.14933. eprint: https://aapm.onlinelibrary.wiley.com/doi/pdf/10.1002/mp.14933. URL: https://aapm.onlinelibrary.wiley.com/doi/abs/10.1002/mp.14933.

[55] Uwe Titt et al. “Design and validation of a synchrotron proton beam line for FLASH radiotherapy preclinical research experiments”. In: *Medical Physics* 49.1 (2022), pp. 497–509. DOI: https://doi.org/10.1002/mp.15370. eprint: https://aapm.onlinelibrary.wiley.com/doi/pdf/10.1002/mp.15370. URL: https://aapm.onlinelibrary.wiley.com/doi/abs/10.1002/mp.15370.

[56] R. Corsini et al. “First Experiments at the CLEAR User Facility”. In: *Proc. 9th International Particle Accelerator Conference (IPAC’18), Vancouver, BC, Canada, April 29-May 4, 2018* (Vancouver, BC, Canada). International Particle Accelerator Conference 9. https://doi.org/10.18429/JACoW-IPAC2018-THPMF014. Geneva, Switzerland: JACoW Publishing, 2018, pp. 4066–4069. ISBN: 978-3-95450-184-7. DOI: doi:10.18429/JACoW-IPAC2018-THPMF014. URL: http://jacow.org/ipac2018/papers/thpmf014.pdf.

[57] F. Stephan et al. “Detailed characterization of electron sources yielding first demonstration of European X-ray Free-Electron Laser beam quality”. In: *Phys. Rev. ST Accel. Beams* 13 (2 2010), p. 020704. DOI: 10.1103/PhysRevSTAB.13.020704. URL: https://link.aps.org/doi/10.1103/PhysRevSTAB.13.020704.

[58] Nolan Esplen et al. “Design optimization of an electron-to-photon conversion target for ultra-high dose rate x-ray (FLASH) experiments at TRIUMF”. In: *Physics in Medicine & Biology* 67.10 (2022), p. 105003. DOI: 10.1088/1361-6560/ac5ed6. URL: https://doi.org/10.1088/1361-6560/ac5ed6.

[59] Feng Gao et al. “First demonstration of the FLASH effect with ultrahigh dose rate high-energy X-rays”. In: *Radiotherapy and Oncology* 166 (2022), pp. 44–50. ISSN: 0167-8140. DOI: https://doi.org/10.1016/j.radonc.2021.11.004. URL: https://www.sciencedirect.com/science/article/pii/S016781402108796X.

[60] Allison Palmiero et al. "On the acceptance, commissioning, and quality assurance of electron FLASH units". In: *Medical Physics* 52.2 (2025), pp. 1207–1223. DOI: https://doi.org/10.1002/mp.17483. eprint: https://aapm.onlinelibrary.wiley.com/doi/pdf/10.1002/mp.17483. URL: https://aapm.onlinelibrary.wiley.com/doi/abs/10.1002/mp.17483.

[61] Muhammad Ramish Ashraf et al. "Dosimetry for FLASH Radiotherapy: A Review of Tools and the Role of Radioluminescence and Cherenkov Emission". In: *Frontiers in Physics* Volume 8 - 2020 (2020). ISSN: 2296-424X. DOI: 10.3389/fphy.2020.00328. URL: https://www.frontiersin.org/journals/physics/articles/10.3389/fphy.2020.00328.

[62] R Kranzer et al. "Response of diamond detectors in ultra-high dose-per-pulse electron beams for dosimetry at FLASH radiotherapy". In: *Physics in Medicine & Biology* 67.7 (2022), p. 075002. DOI: 10.1088/1361-6560/ac594e. URL: https://doi.org/10.1088/1361-6560/ac594e.

[63] Alexandra Bourgouin et al. "Calorimeter for Real-Time Dosimetry of Pulsed Ultra-High Dose Rate Electron Beams". In: *Frontiers in Physics* Volume 8 - 2020 (2020). ISSN: 2296-424X. DOI: 10.3389/fphy.2020.567340. URL: https://www.frontiersin.org/journals/physics/articles/10.3389/fphy.2020.567340.

[64] Faustino Gómez et al. "Development of an ultra-thin parallel plate ionization chamber for dosimetry in FLASH radiotherapy". In: *Medical Physics* 49.7 (2022), pp. 4705–4714. DOI: https://doi.org/10.1002/mp.15668. eprint: https://aapm.onlinelibrary.wiley.com/doi/pdf/10.1002/mp.15668. URL: https://aapm.onlinelibrary.wiley.com/doi/abs/10.1002/mp.15668.

[65] Patrik Gonçalves Jorge et al. "Technical note: Validation of an ultrahigh dose rate pulsed electron beam monitoring system using a current transformer for FLASH preclinical studies". In: *Medical Physics* 49.3 (2022), pp. 1831–1838. DOI: https://doi.org/10.1002/mp.15474. eprint: https://aapm.onlinelibrary.wiley.com/doi/pdf/10.1002/mp.15474. URL: https://aapm.onlinelibrary.wiley.com/doi/abs/10.1002/mp.15474.

[66] Kevin Liu et al. "Dual beam-current transformer design for monitoring and reporting of electron ultra-high dose rate (FLASH) beam parameters". In: *Journal of Applied Clinical Medical Physics* 24.2 (2023), e13891. DOI: https://doi.org/10.1002/acm2.13891. eprint: https://aapm.onlinelibrary.wiley.com/doi/pdf/10.1002/acm2.13891. URL: https://aapm.onlinelibrary.wiley.com/doi/abs/10.1002/acm2.13891.

[67] Roxane Oesterle et al. "Implementation and validation of a beam-current transformer on a medical pulsed electron beam LINAC for FLASH-RT beam monitoring". In: *Journal of Applied Clinical Medical Physics* 22.11 (2021), pp. 165–171. DOI: https://doi.org/10.1002/acm2.13433. eprint: https://aapm.onlinelibrary.wiley.com/doi/pdf/10.1002/acm2.13433. URL: https://aapm.onlinelibrary.wiley.com/doi/abs/10.1002/acm2.13433.

[68] C DesRosiers et al. "150-250 MeV electron beams in radiation therapy". In: *Physics in Medicine & Biology* 45.7 (2000), p. 1781. DOI: 10.1088/0031-9155/45/7/306. URL: https://doi.org/10.1088/0031-9155/45/7/306.

[69] Maria Grazia Ronga et al. “Back to the Future: Very High-Energy Electrons (VHEEs) and Their Potential Application in Radiation Therapy”. In: *Cancers* 13.19 (2021). ISSN: 2072-6694. DOI: 10.3390/cancers13194942. URL: https://www.mdpi.com/2072-6694/13/19/4942.

[70] Sophie Renard et al. “Electron radiation therapy: Back to the future?” In: *Cancer/Radiothérapie* 28.6 (2024). 35e congrès de la Société française de radiothérapie oncologique, pp. 553–559. ISSN: 1278-3218. DOI: https://doi.org/10.1016/j.canrad.2024.07.013. URL: https://www.sciencedirect.com/science/article/pii/S1278321824001409.

[71] Thomas R. Bortfeld and Jay S. Loeffler. “Three ways to make proton therapy affordable”. In: *Nature* 549 (7673 2017), pp. 451–453. DOI: 10.1038/549451a. URL: https://doi.org/10.1038/549451a.

[72] B F Wall et al. “What are the risks from medical X-rays and other low dose radiation?” In: *British Journal of Radiology* 79.940 (2014), pp. 285–294. ISSN: 0007-1285. DOI: 10.1259/bjr/55733882. eprint: https://academic.oup.com/bjr/article-pdf/79/940/285/54466446/bjr_55733882.pdf. URL: https://doi.org/10.1259/bjr/55733882.

[73] Anish Kumar and Walter Arnold. “High resolution in non-destructive testing: A review”. In: *Journal of Applied Physics* 132.10 (2022), p. 100901. ISSN: 0021-8979. DOI: 10.1063/5.0095328. eprint: https://pubs.aip.org/aip/jap/article-pdf/doi/10.1063/5.0095328/20035550/100901_1_5.0095328.pdf. URL: https://doi.org/10.1063/5.0095328.

[74] Deutsches Institut für Normung. *Strahlenschutz – Röntgen- und Gamma-Referenzstrahlungsfelder zur Kalibrierung von Dosimetern und Dosisleistungsmessgeräten und zur Bestimmung ihres Ansprechvermögens als Funktion der Photonenenergie: Teil 1: Strahlungseigenschaften und Erzeugungsmethoden (ISO 4037-1:2019); Deutsche Fassung EN ISO 4037-1:2021*. 2021.

[75] G. Hernández and F. Fernández. “A model of tungsten anode x-ray spectra”. In: *Medical Physics* 43.8Part1 (2016), pp. 4655–4664. DOI: https://doi.org/10.1118/1.4955120. eprint: https://aapm.onlinelibrary.wiley.com/doi/pdf/10.1118/1.4955120. URL: https://aapm.onlinelibrary.wiley.com/doi/abs/10.1118/1.4955120.

[76] Guillermo Hernández and Francisco Fernández. “xpecgen: A program to calculate x-ray spectra generated in tungsten anodes”. In: *Journal of Open Source Software* 1.7 (2016), p. 62. DOI: 10.21105/joss.00062. URL: https://doi.org/10.21105/joss.00062.

[77] Siemens Healthineers. *Megalix Cat*. URL: https://oem-products.webassets.siemens-healthineers.com/2ac8092aad312a64/7cfd9c5f4e08/Siemens-Healthineers_OEM_Data-Sheet_MEGALIX-Cat_2026-01.pdf.

[78] Center for X-ray Optics and Advanced Light Source. *X-RAY DATA BOOKLET, accessed at 12.03.2026*. 2009.

[79] Barbara Marchetti et al. "SINBAD-ARES - A Photo-Injector for external Injection Experiments in novel Accelerators at DESY". In: *Journal of Physics: Conference Series* 1596.1 (2020), p. 012036. DOI: 10.1088/1742-6596/1596/1/012036. URL: https://doi.org/10.1088/1742-6596/1596/1/012036.

[80] Florian Burkart et al. "The ARES linac at DESY". In: *Proc. LINAC'22* 31 (2022), pp. 691–694.

[81] Frank Stephan et al. "FLASHlab@PITZ: New R&D platform with unique capabilities for electron FLASH and VHEE radiation therapy and radiation biology under preparation at PITZ". In: *Physica Medica* 104 (2022), pp. 174–187. ISSN: 1120-1797. DOI: https://doi.org/10.1016/j.ejmp.2022.10.026. URL: https://www.sciencedirect.com/science/article/pii/S1120179722020877.

[82] Thomas Gabor. *Simulationen und Experimente zur Anwendung eines neuartigen spektroskopischen Pixeldetektors in der Personendosimetrie, diploma's thesis*. 2012.

[83] F. Krummenacher. "Pixel detectors with local intelligence: an IC designer point of view". In: *Nuclear Instruments and Methods in Physics Research Section A: Accelerators, Spectrometers, Detectors and Associated Equipment* 305.3 (1991), pp. 527–532. ISSN: 0168-9002. DOI: https://doi.org/10.1016/0168-9002(91)90152-G. URL: https://www.sciencedirect.com/science/article/pii/016890029190152G.

[84] Florian Beißer. *Temperature Dependence of the Hybrid Pixel Detector Dosepix with Respect to I_{Krum} Variation*. 2019.

[85] Florian Beißer. "Eye Lens Dosimetry with the Hybrid Photon-Counting Pixel Detector Dosepix". MA thesis. Friedrich-Alexander-Universität Erlangen-Nürnberg, 2022.

[86] Nico Kießl. *Untersuchung der temperaturabhängigen Dosisrekonstruktion des hybriden Pixeldetektors Dosepix, Bachelor's thesis*. 2025.

[87] Dennis Haag. "Radiation protection dosimetry and X-ray polarimetry with hybrid pixel detectors". PhD thesis. Friedrich-Alexander-Universität Erlangen-Nürnberg, 2022.

[88] Jan Jakubek et al. "Pixel detectors for imaging with heavy charged particles". In: *Nuclear Instruments and Methods in Physics Research Section A: Accelerators, Spectrometers, Detectors and Associated Equipment* 591.1 (2008). Radiation Imaging Detectors 2007, pp. 155–158. ISSN: 0168-9002. DOI: https://doi.org/10.1016/j.nima.2008.03.091. URL: https://www.sciencedirect.com/science/article/pii/S0168900208004245.

[89] Jan Jakubek. "Precise energy calibration of pixel detector working in time-over-threshold mode". In: *Nuclear Instruments and Methods in Physics Research Section A: Accelerators, Spectrometers, Detectors and Associated Equipment* 633 (2011). 11th International Workshop on Radiation Imaging Detectors (IWORID), S262–S266. ISSN: 0168-9002. DOI: https://doi.org/10.1016/j.nima.2010.06.183. URL: https://www.sciencedirect.com/science/article/pii/S0168900210013732.

[90] X. Llopart et al. “Timepix, a 65k programmable pixel readout chip for arrival time, energy and/or photon counting measurements”. In: *Nuclear Instruments and Methods in Physics Research Section A: Accelerators, Spectrometers, Detectors and Associated Equipment* 581.1 (2007). VCI 2007, pp. 485–494. ISSN: 0168-9002. DOI: https://doi.org/10.1016/j.nima.2007.08.079. URL: https://www.sciencedirect.com/science/article/pii/S0168900207017020.

[91] I Ritter et al. “Characterization of the Dosepix detector with XRF and analog testpulses”. In: *Journal of Instrumentation* 9.05 (2014), p. C05069. DOI: 10.1088/1748-0221/9/05/C05069. URL: https://doi.org/10.1088/1748-0221/9/05/C05069.

[92] Marek Sommer et al. “High-energy per-pixel calibration of timepix pixel detector with laboratory alpha source”. In: *Nuclear Instruments and Methods in Physics Research Section A: Accelerators, Spectrometers, Detectors and Associated Equipment* 1022 (2022), p. 165957. ISSN: 0168-9002. DOI: https://doi.org/10.1016/j.nima.2021.165957. URL: https://www.sciencedirect.com/science/article/pii/S0168900221009049.

[93] NIST National Measurement Laboratory. *ASTAR: Stopping Power and Range Tables for Alpha Particles, accessed at 25.02.2026*. URL: https://physics.nist.gov/cgi-bin/Star/ap_table.pl.

[94] S. Agostinelli et al. “Geant4—a simulation toolkit”. In: *Nuclear Instruments and Methods in Physics Research Section A: Accelerators, Spectrometers, Detectors and Associated Equipment* 506.3 (2003), pp. 250–303. ISSN: 0168-9002. DOI: https://doi.org/10.1016/S0168-9002(03)01368-8. URL: https://www.sciencedirect.com/science/article/pii/S0168900203013688.

[95] Michael F. L’Annunziata. “Chapter 16 - Cosmic Radiation”. In: *Radioactivity (Third Edition)*. Ed. by Michael F. L’Annunziata. Third Edition. Boston: Elsevier, 2023, pp. 795–822. ISBN: 978-0-323-90440-7. DOI: https://doi.org/10.1016/B978-0-323-90440-7.00023-5. URL: https://www.sciencedirect.com/science/article/pii/B9780323904407000235.

[96] J E Gaiser. “Charmonium spectroscopy from radiative decays of the J/psi and psi’”. PhD thesis. Jan. 1983. URL: https://www.osti.gov/biblio/5211117.

[97] S.P. George et al. “Very high energy calibration of silicon Timepix detectors”. In: *Journal of Instrumentation* 13.11 (2018), P11014. DOI: 10.1088/1748-0221/13/11/P11014. URL: https://doi.org/10.1088/1748-0221/13/11/P11014.

[98] Leonie Ullmann. “Clinical and Laboratory Measurements and Energy Range Enhancement in Eye Lens Dosimetry using the Hybrid Photon-Counting Pixel Detector Dosepix”. MA thesis. Friedrich-Alexander-Universität Erlangen-Nürnberg, 2024.

[99] S. Spannagel et al. “Allpix2: A modular simulation framework for silicon detectors”. In: *Nuclear Instruments and Methods in Physics Research Section A: Accelerators, Spectrometers, Detectors and Associated Equipment* 901 (2018), pp. 164–172. ISSN: 0168-9002. DOI: https://doi.org/10.1016/j.nima.2018.06.020. URL: https://www.sciencedirect.com/science/article/pii/S0168900218307411.

[100] A. Schübel et al. "A Geant4 based framework for pixel detector simulation". In: *Journal of Instrumentation* 9.12 (2014), p. C12018. DOI: 10.1088/1748-0221/9/12/C12018. URL: https://doi.org/10.1088/1748-0221/9/12/C12018.

[101] Walter Hartong. "Plan-Based Analog Verification Methodology". In: *cadence* (). URL: https://www.cadence.com/en_US/home/resources/white-papers/plan-based-analog-verification-methodology-wp.html.

[102] M Kroupa, J Jakubek, and P Soukup. "Optimization of the spectroscopic response of the Timepix detector". In: *Journal of Instrumentation* 7.02 (2012), p. C02058. DOI: 10.1088/1748-0221/7/02/C02058. URL: https://doi.org/10.1088/1748-0221/7/02/C02058.

[103] Takuya Yabu. *A study of exponential and Poisson distributions*. 2025. DOI: 10.31219/osf.io/sp8ev_v2. URL: osf.io/sp8ev_v2.

[104] Jürgen Hedderich and Lothar Sachs. *Angewandte Statistik, 17. edition*. Springer Nature, 2020.

[105] Leslie H. Miller. "Table of Percentage Points of Kolmogorov Statistics." In: *Journal of the American Statistical Association* 51.273 (1956), pp. 111–121. DOI: https://doi.org/10.2307/2280807.

[106] Danilo Giulietti and Leonida A. Gizzi. "X-ray emission from laser-produced plasmas". In: *La Rivista del Nuovo Cimento (1978-1999)* (1998). DOI: 10.1007/BF02874624. URL: https://doi.org/10.1007/BF02874624.

[107] R. Behrens and P. Ambrosi. "A TLD-based Few-channel Spectrometer for Mixed Photon, Electron, and Ion Fields with High Fluence Rates". In: *Radiation Protection Dosimetry* 101.1-4 (2002), pp. 73–76. ISSN: 0144-8420. DOI: 10.1093/oxfordjournals.rpd.a006062. eprint: https://academic.oup.com/rpd/article-pdf/101/1-4/73/9924012/73.pdf. URL: https://doi.org/10.1093/oxfordjournals.rpd.a006062.

[108] Rolf Behrens. "Wenig-Kanal-Spektrometer zur Messung von Elektronen- und Photonenspektren in ultrakurz gepulsten Strahlungsfeldern". PhD thesis. Friedrich-Schiller-Universität Jena, 2003.

[109] Rolf Behrens, Hayo Zutz, and Julian Busse. "Spectrometry of pulsed photon radiation". In: *Journal of Radiological Protection* 42.1 (2022), p. 011507. DOI: 10.1088/1361-6498/ac3dd0. URL: https://doi.org/10.1088/1361-6498/ac3dd0.

[110] R. Behrens et al. "Radiation measurements and simulations at the PHELIX laser facility, GSI". In: *Journal of Instrumentation* 17.05 (2022), P05033. DOI: 10.1088/1748-0221/17/05/P05033. URL: https://doi.org/10.1088/1748-0221/17/05/P05033.

[111] Hanno Krieger. *Grundlagen der Strahlungsphysik und des Strahlenschutzes, 7. edition*. Springer Spektrum, 2023.

[112] H. A. Kramers. "XCIII. On the theory of X-ray absorption and of the continuous X-ray spectrum". In: *The London, Edinburgh, and Dublin Philosophical Magazine and Journal of Science* 46.275 (1923), pp. 836–871. DOI: 10.1080/14786442308565244. eprint: https://doi.org/10.1080/14786442308565244. URL: https://doi.org/10.1080/14786442308565244.

[113] J. H. Hubbell and S. M. Seltzer. *Tables of X-Ray Mass Attenuation Coefficients and Mass Energy-Absorption Coefficients from 1 keV to 20 MeV for Elements Z = 1 to 92 and 48 Additional Substances of Dosimetric Interest*. Tech. rep. Radiation Physics Division, PML, NIST, 1996.

[114] R. Penrose. "On best approximate solutions of linear matrix equations". In: *Mathematical Proceedings of the Cambridge Philosophical Society* 52.1 (1956), 17–19. DOI: 10.1017/S0305004100030929.

[115] The SciPy community. *Scipy.linalg https://docs.scipy.org/doc/scipy/reference/linalg.html, accessed at 11.02.2026*.

[116] Andrew R. Conn, Nicholas I. M. Gould, and Philippe L. Toint. *Trust-Region Methods*. Society for Industrial, Applied Mathematics, and Mathematical Programming Society, 2000.

[117] NIST National Measurement Laboratory. *https://physics.nist.gov/PhysRefData/XrayMassCoef/ElemTab/z82.html, accessed at 26.11.2025*.

[118] Jianming Xie et al. "Extension of the R–L algorithm for γ-ray spectra deconvolution and its experimental results". In: *Nuclear Instruments and Methods in Physics Research Section A: Accelerators, Spectrometers, Detectors and Associated Equipment* 1035 (2022), p. 166812. ISSN: 0168-9002. DOI: https://doi.org/10.1016/j.nima.2022.166812. URL: https://www.sciencedirect.com/science/article/pii/S0168900222003059.

[119] Nicolas Brodusch, Karim Zaghib, and Raynald Gauvin. "Improvement of the energy resolution of energy dispersive spectrometers (EDS) using Richardson–Lucy deconvolution". In: *Ultramicroscopy* 209 (2020), p. 112886. ISSN: 0304-3991. DOI: https://doi.org/10.1016/j.ultramic.2019.112886. URL: https://www.sciencedirect.com/science/article/pii/S0304399119302438.

[120] T. Genetay et al. "RQR beam qualities measurement with the Timepix4 detector". In: *Radiation Measurements* 191 (2026), p. 107570. ISSN: 1350-4487. DOI: https://doi.org/10.1016/j.radmeas.2025.107570. URL: https://www.sciencedirect.com/science/article/pii/S1350448725001994.

[121] Ansh Patel et al. "Reconstruction algorithm for the runaway electron energy distribution function of the ITER hard x-ray monitor". In: *Physica Scripta* 98.8 (2023), p. 085604. DOI: 10.1088/1402-4896/ace135. URL: https://doi.org/10.1088/1402-4896/ace135.

[122] Ibrahim I. Suliman. "Review of various methods for occupational eye lens dosimetry in X-ray interventional procedures". In: *Radiation Physics and Chemistry* 236 (2025), p. 112936. ISSN: 0969-806X. DOI: https://doi.org/10.1016/j.radphyschem.2025.112936. URL: https://www.sciencedirect.com/science/article/pii/S0969806X25004281.

[123] *Liste der Baumusterprüfungen von Personendosimetern für die Messgröße Oberflächen-Personendosis Hp(0,07), Augenlinsen Personendosis Hp(3) und Tiefen-Personendosis Hp(10) gemäß PTB-Anforderungen 23.2*. 2026.

[124] *STM32WB55RG: Ultra-low-power dual core Arm Cortex-M4 MCU 64 MHz, Cortex-M0+ 32 MHz with 1 Mbyte of Flash memory, Bluetooth LE 5.4, 802.15.4, Zigbee, Thread, Matter, USB, LCD, AES-256* https://www.st.com/en/microcontrollers-microprocessors/stm32wb55rg.html. STMicroelectronics.

[125] N. W. Marshall and K. Faulkner. "The dependence of the scattered radiation dose to personnel on technique factors in diagnostic radiology". In: *British Journal of Radiology* 65.769 (2014), pp. 44–49. ISSN: 0007-1285. DOI: 10.1259/0007-1285-65-769-44. eprint: https://academic.oup.com/bjr/article-pdf/65/769/44/55002787/0007-1285-65-769-44.pdf. URL: https://doi.org/10.1259/0007-1285-65-769-44.

[126] Stephen GR Barnard et al. "Radiation protection of the eye lens in medical workers—basis and impact of the ICRP recommendations". In: *British Journal of Radiology* 89.1060 (2016), p. 20151034. ISSN: 0007-1285. DOI: 10.1259/bjr.20151034. eprint: https://academic.oup.com/bjr/article-pdf/89/1060/20151034/54455225/bjr.20151034.pdf. URL: https://doi.org/10.1259/bjr.20151034.

[127] Sophie Jacob et al. "Interventional cardiologists and risk of radiation-induced cataract: Results of a French multicenter observational study". In: *International Journal of Cardiology* 167.5 (2013), pp. 1843–1847. ISSN: 0167-5273. DOI: https://doi.org/10.1016/j.ijcard.2012.04.124. URL: https://www.sciencedirect.com/science/article/pii/S0167527312005608.

[128] *Sensor-CASSY 2,* https://www.leybold-shop.com/sensor-cassy-2-524013.html*, accessed at 12.12.2025.* LEYBOLD®.

[129] *Temperature probe, NiCr-Ni, fast, type K,* https://www.leybold-shop.com/temperature-probe-nicr-ni-fast-type-k-6661261.html*, accessed at 12.12.2025.* LEYBOLD®.

[130] Comet X-ray. *iVario 160.* URL: https://xray.comet.tech/en/products/ivario-160.

[131] *Mavig BR126 Röntgenschutzbrille https://mavig.de/produkt/br126/.*

[132] Tom Tröltzsch. *Examination of the Real Life Application of the Hybrid Pixelated Dosepix Detector on a Humanoid Head Phantom. Bachelor's thesis.* 2023.

[133] R. Behrens and O. Hupe. "Influence of the phantom shape (slab, cylinder or Alderson) on the performance of an Hp(3) eye dosemeter." In: *Radiat Prot Dosimetry. 2016 Mar;168(4):441-9. doi: 10.1093/rpd/ncv366. Epub 2015 Jul 12. PMID: 26170437* (2016).

[134] J. Walbersloh and F. Busch. "A Thin-Layer LiF Thermoluminescence Dosemeter System with Fast Readout for the Use in Personal Dosimetry Services". In: *Radiation Protection Dosimetry* 170.1-4 (2016), pp. 191–194. ISSN: 0144-8420. DOI: 10.1093/rpd/ncv478. eprint: https://academic.oup.com/rpd/article-pdf/170/1-4/191/7456290/ncv478.pdf. URL: https://doi.org/10.1093/rpd/ncv478.

[135] P. Bilski et al. “The new EYE-D™ dosemeter for measurements of HP(3) for medical staff”. In: *Radiation Measurements* 46.11 (2011). International Workshop on Optimization of Radiation Protection of Medical Staff, ORAMED 2011, pp. 1239–1242. ISSN: 1350-4487. DOI: https://doi.org/10.1016/j.radmeas.2011.04.031. URL: https://www.sciencedirect.com/science/article/pii/S1350448711001570.

[136] International Organization for Standardization. *ISO 29661:2012 Reference radiation fields for radiation protection — Definitions and fundamental concepts*. 2012.

[137] Leonie Ullmann et al. “Active Eye Lens Dosimetry With Dosepix: Influence of Measurement Position and Lead Glass Shielding”. In: *IEEE Transactions on Radiation and Plasma Medical Sciences* (2025), pp. 1–1. DOI: 10.1109/TRPMS.2025.3609894.

[138] G. Gualdrini et al. “Air kerma to HP(3) conversion coefficients for photons from 10 keV to 10 MeV, calculated in a cylindrical phantom”. In: *Radiation Protection Dosimetry* 154.4 (2012), pp. 517–521. ISSN: 0144-8420. DOI: 10.1093/rpd/ncs269. eprint: https://academic.oup.com/rpd/article-pdf/154/4/517/4539288/ncs269.pdf. URL: https://doi.org/10.1093/rpd/ncs269.

[139] J. Brunzendorf and R. Behrens. “How to type test the coefficient of variation of an indication”. In: *Radiation Protection Dosimetry* 123.1 (2006), pp. 21–31. ISSN: 0144-8420. DOI: 10.1093/rpd/ncl078. eprint: https://academic.oup.com/rpd/article-pdf/123/1/21/4671803/ncl078.pdf. URL: https://doi.org/10.1093/rpd/ncl078.

[140] F. Perotti and C. Fiorini. “Observed energy dependence of Fano factor in silicon at hard X-ray energies”. In: *Nuclear Instruments and Methods in Physics Research Section A: Accelerators, Spectrometers, Detectors and Associated Equipment* 423.2 (1999), pp. 356–363. ISSN: 0168-9002. DOI: https://doi.org/10.1016/S0168-9002(98)01264-9. URL: https://www.sciencedirect.com/science/article/pii/S0168900298012649.

[141] The SciPy community. *Scipy.optimize https://docs.scipy.org/doc/scipy/reference/optimize.html, accessed at 04.12.2025.*

[142] Johan Nilsson. *Implementing a High-Resolution Time Provider for Windows, accessed on 04.02.2026*. Tech. rep. Microsoft, 2004. URL: https://learn.microsoft.com/en-us/archive/msdn-magazine/2004/march/implementing-a-high-resolution-time-provider-for-windows.

[143] The University of North Carolina at Chapel Hill. *Measurement and Uncertainty Analysis Guide*. URL: https://users.physics.unc.edu/~deardorf/uncertainty/UNCguide.pdf.

[144] International Electrotechnical Commission. *IEC 61267:2025. Medical diagnostic X-ray equipment - Radiation conditions for use in the determination of characteristics*. 2025.

[145] T. Poikela et al. “Timepix3: a 65K channel hybrid pixel readout chip with simultaneous ToA/ToT and sparse readout”. In: *Journal of Instrumentation* 9 (2014). DOI: 10.1088/1748-0221/9/05/C05013. URL: https://iopscience.iop.org/article/10.1088/1748-0221/9/05/C05013.

[146] Hannah Schmidt. *Untersuchung zu den Variationskoeffizienten zweier Prototypen des aktiven Augenlinsendosimeters auf Basis des Dosepix-Detektors. Zulassungsarbeit*. 2024.

[147] Linda Pfohlmann. *Untersuchung der Reproduzierbarkeit von Dosismessung mit dem Dosepix-Detektor. Bachelor's thesis*. 2024.

[148] Joseph Leong and David Shimm. “A method for consistent precision radiation therapy”. In: *Radiotherapy and Oncology* 3.1 (1985), pp. 89–92. ISSN: 0167-8140. DOI: https://doi.org/10.1016/S0167-8140(85)80012-8. URL: https://www.sciencedirect.com/science/article/pii/S0167814085800128.

[149] M. Ave et al. “Spectrally resolved pressure dependence measurements of air fluorescence emission with AIRFLY”. In: *Nuclear Instruments and Methods in Physics Research Section A: Accelerators, Spectrometers, Detectors and Associated Equipment* 597.1 (2008). Proceedings of the 5th Fluorescence Workshop, pp. 41–45. ISSN: 0168-9002. DOI: https://doi.org/10.1016/j.nima.2008.08.052. URL: https://www.sciencedirect.com/science/article/pii/S016890020801276X.

[150] Fernando Arqueros, Jörg R. Hörandel, and Bianca Keilhauer. “Air fluorescence relevant for cosmic-ray detection—Review of pioneering measurements”. In: *Nuclear Instruments and Methods in Physics Research Section A: Accelerators, Spectrometers, Detectors and Associated Equipment* 597.1 (2008). Proceedings of the 5th Fluorescence Workshop, pp. 23–31. ISSN: 0168-9002. DOI: https://doi.org/10.1016/j.nima.2008.08.055. URL: https://www.sciencedirect.com/science/article/pii/S0168900208012734.

[151] D3 Strahlenschutz DESY Hamburg. *Personal Correspondence about unpublished results*.

[152] Basler AG. *Basler Product Documentation: a2A2840-14gmUV, accessed at 18.12.2025*. URL: https://docs.baslerweb.com/a2a2840-14gmuv.

[153] Sony Semiconductor Solutions Corporation. *Ultraviolet (UV) Image Sensor, accessed at 18.12.2025*. URL: https://www.sony-semicon.com/en/products/is/industry/uv.html.

[154] Geant4 Collaboration. *Geant4 Material Database, accessed at 19.03.2026*. URL: https://geant4.web.cern.ch/documentation/dev/bfad_html/ForApplicationDevelopers/Appendix/materialNames.html#g4matrdb.

[155] L. Prado Jr. et al. “Simulation of the fluorescence detector of the Pierre Auger Observatory”. In: *Nuclear Instruments and Methods in Physics Research Section A: Accelerators, Spectrometers, Detectors and Associated Equipment* 545.3 (2005), pp. 632–642. ISSN: 0168-9002. DOI: https://doi.org/10.1016/j.nima.2005.01.346. URL: https://www.sciencedirect.com/science/article/pii/S0168900205007540.

[156] M Nagano et al. “Photon yields from nitrogen gas and dry air excited by electrons”. In: *Astroparticle Physics* 20.3 (2003), pp. 293–309. ISSN: 0927-6505. DOI: https://doi.org/10.1016/S0927-6505(03)00192-0. URL: https://www.sciencedirect.com/science/article/pii/S0927650503001920.

[157] M. Nagano et al. “New measurement on photon yields from air and the application to the energy estimation of primary cosmic rays”. In: *Astroparticle Physics* 22.3 (2004), pp. 235–248. ISSN: 0927-6505. DOI: https://doi.org/10.1016/j.astropartphys.2004.08.002. URL: https://www.sciencedirect.com/science/article/pii/S0927650504001434.

[158] TLK Energy. *Air Density, accessed at 18.03.2026*. URL: https://tlk-energy.de/en/tools/air-density.

[159] Basler AG. *Basler Product Documentation: a2A2440-20gm, accessed at 13.01.2026*. URL: https://docs.baslerweb.com/aca2440-20gm#.

[160] International Commission on Radiation Units and Measurements (ICRU). “Determination of Absorbed Dose in a Patient Irradiated by Beams of X or Gamma Rays in Radiotherapy Procedures. ICRU Report 24”. In: *ICRU 67* (1976).

[161] Alta Vision. *TM-1405GE - Industrial GigE Monochrome Camera*. URL: https://www.altavision.com.br/Datasheets/JAI_EN/TM-1405GE.html.

[162] Edmund Optics BV. *Plankonvexe Linse aus UV-Quarzglas, 25 mm Durchm. x 40 mm BW, unbeschichtet, accessed on 30.01.2026*. URL: https://www.edmundoptics.de/p/25mm-dia-x-40mm-fl-uncoated-uv-plano-convex-lens/37049/.

[163] Joel Herrera et al. “KrakenOS: Python-based general exact ray tracing library”. In: *Optical Engineering* 61.1 (2022), p. 015101. DOI: 10.1117/1.OE.61.1.015101. URL: https://doi.org/10.1117/1.OE.61.1.015101.

[164] Edmund Optics BV. *Plankonvexe Linse aus UV-Quarzglas, 50 mm Durchm. x 100 mm BW, unbeschichtet, accessed on 30.01.2026*. URL: https://www.edmundoptics.de/p/50mm-dia-x-100mm-fl-uncoated-uv-plano-convex-lens/21736/.

[165] Thorlabs. *LD4931f = -25.0 mm, Ø1″ UV Fused Silica Bi-Concave Lens, Uncoated, accessed on 30.01.2026*. URL: https://www.thorlabs.com/item/LD4931.

[166] Wolfgang Demtröder. *Experimentalphysik 2: Elektrizität und Optik*. Springer Spektrum, 2017.

[167] Michael W. Davidson MicroscopyU. *Numerical Aperture*. URL: https://www.microscopyu.com/microscopy-basics/numerical-aperture.

[168] Basler AG. *Basler Product Documentation: acA2500-60uc, accessed at 01.02.2026*. URL: https://docs.baslerweb.com/aca2500-60uc.

[169] Thorlabs. *R1L1S7NNegative 1951 USAF Test Target Groups*. URL: https://www.thorlabs.com/item/R1L1S7N.

[170] European XFEL. *The European X-Ray Free-Electron Laser Facility and the Challenges of Our Time, accessed on 02.02.2026*. Tech. rep.

[171] G. Weber. *X-Ray attenuation & absorption calculator*. URL: https://web-docs.gsi.de/~stoe_exp/web_programs/x_ray_absorption/index.php.

[172] Basler AG. *Basler Product Documentation: a2A4504-5gmBAS, accessed at 02.02.2026*. URL: https://docs.baslerweb.com/a2a4504-5gmbas?.

Acknowledgements

A lot was going on in the last four years, resulting in this thesis at the very end. Almost everything of the stuff that I presented over the last 200 pages would have been impossible without the work, guidance, and support of many different people from many different institutions. Although it is impossible to mention everyone, I want to highlight those people who had the greatest impact on the success of this work:

First of all, I want to thank **Stefan Funk** for the supervision of this PhD thesis after taking over from Thilo Michel. Thanks for all the scientific input, the positive and constructive working atmosphere, the availability in all matters, the commitment to make beamtimes happen, and the trust in letting me work very independently.

Thilo Michel for providing the opportunity for a PhD program in the first place, the very useful and inspiring scientific input, and for establishing all necessary contacts and collaborations.

Ivor Fleck, as the third member of my PhD committee, for his input towards a successful PhD program, as well as for the opportunity to get in touch with the Marienklinik Siegen, and for overseeing the measurement campaign.

Martin Rongen, as the new leader of the TechTransfer group at ECAP. Thanks for the huge amount of super-useful scientific input and the willingness to engage in every topic by 100 %, thanks for the infectious enthusiasm that helped to reignite the spirit of TechTransfer, thanks for proofreading parts of the NitroFLASH-chapter, and thanks for the always constructive scepticism, e.g., by disbelieving in the existence of chocolate bananas at the cafeteria.

ECAP would crumble to dust within a week without the tireless effort of **Gabriele Eckner**. Thanks for the huge support in all bureaucratic matters, the unsurpassed overview in all official matters, serving more than once as the crucial safety net, and the skill to find the best solution for everyone against all odds.

Dennis Haag for the - without doubt - best possible supervision in the field of dosimetry that I can imagine. Without this unmatched expertise in radiation protection dosimetry, metrology, and detector physics, and the will to train me to become the old warrior, I would not be where I am now. Being supervised has never really stopped, even years after Dennis' official departure, and new ideas for measurements are always on their way. An additional great thanks for reading the entire NitroFLASH chapter and providing very constructive feedback.

Sebastian Schmidt for his amazing groundwork and support. Although the overlap

with my PhD program was short, no Dosepix measurement, no energy calibration, and no Allpix simulation would be possible up until this day without this work. Also, thanks for encouraging me to try out self-esteem every once in a while.

Leonie Ullmann for the collaboration in the dosimetry group, the helpful thinking along in the outline of this thesis, the nice discussions on all subjects, and many thanks for proofreading the "eye lens prototype" chapter, introduction, conclusion, and the abstracts.

Markus Schneider for proofreading the spectrometry chapter and for his support in all the needs for TechTransfer, serving as the link between dosimetry and phase-contrast imaging, as well as Franconia and Upper Palatinate.

Constantin Rauch, as the undisputed admin of the TechTransfer group. Thanks for the unmatched support in the resistance against the rise of the machines and the plenty of nice conversations about TTRPGs, politics, and everything else.

Department 6.3 of PTB for opening their doors and experimental halls for our eye lens dosimetry studies, the support and analysis of the lead glass measurements, and for the excellent expertise in dosimetry matters. A special thanks to **Christian Fuhg, Rolf Behrens, Phil Brüggemann, Jürgen Roth, Hayo Zutz, Oliver Hupe**, and **Gerhard Hilgers**.

The radiation protection group **D3** of DESY Hamburg for their collaboration in the NitroFLASH project and support at the various beamtimes at ARES and XFEL. A special thanks to **Hannes Dinter, Oliver Stein, Sven Zander, Ulrike Büchler,** and **Albrecht Leuschner**.

The ARES crew of DESY Hamburg for enabling a huge amount of measurements, carrying this thesis, and for stepping in when PITZ was unavailable. Thanks for the great support before and during the beamtimes. A special thanks to **Florian Burkart, Willi Kuropka,** and **Max Kellermeier**.

DESY Zeuthen and, in particular, the PITZ group, for establishing the NitroFLASH collaboration and enabling the beamtime in 2024. Thanks to **Anna Nelles** for bringing everyone together, **Daniel Villani** as ECAP's outpost in Zeuthen, **Frank Stephan** and **Matthias Groß** for the collaboration, **Stefan Weisse** for providing and helping with the Jai camera, and **Frieder Müller** for the technical support during the beamtime.

The crew at the **EuXFEL** for allowing me to join the beamtime. Thanks to **Peter Zalden** and **Dmitry Khakulin** for operating the FXE beamline.

The crew at the **Marienklinik Siegen** for the warm welcome and the opportunity to take measurements with the eye lens dosemeter. Thanks again to **Ivor Fleck**, and also **Christian Hohl, Maria Lilholt, Hassan Özmanevra, Helena Serr, Lars Maczey,** and **Florian Cunz**.

The crew at the **MPA-NRW** for letting us measure at their facility, helping with the operation of the LiF eye lens dosemeter, and supervising Tom and me excellently for the whole week without any personal benefit. Thanks to **Jörg Walbersloh** for making everything happen, as well as **Elena Lynnyk** and **Marion Schulte** for the excellent support.

Every student I have had the pleasure of supervising, for I have learned new stuff about physics and myself every time. Thanks again to **Leonie Ullmann**, and also **Hannah Schmidt, Aynur Akcay, Tom Tröltzsch, Linda Pfohlmann, Nico Kießl, Sarah Ritzer**, and **Cornelius Hohnhorst**.

Norman Uhlmann for the help in trying to transfer the eye lens dosemeter to industry and establishing the connection with PTW.

Thomas Kurin for the development of the ring-shaped board for NitroFLASH and the ongoing technical support.

Everyone at **ECAP** for the nice working atmosphere. Special thanks to **Kay Graf** for holding ECAP together, **Heike Wilhelm** for the excellent bureaucratic support in the first phase of my PhD, **Adrian Zink** for all his support regarding UV-LEDs and ordering stuff, **Tamás Gál** for his effort to fix the ringboard firmware, **Johannes Schäfer** for admin work and the very helpful introduction into 3D-printing, and **Benjamin Schwab** for his support with the optical Basler camera.

The **PCI Group** for the nice co-working and kind atmosphere. Apart from **Constantin Rauch** and **Markus Schneider**, many thanks go to **Stephan Schreiner, Veronika Ludwig,** and **Bernhard Akstaller**.

The **Mechanical Workshop** for all the many occasions of support, especially the many iterations of making the X-ray chambers safe.

Jürgen Hößl and **Thorsten Kühn** for being the radiation safety responsibles and enabling all measurements with ionizing radiation

Michael Campbell and Rafael Ballabriga from the Medipix Collaboration for the support in solving the mystery of Dosepix's temperature dependence.

Everyone of my friends, family and partnership who supported me emotionally in all ups and downs of the last years.